

Optimization and Application of Flowing Atmospheric-Pressure Afterglow Mass Spectrometry for Direct Surface Sampling and Quantitative Analysis

DISSERTATION

Christopher Kuhlmann

University of Siegen

– Siegen 2019 –

Optimization and Application of Flowing Atmospheric-Pressure Afterglow Mass Spectrometry for Direct Surface Sampling and Quantitative Analysis

DISSERTATION

to obtain the degree of Doctor of Science (Dr. rer. nat.)

submitted by M. Sc. Christopher Kuhlmann
born in Münster

School of Science and Technology
University of Siegen
– Siegen 2019 –

Supervisor and first reviewer
Prof. Dr. Carsten Engelhard
University of Siegen

Second reviewer
Prof. Dr. Ulrich Jonas
University of Siegen

Date of the oral examination

31.01.2020

Für meine Familie

Abstract

Ambient desorption/ionization mass spectrometry (ADI-MS) has emerged as an important field for direct sample analysis since the mid-2000s, when desorption electrospray ionization (DESI) and direct analysis in real time (DART) were introduced. The main goal of ADI-MS is to minimize sample preparation procedures (*e.g.*, solvent extraction) and to overcome the long analysis times, often encountered with chromatographic separations, by directly desorbing the target analytes from the sample surface.

In the first part of this thesis, a brief summary and review will highlight the main achievements for the optimization of plasma-based ADI sources, which can be found in peer-reviewed journal articles. These ADI source optimization parameters are important to improve the methods sensitivity for fast analyte screening and direct surface analysis. Subsequently to this literature overview, own studies for the optimization of instrumental parameters for the flowing atmospheric-pressure afterglow (FAPA) source will be presented in a following chapter.

In the second section of the thesis, DART-MS, FAPA-MS, and low-temperature plasma mass spectrometry (LTP-MS), are compared for the direct analysis of liquid-crystalline materials by MS. With this approach sample preparation is minimized for quick and cheap liquid crystal display (LCD) failure analysis. For DART-MS limits of detection (LODs, absolute amount) in the ng range and for LTP- and FAPA-MS LODs in the pg range are obtained. Additionally, mass-spectral imaging of LCDs by FAPA-MS and laser ablation halo-FAPA-MS (LA-h-FAPA-MS) will be presented. This instrumental setup enables the analysis of very low sample volumes inside an LCD and first experiments suggest an estimated spatial resolution of 1-2 mm and 0.6 mm for FAPA-MS and LA-h-FAPA-MS, respectively. Ultimately, these methods shall help to discriminate between different LCD components and to identify defects within an LCD by lateral profiling.

Despite the versatile application possibilities for ADI-MS methods, these techniques are very sensitive to matrix effects. Thus, thin-layer chromatography (TLC) is used to quickly separate matrix components and reaction byproducts from the target analytes before spatial resolved and quantitative detection by FAPA-MS. Furthermore, different TLC stationary phases (*e.g.*, normal phase, reversed phase, and cyano phase) as well as different particle sizes of the stationary phase are compared for best performance. Moreover, a validated TLC-FAPA-MS method is developed for quantification of 0.32 mg/mL caffeine in energy drinks via stable isotope dilution

analysis. A second application involves the separation and individual detection of active agents in antimalarial preparations.

Finally, FAPA-MS is applied for the analysis of a P_4O_{10} in DMSO mixture, to elucidate the reaction mechanism between both compounds. With these measurements the presence of the important $C_2H_5S^+$ intermediate product could be confirmed.

Zusammenfassung

Seit der Einführung von Desorption Electrospray Ionization (DESI) und Direct Analysis in Real Time (DART) haben sich Ambient Desorption/Ionization Mass Spectrometry (ADI-MS) Techniken zu nachweisstarken analytischen Werkzeugen entwickelt. ADI-MS Methoden ermöglichen es, Analyten direkt von der Probenoberfläche zu desorbieren und massenspektrometrisch zu untersuchen. Hierdurch können zeitaufwändige Probenvorbereitungsschritte (z.B. durch Lösungsmittelextraktion) umgangen und lange Analysenzeiten von chromatographischen Trenntechniken vermieden werden.

Im ersten Teil dieser Dissertation wird eine Übersicht der literaturbekanntesten Optimierungsparameter zusammengestellt. Wichtige Zusammenhänge dieser Parameter werden für die direkte Oberflächenanalyse durch plasma-basierte ADI-MS Techniken diskutiert. Darüber hinaus werden eigene Ergebnisse zur Optimierung von Geräteeinstellungen für die Flowing Atmospheric-Pressure Afterglow (FAPA)-Quelle präsentiert.

Im zweiten Teil dieser Dissertation werden DART-, FAPA- und Low-Temperature Plasma (LTP) Quellen für die direkte massenspektrometrische Analyse von Flüssigkristallen und deren Gemische miteinander verglichen. Zielsetzung ist es diese Substanzen direkt auf der Oberfläche von geöffneten Liquid Crystal Displays (LCDs) zu analysieren, um die zeitaufwändige Probenvorbereitung zur Untersuchung von LCD-Fehlstellen zu minimieren. Im Vergleich der ADI-Quellen können für DART-MS Limits of Detection (LODs) im ng-Bereich und für LTP- und FAPA-MS LODs im pg-Bereich gezeigt werden. Darüber hinaus wird eine Methode zur orts aufgelösten Analyse von LCD-Fehlstellen mittels FAPA-MS und Laser Ablation halo-FAPA-MS (LA-h-FAPA-MS) vorgestellt, die näherungsweise eine örtliche Auflösung von 1-2 mm bzw. 0.6 mm für die jeweilige Methoden bietet.

Auf Grund der Anfälligkeit von ADI-MS Methoden für Matrixeffekte wird Thin-Layer Chromatography (TLC) zur schnellen Abtrennung von Matrixbestandteilen und Reaktionsnebenprodukten eingesetzt. In diesem Zusammenhang wird eine validierte Methode zur quantitativen Bestimmung von 0,32 mg/mL Coffein in Energydrinks durch TLC-FAPA-MS vorgestellt. In einer zweiten Applikation werden Bestandteile aus Antimalaria Medikamenten durch TLC getrennt, um sie orts aufgelöst zu detektieren. Zudem wird der Einfluss von verschiedenen TLC Phasen (z.B. unterschiedliche Oberflächenmodifikationen oder Partikelgrößen der stationären Phase) auf das detektierte Ionensignal von Modellschubstanzen untersucht.

Abschließend wird FAPA-MS für die direkte Analyse von P_4O_{10} in DMSO angewendet um den Reaktionsmechanismus zwischen den beiden Substanzen aufzuklären. Durch diese Messungen kann die Anwesenheit eines $\text{C}_2\text{H}_5\text{S}^+$ Intermediat in der Reaktionslösung bestätigt werden.

Table of Content

Chapter 1	Introduction and Scope of the Thesis	1
1.1	Introduction	2
1.2	Scope of the Thesis	3
Chapter 2	Optimization of Plasma-Based Ambient Desorption/ Ionization Mass Spectrometry Operating Parameters.....	5
2.1	Introduction	6
2.2	Instrumental Modifications of the ADI Source Design	7
	Direct Analysis in Real Time.	7
	Flowing Atmospheric-Pressure Afterglow.	10
2.3	Important Parameters to Improve the Analyte Desorption by Plasma-Based ADI Sources	14
2.4	Parameters for the Adjustment of the Analyte Ionization Process....	16
2.5	Sample Probes and Substrates for Plasma-Based ADI-MS of Liquid Samples.....	19
2.6	Modifications of the MS Interface for Improved ADI-MS Sensitivity.....	23
2.7	Conclusion	26
Chapter 3	Optimization of the Flowing Atmospheric-Pressure Afterglow Plasma-Source Geometry and Development of a Temperature- Controlled Sample Holder for Direct Mass Spectral Surface Analysis	28
3.1	Introduction	29
3.2	Experimental Section.....	31
	Reagents.....	31
	Preparation of Test Mixtures for FAPA-MS Analysis.	31
	Thermal Electrolyte Aging.....	31
	Flowing Atmospheric-Pressure Afterglow.	32
	Low-Temperature Plasma Probe with Temperature-Controlled Sample Holder.	33

	High-Resolution Mass Spectrometry.....	34
	Optimization of the FAPA Positioning.....	35
	Infrared (IR)-Thermography.	35
	Sample Handling for TM-FAPA-MS.	37
	Separation of Analyte Mixtures on TLC Plates.....	37
	Mass Spectral Imaging of Analytes on TLC Plates.....	38
3.3	Results and Discussion.....	38
	Optimization of the FAPA Source Positioning in Front of the Mass Spectrometer.....	38
	Influence of the Anode Capillary Length.	41
	Influence of the Interelectrode Distance.	47
	Development of a Temperature-Controlled Sample Holder for the Analysis of Heat Sensitive and Volatile Analytes.	49
3.4	Conclusion	56
Chapter 4	Plasma-Based Ambient Desorption/Ionization Mass Spectrometry for the Analysis of Liquid Crystals Employed in Display Devices.....	58
4.1	Introduction	59
4.2	Experimental Section.....	62
	Reagents.....	62
	Direct Analysis in Real Time.	62
	Low-Temperature Plasma Probe.	63
	Flowing Atmospheric-Pressure Afterglow.	63
	High-Resolution Mass Spectrometry.....	64
4.3	Results and Discussion.....	64
	Analysis of Commercially Available Liquid Crystals.	64
	Plasma-Based ADI-MS Applied to Liquid Crystals Used in Display Technology.	78
	Comparison of Plasma-Based ADI Sources for Direct Surface Sampling.	81

4.4	Conclusion	88
Chapter 5	Spatially-Resolved Analysis of Liquid Crystals in Liquid Crystal Display Test Cells via Flowing Atmospheric-Pressure Afterglow Mass Spectrometry.....	89
5.1	Introduction.....	90
5.2	Experimental Section.....	92
	Reagents.....	92
	Sample Preparation.	92
	Flowing Atmospheric-Pressure Afterglow.	93
	Laser Ablation and Halo-Flowing Atmospheric-Pressure Afterglow.....	93
	High-Resolution Mass Spectrometry.....	94
	Mass Spectral Imaging and Data Processing.	95
5.3	Results and Discussion.....	95
	Mass Spectral Imaging of the Liquid-Crystal Spatial Distribution in Model LCDs via FAPA-MS.	95
	Improved Spatial Resolution for LCD Analysis via LA-h-FAPA-MS.	99
	Differentiation of Liquid Crystals and Adhesive Materials in LCDs.	101
5.4	Conclusion	105
Chapter 6	Fast Screening and Quantitative Mass Spectral Imaging of Thin-Layer Chromatography Plates with Flowing Atmospheric-Pressure Afterglow High-Resolution Mass Spectrometry	107
6.1	Introduction.....	108
6.2	Experimental Section.....	112
	Reagents.....	112
	Test Mixture Preparation.	112
	TLC Separation and Conditioning.....	112
	Preparation of Energy Drink Samples for TLC-FAPA-MS.....	113
	Desorption Electrospray Ionization.	113

	Flowing Atmospheric-Pressure Afterglow.	113
	High-Resolution Mass Spectrometry.....	114
	Mass Spectral Imaging and Data Processing.....	114
6.3	Results and Discussion.....	115
	Comparison of Selected Spray-Based and Plasma-Based ADI-MS Sources for Direct Screening of TLC Plates.....	115
	Comparison of Different Post-Separation Drying Conditions for HPTLC-FAPA-MS.....	119
	Influence of Stationary Phase Chemistry on Analyte Ion Abundance in HPTLC-FAPA-MS.....	122
	Influence of the TLC Grade on TLC-FAPA-MS Response.....	125
	Influence of Stationary Phase Thickness and Particle Size on TLC-FAPA-MS Response.	126
	Caffeine Quantification in Energy Drinks via TLC-FAPA-MS.	128
6.4	Conclusion	131
Chapter 7	High-Performance Thin-Layer Chromatography Flowing Atmospheric-Pressure Afterglow Mass Spectrometry for Fast Antimalarial Agent Screening in Drug Tablets	133
7.1	Introduction.....	134
7.2	Experimental Section.....	136
	Reagents.....	136
	Standard and Sample Preparation.....	136
	HPTLC Separation and Conditioning.....	137
	Flowing Atmospheric-Pressure Afterglow.	137
	High-Resolution Mass Spectrometry.....	137
	Mass Spectral Imaging and Data Processing.....	138
7.3	Results and Discussion.....	138
7.4	Conclusion	147
Chapter 8	Decomposition of P₄O₁₀ in DMSO	148

Chapter 9	Concluding Remarks and Future Perspectives	165
9.1	Summary and Conclusion	166
9.2	Future Perspectives	169
References	171
Appendix	182
11.1	Mass Spectrometer Operating Conditions for ADI-MS.....	182
11.2	IR-Thermography	187
11.3	Data Evaluation Procedure for Transient Signals	191
11.4	Data Evaluation Procedure for Mass Spectral Imaging.....	192
11.5	Data Evaluation Procedure for the Determination of Instrumental Detection Limits Measured with High-Resolution Mass Spectrometry.....	195
11.6	Supporting Information for the Analysis of Lithium-Ion Batteries	198
11.7	Supporting Information for the Analysis of Liquid Crystals via Plasma-Based ADI-MS	199
11.8	Supporting Information for Spatially-Resolved Liquid Crystal Analysis via FAPA-MS and LA-h-FAPA-MS	204
11.9	Supporting Information for the Analysis of TLC plates via FAPA-MS	211
11.10	Supporting Information for the Analysis of Antimalarial Agent Screening via HPTLC-FAPA-MS	217
Abbreviations	218
List of Figures	221
List of Tables	228
Acknowledgements	230
Curriculum Vitae	232
List of Publications	234

Chapter 1

Introduction and Scope of the Thesis

1.1 Introduction

During the last 15 years the research field of organic mass spectrometry significantly changed. New types of high-resolution (HR) mass spectrometers, such as the orbitrap mass analyzer, were commercialized and revolutionized mass spectral screening methods and molecular structure elucidation by the extremely high mass spectral resolving power of such instruments. For example, with the orbitrap mass analyzer a mass resolution up to 500,000 (full width at half maximum (FWHM)) and with Fourier-transform ion cyclotron resonance mass spectrometry (FT-ICR-MS) a mass resolution even higher than 500,000 is possible. Moreover, with ambient desorption/ionization mass spectrometry (ADI-MS) a new type of analyte sample introduction to the mass spectrometer and analyte ionization at ambient pressure was established, which can be applied for solid, liquid and gaseous samples.¹⁻⁴ ADI-MS made it possible to analyze samples in their natural (ambient) environment and therefore lengthy sample preparation procedures can be avoided. As the name of the method describes, ADI sources combine both steps of analyte desorption from the sample surface and the molecule ionization while the whole process is performed at atmospheric pressure, typically directly in front of the inlet of the mass spectrometer. Due to three basic operation methods, ADI sources are differentiated in three separate categories, namely spray-based, plasma-based, and laser-based sources.^{3,5} Very prominent and often applied ADI-MS techniques belonging to these categories are *e.g.*, desorption electrospray ionization (DESI),⁶ direct analysis in real time (DART),⁷ the low-temperature plasma (LTP) probe,⁸ and the flowing atmospheric-pressure afterglow (FAPA) source.⁹⁻¹¹

In plasma-based ADI-MS, most frequently helium is used as plasma gas and the plasma species consisting of helium metastables, ionized helium species, and free electrons are generated by an electrical discharge typically between two electrodes. The generated flowing afterglow is then directed to the sample surface where desorption and ionization of the analyte molecules in the open atmosphere occurs before the ions are sampled by the mass spectrometer. Usually, protonated molecules and positively charged molecules are observed, when the mass spectrometer is operated in positive-ion detection mode.

Beside the above mentioned ADI-MS techniques, FAPA-MS⁹⁻¹¹ emerged in the recent years to be a versatile technique for direct surface sampling, which also offers adjustable operating modes for molecular^{10,11} as well as elemental analysis.¹²

Due to the inherently high plasma temperature ($\sim 235\text{ }^{\circ}\text{C}$)¹³ the FAPA source does not require external heating to enhance the analyte desorption and therefore the number of publications comprising FAPA-MS increased in the recent years.¹⁴⁻¹⁹

1.2 Scope of the Thesis

Aim of this dissertation is to investigate fundamental properties of the FAPA source and to develop new methods for the direct analysis of sample systems as they are. For this task FAPA-MS is applied to various sample types and its analytical performance for the respective applications is compared to other plasma-based ADI sources, namely DART and the LTP probe.

The thesis starts with an introduction to the topic of plasma-based ADI-MS and an overview about the fundamental properties of prominent plasma-based ADI-MS methods (chapter 2). Specifically, different instrumental geometries of the DART and FAPA source are highlighted and their benefits as well as their challenges are discussed. Furthermore, several parameters for the optimization of analyte desorption and ionization are presented. In the last sections of this chapter, instrumental developments for the sample introduction into the plasma afterglow, as well as the transfer of ions into the mass spectrometer are discussed.

In chapter 3, the FAPA source performance is optimized for direct surface analysis. This is achieved by the determination of the ideal FAPA positioning – angle and distance – in front of the mass spectrometer. The desorption capabilities of the pin-to-capillary (p2c) FAPA source are optimized by evaluating the surface heating abilities of anode capillaries with different capillary length. Furthermore, the interelectrode distance of the FAPA source is altered to investigate the optimal conditions for best analyte ion signal abundance detected by the mass spectrometer. Lastly, in this chapter a new temperature-controlled sample platform is developed to analyze volatile analytes by LTP-MS such as electrolytes in lithium-ion batteries.

DART-, FAPA-, and LTP-MS are compared for the analysis of liquid crystals in chapter 4. Therefore, commercially available liquid crystals are analyzed via transmission-mode (TM) ADI-MS and the resulting mass spectra are compared regarding the observed ion abundances, molecular-ion species, ion fragmentation, and analyte oxidation. Identical experiments are presented for liquid crystals extracted from a liquid crystal display (LCD). Moreover, DART, FAPA, and LTP are compared for direct surface sampling of liquid crystals from a glass surface.

In the following chapter 5, FAPA-MS is applied for mass spectral imaging of liquid crystals and adhesive materials in an LCD test cell to obtain spatial resolved information of the analyte distribution on the glass surface. These results are compared to laser ablation halo-FAPA-MS (LA-h-FAPA-MS), which enables the desorption of smaller spot sizes.

In chapter 6 the influence of different thin-layer chromatography (TLC) stationary phases on the analyte signal response for FAPA-MS analysis is investigated. Specifically, in this study TLC plates with different modifications of the stationary phase (*e.g.*, polar, medium polar, non-polar), various layer thicknesses, and diverse purity of the silica material are compared. Therefore, the ion abundances of the model analytes caffeine, nicotine, acetaminophen, and cortisone are semi-quantitatively compared by mass spectral imaging of the analyte spots via TLC-FAPA-MS. Furthermore, caffeine is quantified in energy drinks by stable isotope dilution combined with TLC-FAPA-MS analysis. Prior mass spectral detection, the complex sample matrix and possible isobaric interferences were removed from the analyte molecules via TLC to improve the methods' accuracy.

Another application for TLC-FAPA-MS is demonstrated in chapter 7. Antimalarial active agents extracted from drug tablets are separated on TLC plates to separately detect the synthesis products and byproducts via FAPA-MS mass spectral imaging. Furthermore, the analyte fragmentation mechanism for labile molecular structures of artemether and lumefantrine are discussed.

In chapter 8 the complex reaction mixture of dimethyl sulfoxide (DMSO) and phosphorus pentoxide (P_4O_{10}) is analyzed to investigate possible intermediate states and decomposition products of P_4O_{10} . Therefore, TM-FAPA-MS, nuclear magnetic resonance (NMR), and density functional theory (DFT) are applied as analytical tools to finally propose a decomposition scheme for P_4O_{10} .

Lastly, in chapter 9 the results obtained in this thesis are concluded and future perspectives are discussed.

Chapter 2

Optimization of Plasma-Based Ambient Desorption/Ionization Mass Spectrometry Operating Parameters

2.1 Introduction

Analyte ionization and transfer of ionized molecules into the mass spectrometer has ever been an important step in organic mass spectrometry. For this purpose, atmospheric-pressure ionization techniques such as electrospray ionization (ESI),²⁰ atmospheric-pressure chemical ionization (APCI),²¹ and Atmospheric-pressure photoionization (APPI)²² evolved as versatile tools for mass spectral analysis of small and large organic molecules (*e.g.*, medication drugs, metabolites in biofluids, or proteins) in the liquid phase.²³ Very volatile or gaseous samples are mainly ionized by electron impact (EI) or chemical ionization (CI) for mass spectrometry after gas chromatography (GC) separation. Lastly, for the introduction of large biomolecules and solid samples to mass spectrometry often matrix-assisted laser desorption/ionization (MALDI),²⁴ secondary-ion mass spectrometry (SIMS),²⁵ or fast atom bombardment (FAB)²⁶ are reported in the literature, respectively. Despite the available methods for different sample types, all above stated techniques typically require some time-consuming sample pretreatment or have special requirements for analyte molecules. However, to avoid these time extensive procedures of sample preparation with *e.g.*, analyte extraction or dilution/preconcentration new tools for the transfer and ionization are required.

To fulfill this need for minimized sample pretreatment DESI⁶ and DART⁷ were developed in 2004 and 2005, respectively. These new tools enabled rapid analyte desorption from a sample surface in a combined step with molecule ionization in the gas phase. In the following years, ADI-MS established as the name for this sort of techniques and until today more than 40 acronyms of ADI sources are published.²⁷ All these sources can be categorized in spray-based, plasma-based, and laser-based ADI sources.^{3,5} This categorization relies on whether the ADI source uses a solvent spray, a plasma afterglow, or a laser beam to desorb and ionize the analyte molecules. However, also ADI sources as a combination of two of these categories are reported.^{28,29}

The most prominent ADI source based on a plasma discharge is surely the DART source because it is commercially available and can be purchased in many different configurations for *e.g.*, surface analysis or the analysis of liquids from a mesh in transmission-mode. Furthermore, the LTP probe,⁸ dielectric-barrier discharge ionization (DBDI),^{30,31} the FAPA,^{9,10} atmospheric-pressure solids analysis probe (ASAP),³² plasma-assisted desorption/ionization (PADI),³³ or desorption

atmospheric-pressure chemical ionization (DAPCI)^{34,35} are only few of the reported plasma-based ADI sources. In the past, several reviews about these plasma-based ADI sources highlighted the possible applications and multiple publications summarized the quantification capabilities.^{5,36-38}

Despite the available applications are already well summarized and numerous new applications are published every year an overview for optimizable parameters for plasma-based ADI sources have never been reported. For this reason, the optimization possibilities for the direct sample analysis via DART- and FAPA-MS are highlighted in this chapter. First, an overview about the different instrumental modifications and geometries for the ADI sources will be given and improvements of instrumental settings will be discussed. Second, important parameters for the analyte desorption/ionization process will be highlighted and optimization of such parameters for best analytical performance will be described. Furthermore, different analyte probes for more reproducible analyte deposition and a more reproducible analyte ion abundance detection will be presented. Moreover, sample substrates for trace analyte preconcentration will be presented. Lastly, achievements and challenges for the improved transfer of the analyte ions into the mass spectrometer will be discussed.

2.2 Instrumental Modifications of the ADI Source Design

Direct Analysis in Real Time. Because the DART source was the first plasma-based ADI-MS technique several publications and reviews are available which summarize the basic instrumental setup and the classical experimental conditions.³⁹ Hence, only a brief explanation of the DART source is given here. The original DART source (*cf.* Figure 2.1a) is operated by applying a direct current (DC) discharge voltage to a pin electrode inside the discharge chamber of the plasma source. At this electrode a corona-to-glow discharge (C-G discharge, current in the μA to low mA regime)¹³ is formed in a helium gas atmosphere which serves as the plasma gas. However, also other gases such as nitrogen or argon can be used. Besides excited-state (metastable) helium atoms (He^*) also positively charged helium species and free electrons are produced in the plasma. To avoid the direct contact between the charged gas species and the analyte molecules, the ions in the flowing plasma gas are reportedly filtered out by two perforated disc electrodes as well as a wire electrode before the plasma gas exits the DART source into the open atmosphere. Thermal evaporation of the analyte molecules is reported in the literature as the main analyte desorption process.^{40,41}

However, because the C-G discharge has a temperature of only 50-60 °C¹³ thermal desorption of high boiling point compounds would not be possible. This is why a plasma gas heater is attached to the front part of the DART source to enhance the analyte evaporation. With the heater, plasma gas temperatures of up to 450 °C can be achieved.³⁹ This instrumental design is typically referred to as DART SVP source and enables on-axis analysis of sample probes, as well as angled positioning of the ADI source for direct surface sampling. For the analysis of objects, the angled positioning appeared to be the most effective.⁴²

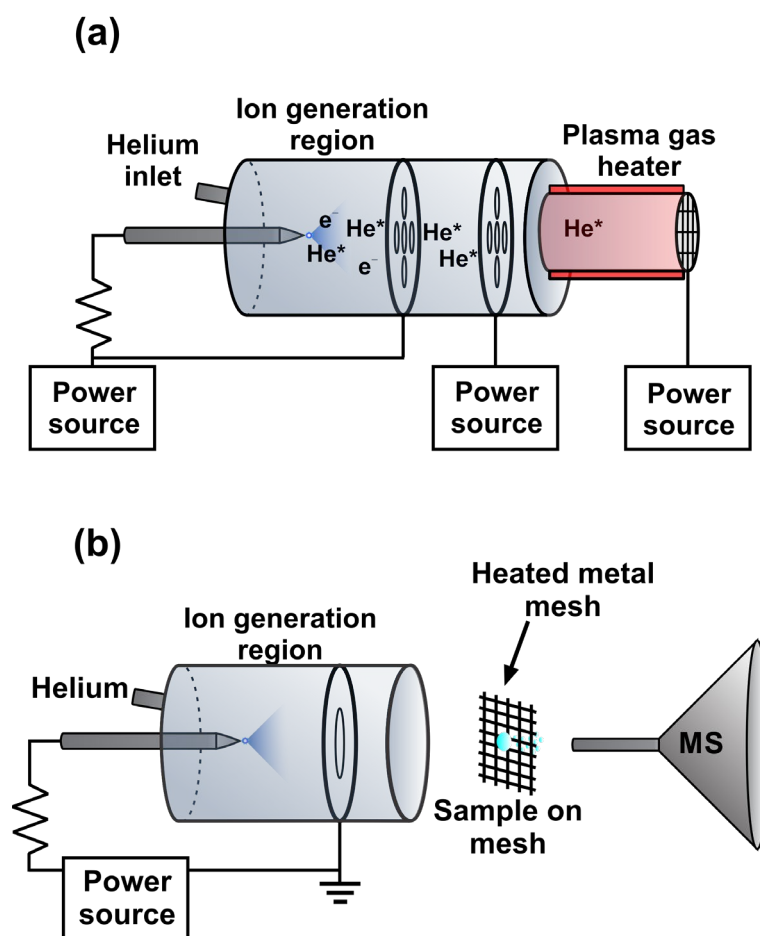


Figure 2.1 Schematic of the DART source instrumental setup published by Cody *et al.*⁷ (a) and schematic of the DART ID-Cube (b).

With the development of the DART ID-Cube the DART source was altered to a simpler design with just two electrodes for plasma generation (*cf.* Figure 2.1b). For this modification the filtering electrodes were removed and only one grounded disc electrode at the front end of the ceramic discharge chamber remained.³⁹ The main advantage of this altered instrumentation is the more simplified sample

introduction. For analysis the sample solution is typically deposited on a stainless-steel wire mesh of an OpenSpot Card sample target. Subsequently, the card is inserted in the space between DART source and inlet capillary of the mass spectrometer in so called transmission-mode (*cf.* chapter 2.5).⁴³ Because the OpenSpot Card is a single-use product it is discarded and therefore carryover effects are minimized for routine analysis. Another modification of the DART ID-Cube is that the external gas heater was removed and for this reason the plasma gas temperature interacting with the sample has an approximate temperature of ~ 55 °C.¹³ However, for enhancement of the analyte desorption the wire mesh of the single-use OpenSpot Card can be resistively heated by applying 3, 4, or 5 A to the stainless-steel wire mesh. Important to note is that the wire mesh is shaped to a narrow section in the middle, with a width of approximately 3 mm. This eases the reproducible, manual deposition of the analyte solution in the middle of the wire mesh for the operator and the alignment of DART source with respect to the sample droplet is more accurate. Moreover, the narrow section increases the heating current density in this position of the wire screen and consequently increases the temperature for analyte evaporation.

In addition to the different designs of commercially available DART sources, Häbe *et al.* modified the front-end geometry of the DART SVP source to optimize the spatial resolution for direct surface sampling.⁴⁴ Specifically, the eighteen different front caps (made out of MACOR glass-ceramic) for the DART SVP source were custom built and the inner dimensions of the caps (inner diameter (i.d.), inner length of the cap (i.l.), exit diameter (e.d.), and inside shape) were modified to optimize the transfer of helium metastables from the inside of the DART source to the sample surface. The study confirmed the hypothesis that a shorter inner length (6.5 mm) and a wider exit diameter (1.0 mm) improve the detected ion abundance of the model analyte by 66% in comparison to the original DART cap geometries of 13.0 mm inner length and 1.0 mm exit diameter. This observation is explained by less plasma cooling due to the shorter distance between plasma generation region and analyte. Furthermore, close distance between plasma and analyte might also increase the amount of He* species transferred to the sample surface and presumably this contributes to a higher analyte signal abundance.⁴⁴ Furthermore, the spatial resolution for the caps with 1.0 mm and 0.5 mm exit diameter were compared. Interestingly, and in contradiction to the assumption that smaller exit diameters will cause an improved spatial resolution, no improvement of such was observed (0.8 mm and 0.9 mm spatial resolution for 1.0 mm and 0.5 mm exit diameters, respectively).

In addition to the instrumental improvement of the DART source, Cody investigated positioning of the DART SVP source in front of the mass spectrometer

and studied the ion abundance of the reagent ions of $O_2^{+\bullet}$, NO^+ , NH_4^+ , and $(H_2O)_2+H^+$ with altered conditions.⁴⁵ In his study, he could demonstrate for the very first published DART source⁷ that the abundance of $O_2^{+\bullet}$ rapidly decreased, while the abundance of NO^+ , NH_4^+ , and $(H_2O)_2+H^+$ increased with increased distance between DART source and mass spectrometer. Specifically, he could identify the distance of 15 mm from the tip of the DART source towards the mass spectrometer sampling orifice to be a sweet spot for the protonated water dimer. Consequently, this distance is an ideal position for the detection of protonated analyte molecules. He could also demonstrate that a shorter distance is beneficial for the generation of molecular ions by charge transfer of the $O_2^{+\bullet}$ -ion. Furthermore, Häbe *et al.* studied the orientation angle of the DART source towards the sample surface at different gas flow rates.⁴⁶ The obtained results were also compared to different line scan speeds above the sample target. To visualize the impacting plasma gas stream, and to compare the above stated parameters, TLC plates were derivatized with a heat sensitive indicator. It was found that, an angle of 60° , combined with a plasma gas flow rate of 2.5 L/min and a line scan speed of 1 mm/sec caused the most homogeneous line scan with a 3 mm broad line across the sample plate and a 1 mm wide impact area. For lower gas flow rates (<2 L/min) and slower scan speeds (0.2 mm/sec) the fluorescence of the visualized line scan appeared to be inhomogeneous and much wider impact areas were observed, respectively.

Flowing Atmospheric-Pressure Afterglow. The original design of the FAPA source was developed by Andrade *et al.* and was built with a pin cathode and an anode pin hole plate, which were placed on opposing sides of an isolating cylindrical discharge chamber.^{9,10} For operation a negative potential is applied (discharge current typically in the range of 5-70 mA) to the pin electrode to sustain a glow-to-arc discharge (G-A discharge) in a helium gas atmosphere.¹³ Contrarily to the DART source, the generated plasma species are not filtered but all plasma species in the flowing afterglow are exiting the discharge chamber via the pin hole in the anode plate. In the first publications about the p2p-FAPA source the ADI source was optimized for the highest total ion signal of all background ions to improve the overall performance of the source.^{9,10} Therefore, the atmospheric-pressure glow discharge (APGD) operating current as well as potentials applied to the plate anode of the FAPA and the potential of the mass spectrometer front plate were studied. It was found that the total ion abundance steadily increased with increasing operating current until it reached a maximum at approximately 25 mA. Altering the potentials

of the anode plate as well as the mass spectrometer front plate revealed that the highest ion abundances were observed when an almost field-free region was generated in the afterglow region between these two electrodes.

Despite the successful application of FAPA-MS to analyze *e.g.*, pharmaceuticals,¹⁰ caffeine in beverages,¹⁰ and pesticides,⁴⁷ oxidation of the detected analyte species and therefore complicated mass spectra were observed especially for aromatic compounds with this pin-to-plate (p2p) FAPA source.¹³ As explained by the authors, this phenomena of analyte oxidation is mainly caused by the diffusion of ambient molecular oxygen into the discharge region. By reaction with the plasma gas, O₂ is reacting to oxygen radicals (O•) which subsequently may oxidize especially aromatic compounds in the sample. This issue of rather complex mass spectra due to analyte oxidation could be solved with the development of the p2c-FAPA source.¹¹ In the new designed FAPA source the anode plate was replaced by a capillary anode of 25 mm length and 1.3 mm i.d. The benefit of this instrumental modification was demonstrated for the model analyte diphenylamine (DPA) and it was shown that analyte oxidation by gas phase reactions can be significantly decreased with the p2c-FAPA source. Due to the long capillary the diffusion of molecular oxygen into the plasma generation region is unlikely and minor ion abundances of the oxidized analyte may be caused by tiny leakages in the FAPA source body. Also, the figures of merit for the analysis of pesticides by both FAPA geometries were compared and it was found that the analytical precision for the analysis of pesticides are comparable. For some analytes the p2c-FAPA was even more sensitive compared to the p2p-FAPA source.¹¹ However, the elongated path from the plasma generation region to the sample surface also caused the drawback of a colder afterglow temperature due to plasma cooling. This finding is unfortunate, because the desorption mechanism for plasma-based ADI sources is largely depending in thermal evaporation.^{48,49} Consequently, the colder afterglow can result in a decreased sensitivity for high boiling point analytes. Furthermore, Badal *et al.* compared the two FAPA geometries more closely to gain a better understanding of the reagent ion formation.¹⁴ In this study, three parameters were found to be influential on the reagent ion formation: the discharge current, discharge gas flow rate, and spatial position within the afterglow.

To simplify the introduction of gaseous samples and aerosols the halo-FAPA (h-FAPA) source was developed by Pfeuffer *et al.*⁵⁰ with a completely different geometry compared to the above described FAPA sources. As demonstrated in Figure 2.2, the h-FAPA is setup by two concentric steel electrodes which are electrically shielded from each other by a concentric insulator material (*e.g.*, aluminum oxide). The plasma generation region is located at the front tip of the h-FAPA source

(approximately 1 mm width) and therefore the insulator is removed in this region between the electrodes. The plasma discharge gas is introduced to the discharge region via a small space between the outer capillary and the insulator. The ring-shaped discharge (purple color) is formed by applying a DC current to the central cathode capillary. Contrarily to the p2p- and p2c-FAPA sources the evaluation of the current-voltage characteristics demonstrated that instead of a G-A discharge a normal glow discharge is formed in the h-FAPA.⁵⁰

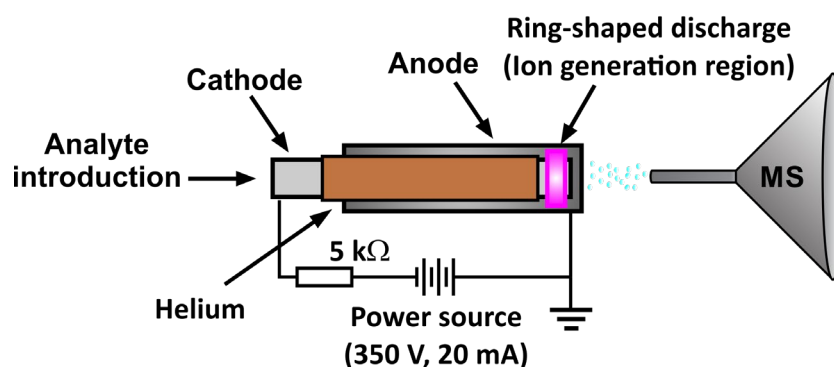


Figure 2.2 Schematic of the h-FAPA source in front of the mass spectrometer inlet.

In addition to the characterization of the plasma glow discharge by optical emission spectroscopy the authors discussed the versatile sample introduction capabilities for this h-FAPA. Besides the stand-alone operation, h-FAPA-MS was coupled with a laser ablation (LA) to introduce caffeine as a model analyte. The sensitivity of the LA-h-FAPA-MS method was tested by analyzing 1 μg of caffeine (in solution) with a single laser shot (10 μm diameter) and signal-to-noise (S/N) ratios of 30 could be achieved for the detected protonated molecule. Analyte fragmentation caused by the laser ablation or the FAPA source was not observed. Additionally, single droplets with a volume of ~ 30 pL were generated by a drop-on-demand (DOD) generator and introduced into the h-FAPA source. As stated by the authors, the coupling of these the techniques was much easier than coupling of DOD with the p2p-FAPA source⁵¹ and a better reproducibility for the h-FAPA source versus the p2p-FAPA was achieved (relative standard deviation (RSD): 0.9% compared to 2.2%, respectively). The detection limit for lidocaine with the DOD-h-FAPA-MS setup was found to be 9 fg (total amount). Furthermore, a nebulized analyte solution of 10 ppm tebuthiuron could easily analyzed by introduction of the aerosol to the central cathode

capillary of the h-FAPA source and the protonated molecule could be detected at m/z 229.

Another modification of the FAPA source was reported in 2016 by Zeiri *et al.* who introduced the micro-FAPA (μ -FAPA), which is a smaller version of the above described h-FAPA source with the same possibilities for sample introduction.¹⁵ Identical to the other FAPA sources, a DC voltage is applied for plasma generation and identical to the h-FAPA source the current-voltage characterization of the new FAPA design revealed a plasma in the normal glow discharge regime. However, the smaller dimensions of the μ -FAPA are accompanied by important differences compared to the h-FAPA. The polarity of the two electrodes was interchanged for the μ -FAPA because (cathode at the outer electrode) because the cathode electrode is heated the most and the outer electrode offers the larger thermal mass to withstand higher temperatures. Furthermore, due to the smaller dimensions of the capillaries a more compact plasma is generated, which can be operated for several hours with 1 L/min helium gas flow rate and a discharge current >25 mA. The μ -FAPA source was also characterized by IR-thermography to detect the surface temperature of a microscope slide, which was heated by the plasma afterglow and temperatures of up to 375 °C could be observed. These temperatures are drastically higher than the temperatures of the p2p- and p2c-FAPA sources and are attributed to the higher power density of the glow discharge in the μ -FAPA source. Furthermore, IR-thermography measurements with the μ -FAPA and p2p-FAPA source revealed that the spatial-temperature gradient for the afterglow temperature is about 25% lower for the μ -FAPA source, which might be a beneficial feature for spatially resolved analysis in future applications.

In addition to the development of new FAPA source designs, a study by Orejas *et al.*⁵² pursued the optimization of the p2p-FAPA source geometry to improve the analyte desorption by elevated plasma temperatures. The authors could demonstrate that the power consumption of the FAPA source linearly increases with the increase of the interelectrode distance between pin cathode and plate anode and therefore a more arc-like plasma condition is assumed. Consequently, the plasma afterglow temperature at different interelectrode distances at different operating-currents was studied and a linear increase of the temperature from ~ 80 °C to ~ 250 °C was observed when one or both parameters were increased.

Lastly, Badal *et al.*¹⁴ optimized the FAPA source positioning in front of the mass spectrometer. For this task, the spatial distribution of important reagent-ions such as O_2^{+} (charge transfer) and $(H_2O)_2+H^+$ (proton transfer) in the plasma

afterglow was monitored via the ion abundance of the respective reagent. The experiments were performed by aligning the FAPA source on-axis to the mass spectrometer inlet capillary. It was found that the proton-transfer reagents remain more focused and in the central region of the afterglow, while the charge-transfer species are more likely to dissipate to the outer edges of the flowing plasma. However, it is also stated that the applicability of the found reagent-ion distribution for a tunable analyte ionization is very limited. Furthermore, the abundance of $O_2^{+\bullet}$ and $(H_2O)_2+H^+$ was recorded downstream the flowing afterglow by detection of the ion abundance at FAPA to mass spectrometer distances between 10 and 20 mm. In these experiments it was found that at low plasma gas flow rates (0.5 L/min) the ion abundances of both reagent-ion decrease to below 20% relative abundance with increasing distance of the FAPA source towards the mass spectrometer. At higher gas flow rates (1.5 L/min) only the ion abundance of the $(H_2O)_2+H^+$ -ions decreased to 20% relative abundance and the abundance of $O_2^{+\bullet}$ remained at approximately 80% with increasing distance between FAPA and mass spectrometer. Consequently, these findings suggest that the analyte ionization mechanism can be tuned by the positioning of the FAPA source when high plasma gas flow rates of 1.5 L/min are used. Moreover, due to the laminar flow of the FAPA plasma gas the same adjustments of the analyte ionization mechanism can be made by altering the plasma gas flow rate with a fixed position of the FAPA source.

2.3 Important Parameters to Improve the Analyte Desorption by Plasma-Based ADI Sources

One key aspect of ADI-MS is the direct desorption of the analyte molecules from the sample surface and, consequently, the understanding of these desorption processes is important to improve the sensitivity of the method. For plasma-based ADI-MS one of the most accepted mechanisms appears to be thermal desorption of analyte molecules from the sample surface due to the elevated temperatures generated by the plasma sources.^{13,40,48,49,53} However, also chemical sputtering or photo-induced desorption are suggested in the literature as possible pathways for analyte desorption.^{4,7,40} It is hypothesized for these desorption mechanisms that excited species impact on the sample surface and liberate analytes through the transfer of energy. Unfortunately, peer-reviewed publications about this topic which give evidence for such desorption mechanisms are rare. However, it was shown for

DART-MS that mass spectra of covalently surface-bonded monolayers could be detected.⁵⁴

In the past years, several studies have been made to investigate the fundamental properties of plasma-based ADI sources and in this context also parameters for the enhancement of analyte desorption were presented. In studies by Shelley *et al.*^{11,55} and Orejas *et al.*,⁵² the authors could demonstrate for the FAPA source that the afterglow temperature is influenced by the flow rate of the plasma gas as well as the applied discharge current. Due to the inherently high plasma temperatures of the FAPA source (~ 235 °C) these findings might give the opportunity to optimize the plasma gas temperature for future applications. In all three studies, it was found that lower gas flow rates cause higher plasma temperatures and subsequently the analyte desorption from the sample surface can be improved. The maximum afterglow temperature for the p2p- and p2c-FAPA source was measured in 5 mm distance from the anode capillary. Interestingly, for both FAPA designs the temperature increased linearly with increased helium flow rate. Once a maximum the temperature of ~ 230 °C and ~ 160 °C was reached, respectively, the temperatures slowly decayed with further increased helium flow rate. The linear increase of the afterglow temperature for the p2p-FAPA was significantly steeper and higher temperatures were achieved. This effect occurs due to the much closer distance between discharge generation region and the temperature measurement spot because of the thin anode plate. Moreover, the elongated anode capillary of the p2c-FAPA source can act as a heat sink. The decay of the plasma gas temperature after the temperature maximum at higher gas flow rates can be explained by the development of a turbulent flow which then causes a more rapid cooling of the afterglow.

With alteration of the FAPA discharge current the temperature of the discharge could be linearly increased. In this regard, for the p2p-FAPA temperatures from ~ 175 °C (at 15 mA) to ~ 275 °C (at 55 mA) could be detected, while for the p2c-FAPA source lower temperatures of ~ 55 °C (at 5 mA) to ~ 125 °C (at 35 mA) were detected.¹¹ Consequently, Shelley *et al.* further suggested that the modulation of the discharge current might be an opportunity to selectively desorb low vapor pressure analytes from high vapor pressure compounds, as has been done with the DART source.⁴⁹

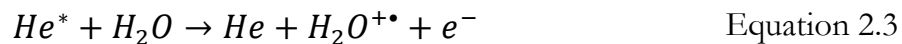
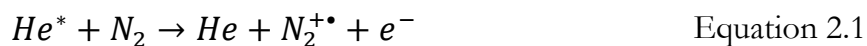
Because the C-G discharge of the DART source is typically colder than the G-A discharge of the FAPA source, the aforementioned external plasma gas heater was added to the plasma source to enhance the analyte desorption. Consequently, several studies have demonstrated that the modulated increase of the plasma gas temperature can be used to somewhat separate analytes with different vapor pressures by delayed

evaporation.^{49,56} For example, Nilles *et al.* used a temperature program to separate the chemical warfare agent sarin from the interference compounds 5-Nitro-1*H*-pyridin-2-one (HNP) and *N,N*-Dimethyloctan-1-amine (DMOA) and to avoid the isobaric interference at m/z 158. At this m/z the protonated molecule of DMOA interferes with the ammonium-adduct ions of sarin and HNP and a mass resolution greater than 10,000 is required to resolve these ions and to avoid false positives for the warfare agent. However, with a slowly increasing temperature gradient of the plasma gas temperature (gradient ~ 1.5 °C/sec) this DART-MS method was also made accessible for low resolution mass spectrometer used in the field for warfare agent detection.

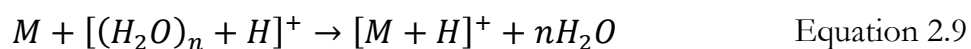
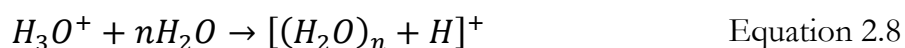
2.4 Parameters for the Adjustment of the Analyte Ionization Process

Similar to analyte desorption, the ionization of the target molecules is a very important step in mass spectral analysis. With a mass spectrometer only charged molecules or atoms can be detected and therefore the analyte ionization efficiency partially determines the sensitivity of the ADI-MS technique. For this reason, the knowledge about the ionization mechanism, for plasma-based ADI-MS techniques, is crucial, so the plasma conditions can be optimized for ionization of a specific application and analyte. For plasma-based ADI sources several studies have been made to elucidate the ionization mechanism,^{7,9,57} and theories from other plasma-based techniques (*e.g.*, APCI)²¹ have been used to explain the ions generated by ADI sources (*e.g.*, Penning ionization).⁵⁸ In the following, a brief overview about the reaction pathways for analyte ionization by plasma-based ADI sources is presented.

When DART-MS was introduced,⁷ Cody *et al.* researched the ionization mechanism for the protonated molecules and molecular ions, of model analytes, generated by the DART source. Because the C-G discharge in the DART source is known to generate metastable helium atoms (He*) in the (2³S) excited state, an ionization pathway similar to APCI was suggested and this theory was confirmed by following studies.¹³ In this ionization mechanism, the generated He* reacts with nitrogen, oxygen, or water molecules from the ambient air (*cf.* Equation 2.1 to Equation 2.3). Furthermore, the direct reaction of He* with the analyte molecule (M) is possible. Due to the typically faster and thermodynamically better reaction between He* and nitrogen the ion yield of the nitrogen radical cations is much higher compared to direct Penning ionization of the analyte.



However, the reaction between $N_2^{+\bullet}$, $O_2^{+\bullet}$, or $H_2O^{+\bullet}$ with the analyte molecule would produce molecular ions, but in plasma-based ADI-MS for most of the analytes protonated molecules are observed. Therefore, a continuation of the plasma gas reaction cascade is suggested (Equation 2.5 to Equation 2.9), in which the nitrogen reacts with water molecules in the ambient air (humidity) and protonated water clusters with highly acidic protons are formed. This proton is transferred in a subsequent reaction to a proton accepting analyte molecule.^{59,60} A more detailed explanation of this mechanism for the DART source is also summarized in the review by Gross.³⁹



Due to the variety of different analyte molecules and diverse sample matrices both ionization pathways – the formation of molecular ions and protonated molecules – are important and need to be optimized for the application. As described in the previous chapter the formation of molecular ions by the reaction of *e.g.*, $O_2^{+\bullet}$ with the analyte molecule can be enhanced via an optimized positioning between ADI source and the mass spectrometer inlet. However, the following explanations will focus on the optimization of the analyte ionization via proton transfer by protonated water clusters.

Cunningham *et al.* demonstrated in a publication that the plasma gas temperature can have an effect on the formation of the protonated water clusters.⁶¹ The authors could show that the ion abundance of clusters with water molecules of $n > 3$ significantly decreased at higher temperatures of the plasma and explained this finding with the weak bonding strength between the water molecules in the clusters. Due to the higher temperatures the water clusters dissociate to smaller clusters and water molecules “evaporate” from these clusters.^{61,62} However, for lower plasma temperatures the water molecules are more likely to condensate together, which is why the population of water clusters with $n > 3$ is larger. The ionization mechanism for analyte protonation is largely influenced by these findings because the proton acidity of the water clusters correlates with the number of attached water molecules.⁵² Larger clusters have a higher proton acidity and therefore might be required to detect a sufficient mass spectral signal for analytes with low proton affinity. Consequently, it might be necessary to operate the plasma at lower operating currents or higher gas flow rates to improve the sensitivity for such analytes. Furthermore, a separation of the analyte desorption and the ionization might need to be considered, if the analytes cannot be desorbed with lower plasma temperatures.

Badal *et al.* studied the addition of oxygen to the helium plasma gas for FAPA-MS and found that only a very small fraction of oxygen (*e.g.*, 0.1% (v/v)) is needed to enhance the $(\text{H}_2\text{O})_2\text{H}^+$ production by a factor of 3.4.¹⁶ This trend was also observed for the protonated water clusters with 3, 4, and 5 attached water molecules. Interestingly, with these plasma conditions the abundance of all other reagent ion species (*e.g.*, NO^+ , HCO^+ , and O_2^+) decreased and, therefore, analyte protonation was significantly improved over the formation of molecular ions. However, it has to be noted that the addition of elemental oxygen also caused minor abundances of irreversibly oxidized species for analytes with a conjugated π -system. Through this reaction a stable alcohol functional group was attached to the analyte molecules.

Furthermore, the addition of NH_3 to the plasma gas was found to be useful for some applications to produce ammonia adducts of the analyte molecule.^{63,64} This additive can be useful in some application because it can act as a dopant to mediate the ionization process. Typically, the formation of these adduct ions can be promoted by placing a small vial of ammonia solution in close proximity to the location of desorption and ionization or a small capillary with a steady gas flow of NH_3 vapors is directed to the sampling spot. In this case, a NH_3 atmosphere with a low ammonia concentration will be established.

Lastly, the addition of hydrogen to the plasma gas was studied by Wright *et al.*⁶⁵ as well as Ellis *et al.*⁶⁶ In both studies, a significant enhancement of the $[M+H]^+$ -ion could be observed. Moreover, Na *et al.* used the addition of hydrogen to perform a Birch reduction of benzene to 1,4-cyclohexadiene with an LTP source.⁶⁷

2.5 Sample Probes and Substrates for Plasma-Based ADI-MS of Liquid Samples

Aim of ADI-MS is typically the identification and quantitation of analytes from the samples as they are, without elaborative sample preparation. Consequently, the large variety of samples and sample matrices require different sample substrates and sample holder. Very first applications of *e.g.*, DART-MS or FAPA-MS were performed by directly desorbing the analyte from a glass rod or melting-point tube (probe-mode (PM) ADI-MS).^{7,10} With this simple and cost effective “device” especially liquid samples could be easily probed by dipping the glass rod into the solution and subsequently positioning the rod in between the ADI source and the mass spectrometer. Due to the manual sample positioning and the resulting poor reproducibility of the analyte signal, efforts were made to improve this type of liquid analyte sampling. Consequently, IonSense Inc. (Danvers, MA, USA) introduced the Dip-it sampling probe, which is a typical glass sampling probe for liquid samples which can be mounted to a rail guided holder. For reproducible sample probe introduction, the probe holder is moved in front of the DART source at a fixed position, where the hot plasma gas stream desorbs the analyte molecules at the tip of the Dip-it probe. Unfortunately, for the use of melting point tubes as well as for the commercially available Dip-it probe examples for the optimization of the probe in the plasma gas stream are often not explicitly explained in the literature,⁶⁸ if not the optimization of the probe positioning is completely neglected during analysis.⁶⁹ To address this issue, Pfeuffer *et al.* performed Schlieren imaging experiments to visualize the mass transport of the plasma gas into the mass spectrometer when performing PM-FAPA-MS.⁷⁰ In this study, the interaction between plasma and the melting point probe was investigated and turbulences in the plasma afterglow were studied at different plasma gas flow rates (0.5-1.5 L/min) altered distances between FAPA and the sample probe (2 mm, 4 mm, and 6 mm). At low flow rates (0.5 L/min) the sample probe caused distinct turbulences of the laminar plasma afterglow. Pfeuffer *et al.* explained this observation by a helium boundary layer which interacts with the glass surface of the sample rod. With increasing gas flow rate, the helium gas

appears to spread further around the rod until it fully envelops the probe. The wide spreading helium gas stream, the collection of the plasma gas by the simulated mass spectrometer interface was only influenced to a minimal extend. Consequently, it is assumed that nearly the total amount of desorbed analytes is transferred into the mass spectrometer. However, at higher plasma gas flow rates (≥ 1.5 L/min) the tube disrupts the gas flow so much that the uptake of the gas into the mass spectrometer is no longer efficient. Furthermore, it was found that farther distances between FAPA source and sample probe are advantageous for a better helium aspiration of the mass spectrometer. Especially at higher gas flow rates of 1.25 L/min or 1.5 L/min.

Despite the optimization of the glass rod positioning, quantification of analytes without internal (isotopically-labeled) standard remains to be very challenging because of unsatisfying deviations of the analyte signal abundance between different measurements. This issue was addressed by Jeckelmann *et al.*,⁷¹ who developed a new type of probe for the deposition of liquid samples in the DART afterglow region. The new probe consists of a 0.12 mm nickel chromium wire which was coiled 12-times around a 0.8 mm thick stainless-steel rod. In the following text this probe will be named “wire probe”. In the original publication a disposable syringe needle with cut off needle tip was used. The new sampling probe was compared with the commercial Dip-it probe and calibration curves for the N-ethyl-5-methyl-2-(1-methylethyl) analyte were determined. It was found that with the new probe the overall RSD was drastically lower (RSD range between 5 and 20%) for the wire probe than the for the Dip-it probe (RSD range between 20 and 80%) even though both probes were placed in between DART source and mass spectrometer by hand. The comparison of the two calibration curves revealed a drastically better signal-to-noise ratio for the wire probe and consequently better limits of detections were achieved with the now probe.

As an alternative analyte target for improved and more reproducible analyte desorption Perez *et al.* introduced in 2010 the first application of TM-DART-MS and analyzed insecticides deposited on the wire screen.⁴³ This modification in the instrumental setup significantly improved the accuracy of DART-MS measurements and the authors achieved detection limits for 10 ng for the deltamethrin analyte. The comparison of the analyte ion signal with computational fluid dynamic simulations from the same study confirmed that for larger distances between the DART source and the mesh (4 mm) lower gas flow rates (gas velocities) are beneficial to avoid the plasma gas to be deflected away from the mesh. However, with close proximity (0 mm) of the DART source and the mesh the gas stream is forced through the net without deflection. In this case, an increase in the plasma gas flow rate also caused an increase in the analyte signal abundance. Jones *et al.* evaluated sampling strategies for

the analysis of non-target screening of blood samples via TM-DART-MS.⁷² The authors confirmed the observations of Perez *et al.* that a close proximity between DART source and the wire mesh is beneficial for the analyte signal abundance. Additionally, it was found that a short distance (*e.g.*, 5 mm) between mesh and mass spectrometer interface also improved the detected ion abundance. The direct comparison of TM-DART-MS and PM-DART-MS demonstrated the improved precision of TM in comparison to the PM due to the easier positioning of the wire mesh in the plasma gas stream and calibration curves with improved variation coefficients were obtained.⁷² However, the improved repeatability and reproducibility were accompanied with lower sensitivities for TM in comparison to PM. Jones *et al.* explained this observation by a worse analyte evaporation from the sample target. Due to the good heat conductivity of the stainless-steel wire mesh the high temperatures of the plasma gas are better dissipated by the metal mesh compared to the glass rod in PM. Consequently, less heat is available for the prompt desorption of the analyte from the mesh and lower signal-to-noise ratios are detected for TM mode in comparison to the PM mode. For this reason, it might be useful for future TM applications to manufacture wire screens from materials with low heat conductivity to further improve TM sensitivity.

The above described capability of rapid and straightforward screening of solid, liquid, and gaseous samples is a key advantage for plasma-based ADI sources. However, the simple sampling of analytes sometimes includes the disadvantage of a lower sensitivity in comparison to established analysis techniques such as GC or high-performance liquid chromatography (HPLC) coupled to MS.⁷³ To overcome this challenge solid-phase microextraction (SPME) devices have been combined with plasma-based ADI source such as DART,⁷⁴⁻⁷⁶ LTP,⁷⁷ or DBDI.⁷⁸ For example in the study of Wang *et al.* an in-tube solid-phase microextraction (IT-SPME) device was coupled to DART-MS for the analysis of triazine herbicides in lake water and orange juice.⁷⁴ With a new developed adsorbent material, which combines carbon nanotubes (CNT) with a monolithic polymer, IT-SPME was capable to improve the sensitivity of the DART-MS method for triazine herbicides. Further, it was demonstrated that the sample can be probed online via IT-SPME-DART-MS and the sensitivity was found to be comparable to state-of-the-art HPLC-MS methods with limits of quantification in the sub-ng/mL concentration range.

Identical to the modification of a sample probe for SPME also transmission-mode substrates can be chemically modified to enhance the analyte adsorption, preconcentration, and matrix removal as demonstrated by Mirnaghi *et al.*⁷⁹ The authors introduced a biocompatible and two layered SPME coating with a first layer

of C18-modified polyacrylonitrile (C18-PAN) covered by a second layer of PAN. The SPME layer could be reproducibly deposited on a wire mesh by brush painting and was used to separate the interfering matrix components from diazepam in blood samples. For this application, bloodspots (5 μL) were deposited on the SPME coating and matrix components, such as intact cells or large biomolecules, were washed of the wire screen after an incubation time of 5 minutes with purified water. It is important to note that the wire screen was completely dried before the samples were analyzed. Otherwise a significant increase in the RSD of the analyte signal abundance was observed. With this method, Mirnaghi *et al.* were able to minimize the ion suppression for the analysis of diazepam in blood samples, while achieving detection limits of 0.3 $\mu\text{g}/\text{mL}$. Furthermore, it is noteworthy that the SPME-TM sample substrate could be reused up to 30 times for the analysis of the same sample. However, the deposition of the SPME coating appears to be not ideal and the holes of the mesh are partially blocked. This hinders the gas stream of exited species to flow through the mesh into the mass spectrometer and ultimately limits the methods' sensitivity. This issue was solved by Gómez-Ríos *et al.*⁸⁰ who developed a method to accurately deposit the SPME coating on the wires of the mesh and leaving the space between the strands open. With this improvement the interaction of the plasma gas and the analytes on the wire surface as well as the mass transport of ions into the mass spectrometer were enhanced. This claim could be verified with the analysis of diazepam and cocaine in urine and blood samples. In these experiments, very good linearity was obtained for the SPME-TM-DART-MS method. For the analysis of cocaine in urine and blood plasma quantification limits of 2 pg/mL and 5 pg/mL were obtained, respectively. Furthermore, the authors demonstrated that 15 seconds are sufficient to extract quantifiable amounts of diazepam or cocaine out of a 50-ppm solution with the SPME-TM device from the sample solution. However, for these short extraction times (<1 minute) it is important to precisely control the variables (*e.g.*, SPME coating distribution, composition, or thickness) of the extraction process to obtain reproducible results. It is also important to note that the used DART source was not capable to completely desorb the analytes from the mesh within the ~ 20 seconds of analysis, and therefore carry-over effects are expected. Consequently, Gómez-Ríos *et al.* recommended SPME-TM devices for single use if drastically different analyte concentrations shall be probed (*e.g.*, low ppt to ppm levels) to avoid false positive results.

Another device for the reproducible introduction of small sample droplets into the plasma afterglow is the DOD generator. This instrument uses a piezoelectric crystal to emit small droplets at a kilohertz (kHz) repetition rate with a typical volume

of several picoliter. The first application of this device in combination with a plasma-based ADI source was demonstrated by Schaper *et al.* who coupled the DOD to a FAPA source for mass spectral analysis and applied the method for the direct analysis of urine samples.⁵¹ The authors could show that with this technique a very stable analyte signal (RSD of 4%) can be detected over a long period of time, due to the precise sample introduction. Due to this very stable signal over a long period of time the authors suggested that DOD might be a very good introduction system for different standards while another sample is probed by the FAPA source.

Furthermore, TLC is frequently reported to be a useful tool for the separation of matrix components from the analyte molecules. Because TLC-FAPA-MS is also applied in chapter 6 of this thesis a comprehensive summary of TLC-ADI-MS methods can be found in the corresponding chapter.

2.6 Modifications of the MS Interface for Improved ADI-MS Sensitivity

Ion transfer from the location of their desorption and ionization into the mass spectrometer is as important as the desorption/ionization process by the ADI source. Several modifications to the atmospheric-pressure interface (API) of the mass spectrometer have been reported in the literature to improve the ADI-MS ion-transfer efficiency.

For the analysis of sample surfaces typically the API is modified to enable analyte sampling further away from the mass spectrometer inlet (*e.g.*, 30 cm extended inlet of the mass spectrometer for DESI-MS by Takats *et al.*⁶). This modification is necessary to also probe analytes in the center of larger sample surfaces and the optimization of this inlet extension is important to gain maximum signal abundance. For this reason, Takats *et al.* applied a funnel shaped ion transfer capillary to probe a larger surface via DESI-MS and to collect as much secondary droplets of the spray as possible for ion detection.⁸¹ This funnel transfer capillary was further characterized for ESI- and DESI-MS by Wu *et al.*, who determined the dependence of the tip position relative to the capillary central axis with an i.d. of 2.2 mm at the flared end of the capillary.⁸² The funnel capillary tolerated in the case of a short sprayer to inlet capillary distance of 1 mm a further offset of the ESI sprayer from the central axis (1.2 mm) in comparison to the regular inlet capillary (0.8 mm) and maintained the high analyte ion abundance. This observation was also made for the second experiment with a sprayer to inlet capillary distance of 10 mm. Here, the longer

distance between ESI source and inlet capillary allowed an increased influence of droplet charge repulsion. However, the funnel capillary was capable to aspirate analyte ions even with an ESI probe offset of 20 mm while the analyte ion abundance collapsed at 10 mm for the regular mass spectrometer inlet capillary. This overall increased tolerance for the ESI probe position was transferred to DESI-MS and revealed an enhanced analyte signal abundance with 5-fold improved detection limits for angiotensin II (10 fmol/mm² with funnel capillary; 50 fmol/mm² with regular inlet capillary).⁸²

Despite the improved sensitivity for spray-based ADI sources, the use of a funnel capillary in combination with ADI plasma sources might cause problems with the vacuum inside the mass spectrometer. Due to the different behavior of the helium plasma gas in comparison to other ambient gases (N₂ or O₂) the vacuum system of the mass spectrometer instrument may have problems in removing this gas. Consequently, the instrument cannot be operated with proper performance. To overcome this issue, Yu *et al.* applied additional pumping via a diaphragm pumping stage in front of the regular API inlet and compensated for the increased vacuum load.⁸³ This additional vacuum stage attached to the API is called Vapur interface. During sample analysis the desorbed/ionized analyte molecules are sucked into the Vapur interface via a ceramic tube (i.d. typically 4.75 mm) and inside the low vacuum region of the Vapur interface excess helium is separated from the analyte ions before they enter the original inlet capillary of the mass spectrometer. This instrumental modification improved the sensitivity of the DART-MS method by a factor of 10 to 100 times.⁸³ The authors explain the improved performance by the reduced potential of the plasma and analyte gas to drift away into the surrounding atmosphere before entering the Vapur interface capillary. Furthermore, the vacuum inside the mass spectrometer is improved and therefore the mean free path inside the instrument is enhanced.

Studies to improve the effectiveness of the Vapur interface were performed by Häbe *et al.*⁴⁶ The authors shortened the length of the ceramic transfer tube to 50 mm (4.75 mm i.d.) and thus to the shorter distance between orifice and mass spectrometer inlet capillary reportedly better ion abundances were obtained. For improved analyte molecule aspiration by the transfer tube the front tip was cut-off in an angle (5 mm ledge, 20-45° curvature). Furthermore, the analyte aspiration was improved by an 20° angled sample holder so the deflected plasma gas was directly guided into the orifice of the transfer capillary and collisions between the gas stream and the inner transfer tube wall were avoided. Furthermore, Häbe *et al.* developed ceramic transfer capillaries with a conical reduction of the inner diameter to spatially

compress the stream of gas entering the Vapor interface chamber, which helped to improve the transfer of ions into the orifice of the mass spectrometer.⁴⁴ Specifically, with this modification the signal abundance of paraben model analytes could be increased from 100% (regular straight transfer tube) to 156% for the new transfer tube. The new capillary had a standard 4.75 mm bore at the front end with a cut-off tip analogous to the previously reported publication.⁴⁶ Over a distance of the first 15 mm the inner diameter of the transfer tube was reduced to 2 mm and was then continued as a straight bore to the back end of the tube. In addition to the conical inside bore of the transfer tube also the distance between the tube and the mass spectrometer inlet capillary was optimized. Here, a signal improvement of 219% at a distance of 0.5 mm (with narrow transfer tube) was detected in comparison to 100% signal abundance (with standard width transfer tube) at 1 mm distance.

Contrary to the findings by Häbe *et al.*,⁴⁶ which stated that short distances between the location of desorption/ionization and the mass spectral interface are crucial for a high ion abundance, Garimella *et al.* were able to demonstrate with DESI and LTP that a laminar gas flow inside a 6 m long tube can partially sustain the ion in the gas phase.⁸⁴ In an enclosed system the DESI spray was first directed to the sample surface and the desorbed analyte droplets were subsequently forced into transfer tube with 4.3 mm inner diameter. The length of the transfer tube was altered for the experiments from 1 cm to 60 cm. It was observed that the signal abundance for the model analyte cocaine decreased by a factor of six over the first 5 cm. With further increasing length of the transfer tube the ion abundance decreased much less significantly (16% signal decrease between 10 cm and 60 cm tube length). The authors explain this effect by a laminar flow which is established after only 5 cm inside the transfer tube by the DESI spray gas flow rate of 1.1 L/min. Due to the laminar flow and high gas flow rates the ions do not have enough time to diffuse to the walls of the transfer tube and consequently remain in the gas phase. In addition to the spray-based ADI-MS technique these experiments were also performed with the LTP probe and a satisfying signal abundance for 1.7 µg cocaine was detected after the ions were transported through a 1.2 m long Tygon tubing (10 mm ID). Due to the low gas flow rates of the LTP probe (0.5 L/min) additional vacuum pumping at the end of the transfer tube was used to establish the laminar flow. In conclusion these results suggest that the high ion abundance of a very short transfer tube cannot be sustained by a laminar flow inside the transfer tube but the “carrier gas” can help to maintain a certain number of ions to be transported over a longer distance.

2.7 Conclusion

In this chapter, a brief overview about possible optimization parameters for direct analyte sampling by plasma-based ADI-MS is given. Specifically, in the first part different instrumental modifications of DART and the FAPA source are presented. The DART SVP was presented as a versatile ADI source for direct surface sampling. Due to the low plasma temperatures (~ 55 °C) of the C-G plasma discharge of the DART source the analyte desorption is accelerated via an external gas heater. Furthermore, the DART ID-Cube was described, which is typically used to analyze liquid samples in transmission-mode. For the FAPA source different instrumental geometries were presented and the benefits (*e.g.*, less analyte oxidation, higher plasma temperatures) of the respective FAPA source design are discussed.

In the subsequent sections of this chapter the desorption and ionization process for ADI-MS techniques are discussed and possibilities to improve the analyte desorption/ionization are presented. Exemplarily, Nilles *et al.* modulated the analyte desorption process for DART-MS analysis with a temperature gradient of the heated sample substrate. This enabled the separate mass spectral detection of the isobaric analytes. Furthermore, different additives for the modification of the plasma conditions were presented and their benefits for the analyte ionization process were explained. For example, Badal *et al.* investigated the influence of oxygen added to the plasma gas and observed an enhancement of the ion signal for the protonated water clusters, which can be beneficial for the protonation reaction of analyte molecules.

In addition, different methods for sample introduction were reviewed. In the literature it was found that rod shaped sample probes offer the possibility for fast analyte sampling but comprise the drawback of high RSDs between subsequent measurements. This effect is mainly caused by the manual sample positioning in the plasma afterglow. Furthermore, a new wire sample probe was introduced by Jeckelmann *et al.*, which provided a more reproducible analyte signal abundance, even with manual positioning of the wire probe in the DART afterglow. Additionally, SPME was described as a useful tool for analyte preconcentration in the case of low analyte concentrations, and the beneficial and very reproducible analyte introduction by a DOD generator was explained.

In the last section of this chapter, the optimization of the analyte-ion transfer into the mass spectrometer was highlighted. Recent studies were presented, in which the atmospheric pressure interface was modified with a larger inlet capillary so more

analytes were aspirated by the mass spectrometer. Furthermore, the general operating principle and the benefits of the Vapur interface for plasma-based ADI-MS was explained. Specifically, the Vapur interface performs the separation of the helium plasma gas from the analyte ions in a low vacuum stage attached to the atmospheric-pressure inlet and herewith decreases the vacuum load of the mass spectrometer vacuum system. Lastly, studies by Häbe *et al.* and Garimella *et al.* were presented in which the instrumental setup of the Vapur interface was optimized for maximum ion transmission, and ions were transferred over 6 m from the ADI source into a mass spectrometer, respectively.

Chapter 3

Optimization of the Flowing Atmospheric-Pressure Afterglow Plasma-Source Geometry and Development of a Temperature-Controlled Sample Holder for Direct Mass Spectral Surface Analysis

3.1 Introduction

The research field of ADI-MS was introduced in 2004 as a new technique to directly probe samples in their natural environment and as they are. This claim was demonstrated for the first two ADI sources published in literature – DESI and DART – by analyzing drugs and chemical warfare agents in the proof-of-principle publications by Takats *et al.*⁶ and by Cody *et al.*,⁷ respectively. In the following years, the field of ADI-MS expanded with a quickly growing number of different ADI sources comprising (electro-)sprays, plasma sources, and laser beams for sample desorption/ionization.^{5,38,53,85} The large majority of these publications are pointing out the ability for direct surface analysis and, therefore, defining the main purpose of ADI-MS.

Despite the rather simple appearing workflow for the application of ADI-MS to real world samples, these methods need to be carefully optimized to improve the sensitivity as well as the selectivity. For the DART source, multiple modifications have been presented to optimize the analyte desorption/ionization and the ion transfer into the mass spectrometer. First, the ADI source comprises an external gas heater to increase the plasma gas temperature and to enhance the analyte desorption by evaporation.⁷ Second, the Vapur[®] atmospheric pressure ionization (API) interface was developed by IonSense Inc. (Saugus, MA, USA) for this commercialized product to remove excess helium, originating from the plasma, with a diaphragm pump in a pumping stage before the inlet to the mass spectrometer. Furthermore, Häbe *et al.* improved the front tip of the DART source to enhance the lateral resolution for surface scanning as well as the transfer of desorbed species into the Vapur[®] interface and mass spectrometer, respectively.^{44,46} Another ADI plasma source frequently reported in literature is the LTP probe which is of special interest for direct mass spectral analysis as a hand-held instrument. The low energy and plasma-gas consumption was used by Huang *et al.*⁸⁶ as well as Soparawalla *et al.*⁸⁷ to perform in situ analysis of melamine in milk products and agrochemical residues in fruits with an LTP probe coupled to a miniaturized mass spectrometer. The source design of the LTP as well as the positioning of the source in front of the mass spectrometer was later optimized by Albert *et al.* via the chemometric approach named design-of-experiments (DoE).⁸⁸ Moreover, Lu *et al.* optimized the frequency and applied voltage for the dielectric-barrier discharge and altered the plasma gas composition by adding nitrogen to the helium gas to change the plasma reactivity.⁸⁹ The FAPA source went

through a whole series of instrumental changes in order to optimize the plasma-based ADI source for the analysis of solids, liquids and gaseous sample. The original p2p-geometry of the source was changed to a p2c-geometry in order to minimize analyte oxidation by atomic oxygen from the ambient air.¹¹ A redesign of the plasma source was introduced by Pfeuffer *et al.*, in which a toroidal shaped glow discharge was formed and the analysis of gases and aerosols was improved.⁵⁰ Furthermore, the Hieftje research group investigated the positioning of the FAPA in front of the mass spectrometer (*e.g.*, angle and distance) and the operating parameters (*e.g.*, helium flow rate).^{70,90} In addition to the optimization of the ADI source geometry also the analyte sampling position offers possibilities to optimize the overall performance of the analysis method. For example, volatile compounds such as electrolytes used in a lithium-ion battery (LIB) can easily evaporate at room temperature due to their low vapor pressure. To avoid the unwanted evaporation of the analytes prior the analysis by the ADI-MS Campbell *et al.* developed a Peltier-cooled sample holder to analyze semi-volatile fragrances on various sample substrates (*e.g.*, glass, paper, or cloth) by LTP-MS.⁹¹ With the aid of this cooled sample substrate detection limits down to 0.2 pg for β -naphthyl methyl ether were achieved. Furthermore, mass spectral imaging of fragrance droplets in a filter paper was possible with this LTP-MS method and a modest spatial resolution better than 1 cm could be achieved.

In this chapter, different parameters of the FAPA source are investigated. The positioning of the FAPA is related towards the signal abundance of the model analyte caffeine and the results expand the range of geometry settings discussed by Pfeuffer *et al.* in previous studies.^{70,90} Additionally, a shortened anode capillary (11 mm) is installed into the p2c-FAPA source and will be compared to the originally used capillary length (25 mm)¹¹ by IR-thermography. The two anodes will be also compared in regard of their capability to analyze compounds with high vapor pressure and the amount of analyte oxidation of both anode capillaries will be discussed.¹¹ Furthermore, the interelectrode distance between pin cathode and capillary anode will be optimized for their best performance to analyze the model analytes caffeine and nicotine on TLC plates. For semiquantitative signal comparison these substances on the TLC plates are probed by mass spectral imaging. In the last section of this chapter, the development of a temperature-controlled sample platform is presented and applied for the analysis of volatile lithium-ion battery (LIB) electrolytes via LTP-MS.

3.2 Experimental Section

Reagents. The ADI source performance with different geometries and settings was tested with self-made test mixtures containing caffeine (>99.9%) and nicotine (>99.9%), and DPA (analytical grade). The caffeine and nicotine standards were purchased from Sigma Aldrich Chemie GmbH (Taufkirchen, Germany), while DPA was purchased from Honeywell Riedel-de Haën AG (Seelze, Germany). Isopropyl alcohol (analytical grade), n-heptane (analytical grade), and methanol (HPLC grade) were purchased from Fisher Scientific GmbH (Schwerte, Germany). The deionized and double distilled water was produced in the laboratory with a distillation apparatus from Heraeus-Quarzschmelze GmbH (Hanau, Germany).

The electrolyte LP30 SelectiLyte™ was purchased from Merck KGaA (Darmstadt, Germany) and contained 1M of LiPF₆ salt dissolved in ethylene carbonate (EC, 99.9%) and dimethyl carbonate (DMC, 99.9%) in a solvent ratio of 1:1. The cycled battery electrodes with LP30 electrolyte were supplied by the MEET battery research center (Münster, Germany). The batteries contained graphite electrodes, with SLP 30 (90%), polyvinylidene difluoride (PVDF, processed in N-Methyl-2-pyrrolidone, 5%), conductive carbon black (5%), and the LP30 electrolyte (1M LiPF₆, EC/DMC 1:1).

Preparation of Test Mixtures for FAPA-MS Analysis. For the FAPA angle and distance optimization an 8 mg/mL caffeine solution was prepared and directly used for analysis. 2 µL of this standard was deposited on the glass slide prior to each analysis. For the comparison of the short (11 mm) and long (25 mm) FAPA anode capillary, six DPA solutions in the concentration range between 2 mg/mL and 100 mg/mL were prepared with methanol used as solvent. The influence of the FAPA interelectrode distance was tested via a test mixture containing caffeine and nicotine. The solution was prepared with 1 mg/mL stock solutions of both analytes, which were combined in one vial and filled up with methanol to obtain a final concentration of 0.1 mg/mL for each analyte.

Thermal Electrolyte Aging. Before thermal aging of the electrolyte 1 mL of fresh LP30 electrolyte (not diluted) was transferred from the storage container into a 10 mL air tight aluminum container with PVDF seal (Leicht & Appel GmbH, Bad Gandersheim, Germany). This sample preparation was done in a glove box under

argon atmosphere to avoid the contamination of the electrolyte with ambient air. The LP30 electrolyte was thermally stressed for 0, 1, 2, 4, 7, and 14 days inside an oven (Universal Oven U 50, Memmert GmbH + Co. KG, Schwabach, Germany) at 85 °C. For each aging period three replicates were prepared. All samples were prepared on the same day. All thermally stressed samples were placed inside the oven on day 0 and were removed from the oven after the desired time. After removing the samples from the oven, the samples were stored until the end of the 14-day aging period at -18 °C to avoid further degradation of the electrolyte. All aged LP30 samples were analyzed together after the 14-day aging period was completed.

Flowing Atmospheric-Pressure Afterglow. For direct surface analysis of the TLC plates by FAPA-MS a p2c-geometry of the FAPA source, described by Shelley *et al.*,¹¹ was used. A stainless-steel pin-electrode (1.6 mm outer diameter, o.d.) was positioned inside a ceramic discharge chamber (Macor®, Schröder Spezialglas GmbH, Ellerau, Germany). The tip of the pin-electrode inside the discharge chamber was sharpened to a point. On the opposite side of the ceramic body a capillary electrode (1.6 mm o.d., 1.3 mm i.d., length 11 mm or 24 mm) was positioned with a distance between the electrodes of 8 mm. The plasma was operated by applying a negative potential (25 mA, 663 V, constant-current mode) to the pin-electrode through a 5 kΩ ballast resistor, while the capillary anode was grounded. For power generation, a Kepco BHK 1000-0.2MG DC power supply (Kepco Inc., Flushing, NY, USA) was used. Helium 5.0 (99.999%, Messer Industriegase GmbH, Siegen, Germany) served as plasma gas with a flow rate of 0.5 L/min for all experiments presented in this chapter. For surface desorption (*cf.* Figure 3.1a) the FAPA was mounted in a 60° angle related to the horizontal sample surface plate. The glass slide or TLC plate was positioned <0.5 mm below the inlet capillary of the mass spectrometer and 3 mm below the FAPA source. If not stated differently, the distance between the FAPA and inlet capillary was 2 mm. For TM-FAPA-MS analysis (*cf.* Figure 3.1b) of the DPA analyte the FAPA source was positioned in a 7-mm distance (on-axis) towards the inlet capillary of the mass spectrometer. The analyzed sample was deposited on a stainless-steel mesh, which was positioned between FAPA source and mass spectrometer inlet capillary (distance to mesh ~1 mm). The metals mesh was fixed on a custom-made rail system to ensure reproducible mesh positioning.

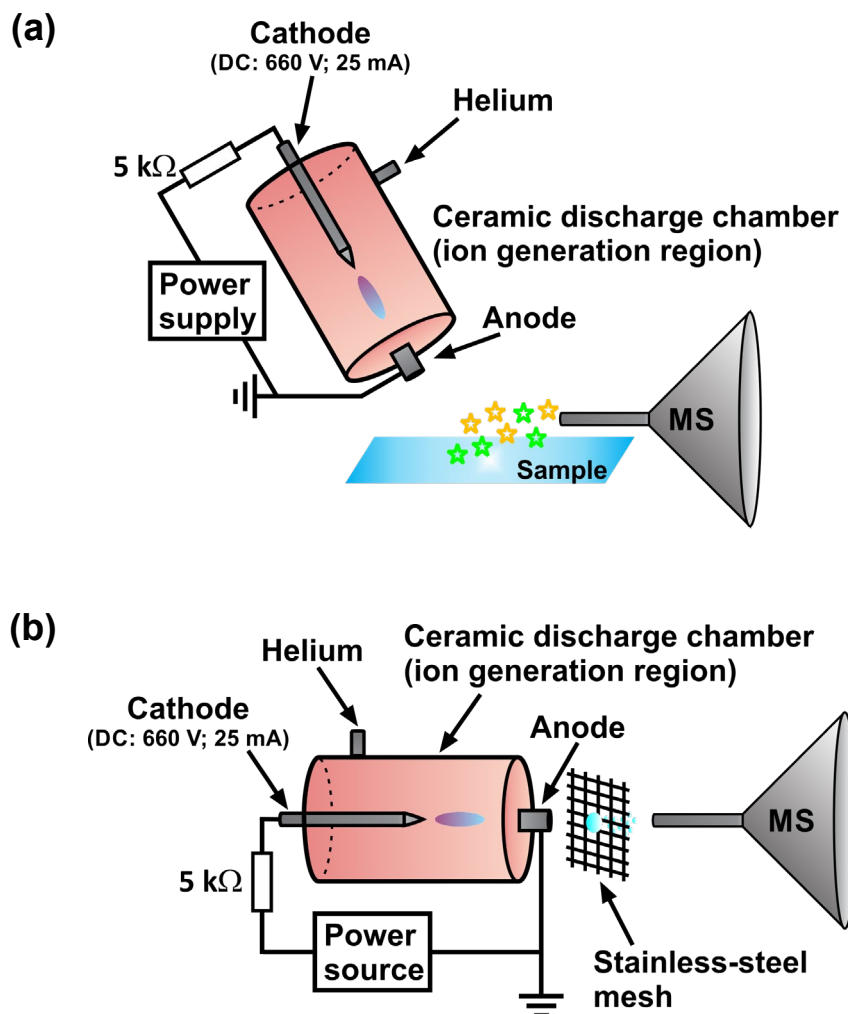


Figure 3.1 Schematic of the instrumental setup for FAPA-MS measurements operated in surface-sampling mode (a) and transmission-mode (b).

Low-Temperature Plasma Probe with Temperature-Controlled Sample Holder. For the presented experiments a home-built LTP source as described earlier by Albert *et al.* was used.⁹² For the construction of the LTP probe a stainless-steel needle electrode (0.5 mm o.d.) was positioned inside of a quartz capillary (7 mm o.d., 1 mm i.d.). A copper ring electrode of 20 mm width was installed on the outside of the glass capillary. During operation, 0.3 L/min helium (99.999%, Messer Industriegase GmbH) was introduced into the LTP source. An alternating-current (AC) voltage of 14 kV_{p-p} at 31 kHz was applied to the steel electrode, while the copper electrode was grounded, to form a dielectric barrier discharge inside the quartz tube. The LTP probe was powered with a Voltagezone Electronics e.U. DC-AC converter (model HVGEN10AC v3.1, Graz, Austria). For surface analysis the LTP source was positioned in front of the mass spectrometer according to the optimized geometry parameters published by Albert *et al.*⁸⁸ Specifically, the LTP source was positioned in

a 60° angle and 2 mm distance towards the MS inlet capillary, while the distance between LTP and sample surface was 5 mm (*cf.* Figure 3.2). For the analysis 0.5 μL of the sample was deposited on a custom-made 32-well plate and positioned 1 mm underneath the MS inlet capillary on the temperature-controlled sample holder.

The temperature-controlled sample holder was constructed with a computer Raystorm graphics processing unit (GPU) water cooling block (XSPC, Great Britain, purchased at casekin.de, Berlin, Germany) and a Peltier element (4x4 cm, TEC1-12706 thermoelectric module, Conrad Electronic SE, Hirschau, Germany). A constant flow of 19 $^\circ\text{C}$ cold water was pumped through the GPU chiller and between the cooling block and the Peltier element a heat conducting paste was deposited for improved heat removal from the Peltier element.

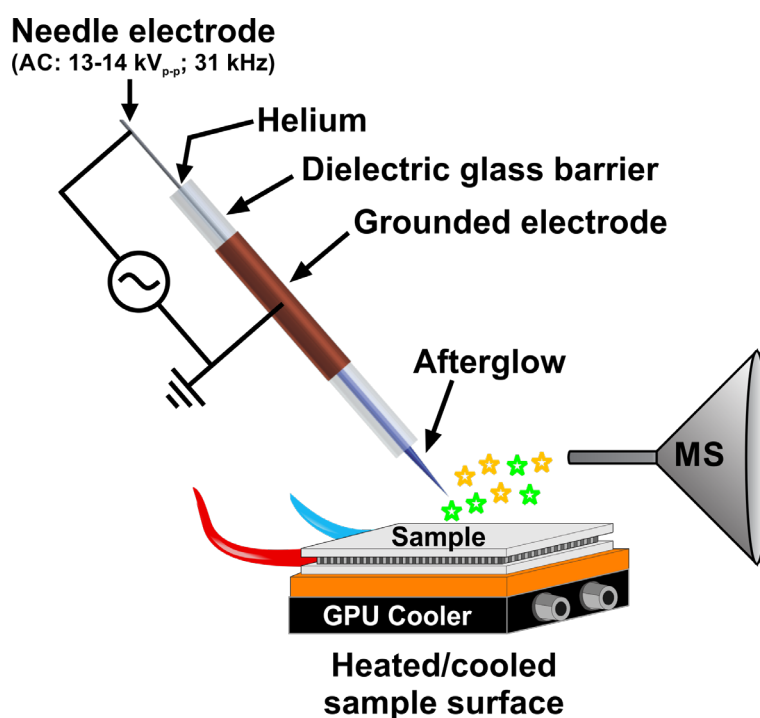


Figure 3.2 Schematic of the instrument setup for direct surface-sampling by LTP-MS. For heating and cooling of the sampling surface a Peltier element with attached heat exchanger was used.

High-Resolution Mass Spectrometry. For mass spectral analysis, a high-resolution mass spectrometer (Exactive, Thermo Fisher Scientific GmbH, Bremen, Germany), equipped with an Orbitrap mass analyzer was used. To install the ADI source in front of the inlet capillary of the mass spectrometer, the electro spray ionization housing was removed and the conventional inlet capillary was replaced by a 4-cm extended inlet capillary (0.6 mm i.d.), which was bent downward to the

sampling surface by 12°. The mass spectrometer was calibrated each time before the ADI-MS experiments were performed to ensure precise mass-to-charge ratio (m/z) measurement. For mass calibration, a solution of caffeine (Sigma-Aldrich Inc., St. Louis, MO, USA), MRFA (Met-Arg-Phe-Ala acetate salt, Sigma-Aldrich Inc.), and Ultramark 1621 (Sigma-Aldrich Inc.) was used. The Exactive instrument parameters used for mass spectral analysis are listed in Table 11.1 in the appendix.

Optimization of the FAPA Positioning. Prior to sample analysis the FAPA sources was positioned in the desired angle (50°, 60°, or 70°) related to the horizontal sample surface. Subsequently, the distance between the FAPA and sample surface was set to 3 mm and the desired distance between FAPA and MS was adjusted between 1-10 mm. For the previously described measurements of the FAPA positioning, a caffeine test solution was deposited (2 μ L) via a pipette on a custom made 32-well plate (material: quartz glass, 5 mm diameter and 0.5 mm depth for each well) and immediately positioned underneath the plasma afterglow for analysis. Each sample was analyzed for 60 seconds. The combined extracted-ion chromatogram (EIC) of m/z 195.0875 (protonated molecule ($[M+H]^+$), mass accuracy ± 0.8 ppm) and m/z 196.0910 ($[M+H]^+$ with one ^{13}C -isotope, mass accuracy ± 0.1 ppm) was used during data processing to determine the average caffeine ion-abundance for the individual FAPA setting. This ion abundance is compared to the distance between FAPA and mass spectrometer.

Infrared (IR)-Thermography. To visualize the surface temperature distribution on a microscope glass-slide underneath the FAPA source, IR-thermography measurements were done with a testo 875i camera (Testo SE & Co. KGaA, Lenzkirch, Germany). The camera can detect radiation in a wavelength region between 8-14 μm . For accurate temperature measurement, the IR radiation reflected from the glass slide plate – also referred to as reflected temperature – as well as the emissivity (ϵ) were determined manually. These corrections are necessary because the glass slide might reflect thermal radiation from the inside of the plasma source towards the IR detector. Also, the glass slide is not an ideal (black) radiator and the emissivity of thermal radiation for this sample target is not equal to one. Consequently, the manually determined emissivity and the reflected temperature are important factors for precise measurement of thermal radiation and need to be considered in the context of thermal energy transfer or transformation. In this context, the transport of thermal radiation is summarized by the three wavelength

dependent dimensions, the absorptivity (α), reflectance (ρ), and the transmission factor (τ), which can be combined in one formula (*cf.* Equation 3.1).⁹³

$$\alpha(\lambda) + \rho(\lambda) + \tau(\lambda) = 1 \quad \text{Equation 3.1}$$

$\alpha(\lambda)$	absorptivity
$\rho(\lambda)$	reflectance
$\tau(\lambda)$	transmission factor

The absorptivity, reflectance, and transmission factor are measures for the absorbed, reflected and transmitted heat by a body, respectively. Summarized the three factors are equal to one. Based on the Kirchhoff law of thermal radiation the absorptivity is equal to the emissivity for a body in thermal equilibrium and therefore Equation 3.1 can be transformed into Equation 3.2.⁹³ This formula is then applicable to thermal imaging via thermal imaging instruments and defines the fractions of heat emitted, reflected and transmitted by the analyzed object.

$$\varepsilon(\lambda) + \rho(\lambda) + \tau(\lambda) = 1 \quad \text{Equation 3.2}$$

$\varepsilon(\lambda)$	emissivity
------------------------	------------

To determine the temperature reflected by the sample surface, it is critical to keep the experimental setup with plasma source, sample target and IR camera in a fixed alignment because the reflected temperature is dependent on the radiation angle. For the measurements the microscope slide was covered with an aluminum surface, which has a very low emissivity ($\varepsilon(\lambda)=0.03$). Thus, the major fraction of the thermal radiation is reflected or transmitted.⁹⁴ The IR transmission through the aluminum plate can be neglected due to the fact that the surface is not transparent. Consequently, the detected IR radiation in this experimental setup is exclusively dependent on the radiation emitted and reflected by the surface (*cf.* Equation 3.3).

$$\rho(\lambda) = 1 - \varepsilon(\lambda) \quad \text{Equation 3.3}$$

With an emission of $\varepsilon(\lambda)=0.03$ the reflectance is $\rho(\lambda)=0.97$. To determine the exact reflected temperature from the aluminum surface this $\rho(\lambda)$ value is entered into the IRSoft software (Testo SE & Co. KGaA) as the emissivity value, while the

reflected temperature value is set to the ambient laboratory temperature of 19 °C. Hereby, the temperatures shown in the Testo data evaluation software are the actual reflected temperature and not the temperature emitted by the aluminum plate. The reflected temperature was measured for each individual current setting applied to the FAPA source and were used for the correlating temperature measurements in the following experiments. A graph with the measured reflected temperatures and an IR image of a measurement at 40 mA with the short capillary is presented in the appendix in the chapter 11.2.

The emissivity of a glass plate was determined by placing a tape (Scotch™ Brand 88, 3M, Neuss, Germany) with a constant emissivity of $\epsilon(\lambda)=0.95$ on the glass surface and heating up the plate with a heating mat to ~ 150 °C (the FAPA source was removed from this experimental setup). Subsequently, the temperature of the tape was measured precisely via IR thermography with the aforementioned emissivity and a reflected temperature of 19 °C (ambient temperature in the laboratory). The emissivity of the glass plate was determined by adjusting the ϵ parameter in the IRSoft software so the same surface temperature is measured on the glass surface and the tape surface. Repeated measurements ($n=3$) at different spots on the tape and glass surface reveal an $\epsilon(\lambda)=0.91$ ($\lambda=7.5-14$ μm) for the sample substrate.

In the subsequent measurements of the glass plate surface temperature with FAPA source at different operating currents, the measured reflected temperature and the determined emissivity were used for the data evaluation in the IRSoft software. To compare the surface temperature of the spot heated by the plasma afterglow, a circle (diameter (\varnothing): 5 mm) was placed around the hot spot with a tool of the data processing software. Within the circle, the highest temperature was selected for the comparison of the surface temperatures. A detailed description of this data evaluation method as well as an IR picture can be found in the chapter 11.2.

Sample Handling for TM-FAPA-MS. Prior to analysis the sample solution (2 μL) was deposited on the stainless-steel mesh. The solvent was evaporated at ambient laboratory conditions followed by the positioning of mesh in between the FAPA and mass spectrometer for direct mass spectral analysis of the sample.

Separation of Analyte Mixtures on TLC Plates. To separate the caffeine and nicotine analytes the following TLC separation procedure was applied. The sample mixture was deposited (2 μL) with a syringe on the starting line on a normal phase (NP) silica TLC plate. The samples were applied in ~ 5 mm wide and ~ 2 mm broad lines. Solvent was evaporated at room temperature for two minutes. Separation

of the analyte mixture was performed by placing the TLC plate in a MINIPLAK developing chamber (Fungilab Inc., New York, NY, USA) and using a mobile phase solvent mixture of isopropyl alcohol, n-heptane, and water (ratio of 7:3:1 (v/v/v)). Separation was completed within in ~25 minutes. Subsequently, the solvent was evaporated from the TLC plate for 15 minutes on a temperature controlled hot plate at 50 °C and afterwards placed in front of the FAPA source ready to be probed.

Mass Spectral Imaging of Analytes on TLC Plates. For mass spectral imaging, line scans across the TLC plates were performed with a motorized translational x-y-stage (Newport Corporation, Irvine, CA, USA) with a translational speed of 0.3 mm/s and a line to line distance of 0.5 mm. The stage was controlled by a self-written LabVIEW (National Instruments, Austin, TX, USA) routine with a triggered line scan signal to start the data acquisition of the mass spectrometer. Mass spectral data was acquired via the Exactive Tune 1.0 software (Thermo Fisher Scientific GmbH). For further data processing, the analyte EICs were extracted from the mass spectrometer software to Origin 2017 (OriginLab Corporation, Northampton, MA, USA). The mass window of the analyte EICs were defined for all presented results to be 8 ppm above and below the detected exact mass of the analyte (*e.g.*, caffeine: m/z 195.0879 \pm 8 ppm corresponds to the mass range 195.0864 - 195.0895). In a subsequent step the line scans were combined to a contour plot to semi-quantitatively compare the detected signal abundance of the analyte spots. Therefore, a region-of-interest (ROI) was defined, which completely covered the respective analyte spot and all voxel volumes within this ROI were summed to a sum of voxel volumes. This sum of voxel volumes is directly proportional to the amount of analyte on the probed surface and can be used as a measure of the sensitivity of the FAPA-MS setup with different FAPA interelectrode distances. A detailed description of the data processing procedure with examples is given in chapter 11.4.

3.3 Results and Discussion

Optimization of the FAPA Source Positioning in Front of the Mass Spectrometer. To enhance the ion transfer from the analyte sampling position into the mass spectrometer, and therefore the method sensitivity, the orientation of the FAPA source is critical. Here, multiple geometry parameters of the FAPA-MS setup can be optimized such as the distance between the MS and the sample, the distance

between FAPA and sample, the distance between FAPA and MS, and also the angle of the FAPA related to the sample surface. Additionally, the inlet capillary of the MS can be a straight tube, orthogonal to the sample surface, or a downwards bent capillary pointing at the sample surface. In this chapter, the FAPA distance in relation to the mass spectrometer inlet capillary (1-10 mm) and the angle of the FAPA source (50°, 60°, and 70°) related to the horizontally positioned sample surface was optimized. The parameter of the distance between the MS inlet capillary and the sample surface has been discussed by Pfeuffer *et al.*, who found that the distance between the sample surface and the mass spectrometer inlet capillary needs to be as small as possible, due to a boundary layer of helium which is sticking to the glass surface.⁹⁰ Hence, the distance was kept at <0.5 mm for all experiments, and a downwards bent MS inlet capillary (12°) was used to improve the ion transfer by the vacuum of the mass spectrometer. Also, the vertical distance between FAPA source and sample surface was kept constant for all experiments. The horizontal distance between the FAPA source and the sampling spot was adjusted for each measurement, so the plasma afterglow was directly pointing in the direction of the analyte droplet. The model analyte caffeine was directly desorbed – together with residues of methanol solvent – in the moment it was moved underneath the FAPA source. A combined EIC of m/z 195.0875 (protonated molecule ($[M+H]^+$), RMA ± 0.8 ppm) and m/z 196.0910 ($[M+H]^+$ with three ^{13}C -isotope labels, RMA ± 0.1 ppm) was used to determine caffeine ion-abundance, which is compared with the distance of the FAPA and the mass spectrometer (*cf.* Figure 3.3).

For the three angle settings of 50°, 60°, and 70° signal abundances of $6 \cdot 10^5$ a.u., $3 \cdot 10^6$ a.u., and $1 \cdot 10^7$ a.u., respectively. With increasing distance between FAPA and MS the signal abundance of the caffeine analyte increases up to $\sim 1.4 \cdot 10^7$ a.u. for all angles. Continuous growth of the distance between FAPA and MS the signal abundance decreases down to $1 \cdot 10^6$ a.u. and lower. The RSDs for the individual measurements range between 8 and 28%. In comparison to larger FAPA-to-MS distances rather low RSDs (8-11%) are observed for short distances between FAPA source and mass spectrometer (2-4 mm), and if the signal abundance is $> 5 \cdot 10^6$ a.u.

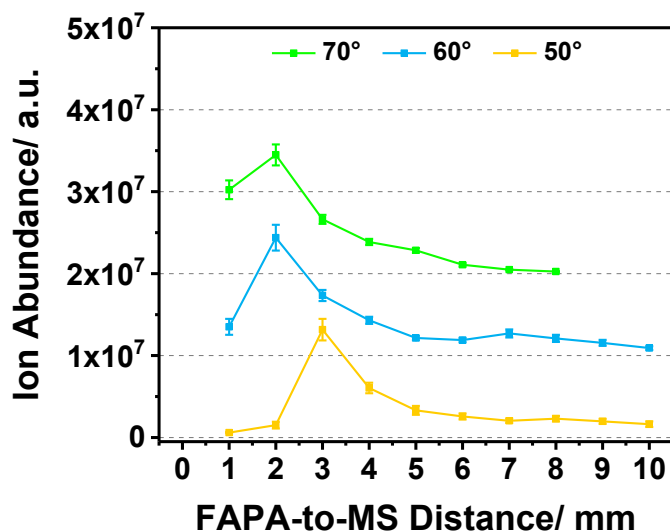


Figure 3.3 Absolute ion-abundance of caffeine (EIC of m/z 195.0879 \pm 8 ppm) detected via FAPA-MS with altered distance between FAPA anode tip and MS inlet capillary tip. For visualization purposes a y-axis offset of $1 \cdot 10^7$ and $2 \cdot 10^7$ was chosen for the 60° and 70° data points, respectively. Error bars represent $\pm 1\sigma$ of three replicate measurements.

For the angles 60° and 70° a closer distance of 2 mm was found to be most effective, while for 50° a distance of 3 mm was found to be better for the ion transfer into the mass spectrometer. In comparison of 50° , 60° , and 70° the FAPA angle did not significantly affect the analyte signal abundance at the optimum FAPA position of 2 mm or 3 mm distance, respectively. The differences in the optimum desorption distance, *e.g.*, 2 mm for 60° and 3 mm for 50° , are most probably caused by the angle of incidence at which the FAPA is pointing in the direction of the sample surface and the angle of reflection to the mass spectrometer. With decreasing angle θ_1 in respect to the normal vector of the sample surface also the angle θ_2 related to the mass spectrometer is decreased. Consequently, the ideal distance between FAPA and mass spectrometer for surface analysis increases with decreasing θ_1 .

Similarly, Pfeuffer *et al.*,⁷⁰ studied the influence of the FAPA angle and plasma gas flow rate on the plasma gas stream spread impacting on the sample surface and the subsequent transfer to the MS. In this study, the authors detected a higher surface temperature at a steeper FAPA angle (45°) compared to a 30° angle. Furthermore, higher surface temperatures were detected when the helium flow rate was increased from 0.5 L/min to 1.5 L/min. The authors hypothesized that the higher gas velocity causes an improved analyte desorption by backscattering of the helium stream from the helium boundary layer. Together with the above stated results it can be concluded

that steeper FAPA angles ($>50^\circ$), a close distance between FAPA and mass spectrometer inlet capillary (2-3 mm), and high plasma gas flow rates (~ 1 L/min) are advisable to improve the FAPA-MS sensitivity.

Influence of the Anode Capillary Length. With the introduction of the p2c-FAPA source by Shelley *et al.*¹¹ an ionization source with less oxidized analyte species and improved detection limits compared to the original FAPA source, p2p-geometry,^{9,10} was developed. This improvement of performance and sensitivity goes along with a ~ 100 °C lower temperature of the flowing afterglow at the front tip of the p2c-FAPA source in comparison to the p2p-FAPA. This observation probably is due to cooling of the plasma gas as it travels down the capillary.^{11,13} However, the temperature is thought to play an important role in the analyte desorption process due to enhanced analyte evaporation at elevated temperatures. To decrease the effect of plasma cooling by a long anode capillary a shorter, 11 mm long, capillary is compared to the 25 mm long capillary, used in the original p2c-FAPA publication (*cf.* photograph of the capillaries in Figure 3.4).

In this chapter, the capillaries are compared by the resulting sample surface temperature, which was measured by IR thermography. For these measurements, the FAPA source was positioned at 60° angle with 3 mm distance to the horizontal microscope slide. The surface temperature was measured, after an equilibration time of 3 minutes, at different FAPA operating-currents between 2.5 mA and 50 mA. Emissivity and reflected temperature of the surface were manually measured and corrected before the experiment (*cf.* chapter 3.2 and 11.2). The detected sample surface temperatures caused by the FAPA plasma are plotted in respect to the current applied to the FAPA pin-electrode in Figure 3.4a. For both capillary types a linear relationship is observed between increasing surface temperature and current, respectively. For the 25 mm long capillary, the temperature at 2.5 mA was very similar to the surrounding surface temperature. Hence, this datapoint was omitted from the graph Figure 3.5a.



Figure 3.4 Photograph of the 11 mm (upper) and 25 mm (lower) anode capillary used for the FAPA source.

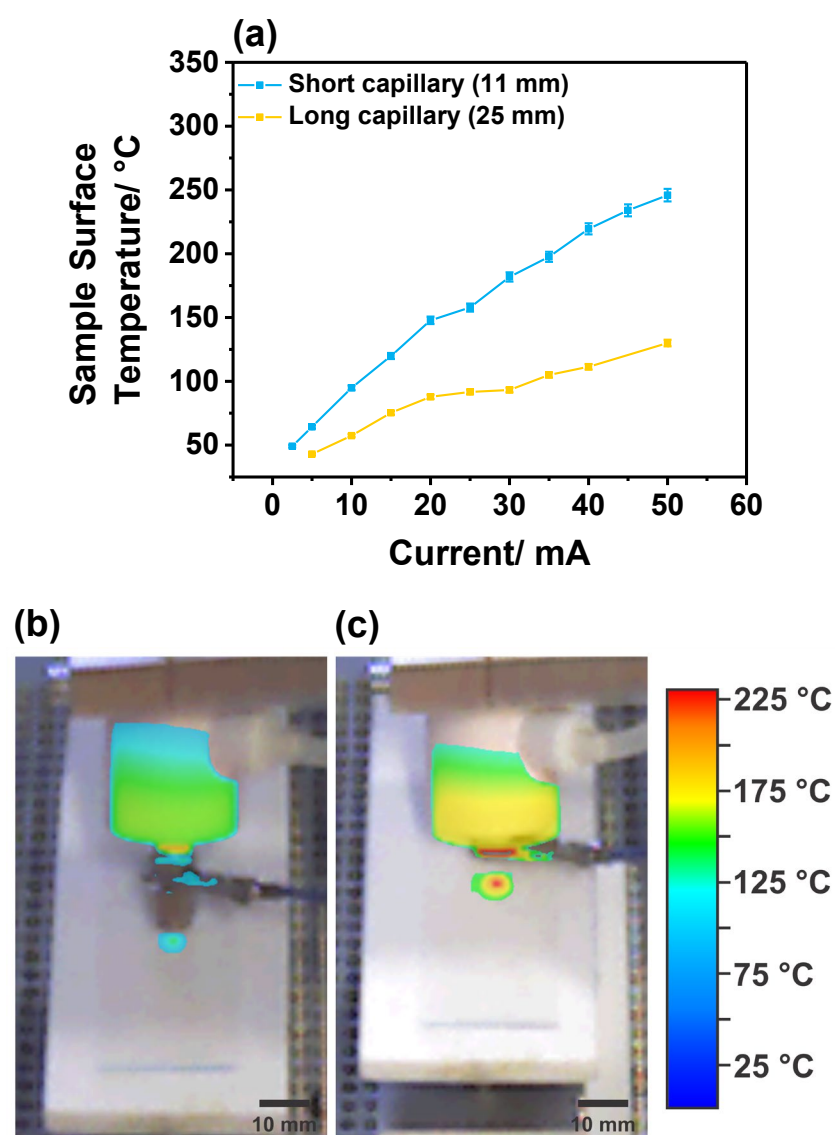


Figure 3.5 IR-thermography of the glass slide surface temperatures at the afterglow impact position of the FAPA source relative to the applied discharge current (a). Thermographic images of the FAPA with long (b) and short (c) anode capillary operated at 40 mA DC.

At low currents (*e.g.*, 5 mA or 10 mA) the shorter anode capillary cause 20 °C or 50 °C higher surface temperatures compared to the longer capillary. With further increasing operating current the temperature difference constantly increases and consequently at 50 mA temperatures of 246 °C and 130 °C were detected for the short and long capillary, respectively (temperature difference 116 °C). The obtained results indicate that with a shorter anode capillary the plasma cooling between the plasma generation region inside the ceramic FAPA body and the sample surface is decreasing. This effect is probably because of a shorter distance between the two locations, and has also been suggested by Shelley *et al.*¹¹ Especially, the shorter metal fitting on the outside of the ceramic body is believed to be beneficial for less plasma gas cooling because stainless steel is a good heat conducting material^{95,96} and can act as a heat sink from the plasma to the ambient air. These observations are visually demonstrated by two IR-thermography pictures in Figure 3.5b and c. For the FAPA with short capillary (*cf.* Figure 3.5c, 40 mA applied) higher temperatures (213 °C) as well as a larger heated spot is observed in comparison to the FAPA with long capillary (*cf.* Figure 3.5b, 40 mA applied), for which a temperature of 111 °C was detected. The criterium for the comparison of the spot size an area with a temperature with $\geq 70\%$ of the maximum detected temperature is considered. Here it was found that with the long capillary a surface area of 0.72 cm² was covered between 78 °C and 111 °C, while with the short capillary a surface area of 1.55 cm² was covered in the temperature range of 149 °C and 213 °C. In comparison to the results obtained by Pfeuffer *et al.* the glass plate is heated in a similar elliptical shape because the FAPA is oriented in a 60° angle with respect to the surface.⁷⁰

An aforementioned benefit of the p2c-FAPA compared to the p2p-FAPA is the minimized analyte oxidation by ambient oxygen and therefore less possibilities of mass spectral interferences of these oxides with other analytes of interest. Also, less oxidation could be advantageous for the instrument sensitivity because less competitive oxidation of analyte molecules might result in improved ion signals of protonated molecules. To compare the 25 mm and 11 mm anode capillaries of the FAPA; in this regard mass spectra of DPA are presented in Figure 3.6. This compound has also been used by Shelley *et al.* when p2c-FAPA was introduced in 2011.¹¹

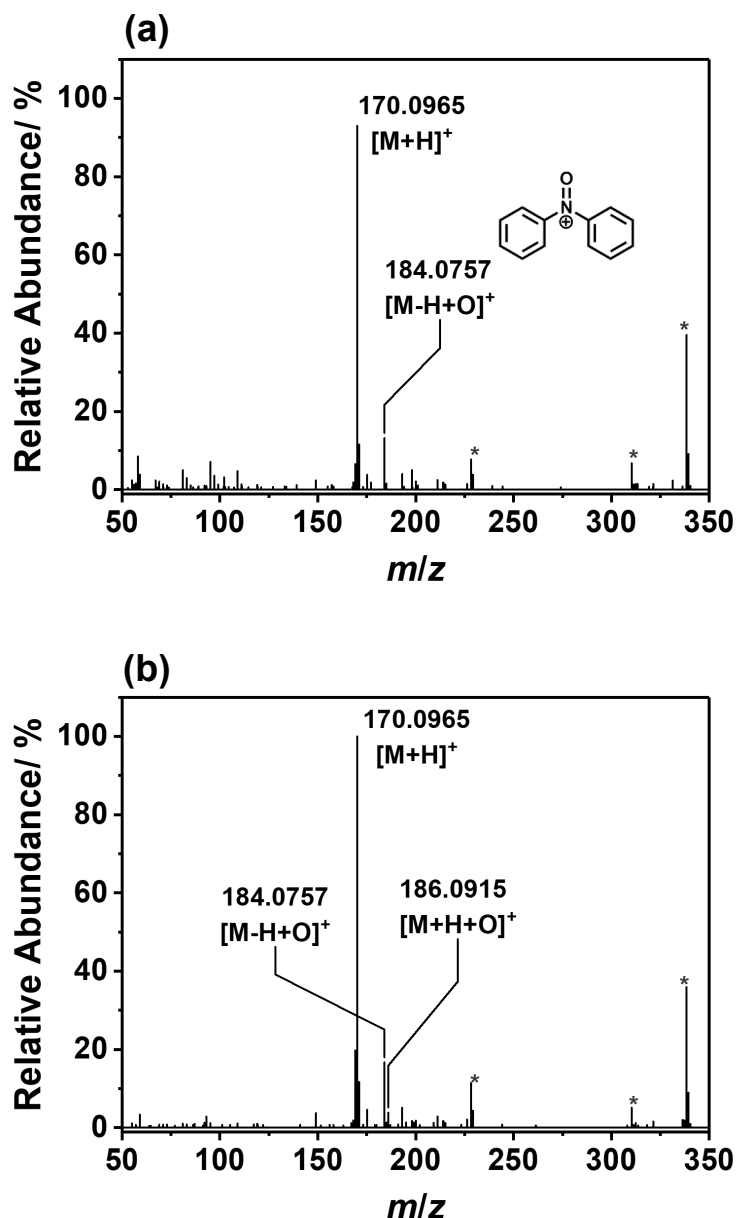


Figure 3.6 Mass spectra of DPA analyzed via TM-FAPA-MS with the 25 mm (a) and 11 mm (b) anode capillary of the FAPA source (positive-ion detection mode). The analyte solution (2 μ L, 20 μ g/mL) was deposited on a stainless-steel mesh and the solvent was evaporated at ambient conditions prior analysis. Relative mass accuracy (RMA) better than ± 1 ppm. The black stars indicate degradation products and synthesis byproducts of the DPA standard.

By comparing the mass spectra of DPA detected with the two different FAPA source geometries only minor differences can be observed. Base peak in both mass spectra is the $[M+H]^+$ peak of DPA (m/z 170.0965, mass accuracy 0.4 ppm). Another abundant peak at m/z 184.0757 (mass accuracy 0.1 ppm, relative abundance to base peak 9-15%) originates from an oxidized species with the sum formula $C_{12}H_{11}ON$ which might originate from oxidation of the standard compound in the storage

container by ambient air. This reactivity is also described by Vogt and Gerulis in Ullmann's Encyclopedia of Industrial Chemistry.⁹⁷ However, a typical oxidation product formed by FAPA during the ionization process is the $[(M+O)+H]^+$ -ion, in this case with m/z 186.0915 (mass accuracy 0.9 ppm). This ion is only observed for the FAPA source with shorter anode capillary (relative abundance to the base peak 4%) and is not observed for the FAPA source with 25-mm anode capillary (*cf.* Figure 3.6) The peaks in the mass spectrum marked with a black star are originating from background ions also observed in mass spectra detected with a caffeine analyte in the same concentration range.

For direct and semiquantitative comparison of the m/z 170.0965, m/z 184.0757, and m/z 186.0915 ion abundances the transient signal of the respective ions were integrated and the resulting EIC areas are shown in relation to the current applied to the FAPA cathode (*cf.* Figure 3.7). It is observed for both FAPA anodes that the $[M+H]^+$ -ion abundance significantly increases when the FAPA operating current is increased from 5 mA to 25 mA. With higher operating currents signal abundance of the DPA $[M+H]^+$ -ion reaches a plateau at $\sim 1.4 \cdot 10^4$ a.u. and $\sim 0.7 \cdot 10^4$ a.u. for the 25-mm and 11-mm capillary, respectively. It is worth mentioning that the RSDs for all measurements of m/z 170.0965 are approximately 35% for both anode lengths. The ion abundance of the oxidized DPA at m/z 184.0757 behaves slightly different to the trend of the $[M+H]^+$ -ion. In case of the 25-mm anode capillary the $[M+O-H]^+$ -ion abundance remains at an abundance of approximately $0.1 \cdot 10^4$ a.u. over the whole range of applied currents. Contrary, the m/z 184.0757 ion-signal increases from $0.001 \cdot 10^4$ a.u. (5 mA) to $0.3 \cdot 10^4$ a.u. (25 mA) for the 11-mm anode FAPA source, and remaining constant with further increasing currents, identical to the $[M+H]^+$ -ion. However, it is interesting to observe that for example at 45 mA applied to the 11-mm anode the signal abundance of m/z 170.0965 and m/z 184.0757 behave differently. Here the $[M+H]^+$ signal increases, while the $[M+O-H]^+$ signal abundance decreases, which raises the question whether the ions are dependent on each other due to analyte oxidation during the ionization process or if the oxidation is also (partially) caused in the analyte container during storage. The oxidized and protonated analyte molecule with sum formula $[(M+O)+H]^+$ (m/z 184.0757) is observed at very low abundances (~ 250 a.u.) when DPA is analyzed with the short capillary FAPA source.

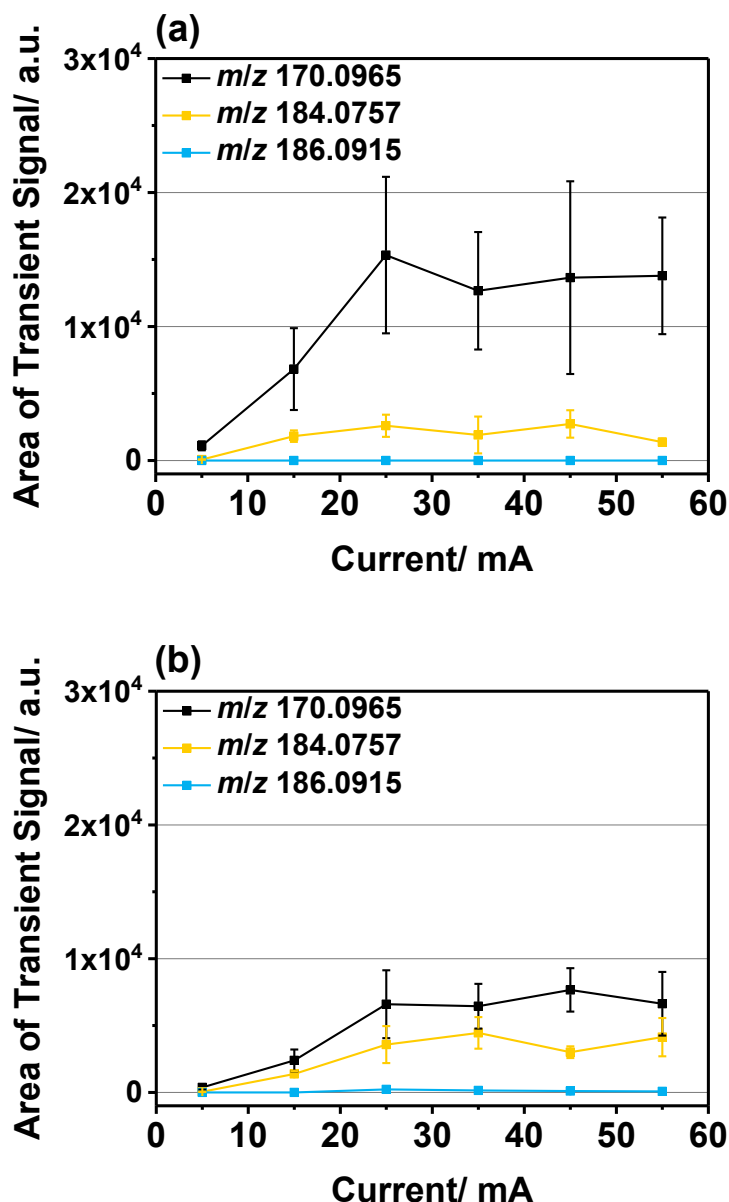


Figure 3.7 Integrated transient signal abundance of the $[M+H]^+$ -ion (black), the $[M-H+O]^+$ -ion (orange), and the $[(M+O)+H]^+$ -ion (blue) analyzed by the FAPA source with 25 mm (a) and 11 mm (b) anode capillary. For the measurements 2 μ L of the DPA analyte solution (20 μ g/mL) was deposited.

In addition to the above presented results also the instrumental detection limit (IDL) for DPA was measured for the TM-FAPA-MS experiment. For the measurements DPA standard solutions in the concentration range 2-100 mg/mL (six calibration levels) and $n=5$ measurements for each calibration level were used. A description of the data evaluation procedure and the calculation of the IDLs can be found in the experimental section and the appendix 11.3 and 11.5, respectively. For the 25 mm anode capillary, an IDL of 2.5 mg/mL and for the 11 mm capillary an

IDL of 0.2 mg/mL was found, when 2 μ L of the analyte solution is deposited on the stainless-steel mesh. In conclusion, a shorter anode capillary significantly increases the surface temperature of the analyte substrate and therefore can aid direct surface desorption and improve the method sensitivity. Coincidentally, the oxidation of the analyte molecule is not significantly increased in comparison to the 25-mm anode capillary.

Influence of the Interelectrode Distance. To further study the fundamental features of the FAPA source and to improve the sensitivity of the desorption/ionization source, the influence of the interelectrode distance is discussed. In the above presented results for all experiments a distance of 8 mm was selected between the tip of the pin cathode and the back end of the anode capillary, positioned inside the ceramic discharge chamber. The interelectrode distance was studied via the mass spectral signal of caffeine and nicotine test substances deposited and separated on a NP-TLC plate. By mass spectral imaging and signal integration of these analyte spots the detected analyte signal can be compared semi-quantitatively and consequently the relationship between the interelectrode distance and the FAPA-MS sensitivity can be interpreted. A detailed explanation of the mass spectral imaging procedure and data evaluation is described in the experimental section 3.2. The sum of voxel volumes detected for the two analytes are presented in Figure 3.8a in relation to the interelectrode distance.

For short interelectrode distances (*e.g.*, 4 mm) signal abundances of $4 \cdot 10^5$ a.u. and $2 \cdot 10^5$ a.u. were detected for caffeine and nicotine, respectively. With increasing interelectrode distance an increase in the signal abundance was observed. For example, ion abundances of $1 \cdot 10^7$ a.u. (caffeine) and $3 \cdot 10^6$ a.u. (nicotine) were detected for an 11 mm interelectrode distance. These results can be explained by the information obtained in Figure 3.8b, in which the power applied to the plasma is plotted against the interelectrode distance. Due to the constant-current mode in which the FAPA was operated the voltage changes with altered FAPA source geometry. With increasing electrode distance, an increase of the power consumption of the glow discharge by an increase of the voltage is observed, which probably leads to the higher plasma temperatures. The higher plasma temperatures cause a higher sample substrate temperature and therefore an enhanced analyte evaporation. Consequently, an increase of the electrode distance could be a useful approach to analyze samples with compounds of higher vapor pressure or low analyte concentrations. However, higher power consumption would lead to increased

operational costs of the method. Most important, the FAPA source would require more frequent maintenance due to wear and deposits on the electrodes.

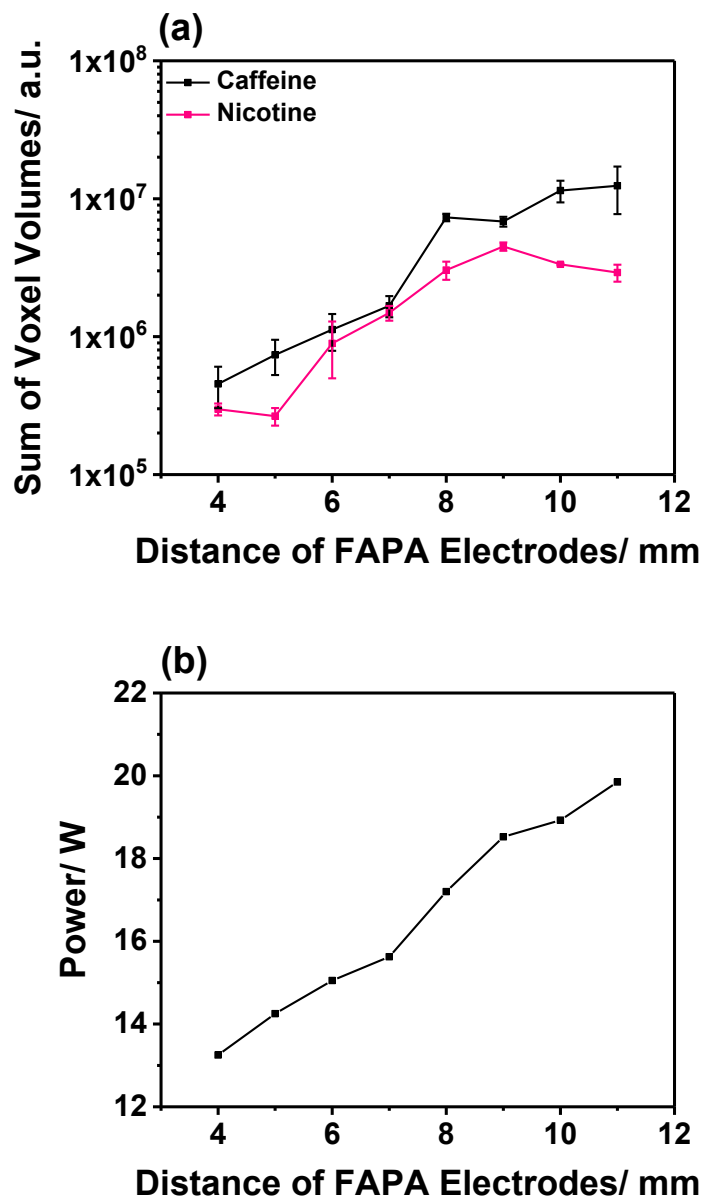


Figure 3.8 Influence of the FAPA (11 mm version) interelectrode distance with respect to the signal abundance of the model substances caffeine (m/z 195.0879 \pm 8 ppm) and nicotine (m/z 163.1229 \pm 8 ppm) (a) and change of the power consumption of the FAPA source with altered electrode distance (b). The analytes were desorbed from a NP-TLC plate after analyte separation.

The FAPA was operated in constant-current mode (25 mA applied to pin electrode).

Development of a Temperature-Controlled Sample Holder for the Analysis of Heat Sensitive and Volatile Analytes. In addition to the optimization of the ADI source the analyte sampling conditions also play an important role for the sensitivity of the ADI-MS method. For example, the analysis of very volatile compounds is a challenging task especially if the analytes can easily evaporate at ambient temperatures due to their low vapor pressures. Compounds with this characteristic are for example carbonates, which serve as electrolytes in lithium-ion batteries (LIBs) and the vapor pressure of the frequently used electrolytes dimethyl carbonate (DMC), ethylene carbonate (EC), or propylene carbonate (PC) are 1.066 kPa, 0.005 kPa, or 0.008 kPa (all at 20 °C), respectively.^{98,99} To avoid sample loss by evaporation before the analytes could be probed by ADI-MS a temperature-controlled sample holder will be developed in this study and applied to the analysis of LIB electrolytes.

Today, extensive work is done in the development of new LIB materials to improve the storage capacity and lifetime span of these devices due to the increased interest in large-scale energy storage and electric vehicles.^{100,101} This development process is accompanied with the elucidation of degradation processes of *e.g.*, conducting salts (*e.g.*, LiPF₆), and electrolytes inside the battery.¹⁰² In this regard, thermal stress, residues of water molecules, and electrical cyclization were identified to be an important factor for these decomposition processes. In the past, investigations have been done by our research group to apply LTP-MS to the analysis of electrolyte degradation products¹⁰³ to avoid the extensive sample preparation for established analysis techniques such as ion chromatography (IC)¹⁰⁴ and ESI-MS,¹⁰⁵ and to perform direct analysis of the LIB at ambient conditions. In this study, a heating and cooling stage for the sample substrate is developed to attenuate the evaporation of the volatile electrolyte components.

The temperature-controlled sample holder was constructed with a Peltier element on which solid samples (*e.g.*, electrodes) were directly deposited. Liquid samples were pipetted into a custom-made well plate, which was then positioned on the above-mentioned Peltier element. Excess heat or cold on the down site of the Peltier element was removed with a GPU water cooling block. To determine the surface temperature of the sampling surface IR thermography was performed with the identical experimental setup as previously used in this chapter. In Figure 3.9, two thermography images of the sampling surface are shown as well as a graph with the measured surface temperatures in relation to the voltage applied to the Peltier element. For these measurements the LTP was turned on to include the temperature influence of the plasma as well.

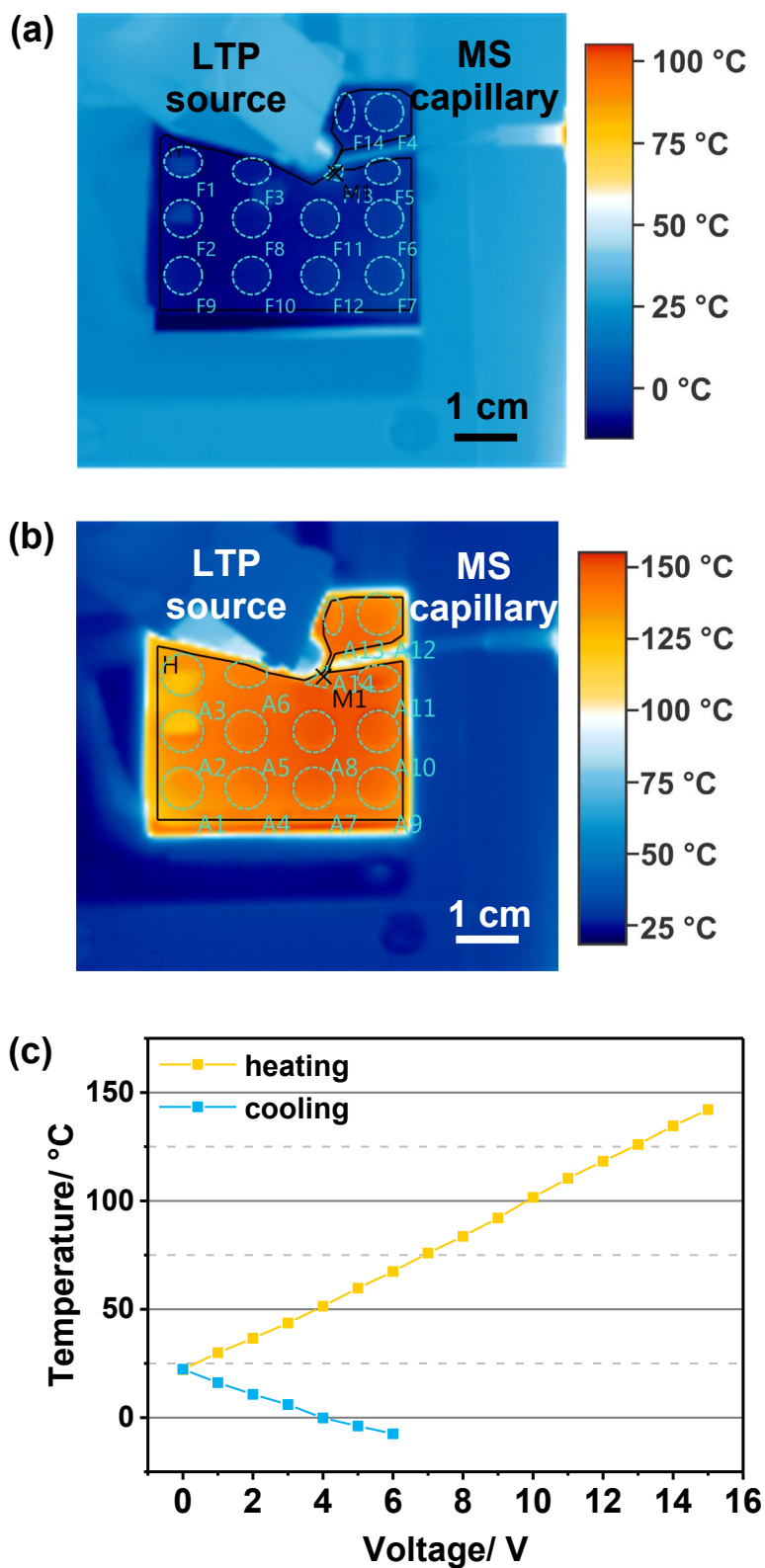


Figure 3.9 IR-thermography images of the cooled (a) and heated (b) sample well plate (quartz glass) and overview of the measured surface temperature in relation to the voltage applied to the Peltier element (c). The surface temperature of the sampling spot was measured while the turned on LTP probe was positioned in front of the mass spectrometer, identical to the true operating setup.

In Figure 3.9a 6 V were applied to the Peltier element and at the sampling position underneath the LTP source and in front of the inlet capillary of the mass spectrometer a temperature of $-3\text{ }^{\circ}\text{C}$ was measured. For the example in (b) the polarity of the applied voltage was interchanged and 15 V resulted in a surface temperature of $140\text{ }^{\circ}\text{C}$. The IR thermography measurements are summarized by Figure 3.9c and the detected surface temperature of the analyte sampling position are related to the voltage applied to the Peltier element ($n=3$ for each datapoint). In this figure, it is observed that a temperature range from $-3\text{ }^{\circ}\text{C}$ to $140\text{ }^{\circ}\text{C}$ can be covered with this new sample holder and even lower temperatures of the sample surface are possible. However, temperatures below $-1\text{ }^{\circ}\text{C}$ caused severe water condensation and ice formation on the sampling surface.

The characterization of the sample holder temperature was followed by identification of possible degradation products in an LP30 electrolyte mixture. For this purpose, the pure electrolyte was thermally stressed over the course of 14 days at $85\text{ }^{\circ}\text{C}$ inside sealed aluminum container. In Figure 3.10 the LTP-MS mass spectra of the pure analyte mixture after 7 days of thermal aging is presented in positive-ion (a) and negative-ion (b) detection mode. In positive-ion detection mode mainly the protonated molecular-ions of the electrolytes EC (m/z 89) and DMC (m/z 91) were detected and could be identified via accurate mass measurement with relative mass accuracy (RMA) better than 3 ppm. In addition to the ions for EC and DMC the degradation product OPF(OCH₃)₂ could be assigned to the ion at m/z 129.0112 (RMA of 2 ppm) and a protonated EC dimer ion was detected at m/z 177.0397 (RMA of 3 ppm). For the former ion, also the degradation product OPF(OH)(OC₂H₅) is reported in the literature with one ethyl ester group instead of two methyl ester groups. However, this molecular structure is very unlikely for the analytes probed in these experiments, because the electrolytes EC and DMC do not involve ethyl groups in their molecular structure. Consequently, this ethyl group cannot be transferred to the PF₆⁻ ion dissolved in these electrolytes. Furthermore, the base peak at m/z 103.0394 (RMA of 2 ppm) could be related to the formation of propylene carbonate (PC), a derivate of EC which was originally not present in the SelectiLite LP30 electrolyte mixture. Mass spectra of the raw electrolyte mixture before electrolyte aging (*cf.* Figure 11.12 in the appendix) prove that this compound is not present and must have formed during the thermal aging procedure. The other ions with the black labeled peaks could be related to the analyzed sample but to this date no specific molecular structure could be related to these ions.

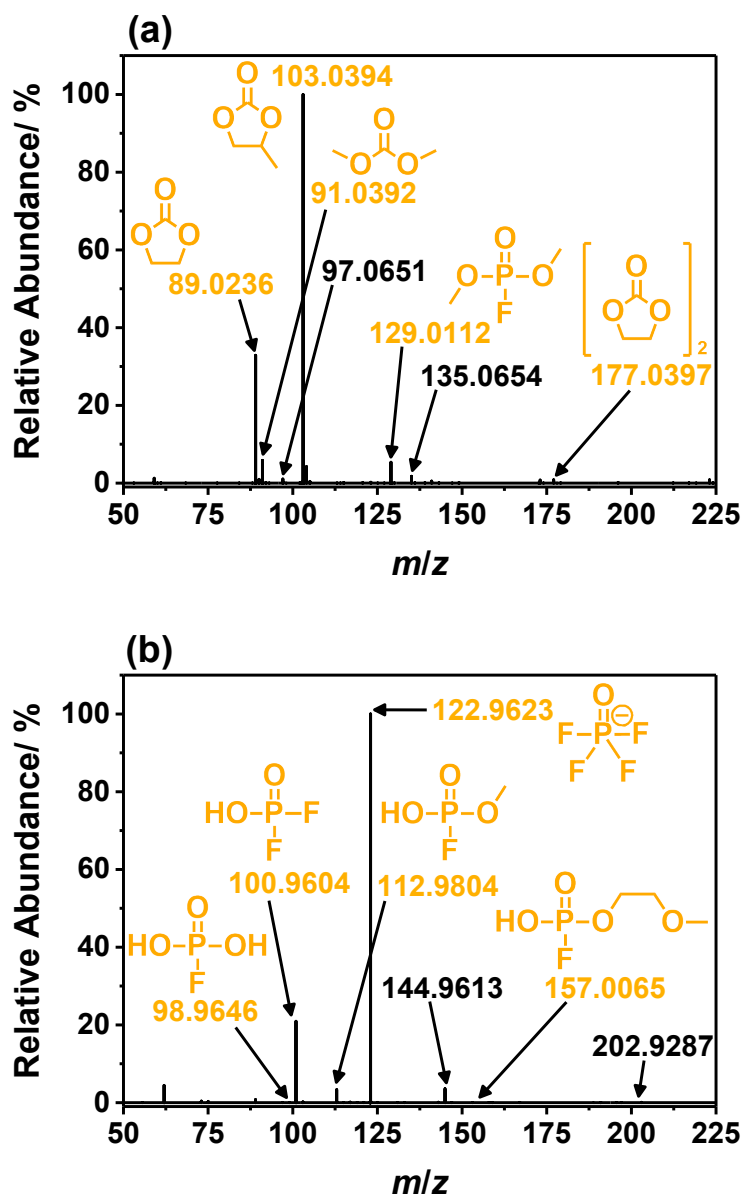


Figure 3.10 Mass spectra of LP30 after 7 days of thermal aging detected in positive-ion (a) and negative-ion (b) detection mode via LTP-MS. The sampling surface temperature was set to 50 °C to aid analyte desorption.

In negative-ion detection mode (Figure 3.10b) ionic phosphorous species could be detected, which originate from degradation of the PF_6^- salt (m/z 144.9613) during thermal aging. In a first application of LTP-MS to the analysis of LIB electrolytes the compounds $\text{OPF}_2(\text{OH})$ (m/z 100.9604) and $\text{OPF}(\text{OH})(\text{OCH}_3)$ (m/z 112.9804) could be already identified by Vortmann *et al.*¹⁰³ Based on the results found in the literature, the authors expanded a decomposition pathway for the hydrolysis of the PF_6^- salt and state that residues of water molecules inside the battery may cause this reaction. The $\text{OPF}_2(\text{OH})$ is clearly formed by this hydrolysis,¹⁰⁴ but the formation of $\text{OPF}(\text{OH})(\text{OCH}_3)$ (monofluorophosphoric acid methyl ester)

requires a different or modified reaction mechanism than pure hydrolysis because a substitution with a methoxy group at the phosphorous atom is observed. Campion *et al.* suggested in this regard an autocatalytic reaction of the intermediate degradation product phosphorus oxyfluorid (OPF_3) with the carbonate solvent molecules ($\text{RO}(\text{CO})\text{OR}$, $\text{R}=\text{organic substituent}$) and with the loss of CO and RF the methoxy group is bound to the phosphorous atom. Furthermore, the number of detected decomposition products could be expanded for LTP-MS with the new temperature-controlled sampling plate (surface temperature $50\text{ }^\circ\text{C}$). The degradation product OPF_4^- was detected as the base peak of the above shown mass spectrum at m/z 122.9623 (RMA of 4 ppm) and the molecules $\text{OPF}(\text{OH})_2$ and $\text{OPF}(\text{OH})(\text{O}(\text{C}_2\text{H}_5)\text{OCH}_3)$ were detected at m/z 98.9646 and m/z 157.0065 (relative ion abundances of $\sim 1\%$), respectively.

To investigate the long-term formation of the decomposition products the pure electrolyte solutions were thermally stressed ($85\text{ }^\circ\text{C}$) over the course of 14 days in sealed containers. Doing this, separate samples after 0, 1, 2, 4, 7, and 14 days (each $n=3$) were collected and the sample solutions were probed by LTP-MS after the 14 days were completed. To quench the electrolyte decomposition reactions the sealed aluminum containers were stored at $-18\text{ }^\circ\text{C}$ immediately after they were removed from the oven. For semi-quantitative comparison of the analyte abundance in the samples the transient ion-signal of the respective degradation product was integrated and the resulting ion abundances are summarized in Figure 3.11.

For better readability only the nominal masses of the ions are stated in the following text of this chapter. In Figure 3.11 the abundances of the ions at m/z 98, 100, 112, 122, and 125 are compared to the hyperbolic decreasing ion abundance of PF_6^- . For these decomposition products a significant increase of the ion abundance is observed in the very beginning of the aging period. As an example, the ion abundance of m/z 112 increases nearly two orders of magnitude within the first four days of thermal aging. After these four days of thermal electrolyte aging the signal abundance of the reaction products reach a plateau and therefore it can be assumed that the reaction kinetics of the electrolyte decomposition slow down. In the study published by Vortmann *et al.*¹⁰³ this plateau for the electrolyte degradation was not observed. However, this observation can be explained by the different storage temperatures ($20\text{ }^\circ\text{C}$ in comparison to $85\text{ }^\circ\text{C}$), which were used for the electrolyte aging experiments. Due to the higher storage temperature in this presented chapter the electrolyte is aged at more drastic conditions and therefore the ion abundance plateau could be observed after only several days.

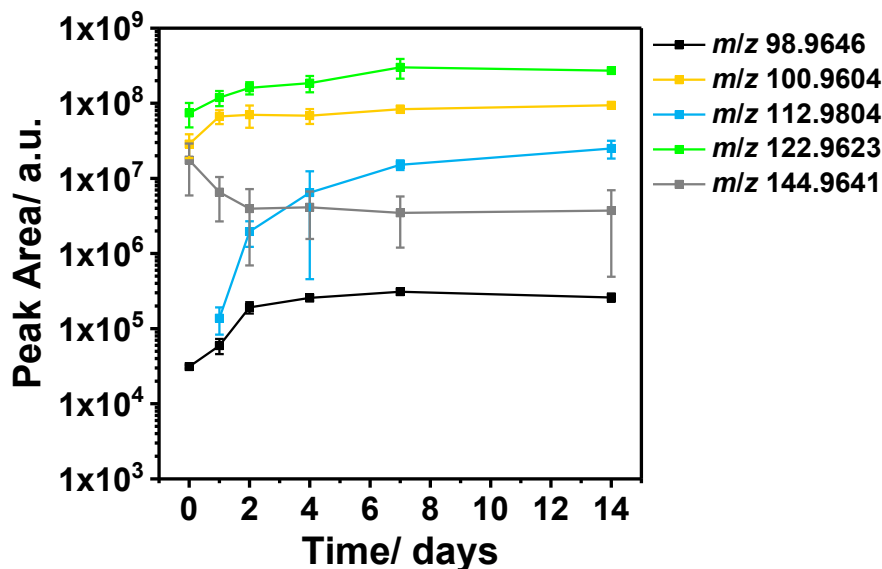


Figure 3.11 Integrated ion abundance of electrolyte degradation products and raw electrolyte compounds after the electrolyte LP30 was thermally stressed for two weeks, and subsequently analyzed via LTP-MS in negative-ion detection mode. Error bars represent $\pm 1\sigma$ of three replicate measurements.

In the last part of this chapter section the new temperature-controlled sampling surface is applied for direct surface sampling of electrolytes on a LIB electrode. The sample for this experiment was taken from a cycled LIB which was prepared by the MEET battery research center (Münster, Germany). For cyclization the battery was charged and discharged for 60 cycles at 20 °C. After cyclization the battery was opened and the thin electrode sheets (thin film of SLP30, polyvinylidene fluoride (PVdF), and conductive carbon black on a 11 μm copper foil) were disassembled from the battery housing. EC and DMC were used as electrolytes (LP30 mixture) in this battery. Unfortunately, the electrodes were not cooled during the transport from the MEET to our analytical laboratory and thus it is expected that large amounts of the electrolyte and decomposition substances on the electrodes surface evaporated. Due to this reason, no distinct signal can be observed in the extracted ion-chronogram (EIC) of the EC (*cf.* Figure 3.12a) or DMC analyte (data not shown). However, via a LTP-MS line scan across the LIB electrode surface the analyte signals at $m/\bar{z} \approx 125.0804$ and $m/\bar{z} \approx 126.9951$ could be assigned to the electrode material (*cf.* Figure 3.12 c and d). For this experiment, the electrodes were probed at two different sample surface temperatures (5 °C and 50 °C) to verify the effect of the cooled sample holder on the analyte signal abundance and a possible influence on spatial resolved analysis of such compounds in future applications.

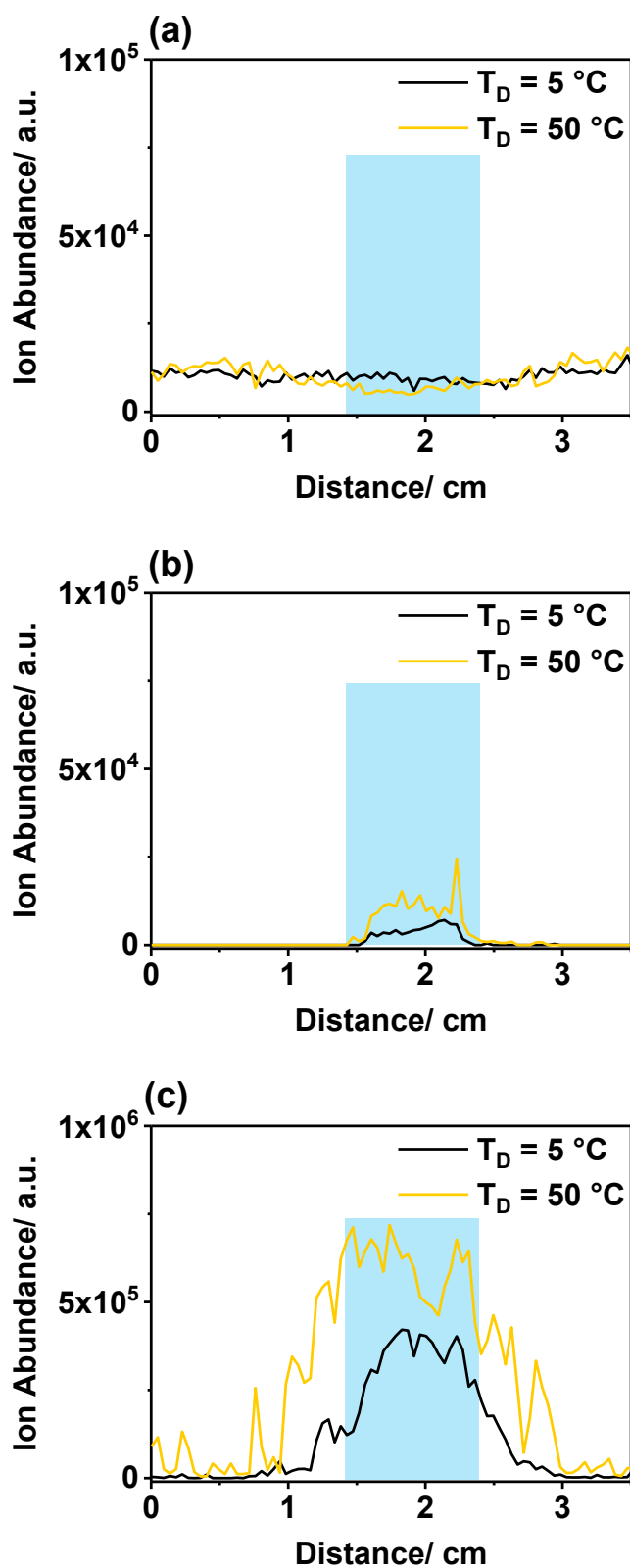


Figure 3.12 Extracted-ion chromatogram of the electrolyte EC (a, m/z 89.0236 ± 8 ppm), the m/z 126.9951 ± 8 ppm (b) and m/z 125.0804 ± 8 ppm (c) detected by an LTP-MS line scan across a cycled LIB electrode. The samples were analyzed at a glass plate surface temperature of $5\text{ }^\circ\text{C}$ (black) and $50\text{ }^\circ\text{C}$ (orange). The blue rectangle demonstrates the 1 cm width of the LIB electrode.

The EIC of m/z 126.9951 demonstrates that the position of this analyte can be located on the 1 cm wide electrode, while the analyte signal remains zero when the LTP-MS is probing the glass surface to the left and right of the electrode. For m/z 125.0804 a more wide spread transient signal is observed, which assumedly originates from a more volatile analyte molecule in comparison to the m/z 126 molecular-ion. The greater volatility of the analyte then causes the molecule to evaporate even if the LTP source is in close proximity to the electrode, but not above the electrodes' surface. If the sampling surface is cooled to 5 °C a decreased ion abundance is observed for both analytes in comparison to the analysis at 50 °C surface temperature. At 5 °C also the background signal of m/z 125 is reduced to zero ion abundance for the case the LTP is 1 cm away from the electrodes' edges. Despite the benefit of improved analyte localization on the sample target with decreased surface temperatures, the overall lower ion abundances may also cause a lower sensitivity for the target molecules because less analyte is desorbed by the LTP source. However, these preliminary results for the analysis of an electrode and electrolyte sample system have to be evaluated in more detail in future studies. As described above, not enough sample material in a good quality was available at that time to perform further experiments for *e.g.*, structural elucidation of m/z 125 and m/z 126 by MS/MS experiments or more importantly the detection of electrolytes and their decomposition components on the electrode surface. Furthermore, the ideal temperature for the sample preparation, storage and analysis need to be elucidated for best LTP-MS sensitivity and in order to obtain reproducible results.

3.4 Conclusion

In the above presented results, the positioning of the FAPA source in front of the mass spectrometer was optimized. Additionally, the anode capillary length and the distance between the pin cathode and capillary anode were investigated for best performance for direct surface analysis. The FAPA source positioning in front of the mass spectrometer was optimized by adjusting the FAPA source angle in relation to the horizontal sample surface as well as the FAPA distance towards the mass spectrometer inlet capillary was adjusted. The highest signal abundances for the caffeine analyte were observed when the FAPA source was position in 3 mm distance towards the inlet capillary (angle: 50°) or at 2 mm distance, when the FAPA was adjusted to an angle of 60° or 70°.

The optimization of the FAPA geometry was performed by adjusting the anode capillary length and the interelectrode distance between the pin cathode and the capillary anode. IR thermography revealed that the shorter, 11 mm, capillary caused an increased sample surface temperature of up to 246 °C in comparison to the 25 mm long anode (130 °C at 50 mA applied to the pin electrode). Thus, this modification could be utilized to improve the sensitivity of the FAPA-MS method. This is, because higher surface heating by the plasma might aid the analyte desorption for the case of volatile compounds. However, Shelley *et al.* introduced the p2c-FAPA source (anode length also 25 mm) with the purpose to decrease analyte oxidation by elemental oxygen from the ambient air. In the results presented in this chapter, only minor differences between the 11 mm and 25 mm anode capillary were observed in this regard. The FAPA interelectrode distance between pin and capillary electrodes were altered and compared in regard of the analyte signal of caffeine and nicotine standards desorbed/ionized from TLC plates. Mass spectral imaging of the analytes on the TLC plates enabled the semiquantitative comparison of the analyte signal abundance and it was found that with increasing interelectrode distance also the detected signal abundance of the analytes increased.

In the last section of this chapter a temperature-controlled sample holder for the analysis of lithium-ion battery (LIB) components was developed and the resulting sampling surface temperature was measured via IR thermography. These measurements showed an adjustable temperature range for the sample holder between -3 °C and 140 °C. Subsequently, this sample holder was used for the analysis of a thermally stressed electrolyte (SelctiLite LP30) by LTP-MS to aid analyte desorption with an increased sample surface temperature of 50 °C. This experimental setup helped identify new electrolyte decomposition products via LTP-MS and to monitor the signal abundance of such electrolyte degradation products. However, further studies have to be done to improve the surface sampling capabilities of this method. Due to the volatility of electrolyte components the sample preparation needs to be improved so the loss of analyte compounds at ambient conditions is minimized. A cooled sample holder for LTP-MS was presented in preliminary experiments, but the benefit of this device needs to be evaluated in future experiments.

Chapter 4

Plasma-Based Ambient Desorption/Ionization Mass Spectrometry for the Analysis of Liquid Crystals Employed in Display Devices

Based on: C. Kuhlmann, J. T. Shelley, C. Engelhard.
Journal of the American Society for Mass Spectrometry, **2019**,
30, 2101–2113.
DOI: 10.1007/s13361-019-02280-w.

4.1 Introduction

Liquid-crystal displays (LCDs) are the most commonly used display technology worldwide to visualize graphics or text on electronic devices. In general, LCDs consist of multi-layered structures including glass substrates, polarization layers, transparent electrodes made of indium tin oxide (ITO), orientation layers, and color filters, which are stacked onto each other in the display manufacturing process. Additionally, a homogeneous mixture of rod-shaped liquid-crystalline molecules and additive components is located between the aforementioned materials to enable the functionality of the display. Because of the very delicate LCD manufacturing process with pure, homogeneously distributed liquid crystals (LCs) and additives, even small impurities may cause a failure spot in the display.^{106,107}

For quality control and the analysis of display failures, new and more powerful analytical methods are of great interest. The current state-of-the-art technology for the analysis of these complex mixtures are microscopy-based methods (*e.g.*, optical microscopy) to identify failing pixels inside the LCD, and time-of-flight secondary-ion mass spectrometry (ToF-SIMS)^{108,109} is used for further investigations to clarify the causes of the malfunction. Furthermore, chromatography-based techniques (*e.g.*, HPLC or GC) coupled to MS are frequently used in industry for the analysis and characterization of organic compounds. These techniques can be used to investigate display failure spots by extraction of the liquid crystals from the display panel, followed by chromatography and mass spectrometric detection. However, to the best knowledge of the authors, no publications in peer-reviewed journals on liquid crystal display analysis via HPLC-MS or GC-MS are available. Lately, also laser-ablation atmospheric-pressure chemical ionization mass spectrometry (LA-APCI-MS) was evaluated as a potential surface imaging method for LCD analysis.¹¹⁰ Possible causes for display failure can be contaminations with other liquid-crystal products, or particulates, but also errors in the display manufacturing process.^{106,108,109,111} Therefore, the region of interest of the LCD is cut out of the display panel and the liquid crystals manually extracted, which is time-consuming and requires the use of organic solvents commonly used for chromatography. Furthermore, this sampling and analysis approach leads to a loss in the spatial structure of the display failure spot, which would provide a better indication of the cause for failure. Therefore, alternative methods for faster analyte screening that also provide spatial information are of great importance.

In the field of organic mass spectrometry, ambient desorption/ionization has become an important tool for the direct analysis of complex sample materials in the solid, liquid, or gaseous phase. After Cooks *et al.*⁶ founded the research field of ADI-MS in 2004, by publishing their first results about the DESI source, three major classes of ADI-MS sources evolved in the following years. For example, DESI, desorption sonic spray ionization (DeSSI),¹¹² extractive electrospray ionization (EESI),¹¹³ or easy sonic spray ionization (EASI)¹¹⁴ are examples for spray-based ADI-MS techniques. DART,⁷ ASAP,³² desorption atmospheric pressure chemical ionization (DAPCI),³⁴ the LTP probe,⁸ and FAPA^{9,10} are examples of plasma-based ADI sources. Techniques that involve a laser beam are referred to as laser-based ADI sources and include laser ablation electrospray ionization (LAESI)²⁸ or plasma-assisted laser desorption ionization (PALDI).¹¹⁵ In most cases, these laser-based techniques use the laser for sample desorption/ablation, while analyte ionization is caused by an electrospray or plasma source. Until today, more than 40 ADI sources have been published,²⁷ while more than half of them are plasma-based.³⁸ The first commercially available plasma-based ADI source was DART, developed by Cody *et al.* in 2005.⁷ In the original DART setup, a corona discharge is formed inside a discharge chamber by applying a high direct-current (DC) voltage to a pin electrode. Helium was used as the discharge gas, equal to most of the plasma-based ADI sources. The resulting ionic species are filtered out by an additional electrode, while neutral, excited plasma species leave the source through the externally heated front end of the DART source.⁷ More recently, various DART configurations can be found in the literature and are also commercially available.^{39,43,116-118} The LTP probe is operated with an alternating current (AC) to form a dielectric-barrier discharge (DBD) inside a tube made of a dielectric material. In the first published work by Harper *et al.*,⁸ 2.5-5 kV_{p-p} at 2-5 kHz were applied to a copper ring electrode on the outside of a glass tube, while a needle electrode inside the tube was grounded. The third ADI-MS technique, which will be compared with the aforementioned sources, is the FAPA developed by Andrade *et al.* in 2008.^{9,10} This APGD is formed inside an insulating discharge chamber, by applying a negative potential to a pin cathode, while a pinhole or capillary anode is grounded.¹¹ An overview of the important plasma-based ADI sources including instrumental parameters of DART, LTP, and FAPA is given in a recent review⁵ and a brief summary is presented in Table 4.1.

Table 4.1 Comparison of specific DART-, LTP-, and FAPA parameter.^{5,39}

DART	LTP	FAPA
Inventor/scientist: R. B. Cody <i>et al.</i>	Inventor/scientist: J. D. Harper <i>et al.</i>	Inventor/scientist: F. J. Andrade <i>et al.</i>
Year of development: 2005	Year of development: 2008	Year of development: 2008
Commercialized: Yes	Commercialized: No	Commercialized: No
Type of plasma: Corona-to-Glow discharge	Type of plasma: Dielectric-barrier discharge	Type of plasma: Glow-to-arc discharge
Operation voltage: DC (kV range, ~6 W)	Operation voltage: AC (kV range, <3 W)	Operation voltage: DC (V range, <13 W)
Plasma gas: He (1-3 L/min)	Plasma gas: He and N ₂ (0.08-1 L/min)	Plasma gas: He (0.5-2 L/min)
Plasma temperature: ~55 °C	Plasma temperature: 30-40 °C	Plasma temperature: 250-350 °C
Gas heater: Typically used for analyte desorption of high vapor pressure compounds	Gas heater: Typically used for analyte desorption of high vapor pressure compounds	Gas heater: None, because of self- heating of the plasma gas
Electrode geometry: 1) Pin electrode with high voltage applied 2) Additional mesh electrodes to filter ionic plasma species	Electrode geometry: 1) Grounded needle electrode inside dielectric barrier tube (glass or ceramic) 2) High voltage ring- electrode (Cu) around the dielectric barrier tube	Electrode geometry: 1) Pin electrode with negative potential applied 2) Grounded pinhole plate or capillary

Since the introduction of these plasma-based sources, various applications for the analysis or detection of (illicit) drugs, explosives, pesticides, and other small molecules as well as polymer materials have been presented in literature.^{8,11,47,48,119-121} Additionally, fundamental studies on the operation of DART,¹²² LTP,^{57,92} and

FAPA⁵² have been published in the last decade. Interestingly, only a few studies have been done to compare DART, LTP, and FAPA regarding their performance towards designated applications or analyte types.¹²³ Due to the different plasma formation conditions (*e.g.*, corona discharge, DBD, and APGD, respectively), each ADI source has its own unique features with regard to the desorption and ionization process, which can be beneficial or unfavorable depending on the application. Therefore, this chapter aims to compare DART, LTP, and FAPA sources for the purpose of liquid-crystal analysis from standards, mixtures, and real display samples.

4.2 Experimental Section

Reagents. All chemical solvents and agents were analytical grade. Acetonitrile, methanol, toluene, and water were purchased from Fisher Scientific Inc. (Pittsburgh, PA, USA). The liquid crystals ST00484, ST00552, and ST00553 were obtained from Syntho Chemicals GmbH & Co. KG (Wolfen, Germany). The liquid crystal compound ZLI-1544 was bought from AstaTECH Inc. (Bristol (PA), USA). CB15/E7, the liquid-crystal mixture, used in commercially available LCDs, as well as an LCD test cell, was provided by Merck KGaA.

Direct Analysis in Real Time. For all DART-MS measurements, the commercially available DART ID-Cube (IonSense Inc., Saugus, MA, USA) was used. For these experiments, a flow rate of 700 mL/min of helium (99.999%, Airgas Inc., Radnor, PA, USA) was used. The plasma was operated at 1 kV DC voltage and 45.7 μ A applied to the pin electrode inside the DART source. A liquid sample (2 μ L, dissolved in toluene) was deposited on the narrow waist of the metal mesh on an OpenSpot Card (IonSense Inc.) and positioned between the on-axis aligned DART source and MS inlet capillary. For enhanced sample desorption, 5 A of DC current was applied to the metal mesh to enhance the analyte desorption. The temperature of the wire mesh at the analyte sampling position was determined by IR-thermography and was found to be \sim 305 $^{\circ}$ C (mean value). The aforementioned temperature of the wire mesh was measured without deposited sample and without the DART source pointing towards the mesh. For the determination of the wire mesh surface temperature of the OpenSpot Card a thermal camera (model testo 875) from Testo SE & Co. KGaA was used. The subsequent data evaluation was performed with the software testo IRSoft (version 2.5). Therefore, an emissivity of 0.78 (oxidized steel at a temperature between 125 and 525 $^{\circ}$ C)¹²⁴ and a reflected temperature of 20 $^{\circ}$ C was

used as parameters for the IR-thermography measurement. To avoid excess helium entering the mass spectrometer a VAPUR[®] interface (IonSense Inc.) was used. The ambient gas from the inside of the VAPUR[®] interface was evacuated by a diaphragm vacuum pump (model MZ 2C, Vacuubrand GmbH & Co. KG, Wertheim, Germany). The amount of removed gas was regulated by a carefully optimized needle valve (IonSense Inc.) with the valve positioned at the blue ring and rotated to position 9.5.

Low-Temperature Plasma Probe. The LTP source was home-built and was described earlier by Albert *et al.*⁹² The LTP probe consisted of a needle electrode made of stainless steel (0.5 mm o.d.) inside of a quartz capillary (7 mm o.d., 1 mm i.d.) and a copper ring electrode of 20 mm width on the outside of the glass capillary. During operation, 300 mL/min helium (99.999%, Airgas Inc.) was introduced into the LTP source via a mass flow controller (model EL-FLOW Select, Bronkhorst Mättig GmbH, Kamen, Germany). An AC voltage of 14 kV_{p-p} at 31 kHz was applied to the steel electrode, while the copper electrode was grounded, to form a dielectric-barrier discharge inside the quartz tube. The LTP probe was powered with a Voltagezone Electronics e. U. DC-AC converter (model HVGEN10AC v3.1). In on-axis operation, sample deposition and analysis were performed analogously to the DART analysis. For surface analysis an optimized LTP to MS geometry, published by Albert *et al.*,⁸⁸ was used since the identical LTP configuration with equal instrument parameters was used in this chapter. Therefore, the LTP source was positioned in a 60° angle and 2-mm distance towards the MS inlet capillary, while the distance between LTP and sample surface was 5 mm. For the analysis, 1 µL of the sample was deposited on a microscope slide and positioned 1 mm underneath the MS inlet capillary. To enhance sample desorption, the microscope slide was heated to 150 °C surface temperature by applying 30 V to a silicon resistance heating mat (Thermo Flächenheizungs GmbH, Rohrbach, Germany).

Flowing Atmospheric-Pressure Afterglow. Due to the similarities in the source design of the ID-Cube DART source and the original p2p-FAPA source, the on-axis FAPA experiments were performed with the ID-Cube source housing, but with adjusted operating conditions. Helium (99.999%, Airgas Inc.) at 700 mL/min was used as the plasma gas. The plasma was operated by applying a negative potential to the stainless-steel pin electrode through a 5 kΩ ballast resistor by a Kepco high-voltage DC power supply (model BHK 1000-0.2MG, Kepco Inc.). The FAPA source was operated at 20 mA in constant-current mode. The anode was connected to the ground potential of the power supply. Sample deposition and analysis was analogous

to the DART and LTP analysis as described above. For direct surface analysis, the p2p-FAPA source described by Shelley *et al.* was used.⁵⁵ The discharge was maintained between the stainless-steel pin-electrode and a brass plate anode. The distance between the electrodes was 7.5 mm. Helium (99.999%, Airgas Inc.) was introduced into the discharge chamber with a flow rate of 600 mL/min.

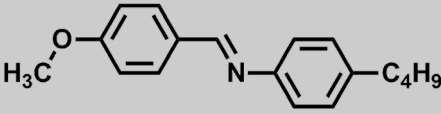
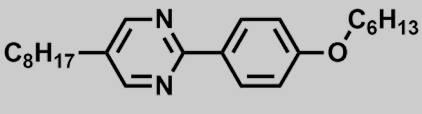
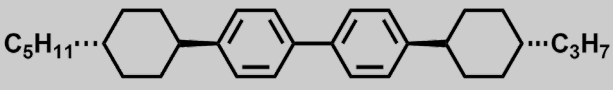
High-Resolution Mass Spectrometry. For this chapter, two high-resolution mass spectrometers equipped with an Orbitrap mass analyzer were used (Exactive and Exactive Plus, Thermo Fisher Scientific GmbH). Before the experiments were performed both mass spectrometers were calibrated with a mass calibration standard containing caffeine (Sigma-Aldrich Inc.), MRFA (Met-Arg-Phe-Ala acetate salt, Sigma-Aldrich Inc.), and Ultramark 1621 (Sigma-Aldrich Inc.), on a daily basis. To ensure accurate m/z measurements, mass calibration was performed with the automated calibration routine implemented in the instrument software. For all identified m/z presented in this chapter (mass range 236-430 u) the RMA was better than 2 ppm. To position the ADI source in front of the mass spectrometer the electrospray ionization housing was removed and the conventional inlet capillary was replaced by a 4-cm extended capillary on the front end. The inner diameter of the inlet capillary (0.6 mm) was the same as the original inlet capillary for ESI-MS. Information of the experimental settings of the mass spectrometers is given in the appendix (*cf.* chapter 11.1, Table 11.1).

4.3 Results and Discussion

Analysis of Commercially Available Liquid Crystals. In this chapter, three plasma-based ADI-MS techniques are compared for their ability to directly analyze liquid crystals. In addition, this method could be a potential tool for fast screening of liquid crystals, degradation products, and impurities in LCDs to investigate display failure spots. Due to the special requirements for the LCD application, liquid-crystal mixtures are specifically formulated with designated liquid crystals and additives. Consequently, even unwanted liquid crystals and additives originating from the former LCD type produced at the manufacturing line could be possible contaminants. Also, adhesive materials (*e.g.*, Loctite 352) on the edges of the display panel may interact with the liquid crystals in case of not sufficient adhesive curing and, in turn, may cause display spots to fail.

To compare the capabilities of DART-, LTP-, and FAPA-MS for direct liquid-crystal analysis, 2 μL of diluted liquid-crystal standard solutions (0.06-0.41 $\mu\text{g}/\mu\text{L}$, dissolved in toluene) was deposited on a stainless-steel mesh and analyzed in TM-ADI-MS. The LC molecules analyzed are listed in Table 4.2 and comprise imide and pyrimidine functional groups as well as aromatic and aliphatic hydrocarbon structures (more detailed information about the LC-I to III is given in Table 11.6).

Table 4.2 List of LCs analyzed by DART-, LTP-, and FAPA-MS.

LC-I	LC-II
	
Product name: ST00484 ^a MW ^c : 267.37 g/mol Sum formula: C ₁₈ H ₂₁ NO	Product name: ST00552 ^a MW: 368.56 g/mol Sum formula: C ₂₄ H ₃₆ N ₂ O
LC-III	
	
Product name: ZLI-1544 ^b MW: 430.71 g/mol Sum formula: C ₃₂ H ₄₆	

^a Product name of Synthon Chemicals, Wolfen, Germany. ^b Product name of AstaTECH Inc., Bristol (PA), USA. ^c MW: molecular weight.

The sample target with the liquid samples was positioned between the ADI source and the inlet capillary of the mass spectrometer. Additional heating of the sample substrate was used to evaporate the main portion of the analytes by thermal desorption. In this regard, Krechmer *et al.* were able to show that aided thermal desorption of the sample can be used to separate the analyte desorption process from the analyte ionization in TM-DART-MS experiments.¹¹⁸ For these experiments, the authors deactivated the plasma gas heater of the DART SVP-A source (IonSense, Inc., Saugus, MA, USA) and detected no analyte signal when the resistively heated sample target was at ambient temperatures. These findings correlate with a study by

Shelley *et al.* who determined the plasma temperature of DART-like discharges (without external heating) to be ~ 55 °C¹³ and concluded that external heating is required to analyze organic molecules of low volatility. Similarly, to the C-G discharge of the DART source, the dielectric-barrier discharge of the LTP probe also operates at temperatures close to ambient temperatures (~ 30 °C).⁸ Based on these findings, it is assumed here that the liquid crystals are desorbed at a very similar rate with both ADI sources, DART and LTP, when external heating is applied to the wire screen between ADI source and the atmospheric pressure inlet of the mass spectrometer. Therefore, the differences in analyte ion abundance reported below are likely governed by other factors than plasma temperature (discussed below). In contrast to DART and LTP, Shelley *et al.* reported afterglow temperatures of up to 235 °C for the G-A discharge of the FAPA source.¹³ The discharge itself is very likely to aid in the thermal desorption process in addition to the resistively heated stainless-steel mesh (~ 305 °C). This hypothesis is discussed in detail below when the analyte signal abundances are compared for different ADI-MS conditions with and without external heating.

Detected and identified m/z in the mass spectra of the single standard compound analysis include positively charged molecules ($[M]^{+}$) and protonated molecules ($[M+H]^{+}$) (*cf.* Figure 4.1). These observed species of the analyte molecules were produced via a charge transfer and proton transfer reaction mechanism, respectively, caused by the reactive plasma species such as H_3O^{+} , N_2^{+} , NO^{+} , and NO .^{55,57,123,125,126}

The imide liquid crystal with the product name ST00484 (*cf.* Figure 4.1a-c) was readily ionized and detected with all three ADI sources. With DART-MS approximately 10- and 2-times higher signals can be detected for the base peak in comparison with LTP- and FAPA-MS, respectively. In addition to the $[M+H]^{+}$ peak, no further m/z values corresponding to analyte fragmentation can be identified when analyzing this LC with DART-MS, but analyte oxidation (*e.g.*, $[(M+O)+H]^{+}$, m/z 284.1646) can be observed at low relative abundances of less than 0.1%. For LTP-MS, similar observations compared with DART-MS can be made. Only a small portion of the analyte ($<0.3\%$) was oxidized by the ADI source. In the mass spectrum of ST00484 detected by FAPA-MS, the protonated molecular ion and the oxidized species can be observed with abundances of 48% (m/z 268.1691) and 1.5% (m/z 284.1646) relative to the maximum intensity of the DART-MS analysis. Further, two abundant peaks can be detected in addition to the $[M+H]^{+}$ -ion.

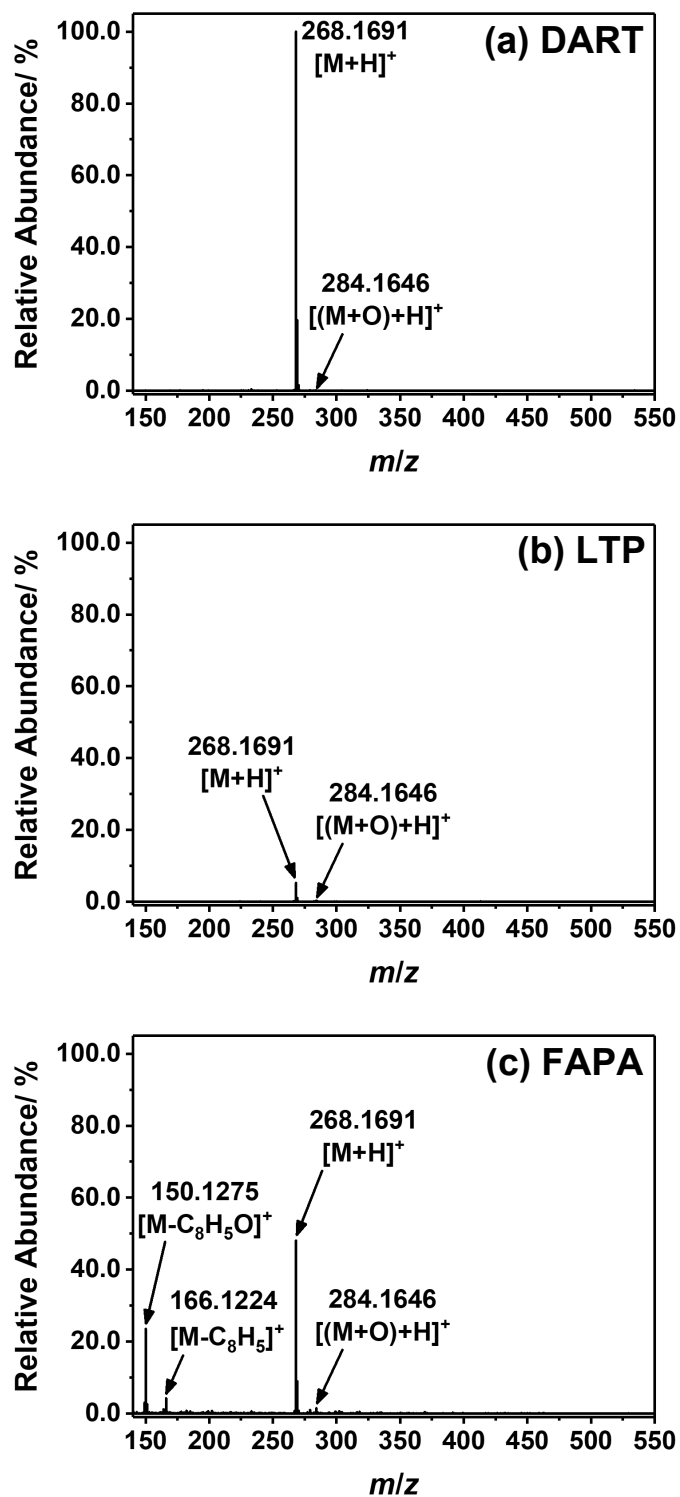


Figure 4.1 Mass spectra of ST00484 (a-c), ST00552 (d-f), and ZLI-1544 (g-i) detected by DART-, LTP-, and FAPA-MS in positive-ion detection mode. DART- and FAPA-MS measurements were performed with an Exactive Plus, while LTP-MS measurements were performed with an Exactive. Analyte signals were identified with an RMA better than ± 2 ppm. For visualization purposes, the peak heights are normalized to the most abundant ion produced by any of the three ADI sources.

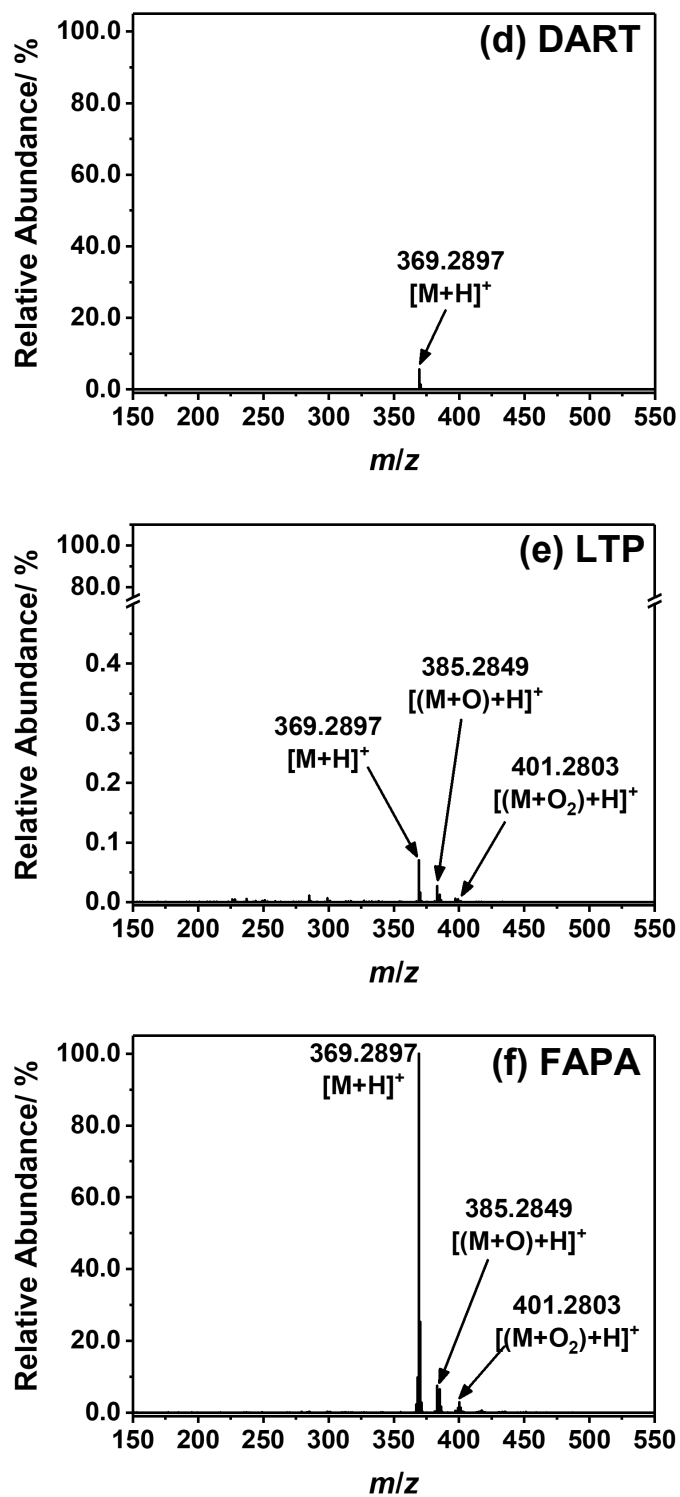


Figure 4.1 Continued.

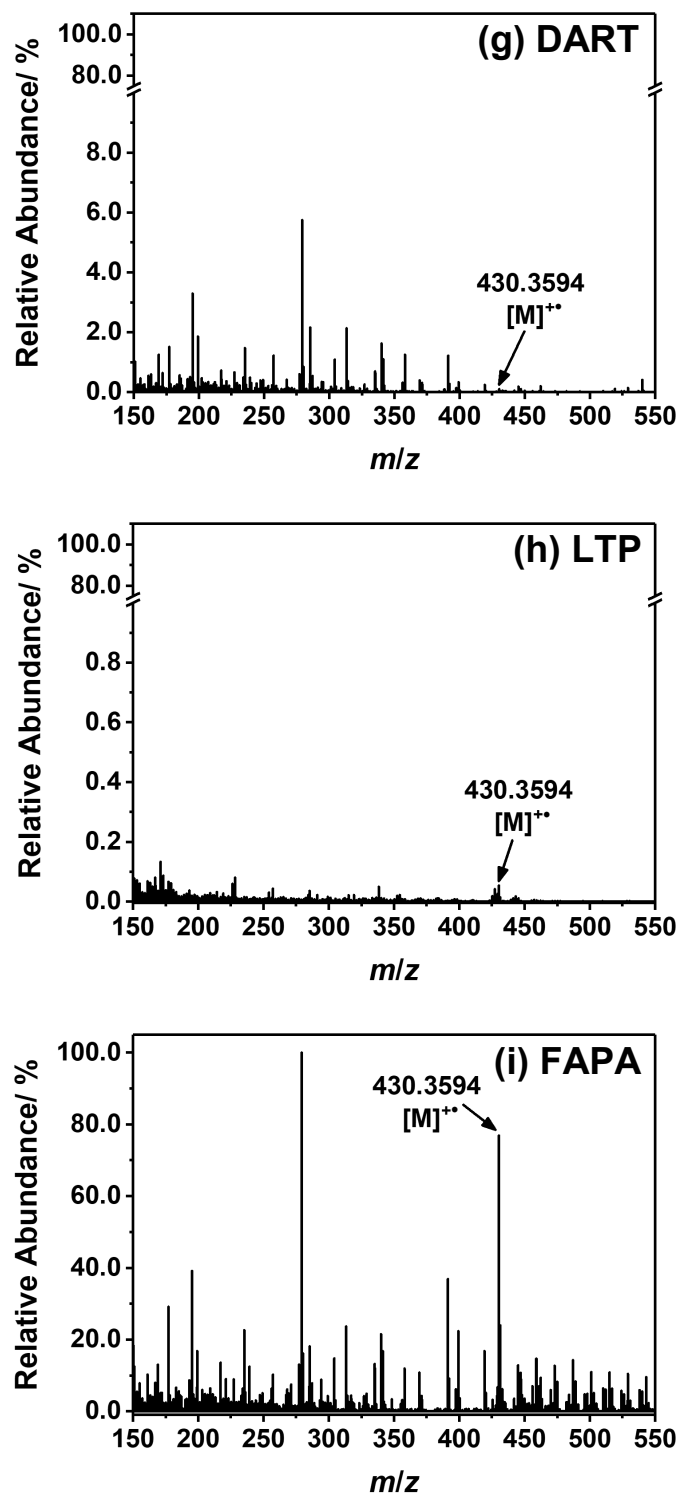


Figure 4.1 Continued.

The m/z 150.1275 ion was identified as $C_{10}H_{16}N^+$, which results from cleavage of the imide bond in the molecular structure of the Schiff base molecule (*cf.* Figure 4.2a). The peak at m/z 166.1224 ($C_{10}H_{16}ON^+$) could be associated to oxidation of the aforementioned fragment at m/z 150.1275 by an oxygen radical formed by the plasma (*cf.* Figure 4.2b). However, by addition of the protonated molecular-ion signal abundance and the fragment ion signal abundance of LC-I, an almost identical signal abundance for this analyte is obtained by DART- and FAPA-MS. The fragmentation and oxidation of ST00484 caused by the FAPA source might be explained by two reasons. First, it is reported in the literature that the p2p-FAPA source may cause analyte oxidation by ambient oxygen. Second, the high temperatures applied to the stainless steel mesh and the additional heating of the FAPA source certainly exceed the flashpoint of LC-I at ~ 113 °C.¹²⁷ The combination of the aforementioned oxygen species and the rather high temperature might promote analyte fragmentation.

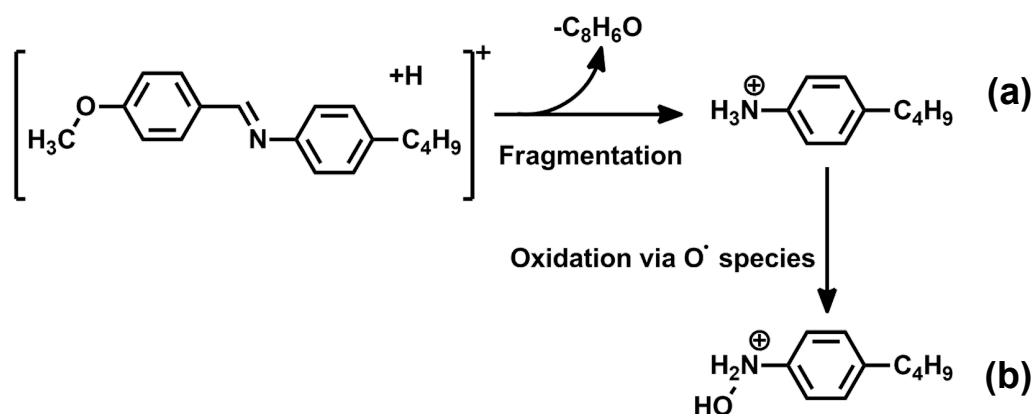


Figure 4.2 Possible reaction pathway of the fragmentation and oxidation of ST00484 by FAPA-MS (a), followed by the oxidation of the fragmentation product (b).

For the analytes ST00552 (LC-II) and ZLI-1544 (LC-III), most abundant analyte-ion signals were detected with FAPA-MS. For LC-II, further peaks in addition to the $[M+H]^+$ -ion were observed (*cf.* Figure 4.1e and f). Via accurate mass detection a mass shift of 15.9952 u and 31.9906 u towards the protonated molecular ion can be determined for the m/z 385.2849 and m/z 401.2803 ions, respectively. This corresponds to oxidation of the analyte with one and two oxygen atoms. In the literature, this type of oxidation by plasma species has already been described by Tosi *et al.*¹²⁸ for corona discharge APCI. Additionally, Chan *et al.*⁵⁷ revealed the presence of atomic oxygen by optical emission spectroscopy inside the helium plasma and afterglow region of the LTP probe. The radical atomic oxygen in the plasma originates

from molecular oxygen in the ambient air diffusing into the discharge region. Therefore, the observed analyte oxidation is caused by a reaction of oxygen radicals with the aromatic system of the molecule.¹¹ For the DART source, an oxidized species at m/z 385.2849 can be identified as well, but the relative abundance of the $[(M+O)+H]^+$ -species is approximately 20 times lower compared with the FAPA-MS measurement. Due to a comparatively high molecular mass of 430.36 u it is difficult to directly desorb the analyte due to the lower vapor pressure. Further, the absence of polar functional groups in LC-III prevents the ionization by protonation, which is the often-observed ionization mechanism for the three plasma sources. Nevertheless, it was possible to detect the $[M]^{+•}$ ion of this LC-III at m/z 430.3594 with aided sample desorption by external heating. The ion at m/z 279.1583 in Figure 4.1g-i was due to a background signal from the ambient conditions around the ADI source.

Comparing the aforementioned results with the analysis of the identical liquid crystals but in this case without external heating (*cf.* Figure 11.13), it was observed that ST00552 and ZLI-1544 cannot be detected with any of the discussed ADI-MS techniques. The most abundant ion in these mass spectra at m/z 279.1583 corresponds to the background and was identified to be the protonated dibutyl phthalate or an isomeric phthalate structure with the sum formula $C_{16}H_{23}O_4^+$ (mass accuracy better than ± 0.2 ppm). The lightest analyzed molecule, ST00484, could be detected with DART-, LTP-, and FAPA-MS, but with a drastic loss in signal compared with the mass spectra detected with external heating. This finding was particularly true for the thermally cooler DART and LTP sources where a decrease in the signal of approximately two orders of magnitude was observed. Due to the higher plasma and afterglow temperatures of the FAPA source, the signal for ST00484 was only 50% lower compared with the case where external heating of the metal mesh was used. These findings confirm that the desorption process of plasma-based ADI sources dramatically depends on the thermal desorption capabilities of the ADI source and the volatility of the analyte(s).

Typically, LCs are used in mixtures to fulfill a designated purpose. Therefore, a commercially available mixture of cholesteric LCs CB15 (33%) and E7 (66%) was analyzed with DART-, LTP-, and FAPA-MS. The LC mixture was dissolved in toluene and a total amount of 0.52 μ g of CB15/E7 was directly analyzed via plasma-based ADI-MS in transmission-mode and from a (heated) stainless-steel mesh. Structures of the analyte molecules, detected ions, m/z ratios, and mass accuracy of the corresponding analyte, are shown in Table 4.3.

Table 4.3 Identified molecular cations for the CB15/E7 liquid crystal mixture detected by DART-, LTP-, and FAPA-MS.

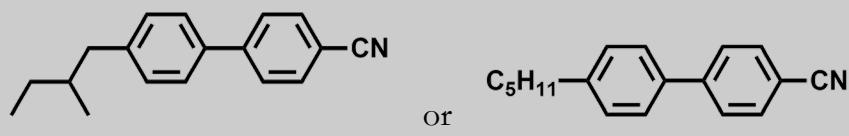
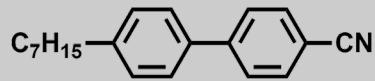
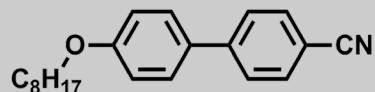
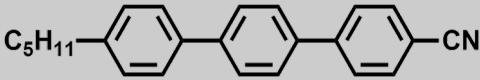
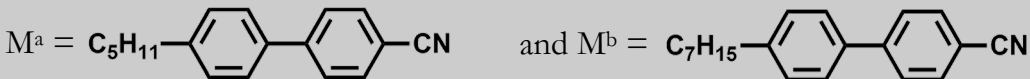
Information	Ion	Theoretical <i>m/z</i>	Observed <i>m/z</i>	Rel. mass accuracy
LC-IV and LC-V				
				
	$[M]^+$	249.1512	249.1512	-0.1 ppm
Prod. name:	$[M+H]^+$	250.1590	250.1588	-1.1 ppm
CB15 or 5CB	$[M-H+O]^+$	264.1383	264.1383	0.3 ppm
MW: 249.35 g/mol	$[(M+O)+H]^+$	266.1539	266.1541	0.5 ppm
Formula: C ₁₈ H ₁₉ N	$[M+NH_4]^+$	267.1856	267.1853	-1.1 ppm
	$[M_2+H]^+$	499.3108	499.3105	-0.6 ppm
LC-VI				
				
Prod. name: 7CB	$[M]^+$	277.1825	277.1823	-0.6 ppm
MW: 277.40 g/mol	$[M+H]^+$	278.1903	278.1900	-1.2 ppm
Formula: C ₂₀ H ₂₃ N	$[M+NH_4]^+$	295.2169	295.2166	-0.9 ppm
LC-VII				
				
Prod. name: 8OCB	$[M+H]^+$	308.2003	308.2010	-0.4 ppm
MW: 307.43 g/mol	$[M+NH_4]^+$	325.2274	325.2274	-0.1 ppm
Formula: C ₂₁ H ₂₅ NO				

Table 4.3 Continued.

Information	Ion	Theoretical m/z	Observed m/z	Rel. mass accuracy
LC-VIII				
				
Prod. name: 5CT	[M+H] ⁺	326.1903	326.1902	-0.2 ppm
MW: 325.45 g/mol	[M+NH ₄] ⁺	343.2169	343.2169	-0.1 ppm
Formula: C ₂₄ H ₂₃ N				
LC-IV and LC-VI				
				
Dimer ion of LC-IV and LC-VI	[M ^a +M ^b +H] ⁺	527.3421	527.3420	-0.2 ppm

The mass spectra of the liquid-crystal mixture CB15/E7 are depicted in Figure 4.3. In Figure 4.3a-c, sample desorption was enhanced by resistively heating the metal-mesh. In all the three mass spectra, the [M+H]⁺-peak of LC-IV and LC-V at m/z 250.1588 was the most abundant peak. DART and FAPA ionization also produced an ammoniated adduct ([M+NH₄]⁺, m/z 267.1853, black star in Figure 4.3a and c). With LTP-MS, no [M+NH₄]⁺ was detected, but a positively charged [M-H+O]⁺-species (double cross in Figure 4.3b) as well as a [(M+O)+H]⁺-species (square in Figure 4.3b) was found at m/z 264.1383 and m/z 266.1541, respectively. For the third liquid crystal of this LC mixture, LC-VI, a [M+H]⁺-peak (m/z 278.1903) was detected with all three ADI sources and also ammoniated adducts were observed (m/z 295.2166) with DART- and FAPA-MS for this analyte. The two additional LCs, LC-VII and LC-VIII, in this liquid-crystal mixture, could be detected as an [M+H]⁺-ion as well with any of the ADI sources. The LC-VII was detected at m/z 308.2010 ([M+NH₄]⁺ at m/z 325.2274) while the LC-VIII was detected at m/z 326.1902 ([M+NH₄]⁺ at m/z 343.2169). For all three ADI sources, a trend of decreasing signal

abundance with increasing molecular weight was observed. Here, the decrease in signal abundance was not as severe for the FAPA source (m/z 250.1588 with $2 \cdot 10^8$ a.u. compared with m/z 326.1902 with $1 \cdot 10^7$ a.u.); the most drastic decrease in analyte signal was observed for the LTP source (m/z 250.1588 with $3 \cdot 10^6$ a.u. compared with m/z 326.1902 with $6 \cdot 10^3$ a.u.). In contrast to the results for ST00484, ST00552, and ZLI-1544, a significant amount of ammonium adduct ions was observed for the liquid crystals containing a nitrile group, when the sample substrate was heated. This observation might be caused by the decomposition of the nitrile group of other analyte molecules due to the high temperatures of the metal mesh (up to 450°C) on which the LC mixture was deposited for analysis. In the literature, ammoxidation is described as a common synthesis for nitriles. These are formed in a strong exothermic reaction by using oxygen, ammonia, and an alkene in combination with a bismuth molybdate catalyst.¹²⁹ Therefore, the high temperatures of the metal mesh and the plasma source might cause a thermodynamically driven degradation reaction in the gas phase, where ammonia is released as a product.

In Figure 4.3d-f the analyte mixture CB15/E7 was analyzed without external heating of the metal mesh. As such, analyte molecules in these samples could only be desorbed by the respective ADI source. In this case, FAPA-MS was the only ADI technique to produce detectable analyte ions at m/z 250.1588 ($[\text{M}+\text{H}]^+$ of LC-IV or LC-V), m/z 267.1853 ($[\text{M}+\text{NH}_4]^+$), m/z 278.1903 ($[\text{M}+\text{H}]^+$ of LC-VI), (m/z 295.2166) ($[\text{M}+\text{NH}_4]^+$), and m/z 308.2010 ($[\text{M}+\text{H}]^+$ of LC-VII) from the sample mixture. This observation can be explained by the significantly higher plasma and afterglow temperatures of the FAPA source.

In the literature, afterglow temperatures of about 235°C can be found for the p2p-FAPA source with similar operating conditions.¹³ In comparison, the corona discharge of the DART source ($\sim 55^\circ\text{C}$)¹³ and the dielectric-barrier discharge of the LTP probe ($\sim 30^\circ\text{C}$)^{8,130} have significant lower gas temperatures, which ultimately leads to less analyte desorption and lower analyte signals. Furthermore, these results point out that the elevated FAPA source temperature presumably assists the thermal desorption of the heated metal mesh.

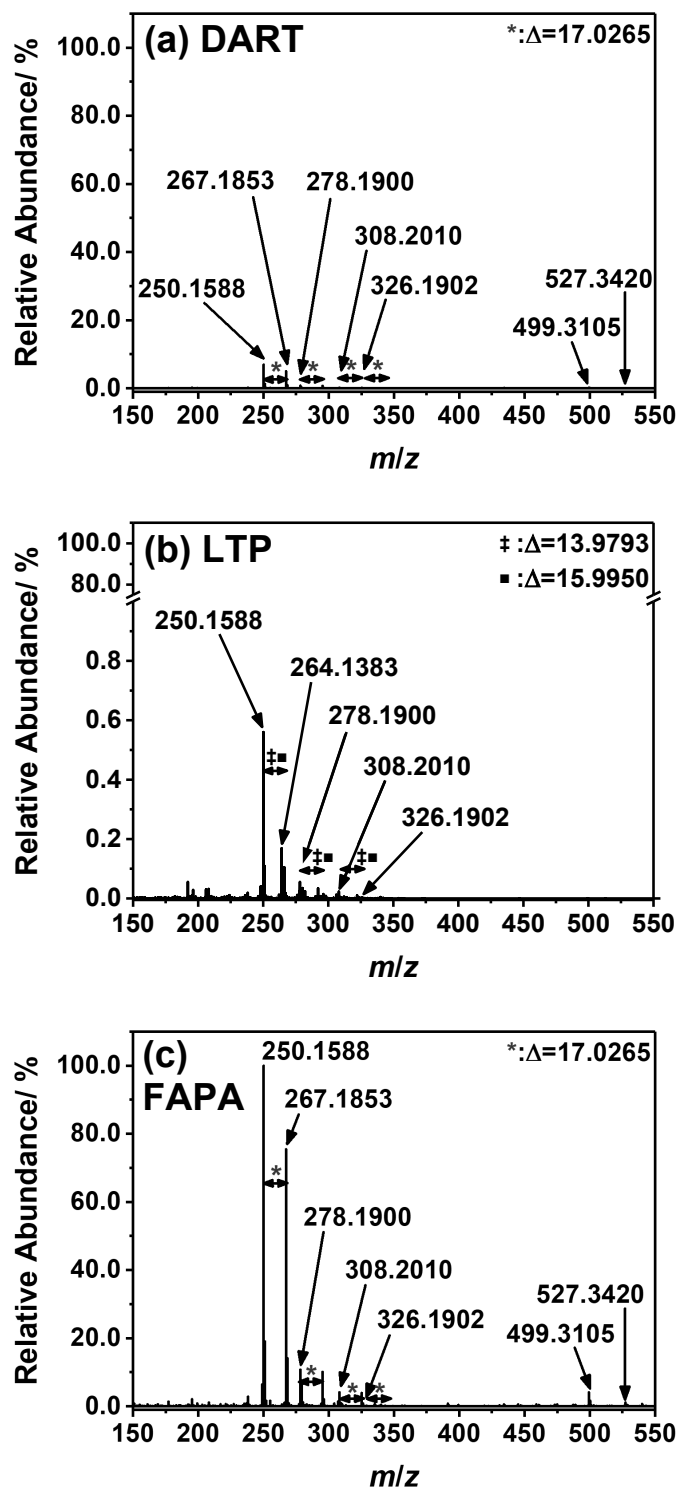


Figure 4.3 Mass spectra of the CB15/E7 liquid-crystal mixture analyzed by DART-, LTP-, and FAPA-MS (a-c) with an Exactive Plus mass spectrometer. External heating was used to enhance sample desorption. In (d-f) no external heating but the plasma source was exclusively used for sample desorption. For visualization purposes, the relative abundances in (a-f) are normalized to $m/z \approx 250.1588$ of (c). Mass spectra were obtained in positive-ion detection mode and ions were identified with an RMA within ± 1.2 ppm.

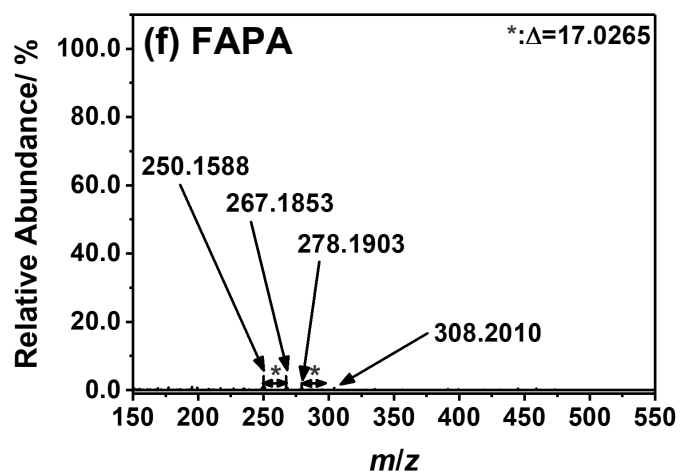
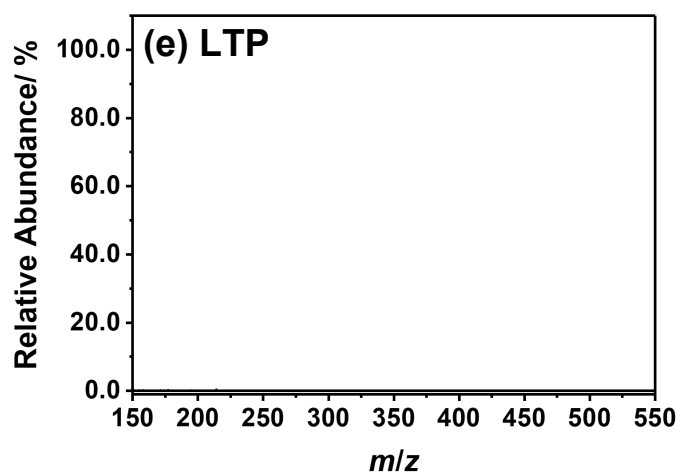
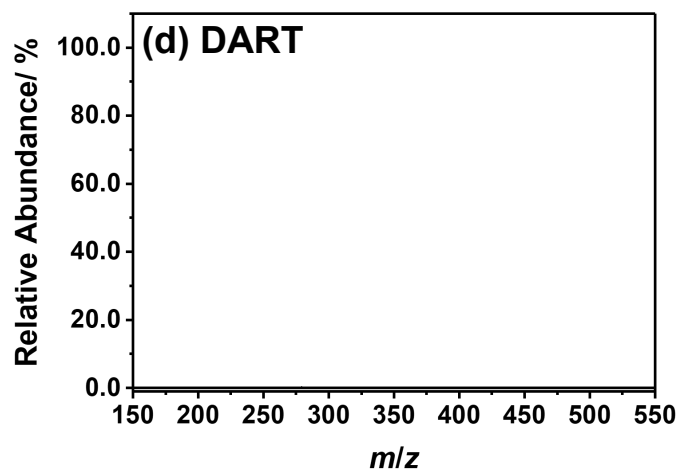


Figure 4.3 Continued.

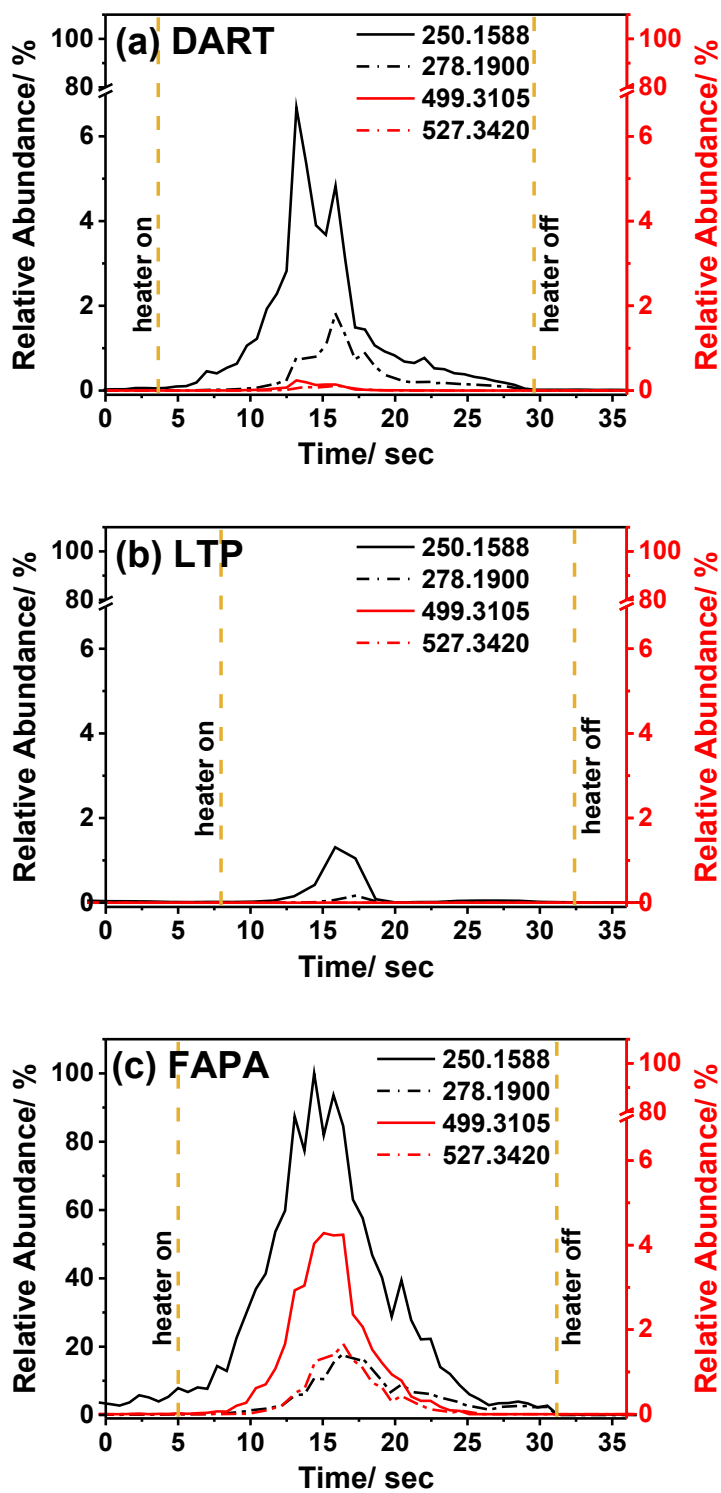


Figure 4.4 Extracted-ion chromatograms (EICs) of m/z 250, 278, 499, and 527 are shown (a-c). For visualization purposes, the relative abundances in (a-c) are normalized to m/z 250.1588 of (c).

Mass spectra were obtained in positive-ion detection mode and ions were identified with an RMA within ± 1.2 ppm.

For the identification of the high m/z signals, the extracted-ion chromatograms (EICs) of the protonated analyte species were compared with the peaks at m/z 499.3108 or m/z 527.3420 (*cf.* Figure 4.4a-c). Here dimerization of LC-IV can be correlated to m/z 499.3108. This dimerization of LC-IV is observed when the LC mixture is analyzed with DART- and FAPA-MS. Further, the mass traces of LC-IV and LC-VI correlate very well with the EIC of m/z 527.3420 and the accurate mass of the mass spectrometer ($\Delta m/z = -0.2$ ppm) indicate the formation of a $[M^a+M^b+H]^+$ adduct, which was observed for DART- and FAPA-MS.

Plasma-Based ADI-MS Applied to Liquid Crystals Used in Display Technology. In subsequent analyses, a mixture of liquid crystals used in an LCD test cell was analyzed with the previously mentioned experimental setup of the three ADI sources. These liquid crystals were provided by Merck KGaA (Darmstadt, Germany) and are different compounds compared with the above presented liquid crystals. Due to confidentiality, no further information about the molecular structures and the exact liquid crystal mass fractions can be provided. For the analysis of the test cell, the sealant on the outer edges was removed (performed by the test cell manufacturer, Merck KGaA, Darmstadt, Germany) and the two LCD test cell halves were separated from each other. Subsequently, a small droplet of the liquid-crystal mixture was transferred with a pipette from the display surface to the OpenSpot Card for the analysis by ADI-MS. The analyzed mixture contained nine liquid crystals with different functional groups. However, aliphatic-chain and saturated ring-structured molecules represent by mass more than 50% of the absolute amount in the mixture. Furthermore, molecules with small aromatic systems (*e.g.*, phenyl or biphenyl) and double bonds were also present. As stated by the LC manufacturer, LC structures with larger aromatic systems and fluorinated phenyl rings represent the smallest fraction of the sample matrix.

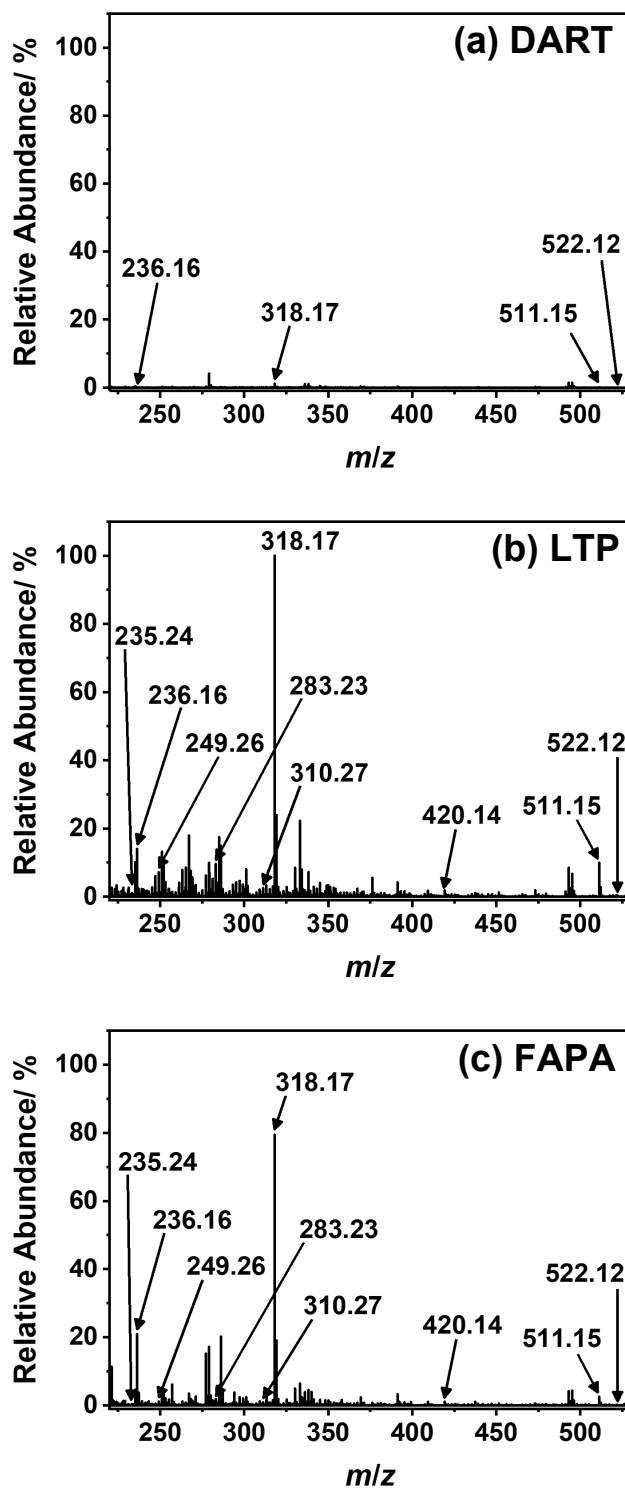


Figure 4.5 Mass spectra of a liquid-crystal mixture extracted from a commercially available LCD provided by Merck KGaA. The mixture was analyzed by DART- (a), LTP- (b), and FAPA-MS (c) (Exacte Plus) in positive-ion detection mode. The relative abundance in (a-c) is normalized to the most abundant signal from any of the ion sources. RMA within ± 0.8 ppm. The accurate mass of the analytes is not shown due to patent reasons.

In Figure 4.5a-c, the obtained mass spectra at the maximum of the transient analyte signal are depicted. With DART-MS, four of the nine components in the mixture could be detected. The detected compounds contain adjacent aromatic rings (*e.g.*, biphenyl and triphenyl) as well as molecules with larger aromatic systems. Liquid crystals with just one double bond could not be detected. In the case of LTP- and FAPA-MS, all nine analytes were detected. In these cases, the heated metal mesh ensured sufficient sample desorption, while the diversity of plasma species from the DBD and APGD enabled ionization of less polar analyte molecules. Both ADI sources were even able to ionize mono- and di-substituted double bonds. Hence, for one species, an abstraction of a CH₃-group combined with an addition of an oxygen atom was observed. Moreover, the peaks at m/z 511.15 and m/z 529.18 the latter attributed to adduct of water were equally observed.

The lowest detectable amount (instrumental limit-of-detection (IDL)) of the respective liquid crystal was determined with a diluted solution of the liquid-crystal mixture. The calculated IDLs for DART-, LTP-, and FAPA-MS are presented in Table 4.4. For the measurements, 2 μ L of the diluted standard solution (five measurement points in the concentration range of 9 μ g to 12 pg absolute deposited amount of sample, standards dissolved in toluene) was deposited on the OpenSpot mesh substrate and directly probed by either of the three plasma-based ADI sources. Additional heating was applied to the sample substrate by an applied current of 5 A. However, for some analytes, the number of calibration points was not sufficient for accurate IDL determination due to comparatively high IDLs. In these cases, the lowest detectable amount (deposited amount of the sample substrate, transient analyte signal abundance at least three times higher than the standard deviation of the background signal) of the analyte is mentioned as a rough estimate for the respective instrumental detection limit. For the IDL determination, the detected ion signal and the corresponding ¹³C-isotope peak of the particular analyte were summed and the transient ion signals were integrated (*cf.* Figure 11.14a-f, three replicates per calibration point measured). The IDLs were derived by dividing three times the standard deviation of the background signal by the slope of the calibration curve.

In relation to the actual amounts of liquid crystals in an LCD, the calculated IDLs are promising results for the future application in LCD analysis. Kelly *et al.* reported the distance between the two substrates of a typical LCD to be 2-10 μ m.¹⁰⁷ By assuming a distance of 5 μ m and a simultaneously probed surface area by the ADI source of 1 mm², the probed volume is 5·10⁻³ mm³ (5 nL). This volume is filled by approximately 4.9 μ g of the liquid-crystal mixture (density of \sim 0.98 mg/ μ L, experimentally determined for the according liquid-crystal mixture), which

corresponds to, *e.g.*, 294 ng of the analyte at m/z 318, and is well above the TM-ADI-MS detection limit for this analyte.

Table 4.4 IDLs for the analysis of liquid crystals incorporated in an LCD by TM-ADI-MS.^a

Nominal m/z of compound	IDL for DART-MS (RSD)	IDL for LTP-MS (RSD)	IDL for FAPA-MS (RSD)
235	N.A. ^b	86 pg ^c	86 pg ^c
236	14 ng (RSD 2.2%)	125 pg (RSD 1.1%)	193 pg (RSD 0.7%)
249	N.A. ^b	235 pg ^c	23 pg ^c
283	N.A. ^b	22 ng ^c	22 ng ^c
310	N.A. ^b	176 ng ^c	176 ng ^c
318	4.3 ng (RSD 0.3%)	17 pg (RSD 0.3%)	30 pg (RSD 0.2%)
420	10 ng ^c	10 ng ^c	10 ng ^c
511	9 ng ^c	9 ng ^c	9 ng ^c
522	118 ng ^c	118 ng ^c	118 ng ^c

^a Number of measurements averaged for IDL calculation $n=3$. ^b N.A.: not detectable. ^c lowest detected amount of the respective liquid crystal in the diluted liquid-crystal mixture.

Comparison of Plasma-Based ADI Sources for Direct Surface Sampling.

To test the three ADI-MS techniques for direct surface desorption of liquid crystals, selected liquid crystals were diluted and combined in a mixture (0.5-2.0 $\mu\text{g}/\text{mL}$, dissolved in toluene) and probed directly from a planar glass surface. The analysis of liquid crystals on a glass substrate via direct surface desorption by the ADI sources simulates the analysis of such liquid crystals from an opened LCD panel surface, which is also a glass substrate. Specifically, for the analysis of future LCD failure spots, a display section with the failing pixels would need to be cut out of the display panel and the two halves of the display would need to be separated. ADI-MS analysis would be used as a tool to investigate the causes of the display failure in the display manufacturing process so adjustments can be made in the production line and further produced LCDs do not comprise this display error. For the purpose of liquid-crystal analysis from a flat surface, liquid crystals with a large variety of functional groups

(*e.g.*, pyrimidine, isothiocyanate, amino, ether, aromatic ring-structures, and cyano groups) and different molecular weights (*cf.* Table 4.5) were selected. Prior to the experiments, the geometry of the experimental setup (*e.g.*, distance of ADI source and mass spectrometer, angle of ADI source towards sample surface) was carefully optimized (*cf.* chapter 3, Figure 3.3). Therefore, findings in studies by Albert *et al.* and Pfeuffer *et al.* were considered for the experimental setup geometry to obtain the best performance for the experiments.^{70,88,90}

Table 4.5 Liquid-crystal mixtures detected by DART-^a, LTP-^b, and FAPA-MS^c.

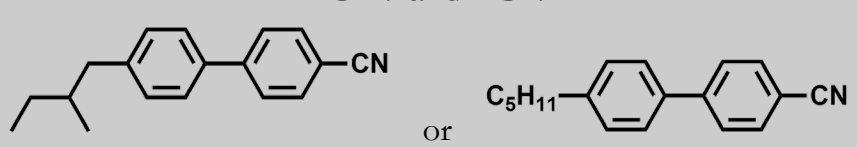
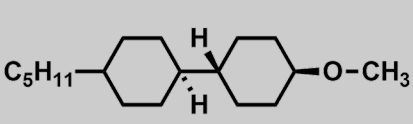
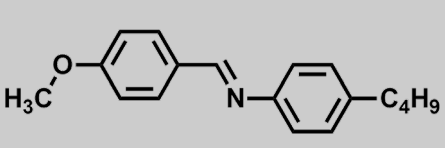
Information	Ion	Theoretical <i>m/z</i>	Observed <i>m/z</i>	Rel. mass accuracy
LC-IV and LC-V				
				
Prod. name: CB15 or 5CB	[M+H] ⁺	250.1590	250.1588	-1.1 ppm
MW: 249.35 g/mol				
Formula: C ₁₈ H ₁₉ N				
LC-IX				
				
Prod. name: ZLI-3005	[M+H] ⁺	267.2682	267.2681	-1.8 ppm
MW: 266.46 g/mol				
Formula: C ₁₈ H ₃₄ O				
LC-I				
				
Prod. name: ST00484	[M+H] ⁺	268.1696	268.1694	-0.9 ppm
MW: 267.37 g/mol				
Formula: C ₁₈ H ₂₁ NO				

Table 4.5 Continued.

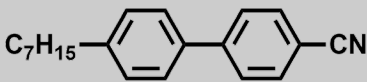
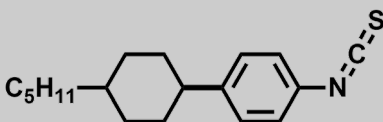
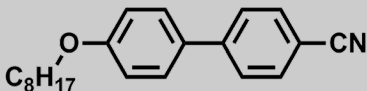
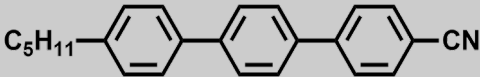
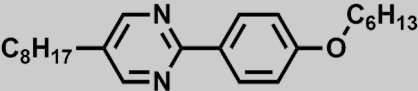
Information	Ion	Theoretical <i>m/z</i>	Observed <i>m/z</i>	Rel. mass accuracy
LC-VI				
				
Prod. name: 7CB				
MW: 277.40 g/mol	[M+H] ⁺	278.1903	278.1901	-0.4 ppm
Formula: C ₂₀ H ₂₃ N				
LC-X				
				
No commercial product				
MW: 287.46 g/mol	[M] ^{+•}	287.1702	287.1701	-0.3 ppm
Formula: C ₁₈ H ₂₅ NS				
LC-VII				
				
Prod. name: 8OCB				
MW: 307.43 g/mol	[M+H] ⁺	308.2003	308.2010	0.4 ppm
Formula: C ₂₁ H ₂₅ NO				
LC-VIII				
				
Prod. name: 5CT				
MW: 325.45 g/mol	[M+H] ⁺	326.1903	326.1902	-0.2 ppm
Formula: C ₂₄ H ₂₃ N				

Table 4.5 Continued.

Information	Ion	Theoretical <i>m/z</i>	Observed <i>m/z</i>	Rel. mass accuracy
LC-II				
				
Prod. name: ST00552				
MW: 368.56 g/mol	[M+H] ⁺	369.2900	369.2900	0.2 ppm
Formula: C ₂₄ H ₃₆ N ₂ O				

^a Analyte desorbed from a heated metal mesh. ^b Analyte desorbed from a heated glass surface (150 °C). ^c Analyte desorbed from a glass surface at room temperature (25 °C).

To perform direct surface desorption, the FAPA and LTP sources were positioned at an angle of 60° towards the horizontally oriented sample surface. The DART source used in this chapter was a DART ID-Cube by IonSense Inc., which is exclusively designed for on-axis operation towards the MS inlet capillary. Also, no plasma gas heater is available for this type of DART source because the sample target – a stainless-steel mesh – is resistively heated by an applied current. However, IonSense Inc. claims in the manual of the DART ID-Cube that the ion signals obtained with the ID-Cube (high heating current at 5 A, ~305 °C mesh temperature) are similar to the ion signals obtained with a DART-SVP ion source (IonSense Inc., Saugus, MA, USA) operated with a plasma gas temperature of 450 °C (uses gas heater). In this chapter, DART-MS analysis was performed in transmission-mode with a heated metal mesh (temperature of the wire mesh ~305 °C), while direct analysis of liquid crystals with FAPA-MS and LTP-MS was performed using a non-heated and a heated (~150 °) glass substrate, respectively. It was found that the FAPA source comprises a sufficiently hot afterglow (~235 °C) to thermally desorb the analytes and no additional heating was required. The corresponding mass spectra are depicted in Figure 4.6.

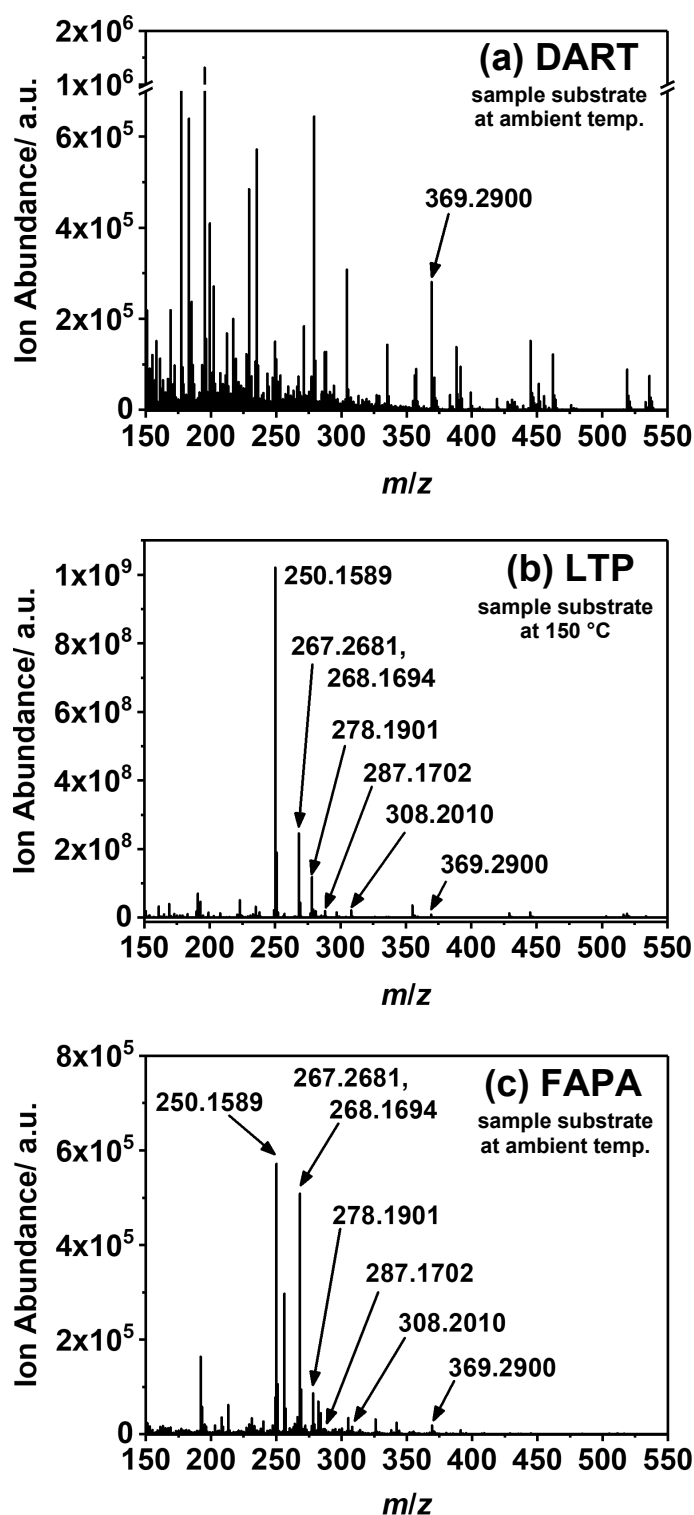


Figure 4.6 Mass spectra of the diluted liquid crystal model mixture analyzed by DART- (a), LTP- (b), and FAPA-MS (c) in positive-ion detection mode with an Exactive Plus mass spectrometer. LTP- and FAPA-MS analysis was performed by desorbing the analyte from a glass substrate (at 150 °C and ambient temperature, respectively). DART-MS was performed in transmission-mode with a sample substrate at room temperature because direct surface desorption was not possible with the available DART ID-cube source. RMA within ± 1.9 ppm.

For DART-MS, the most abundant ion signals were detected for LC-II, LC-IV, and LC-I with ion abundances of $1.1 \cdot 10^7$ counting units, $3.7 \cdot 10^6$ counting units, and $4.6 \cdot 10^7$ counting units, respectively, when operated in transmission-mode with 5 A heating current applied to the metal mesh (*cf.* Figure 4.6a) Furthermore, the liquid crystals LC-VI and LC-VII could be detected at low ion abundances of $<1\%$ relative to the most abundant ion detected by DART-MS. In contrast to these results, only the analyte LC-II (m/z 369) could be detected via DART-MS (data not shown), which demonstrates that the external heating of the analyte substrate or the DART plasma gas stream is necessary to obtain sufficient thermal desorption of the analyte.

The direct analysis of the LC mixture via LTP-MS at ambient sample substrate temperature did not give satisfactory analyte signals for any of the liquid crystals in the mixture (not shown). Hence, the sample plate was heated to a temperature of 150 °C to assist the analyte desorption process. Due to the versatile pool of ionic species in the LTP plasma, it was possible to detect all compounds listed in Table 4.5. In the LTP-MS mass spectrum (*cf.* Figure 4.6b) relatively high ion abundances are observed for all analytes in the mixture. Specifically, low mass LCs have the highest ion signal abundances while m/z species of higher mass feature significantly lower ion signal abundances. However, the detection of LCs from a glass substrate is only possible with external heating to aid analyte desorption.

The mass spectrum of the LC mixture detected by FAPA-MS is depicted in Figure 4.6c. Similarly, to the LTP-MS results, the FAPA-MS approach was successful in detecting all LC compounds, which were present in this artificially made liquid-crystal mixture. The ions in the lower mass range (m/z 150 to 230) in Figure 4.6c may result from potential contaminations of the ADI source or background signals from ambient air. Distinct analyte fragmentation was not observed. Due to the comparatively high plasma temperatures of the FAPA source no additional heating of the sample substrate or the plasma gas was necessary to detect the above-presented ion abundances.

In summary, the surface desorption of the majority of liquid crystal compounds analyzed in this chapter is possible with all three ADI sources. With LTP- and FAPA-MS, it was possible to detect in fact all liquid crystals in the mixture (most probably due to the more versatile ionization pathways which are available with these ionization sources). While this makes fast screening of LCs on sample substrates possible with plasma-based ADI-MS, it will be worthwhile to study the possibility to perform spatially resolved analysis with these types of ADI source in the future. Spatially resolved information may help to identify display failure at an exact location on the display. In this regard, the LTP-MS method in combination with a heating

mat underneath the sample substrate is not an ideal analysis technique, because the spatial resolution is lost by the simultaneous evaporation of the LCs by the heating mat. However, DART- and FAPA-MS seem to be promising ADI sources, because the DART source is commercially available with a gas heater to promote analyte desorption, while the FAPA source itself is capable to thermally desorb the analytes from the sample surface. Even though the current designs and gas outlets are larger than the pixel sizes of LC products, modified source geometries might provide the necessary spatial resolution required for successful mass spectral imaging of LCD panels. In this case, the only sample preparation step required before directly probing the display, would involve cutting out the section of the display panel (typically 5 x 5 cm or 10 x 10 cm) and separating the two glass plates of the LCD where the malfunction is observed. To the best knowledge of the authors the display failure spots on these display panel cut outs have a diameter in the millimeter to micrometer range. Häbe *et al.* optimized the DART source for the spatially resolved surface analysis and with an exit hole diameter of 1 mm on the DART front cap a FWHM of 0.8 mm was determined as spatial resolution for the analysis of HPTLC plates.^{44,46} The FAPA source used in this chapter – a p2p-geometry – comprised an exit hole diameter of 1.6 mm, but measurements of the spatial resolution neither for the p2p-FAPA source nor for the p2c-FAPA source are available in the literature. Comparison and optimization of the attainable spatial resolution with these different types of ADI sources will be an interesting task for a future study. Another approach to improve the spatial resolution for surface analysis is the addition of a laser ablation system for analyte desorption. Müller *et al.*¹¹⁰ used LA-APCI-MS to analyze LCD components (liquid crystals and adhesives) with laser spot sizes down to 150 μm . The combination of such a laser ablation system with plasma-based ADI-MS could also be a promising application because of two reasons. First, the laser beam can be focused to spot sizes in the micrometer range and ensures high spatial resolution. Second, the plasma-based ADI sources presented in this chapter offer versatile ionization pathways to produce, *e.g.*, molecular-ions or protonated molecular-ions, and these ionization pathways can be easily changed by the operation mode of the respective ADI source.^{14,45,57}

4.4 Conclusion

Aim of this chapter was to compare the applicability of DART-, LTP-, and FAPA-MS for liquid-crystal analysis. It was shown in this chapter that the three plasma-based ADI sources show significantly different sensitivities for individual liquid-crystal standards as well as for liquid-crystal mixtures. Analyte oxidation was observed with LTP- and FAPA-MS (*e.g.*, Figure 4.1e and f) and fragmentation was only observed for the analysis of ST00484 with FAPA-MS (*cf.* Figure 4.1c). LTP- and DART-MS do not produce much (if any) fragmentation of liquid crystal molecules but these ADI sources are also limited in the range of detectable analytes. Particularly, in the case when the dielectric-barrier discharge and the corona discharge were operated without external heating of the sample substrate, only one of the probed analytes (ST00484) could be detected at very low abundances. Similarly, the LTP source required aided analyte desorption by external heating of the sample substrate to detect any ion signal. In contrast, FAPA-MS is capable to detect a variety of liquid crystal molecules with a molecular mass of up to approximately 370 u without external heating. Due to the low vapor pressure of analytes with high molecular weight (*e.g.*, > 400 u) the detection of such compounds was difficult with any of the ADI sources, even with additional heating.

Moreover, FAPA-MS was the most sensitive method compared with other ADI sources especially for the analysis of LCs with cyano groups. Protonated molecules and a strong formation of ammonia adducts for liquid crystals with cyano group were equally observed. FAPA-MS has proved to be a promising ADI source for the analysis of liquid crystals without the need to heat the glass substrate or the plasma gas. Hence, this technique could be useful for molecular mapping of liquid crystals and additive materials within the LCD and also rapid analysis of display failure spots.

Chapter 5

Spatially-Resolved Analysis of Liquid Crystals in Liquid Crystal Display Test Cells via Flowing Atmospheric-Pressure Afterglow Mass Spectrometry

5.1 Introduction

In the age of digitization, electronic devices can be found in every part of our daily life. One part most electronic devices have in common is the display which helps the operator to control the device. With the improved performance of the electronic devices also the complexity of these displays dramatically increased and ultra-high-resolution displays are currently becoming state-of-the-art for display technology. In most of these displays, liquid crystals are used to visualize the information.

Due to the increasing complexity of display devices, quality control and assurance of the displays' correct functional capabilities are very important during the liquid crystal display (LCD) manufacturing process. In this industrial process, the correct combination and alignment of multiple layered components (*e.g.*, additives in the liquid-crystal mixture, transparent indium-tin-oxide (ITO) electrodes, or an orientation layer for the liquid crystals) in addition to the liquid crystals need to be precisely combined. A more detailed description of the LCD structure can be found in the book "Liquid Crystals, Display and Laser Materials" in the chapter by Kelly *et al.*¹⁰⁷ However, liquid crystals play an important role for the proper function of the LCD device and a contamination during the manufacturing process (*e.g.*, by other liquid-crystal products and particulates) may have severe consequences for the display functionality.^{106,108,109,111}

State-of-the-art techniques for the elucidation of these display failures comprise microscopy-based methods (*e.g.*, optical microscopy or electron microscopy)¹⁰⁸ as well as ToF-SIMS.¹⁰⁹ Furthermore, chromatography-based techniques (*e.g.*, HPLC or GC) coupled to MS are often used in industry for the analysis of organic compounds. Therefore, one would assume that these techniques also play a major role in the elucidation of display failure spots. However, to the best of the authors' knowledge so far, no publications of HPLC- or GC-MS methods for the analysis of liquid crystals displays exist in peer-reviewed journals. To access the liquid crystals, it is necessary for any of these methods to open the LCD, so that the region around the display failure spot can be analyzed. This is typically done by cutting a region of interest out of the large-format display. Before chromatography and mass spectrometry techniques can be applied for analysis, manual extraction of the liquid crystals with organic solvents (*e.g.*, methanol or acetonitrile) is required. Inevitable dilution of the target molecule(s) with relatively large amounts of solvents, as well as with intact liquid crystals surrounding the failure spot, may cause challenges for the

analyte detection due to the manual extraction procedure. In addition, any spatial information is lost, which may further complicate the identification of the failure causing substances in a complex mixture of various liquid crystals and additives. For this reason, it is suggested to apply direct surface-sampling methods which are able to maintain and resolve the spatial distribution of the analytes, such as ADI-MS or laser ablation coupled to organic mass spectrometry. The latter approach was performed by Müller *et al.* who used LA-APCI-MS to perform first experiments for mass spectral imaging (MSI) of liquid crystals in LCDs.¹¹⁰

Shortly after the introduction of ADI-MS by the two pioneer techniques DESI⁶ and DART,⁷ also MSI via ADI-MS techniques became an important tool for analyzing the sample surfaces in a way that allowed to visualize the spatial distribution of the analytes. Due to the very narrow spray plume of the DESI source the spatial resolution could be optimized down to $\sim 40 \mu\text{m}$ ¹³¹ and applied for the analysis of inks for forensic analysis¹³² or drugs in histological section of organs.¹³³ A recent review which mainly focuses on mass spectral imaging via spray-based ADI techniques, their applications and future use was published by Perez *et al.*¹³⁴ Also, the plasma-based DART source has been successfully applied for MSI of TLC plates, while spatial resolutions of 3 mm¹³⁵ and 0.8 mm⁴⁶ could be obtained. Furthermore, the LTP probe was applied for mass spectral imaging of fragrances on glass, paper, and clothes substrates (spatial resolution better than 1 cm)⁹¹ and for the forensic analysis of paintings and calligraphy artworks (spatial resolution approximately 250 μm).¹³⁶ The limitation of the spatial resolution for such plasma-based ADI sources can be often explained by the fact that the spatial resolution is largely influenced by the diameter of the plasma afterglow leaving the plasma source and interacting with the sample surface.¹³⁶ In this regard, a smaller diameter is expected to result in a better spatial resolution for MSI. In addition to the spatial resolution, the diameter of the plasma afterglow also influences the heat transfer from the inside of the plasma source towards the analyte surface. A smaller diameter causes a decreased heat transfer outside the plasma source and the resulting thinner afterglow stream is cooled more quickly by the ambient air. This ultimately causes less analyte to be desorbed by the plasma because thermal analyte evaporation is largely responsible for the sample desorption with plasma-based ADI sources.

Because of these limitations in spatial resolution lasers were incorporated into the experimental setup to aid or completely take over the analyte desorption. For example, the DART source was combined with laser ablation by Galhena *et al.*¹³⁷ as well as Fowble *et al.*¹³⁸ to spatially resolve small-molecules in biological and non-biological matrices. Furthermore, Shelley *et al.*¹³⁹ coupled laser ablation to the FAPA

source and Pfeuffer *et al.*⁵⁰ modified the geometry of the said plasma source to ease the sample introduction of dry aerosols produced by laser ablation into the afterglow region of the glow-to-arc plasma.

Due to the benefits of FAPA-MS for direct surface sampling of liquid crystals without external surface or plasma heating (*cf.* chapter 4), this technique is applied for the first time for mass spectral imaging of liquid crystals. Aim of the study is to visualize the spatial distribution of the liquid crystals in a “LCD test cell”. These proof-of-principle experiments are performed to verify the capabilities of the ADI-MS method for future application to liquid crystals and contamination analysis in LCDs. Unfortunately, the analytical method could not be applied to real-world display failures because these samples were not provided by a display manufacturer during the time of the experiments. For the experiments, liquid crystals surrounded by a UV-cured Loctite 352 sealant were analyzed by consecutive line scans with FAPA-MS. The resulting extracted-ion chromatograms (EICs) for the target analytes were combined to mass spectral images of the respective compounds. This particular sample system made out of liquid crystals and adhesive material was selected because mixing of the two components at the interface is known to pose a risk for display failure spots. Because FAPA-MS is somewhat limited in its capabilities for spatial resolved analysis the obtained results are compared to measurements by LA-h-FAPA-MS. In this regard, the ability of both methods for spatially-resolved display failure spot analysis – typically very localized phenomena in the mm- to μm -size range – will be discussed.

5.2 Experimental Section

Reagents. The custom-made liquid-crystal mixture for use in the simulated LCD test cell was prepared with the liquid crystals CB15/E7 (Merck KGaA), ST00551 (Synthon Chemicals GmbH & Co. KG), ST00484 (Synthon Chemicals GmbH & Co. KG), ZLI-1184 (AstaTECH Inc.), K18 (BDH Chemicals Ltd., Poole, UK), and K36 (BDH Chemicals Ltd.). Furthermore, the adhesive Loctite 352 (Henkel AG & Co. KGaA, Düsseldorf, Germany) was used.

Sample Preparation. A mixture of the liquid crystals CB15/E7 (5.1 mg), ST00551 (4.0 mg), ST00484 (4.1 mg), ZLI-1184 (4.5 mg), K18 (7.4 mg), and K36 (6.0 mg) was prepared in a HPLC vial. For more information about the liquid crystals *cf.* Table 11.7 in the appendix. The mixture of solid liquid crystal was homogenized

by melting the compounds at 50 °C and vortex mixing for 2 minutes. Afterwards the liquid was ultrasonicated for 30 minutes at 40 °C.

The simulated LCD was prepared by depositing 0.5 μL of the liquid-crystal mixture on a microscope slide. The droplet was spread out on the surface with the pipette tip. A smooth analyte film was obtained by heating the glass slide at 50 °C for 2 minutes (surface area of the analyte film approx. 746 mm²). The liquid-crystal film was surrounded with a ~ 1 mm wide line of the Loctite 352 adhesive, which was applied with a μL -syringe. This sample was covered with a second microscope slide to complete the LCD test cell. The adhesive was cured in an UV cabinet (CAMAG UV Cabinet 4, CAMAG Chemie-Erzeugnisse & Adsorptionstechnik AG, Muttenz, Switzerland) at 254 nm (8 W). Afterwards the two microscope slides were separated with a scalpel and the two halves of the LCD test cell were subsequently analyzed by FAPA-MS and LA-h-FAPA-MS.

Flowing Atmospheric-Pressure Afterglow. The p2p-FAPA source¹¹ used in this study was positioned in a 60° angle towards the horizontal sample surface. The distance between FAPA and the inlet capillary of the mass spectrometer was 2 mm while the FAPA to sample surface distance was 3 mm. The FAPA source itself consisted of a stainless-steel pin-electrode (1.6 mm o.d., sharpened to a point) inside a ceramic discharge chamber (Macor[®], Schröder Spezialglas GmbH) and an anode capillary (25 mm capillary length, 1.3 mm i.d.) with a distance of 8 mm between the electrodes. A negative potential (approx. -730 V) was applied to the pin electrode through a 5 k Ω ballast resistor using a model BHK 1000-0.2MG high-voltage DC power supply (Kepco Inc.) operated in constant-current mode (25 mA), while the anode capillary was grounded. Helium (99.999%, Messer Industriegase GmbH) at 0.5 L/min was used as the plasma gas.

Laser Ablation and Halo-Flowing Atmospheric-Pressure Afterglow. The h-FAPA source used in this study was first described by Pfeuffer *et al.*, who also demonstrated the coupling of laser ablation to h-FAPA.⁵⁰ For laser ablation a model MNL 103 LC N₂ laser (Lasertechnik Berlin GmbH, Berlin, Germany) was used, which was operated at 192 μJ and at repetition rate of 5 Hz. The spot size was measured to be approx. 20 μm . The laser beam was focused into a custom-made, rectangular ablation cell (4x4 cm) and the ablated analyte material was transported into the central stainless-steel capillary of the h-FAPA source with a stream of Helium (0.3 L/min, 99.999%, Messer Industriegase GmbH).

The h-FAPA source was assembled with two concentric stainless-steel capillaries, both separated by a tubular aluminum oxide insulator (i.d. 1.1 mm, o.d. 2.1 mm) to electrically separate the metal tubes from each other. At the front end of the h-FAPA the tip of the inner steel capillary (i.d. 0.6 mm, o.d. 1.0 mm) is aligned with the tip of the outer capillary (i.d. 2.9 mm, o.d. 4.0 mm). The front end of the aluminum oxide tube was retracted by 1 mm, so that the steel electrodes were only insulated in this region by ambient air. The three capillaries were mounted into a 1/8-inch stainless-steel Swagelok tee (Swagelok, Solon, OH, USA) and helium plasma gas (0.5 L/min, 99.999%, Messer Industriegase GmbH) was fed into the outer stainless-steel capillary. To ignite and sustain the plasma a negative potential (approximately -350 V) was applied through a 5 k Ω ballast resistor to the central steel capillary, while the outer metal electrode was grounded. A model BHK 1000-0.2MG high-voltage DC power supply (Kepco Inc.) operated in current-regulated mode (20 mA) served as electrical power source. The toroidal-shaped plasma formed at the tip of the h-FAPA source and was directed towards the mass spectrometer inlet capillary (on-axis, 7 mm distance).

High-Resolution Mass Spectrometry. HR-MS measurements were performed with an Exactive mass spectrometer (Thermo Fisher Scientific GmbH), equipped with an Orbitrap mass analyzer. The ADI sources were installed either in a 60° angle (p2c-FAPA) or on axis (h-FAPA) in front of the inlet capillary of the mass spectrometer. Schematics of these two experimental setups are shown in Figure 3.1a and Figure 5.1. For this, the electrospray ionization housing was removed and the conventional inlet capillary was replaced by a 4-cm extended inlet capillary (0.6 mm i.d.). The mass spectrometer was calibrated daily before the ADI-MS experiments were performed to ensure precise m/z measurement. For mass calibration, a solution of caffeine (Sigma-Aldrich Inc.), MRFA (Met-Arg-Phe-Ala acetate salt, Sigma-Aldrich Inc.), and Ultramark 1621 (Sigma-Aldrich Inc.) was used. The operating conditions of the Exactive mass spectrometer can be found in the appendix in Table 11.3.

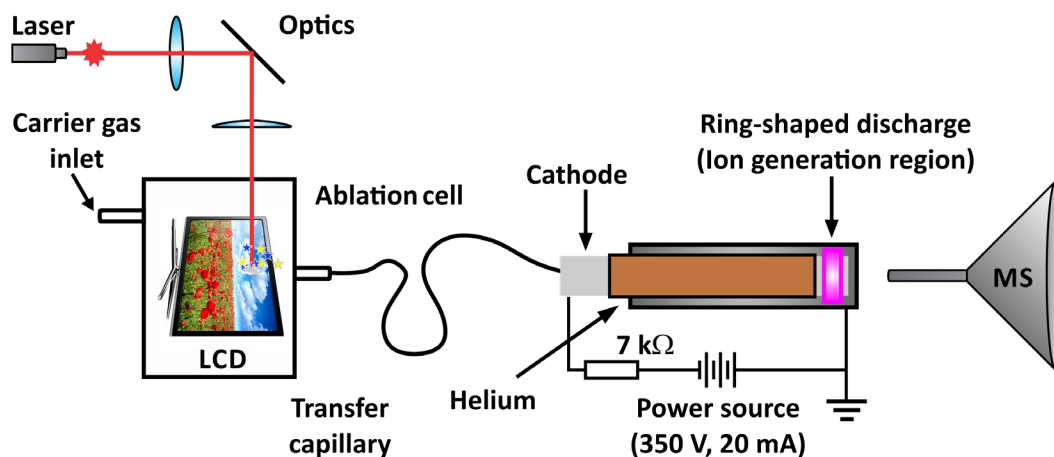


Figure 5.1 Schematic of the LA-h-FAPA-MS setup.

Mass Spectral Imaging and Data Processing. Mass spectral images of the LCD test cells were acquired via consecutive line scans across the sample surface of the microscope slide. Therefore, a motorized translational x-y-stage (Newport Corporation) was used and each line was scanned with a translational speed of 0.3 mm/s. The line to line distance for the FAPA-MS measurements was 1 mm (resulting pixel size: 1x0.12 mm) and for the LA-h-FAPA-MS measurements 0.15 mm (resulting pixel size: 0.15x0.14 mm). The translational stage was controlled by a self-written LabVIEW (National Instruments) routine. The Exactive data acquisition software (Exactive Tune 1.0 by Thermo Fisher Scientific GmbH) was started for each line scan with a trigger signal generated by the translational stage controller. The EICs of the analyte signals (*e.g.*, CB15/E7 at m/z 250.1588 \pm 8 ppm) were manually extracted from the Exactive vendor software and imported into Origin 2017 (OriginLab Corporation) for further data processing and plotting of the mass spectral images as a contour plot. A detailed description of the data extraction procedure can be found in chapter 11.4.

5.3 Results and Discussion

Mass Spectral Imaging of the Liquid-Crystal Spatial Distribution in Model LCDs via FAPA-MS. For the following results the liquid-crystal mixture was directly probed from the glass surface of the manually prepared LCD test cell. Inside the test cell the liquid-crystal mixture was deposited in the middle of the microscope slide and was surrounded by cured Loctite 352. Mass spectral imaging via FAPA-MS was performed immediately after the test cell was opened to elucidate the spatial

distribution of the ten individual liquid crystals (*cf.* Table 11.7) as well as the adhesive material (*cf.* Table 11.8). A photograph of the probed LCD test cell is presented in Figure 5.2a next to a mass spectral image Figure 5.2b of the protonated molecular-ion of LC-XIV (m/z 383.3062 \pm 8 ppm).

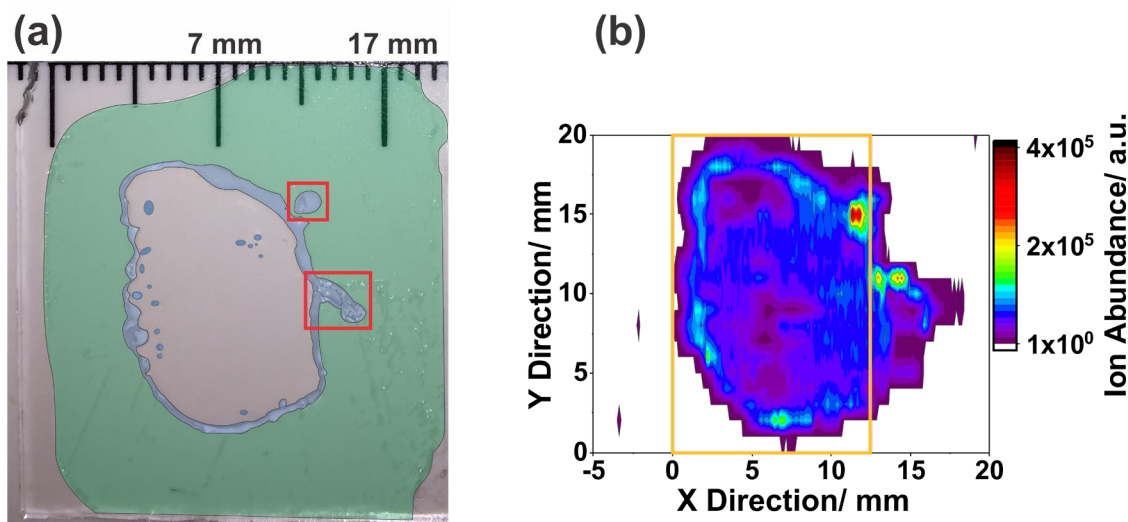


Figure 5.2 Photograph (a) of the LCD test cell and mass spectral image (b) of the protonated molecular-ion of LC-XIV (m/z 383.3062 \pm 8 ppm) detected via FAPA-MS (positive-ion detection mode). The green and blue area in (a) highlight the regions in which the Loctite 352 adhesive and the liquid-crystal mixture, respectively, were located after the LCD test cell was opened. The red squares in (a) indicate the locations where the liquid-crystal mixture intercalated into the adhesive material. The orange rectangle in (b) represents the probed sample area analyzed by LA-h-FAPA-MS (shown in the second section of this chapter).

In addition to the mass-spectral image of LC-XIV further images of the liquid crystals LC-XIII (m/z 348.2688 \pm 8 ppm), LC-IV/V (m/z 250.1588 \pm 8 ppm), and LC-I (m/z 268.1699 \pm 8 ppm) can be found in the appendix in Figure 11.15 to support the following interpretation of the results. It is important to note at this point that with the aid of the Exactive high-resolution mass spectrometer possible isobaric interferences could be resolved from the analyte ion signals of the four detected liquid crystals. Consequently, the presented mass spectral images exclusively originate from the abundance of the specific analyte molecule.

As can be seen in the photograph of the LCD test cell (*cf.* Figure 5.2a) the liquid crystals occupied an elliptical-shaped circle in the middle of the glass slide and the colorless and transparent adhesive material (*cf.* Figure 5.2a, highlighted in light green) surrounded this thin film of the liquid-crystal mixture. Before the test cell was

opened, a homogeneous layer of the liquid-crystal mixture without droplets or enclosed air bubbles was observed. Immediately after the LCD test cell was opened small droplets of the liquid-crystalline material (*cf.* Figure 5.2a, highlighted in lite blue) formed on the outer edges of the elliptical-shaped region. Evaluation of the droplet sizes via manual measurement with a caliper resulted in an approximate droplet size range between 0.5 and 2 mm. Unfortunately, it was not possible to keep the even layer of liquid crystals on the glass surface intact after opening the test cell, but the surface tension of the liquid crystals caused the formation of the droplets. Additionally, two pots are observed in Figure 5.2a where the liquid-crystal mixture intercalated into the adhesive material (highlighted with two red squares). This phenomenon is most probably caused by the manual preparation of the LCD test cell before the adhesive was cured in the UV cabinet. Despite the obviously not perfect LCD test cell preparation the spatial resolved analysis of millimeter sized liquid-crystal droplets can be achieved as demonstrated by the following example. The droplet in the upper red square in Figure 5.2a has a measured diameter of 1.5 mm in x direction and 1.2 mm in y direction (in respect to the y and x scale of the mass spectral image in Figure 5.2b). The maximum signal abundance of this analyte spot can be localized to $x=11.3$ mm and $y=15$ mm with a signal abundance of 393831 a.u. The subsequently calculated diameter of the analyte spot at 20% of the maximum detected ion abundance was found to be $x=2$ mm and $y=1.5$ mm. For the diameter in y direction this is a 20% deviation from the manually measured diameter. Despite these promising results it is important to note for this experiment that the pixel size for the FAPA-MS measurements is 1×0.13 mm. This is due to the distance of 1 mm between the different line scans across the LCD test cell. Consequently, the droplets' width measured by mass spectral imaging in x direction has to be viewed as a preliminary result and has to be verified by further measurements with a smaller pixel width in this direction. However, the smaller pixel width of 0.13 mm in the y direction enables a more detailed description of the LC-XIV (m/z 383.3062 \pm 8 ppm) distribution on the sample surface by 13 pixels.

In addition to the determination of the droplet size first preliminary information about the possible FAPA-MS spatial resolution can be obtained from the mass spectral imaging experiment and for demonstration purposes the EIC of LC-XIV at $y=16$ mm is depicted in Figure 5.3. For the analyte a high ion abundance is detected at $x=1.6$ mm which corresponds to the droplets of the liquid-crystal mixture at the left interface area between liquid crystals and the adhesive material. A second droplet of the liquid-crystal mixture can be observed 1.5 mm (manually measured with the scale bar in Figure 5.2a) to the right of the first droplet. With a FAPA-MS line

scan these two droplets can be individually detected (*cf.* Figure 5.3, highlighted in blue) and the distance between the two transient ion-signal maxima is found to be 1.7 mm. Due to the uniqueness of the sample no repeated measurements of the analyte distribution could be measured to determine the RSD. However, by assuming an RSD of 10% (corresponds to $\sim 150\ \mu\text{m}$) for the manual measurement as well as for the FAPA-MS line scan, these two measured distances appear to be within the margin of error and can be viewed as identical.

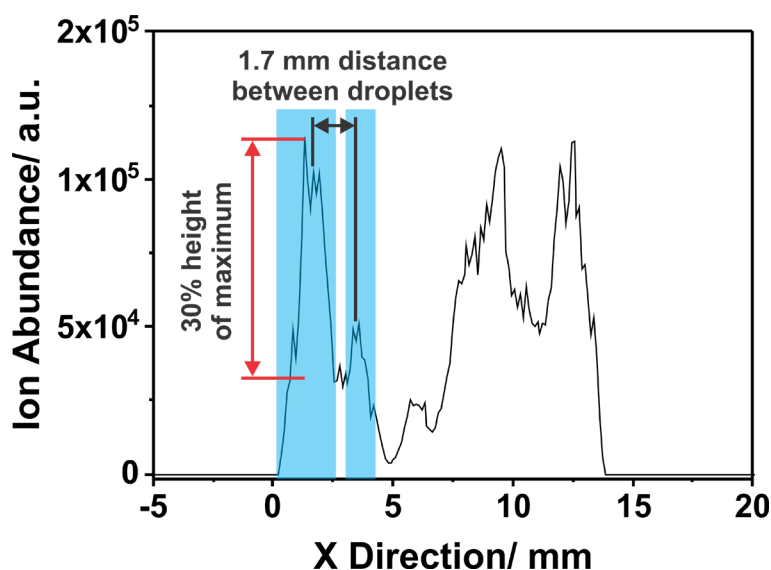


Figure 5.3 EIC of LC-XIV (m/z 383.3062 \pm 8 ppm) detected in positive-ion detection mode by a FAPA-MS line scan across the LCD test cell at $y=16$ mm.

Despite these promising results for the direct analysis of the LCD test cell by FAPA-MS, the plasma afterglow diameter of the p2c-FAPA source is relatively large (1.3 mm i.d. of the anode capillary) in comparison to the (sub-)millimeter sized droplets on the glass surface. Consequently, the above described droplets could not be baseline separated but a signal abundance minimum between the two peaks was detected at $\sim 30\%$ ion abundance height in respect to the maximum ion abundance for the first analyte droplet (*cf.* Figure 5.3, red arrow).

In conclusion this preliminary study suggests that mass spectral imaging via FAPA-MS is a powerful tool for the fast screening of liquid crystals on glass substrates such as opened LCDs. It was possible to localize droplets in the mm-size range and to differentiate droplets with a distance of ~ 1.5 mm to each other. However, the spatially-resolved analysis extremely localized events in the μm -range requires further

instrumental improvements of the FAPA source or other techniques with an inherently better spatial resolution.

Improved Spatial Resolution for LCD Analysis via LA-h-FAPA-MS. To further improve the spatial resolution for the analysis of liquid crystals in the LCD test cell a nitrogen laser (wavelength of 337 nm) was incorporated into the experimental setup and MSI was performed with the second half of the LCD test cell. A photograph and the resulting mass spectral image of LC-XIV (m/z 383.3062) is presented in Figure 5.4. For these measurements a h-FAPA source was used for analyte ionization instead of the p2c-FAPA source. Due to limitations in the travel distance of the x-y-translational stage the excerpt of the test cell for the LA-h-FAPA-MS analysis is slightly smaller (highlighted by an orange rectangle) than the surface area analyzed via FAPA-MS (*cf.* Figure 5.2 and Figure 5.4).

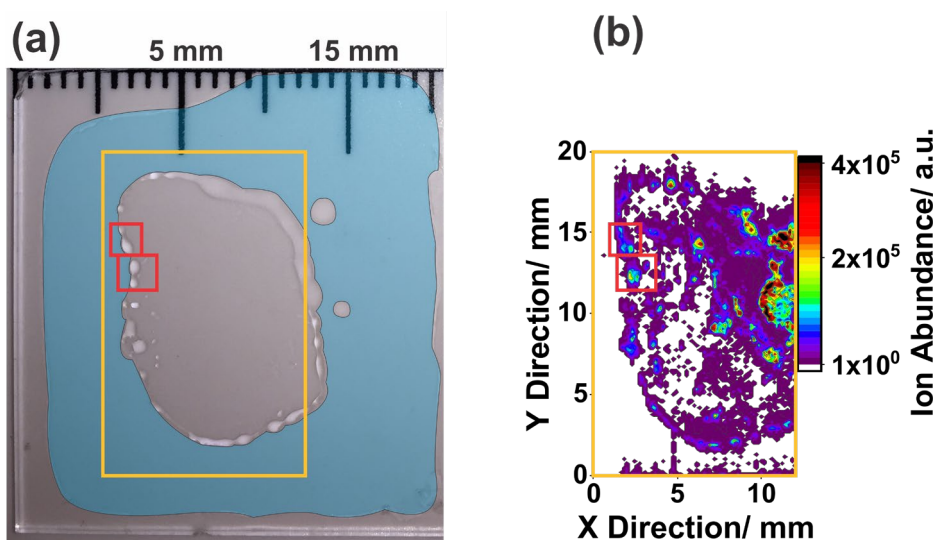


Figure 5.4 Photograph (a) of the LCD test cell and mass spectral image (b) of the protonated molecular-ion of LC-XIV (m/z 383.3062 \pm 8 ppm) detected via LA-h-FAPA-MS (positive-ion detection mode). The blue region in (a) represents the area where the Loctite 352 adhesive is located. The red squares highlight the locations of liquid-crystal mixture droplets in (a) and the related locations of high ion abundance in (b). The orange rectangles represent the probed sample area analyzed by LA-h-FAPA-MS. The x scale has been inverted for visualization purposes to enable an easier comparison between the two halves of the LCD test cell analyzed by FAPA-MS and LA-h-FAPA-MS.

Similar to the observations made for FAPA-MS, small droplets of the liquid-crystal mixture formed on the glass surface especially in close proximity to the interface area of liquid crystals and the Loctite 352 adhesive material (highlighted in

light blue). In the mass spectral image detected by LA-h-FAPA-MS (*cf.* Figure 5.4b) a high ion abundance of the LC-XIV is observed in the locations where liquid-crystal droplets are present in the photograph (highlighted by red squares). Due to the smaller laser spot size of $\sim 20\ \mu\text{m}$ in comparison to the diameter of the FAPA afterglow the mass spectral image appears to have more detailed information about the distribution of the liquid crystals on the glass surface. This observation can be explained by the significantly lower pixel size of $0.15 \times 0.13\ \text{mm}$ for the LA-h-FAPA-MS measurements in comparison to the FAPA-MS measurements with a pixel size of $1 \times 0.13\ \text{mm}$. The pixel width of $0.13\ \text{mm}$ in y direction appear to be the same size in both experiments because of the same mass spectrometer scan rate of $0.65\ \text{recorded spectra/second}$ was used. The lower pixel width of $0.15\ \text{mm}$ in x direction was enabled due to the smaller laser spot size of the laser beam and therefore the distance between the line scans were selected to be smaller in the software of the x-y-translational stage. Additional mass-spectral images of the liquid crystals LC-XIII ($m/z\ 348.2688 \pm 8\ \text{ppm}$), LC-IV/V ($m/z\ 250.1588 \pm 8\ \text{ppm}$), and LC-I ($m/z\ 268.1699 \pm 8\ \text{ppm}$) can be found in the appendix in Figure 11.16.

Identical to the FAPA-MS measurements the diameter of the liquid-crystal droplets can be also measured by LA-h-FAPA-MS. As an example, the droplet diameter was measured for the analyte spot in the upper red rectangle (*cf.* Figure 5.4b) and the manually measured droplet size of $0.8\ \text{mm}$ could be confirmed by results measured via mass spectral imaging for which a droplet diameter of $1\ \text{mm}$ was detected (*cf.* Figure 11.17).

More important for the spatially-resolved detection of the analyte distribution is the differentiation between separate analyte droplets on the glass surface. Unfortunately, a suitable spatial resolution target was not available at the time of the experiments. However, to estimate the capabilities of LA-h-FAPA-MS for spatial resolved analysis the full-width at half maximum (FWHM) of the analyte signal abundance was determined for two analyte droplets in close proximity and the (assumed) spatial resolution is determined as described by Häbe *et al.*⁴⁶ For this task the two droplets highlighted by two red squares in Figure 5.4 were selected. For better visibility of the two droplets in the mass spectral image an excerpt of this region of interest is presented in Figure 5.5. Both droplets in Figure 5.5 have a diameter of approximately $1\ \text{mm}$ and the distance between these two droplets was measured to be $\sim 0.5\ \text{mm}$. For the upper droplet at $x=2.1\ \text{mm}$ and $y=14\ \text{mm}$ a FWHM of $0.7\ \text{mm}$ was measured from the EIC of the line scan across the analyte spot. The second analyte droplet at $x=2.3\ \text{mm}$ and $y=12\ \text{mm}$ a FWHM of $0.6\ \text{mm}$ was determined. Additionally, LA-h-FAPA-MS was also capable to visualize even smaller droplets in

the middle of the glass surface, which were not visible in the photograph taken with a microscope. Consequently, the preliminary determined spatial resolution of 0.6 mm is more of an estimate for the LA-h-FAPA-MS technique and surely a better spatial resolution can be presented if a proper spatial resolution target will be used in future studies.

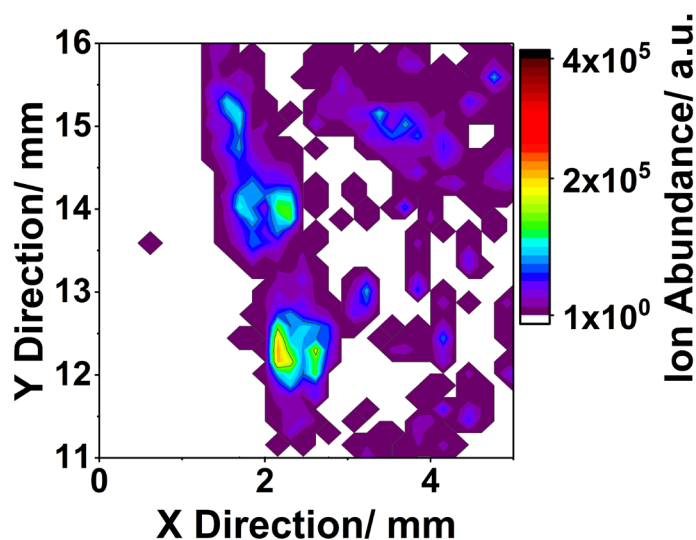


Figure 5.5 Excerpt of Figure 5.4b with the mass spectral image of LC-XIV (m/z 383.3062 \pm 8 ppm) detected via LA-h-FAPA-MS.

Differentiation of Liquid Crystals and Adhesive Materials in LCDs. In addition to the liquid crystals also other chemicals such as adhesives are incorporated in LCDs. During the manufacturing process of display devices, adhesives are deposited on the outer edges of the two glass substrates so that the two halves of the display panel can be glued together. The interface area of these adhesive materials and the liquid crystals in between the glass plates may cause a failing display in the event of chemical reaction or mixing of the two components. Consequently, spatially-resolved information of these components is very valuable to identify the source of error in the display manufacturing process.

Before performing the mass-spectral imaging experiments the pure Loctite 352 adhesive was analyzed to identify the mass spectral signal of the components in the sealant. Consequently, a mass spectrum of Loctite 352 was recorded in positive-ion detection mode via FAPA-MS after curing the adhesive in a UV cabinet (*cf.* Figure 5.6).

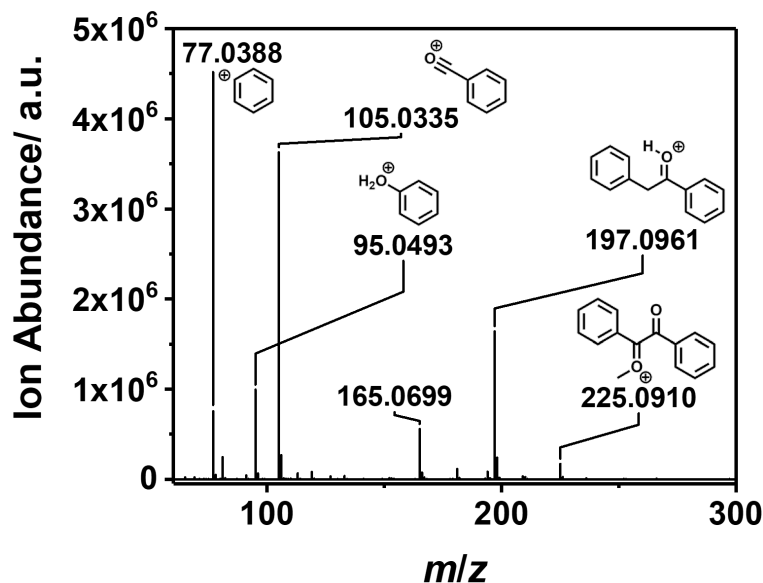


Figure 5.6 Mass spectrum of the Loctite 352 adhesive detected via FAPA-MS in positive-ion detection mode. RMA better than 2.4 ppm.

In the mass spectrum six dominant peaks with nominal m/z 77, 95, 105, 165, 197, and 225 could be related to the compounds used in the adhesive. The peaks were identified by accurate mass measurement with an RMA better than 2.4 ppm. Possible molecular structures of the identified (fragment) ions were elucidated by relating the calculated sum formulas to the reagent compounds present in the Loctite 352 adhesive. These reagent compounds are listed in Table 11.8 in the appendix. It was found that all identified ions have a benzene ring in common and most probably they are related to the compounds 2,2-dimethoxy-1,2-diphenyl ethenone and *tert*-butyl peroxybenzoate. Interestingly, these two compounds have a relative abundance of 1-5 percent by weight (wt%) in the adhesive mixture, and for example the *tert*-butyl peroxybenzoate is used to initiate the polymerization of the adhesive under UV radiation. The presence of these monomers indicates that the polymerization of the adhesive was possibly not completed in this case, which can be an important finding in display failure analysis.

To relate the spatial distribution of the Loctite 352 adhesive to the distribution of the liquid crystals in the test cell the m/z 197 was selected for mass spectral imaging. Therefore, the mass window at m/z 197.0961 \pm 8 ppm was exported from the raw data previously used for the analysis of LCD test cells by FAPA-MS and LA-h-FAPA-MS. The corresponding mass spectral images are shown in Figure 5.7.

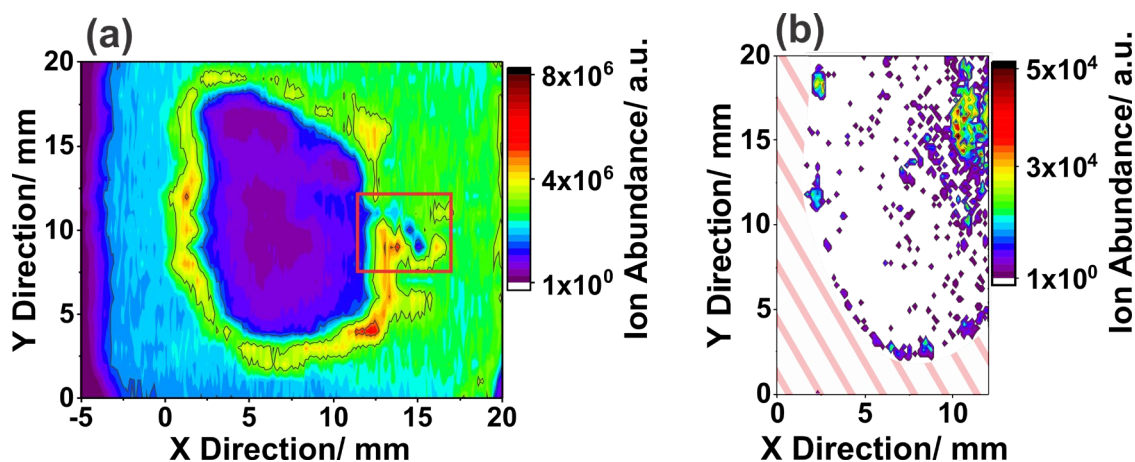


Figure 5.7 Spatial distribution of the Loctite 352 adhesive in the LCD test cell detected via mass spectral imaging by FAPA-MS (a) and LA-h-FAPA-MS (b). For EIC extraction the mass window at m/z 197.0961 \pm 8 ppm was selected (positive-ion detection mode) and the raw data was processed to obtain the presented contour plot. In (a) the red square highlights the intercalation of the liquid-crystal mixture into the adhesive material caused by the manual LCD test cell preparation. The x scale of the LA-h-FAPA-MS has been inverted for visualization purposes to ease the comparison between the FAPA-MS and LA-h-FAPA-MS measurements. The red/white striped zone in (b) was constructed by matching a photograph of the LCD test cell and the LA-h-FAPA-MS image and gives an estimate where the adhesive material is located.

The two mass spectral images detected, appear to be very different from each other even though the same m/z is shown. For the FAPA-MS measurement (*cf.* Figure 5.7a) large areas with similar ion abundance of $\sim 2 \cdot 10^6$ a.u. (light blue on the ion abundance color scale) and $\sim 3 \cdot 10^6$ a.u. (bright green on the ion abundance color scale) are present to the left and right of the elliptical area of liquid crystals, respectively. These areas match with the area of adhesive in the test cell (*cf.* Figure 5.2, highlighted in green). Compared to these ion abundances an up to 3-fold higher signal abundance is detected for the m/z 197 ion in the interface area of liquid crystals and Loctite adhesive. This observation of significantly different signal abundances in the interface region to the liquid crystals and the surrounding area might have two reasons. First, the amount of the adhesive material in these areas of the test cell might be significantly higher and, therefore, more analyte molecules are desorbed/ionized. This hypothesis was examined by optical inspection of the polymerized adhesive material, but no visible differences in the amount of adhesive were found under the microscope in these areas. Second, mixing of the liquid crystals and the liquid adhesive material in the interface region of said materials may have caused defects in the adhesive polymerization. Consequently, the higher signal abundance of the m/z 197 ion, as well as other ions related to the adhesive material (m/z 77, 95, 105, 165, and

225), can be explained by the presence of not polymerized Loctite 352 compounds in the interface area of liquid crystals and adhesive. The effect of liquid crystals and adhesive mixing can be nicely observed in Figure 5.7a highlighted with a red square. Here, a small channel of the liquid-crystal mixture (width of the channel: ~ 1 mm) is spread towards the bottom right corner of the mass spectral image. This defect is most probably caused by the manual preparation of the test cell. In the central locations of this channel the signal abundance of the m/z 197 ion comparatively lower than at the edges of the channel, where the liquid crystals interact with the adhesive before UV-curing. Consequently, these observations support the hypothesis that the interaction of the liquid crystals with the adhesive material interfere with the adhesive polymerization and therefore an enhanced m/z 197 ion abundance is observed in the interface region of the two materials.

Contrary to the results obtained by FAPA-MS imaging, the analyte at m/z 197 could not be detected by LA-h-FAPA-MS imaging outside the surface area occupied by the liquid-crystal mixture (*cf.* red/white striped area in Figure 5.7b). However, in the interface region of liquid crystals and adhesive, the m/z 197 ion is detected with a comparatively high signal abundance in the same locations as the liquid crystals in Figure 5.4b. These observations are very similar to the mass spectral image detected via FAPA-MS in which the highest signal abundances for m/z 197 are observed in this interface region of the two materials. Thus, the LA-h-FAPA-MS mass spectral image supports the hypothesis that liquid crystal mixing with the adhesive cause non-satisfactory curing of the adhesive and consequently the non-polymerized adhesive components can be desorbed by the plasma-based ADI source as well as with the N_2 laser.

These observations lead to the interpretation that with the hot plasma (~ 235 °C) of the FAPA source mass spectral imaging of the adhesive material can be performed whether or not the adhesive is cured. Furthermore, it was observed that the nitrogen laser was not able to desorb the cured adhesive but only the m/z 197 was detected in the locations where the adhesive mixed with the liquid crystals. However, the findings in this preliminary study need to be further investigated and validated. Especially the detection of the Loctite 352 adhesive via FAPA-MS needs to be verified because in the above presented experiments the UV-curing process was not performed in an industrial standardized manner. Also, the reason for the poor desorption capabilities of the N_2 laser for the adhesive need to be investigated and improved.

5.4 Conclusion

In this study, a liquid crystal display (LCD) test cell was constructed by manual preparation of a liquid crystal film in between two glass plates, glued together using a common adhesive. This LCD test cell was used to study the capabilities of FAPA-MS as well as LA-h-FAPA-MS for mass spectral imaging of liquid crystals. With both techniques it was possible to perform mass spectral imaging of the liquid-crystal distribution on the glass surface. Locations with low amounts of liquid crystals could be differentiated from positions with large liquid-crystal droplets. For the FAPA-MS measurements droplets with diameters between 0.5 mm and 2 mm could be differentiated next to each other in the mass spectral image. The mass spectral image detected via LA-h-FAPA-MS revealed more detailed information of the droplet locations due to the smaller laser spot size of $\sim 20\ \mu\text{m}$ and an approximate spatial resolution of 0.6 mm was calculated via the full width at half maximum (FWHM) of an analyte droplet. The analysis of the LCD test cell was completed with the analysis of compounds from the Loctite 352 adhesive. Before mass spectral imaging, separate mass spectra were recorded of the UV-cured sealant, and six components could be identified in the FAPA-MS mass spectrum. Via mass spectral imaging the distribution of the cured adhesive material could be depicted around the central spot with the liquid crystals in the LCD test cell. Furthermore, it was observed for FAPA-MS and LA-h-FAPA-MS that a significantly higher ion abundance for adhesive components can be detected in the interface region between liquid crystals and the adhesive, which is most probably caused by mixing of the two materials and subsequent insufficient UV curing of the adhesive.

In future studies, the exact spatial resolution of the FAPA-MS and LA-h-FAPA-MS methods need to be evaluated. This information is important to evaluate the applicability of both methods to the spatially-resolved analysis of display failure features in the μm -range. Furthermore, the two analytical methods need to be applied to real world LCDs which incorporate true display failure spots to accurately prove whether or not FAPA-MS or LA-h-FAPA-MS are useful tools for LCD failure identification. Another critical aspect to be addressed is the formation of small droplets of liquid crystals on the glass substrates after the LCD is opened. Unfortunately, this agglomeration of the flat liquid-crystal film to droplets is causing a partial loss in spatial information, which ultimately makes the identification of the failure causing compounds more difficult. Consequently, techniques have to be

developed, which make the liquid crystals inside the LCD accessible to mass spectrometry, but keeping the original liquid-crystal layer inside the display intact. Furthermore, it is recommended for future experiments to perform laser scanning microscopy with the opened LCD test cell instead of optical microscopy to get three-dimensional information about the droplet and sealant distribution and to better relate the mass spectral images to the droplets on the sample surface.

Chapter 6

Fast Screening and Quantitative Mass Spectral Imaging of Thin-Layer Chromatography Plates with Flowing Atmospheric-Pressure Afterglow High-Resolution Mass Spectrometry

Based on: C. Kuhlmann, M. Heide, C. Engelhard.
Analytical and Bioanalytical Chemistry, **2019**, *411*, 6213-6225.
DOI: 10.1007/s00216-019-02013-8.

6.1 Introduction

ADI sources have become versatile tools for direct analyte sampling in mass spectrometric analysis. Shortly after the introduction of DESI⁶ and DART⁷ for MS of small molecules, many other spray-, plasma-, and also laser-based techniques evolved. Today more than 40 ADI sources are published and they all share the common aim to perform direct mass spectral analysis of a sample in its natural environment.^{38,140} Most of these ADI sources were developed to avoid lengthy sample preparation (*e.g.*, analyte extraction with organic solvents) and separation procedures (*e.g.*, by HPLC or GC) before analyte detection. Despite these promising features of ADI-MS, some challenges remain including sometimes limited capabilities of analyte desorption, ion suppression in the ionization process, and ion transmission to the mass spectrometer. Furthermore, it is still a common practice in ADI-MS that analyte mixtures are deposited on a flat surface (*e.g.*, a glass substrate) in front of the mass spectrometer without any separation and, thus, matrix effects have to be considered for these experiments. To address these challenges, some selected ADI sources were combined early on with planar chromatography to remove matrix compounds and to separate analytes from each other in the liquid phase prior to desorption/ionization. For example, it was reported for DART-MS that a spatial separation between the target molecule (9-chloro-10-methylphenanthrene, synthesized in a Kodomari reaction) and the reaction educt (9-methylphenanthrene) using TLC enabled the monitoring of the reaction progress.¹⁴¹ TLC-DART-MS was also used to separate and identify the analyte curcumin in the turmeric plant from its derivatives (demethoxycurcumin and bisdemethoxycurcumin) after solvent extraction of the compounds from rhizome powder. Here, protonated molecular ions of the three compounds could be detected in different locations on the TLC plate.¹⁴² Despite the fact that several studies are published on TLC-DART-MS applications, which were recently reviewed by Morlock *et al.*,¹⁴³ no fundamental investigations into the potential benefits of a preceding TLC step to avoid analyte ion suppression due to matrix effects in DART-MS or other plasma-based ADI sources were reported so far. Also, it is still a common practice in ADI-MS that analyte mixtures are deposited on a flat surface (*e.g.*, a glass substrate) in front of the mass spectrometer without any separation and, thus, matrix effects have to be considered for these experiments.

Planar chromatography is defined as a separation technique with a stationary phase on a planar surface and can be divided in two major fields, paper

chromatography and TLC. Paper chromatography¹⁴⁴ is rarely performed as a separation technique today,¹⁴⁵ but the method gained attention as early as 2010 with the introduction of paper spray ionization mass spectrometry (PS-MS).¹⁴⁶ In PS, a mixture of solvent and sample is deposited on a triangular chromatographic paper sheet. By applying an electrical potential, analytes such as small organic molecules, lipids, and peptides can be ionized for mass spectral analysis in a manner similar to ESI. Cooks *et al.* used the PS-MS technique to directly analyze therapeutic drugs (*e.g.*, imatinib) in dried blood spots, while most of the complex blood sample matrix remained on the paper.¹⁴⁷ The other and more dominant field of planar chromatography is TLC, which is a versatile tool for fast screening of reaction mixtures and for the separation of target analytes from a complex sample matrix. During the last decades, the performance of the TLC stationary phase has been improved and new TLC products, such as stationary phases with smaller particle sizes, stationary phases with spherical particles, stationary phases with modified functional groups, and preparative-layer chromatography (PLC) have been commercialized. The separation performance of planar chromatography improved drastically with the commercialization of high-performance TLC (HPTLC) plates in the 1970s.¹⁴⁸ At that time, silica particles with smaller sizes (5-6 μm) and narrower size distribution (4-8 μm) compared to classical TLC (particle size: 10-12 μm , particle size distribution: 5-20 μm) were used. Both stationary phases, TLC and HPTLC, feature particles with a rough and uneven surface structure.¹⁴⁹ Stationary phases with spherical particles, such as the commercial product LiChrospher by Merck KGaA (Darmstadt, Germany), were developed in the beginning of the 2000s and typically have a mean particle size of ~ 7 μm and a particle size distribution between 6-8 μm . The advantages of spherical particles compared to the irregular shaped HPTLC material include shorter separation times as well as more compact spot sizes, while the separation selectivity is reportedly not influenced by the particle shape.^{149,150} The improved resolution and compact analyte spots can be explained by a partially suppressed analyte diffusion during separation with spherical LiChrospher particles.¹⁴⁹ To modify the selectivity of HPTLC silica plates and to match the stationary phase to the analyzed sample, TLC manufacturers offer chemically modified (bonded) phases. For reversed-phase (RP) modified thin-layer chromatography, linear alkanes with a chain length of two (RP-2), eight (RP-8), or eighteen (RP-18) hydrocarbon units directly bond to the SiO_2 surface via di- or trichloroalkylsilanes.¹⁴⁹ Furthermore, amino (NH_2) modified, cyano (CN) modified, and diol (DIOL) modified silica layers can be produced via a linking *n*-propyl group between the silica gel matrix and the functional group. The polarity of these stationary phases decreases in the following order: $\text{SiO}_2 >$

NH₂ > DIOL > CN > RP-2 > RP-8 > RP-18.¹⁴⁹ The use of medium polar solvent mixtures (*e.g.*, toluene/ethyl acetate (95:5 (v/v))), however, poses a challenge for HPTLC, because the solvents are capable of dissolving plasticizers from the packaging material, which consequently may cause ghost spots on HPTLC plates. To avoid this issue, highly pure stationary phases with minimal background are produced by TLC manufacturing companies (*e.g.*, Premium Purity or MS Grade plates by Merck KGaA) and are carefully wrapped in aluminum foil to avoid unwanted contaminations during transportation and storage. The above presented stationary phases are all designed for analytical purposes and only small sample amounts can be deposited. For preparative purification and analyte isolation PLC plates are manufactured on glass substrates with a thicker stationary phase (layer thickness: 500-2000 μm). The sample loading capacity of the PLC plate is linearly correlated to the square root of the layer thickness. Consequently, a 2-mm thick plate can be approximately loaded with twice the amount of a 0.5 mm thick plate.¹⁵¹ However, a drawback is the reduction of chromatographic resolution with increasing layer thickness. A decrease in resolution can also be observed when more coarse silica particles (~25 μm) and broader particle size distribution (5-40 μm) for PLC plates are used.¹⁵¹

The main advantage of TLC compared to other separation techniques, such as HPLC or GC, is that complex sample matrices can be separated via this technique from the target analyte to avoid interferences during the analyte detection. Through this, time-consuming sample preparation before analyte separation can be avoided because TLC plates are made for single use. Moreover, up to 30 samples can be separated simultaneously on a single plate with low solvent consumption, which makes TLC a cost- and time-effective method.¹⁵²

To further enhance the sensitivity and selectivity of the analyte detection and to identify compound spots without additional standards separated on the same TLC plate, efforts were made in the past to couple TLC to MS. For example, lipids and antibiotics (*e.g.*, cephalosporins) were detected on a standard TLC plate via SIMS;^{153,154} glycosphingolipids and small peptides (*e.g.*, bradykinin) were successfully probed via matrix-assisted laser desorption ionization mass spectrometry (MALDI-MS).^{155,156} Furthermore, two different liquid extraction devices were developed by Luftmann¹⁵⁷ and Van Berkel *et al.*¹⁵⁸ which comprise a plunger or a surface sampling probe, respectively, for analyte extraction followed by ESI-MS. The instrument by Luftmann comprises a plunger, which seals the sample spot on the silica plate from the surrounding stationary phase and elutes the analyte with a suited solvent. This solvent flow is then directed to an ESI-MS instrument. In the device by Van Berkel *et al.*, an

appropriate solvent is directed to the TLC surface via a capillary positioned closely above the surface and after online analyte extraction the solvent flow is directed to the ESI emitter via a second concentric capillary around the aforementioned capillary. Additionally, several ADI-MS techniques have been used to directly couple TLC plates with mass spectrometers. Van Berkel *et al.* used DESI-MS to enable the direct desorption of inks, analgesics, alkaloids, and peptides and also gained quantitative information for goldenseal dietary supplements by external calibration.¹⁵⁹⁻¹⁶¹ Additionally, the same research group developed a method with easy ambient sonic-spray ionization (EASI) mass spectrometry to analyze beta blocker and high blood pressure drugs, which were extracted from tablets and separated via TLC.¹⁶² In addition to these spray-based ADI sources also plasma-based ADI techniques were applied for TLC-MS coupling. These plasma-based techniques have the advantage that they do not require the use of solvents, which may distort the shape of the analyte spot by, *e.g.*, molecule diffusion in the liquid phase. The commercially available DART source was used for TLC-MS coupling and direct analysis of, *e.g.*, isopropylthioxanthone in milk products by Morlock *et al.*^{135,163} Additionally, quantitative information could be obtained for the analysis of, *e.g.*, butyl-4-hydroxybenzoate by external calibration⁴⁶ and recent studies reported further instrumental improvements to enhance the performance of TLC-DART-MS.⁴⁴ Another plasma-based source applied for TLC-MS coupling is the FAPA,⁹ which was used in combination with a continuous wave (cw) laser for the qualitative screening of pyrazole derivatives, nicotine, sparteine, and extracts from drug tablets on TLC plates.¹⁶⁴ In these experiments the cw laser aided the sample desorption.

In principle, TLC-ADI-MS can be applied to a variety of sample types and the ADI source itself was frequently optimized to enhance the techniques' sensitivity.^{44,46} However, no fundamental investigations into the potential benefits of a preceding TLC step to avoid analyte ion suppression due to matrix effects were reported so far and the modification or the thickness of the stationary phase has never been considered as a parameter to optimize the sensitivity of the analytical method. For this reason, first a fundamental study about the influence of a variety of different stationary phases on the performance of TLC/HPTLC-ADI-MS is presented in this chapter. Specifically, glass-backed TLC plates with different stationary phases (NP, RP-modified silica plates, CN-modified silica plates), selected TLC grades (TLC, HPTLC, MS Grade), and different stationary phase thicknesses are probed. In addition, the mass spectral response of model analytes (caffeine, acetaminophen, nicotine, cortisone), which are semi-quantitatively detected by mass spectral imaging, is compared. Finally, a carefully optimized HPTLC-FAPA-Orbitrap-MS method

using stable isotope dilution is reported for the quantitative analysis of caffeine in energy drinks. Results are validated by HPLC/UV measurements.

6.2 Experimental Section

Reagents. The used solvents isopropyl alcohol (analytical grade), n-heptane (analytical grade), and methanol (HPLC grade) were all purchased from Fisher Scientific GmbH. Deionized and bidistilled water was produced in the laboratory with a distillation apparatus from Heraeus-Quarzschnmelze GmbH. Caffeine (>99.9%), and nicotine (>99.9%) standards were purchased from Sigma Aldrich Chemie GmbH. Acetaminophen (Ratiopharm GmbH, Ulm, Germany) was extracted from a tablet obtained from a local pharmacy. The caffeine-¹³C₃ reference standard (>99.9%, 1 mg/mL in methanol) was provided by Merck KGaA. A variety of different TLC plates with different stationary phases and quality grades (silica plates in the grades of TLC, HPTLC, MS-grade, LiChrospher, and Premium Purity, RP-HPTLC plates, CN-HPTLC plates, NH₂-HPTLC plates, DIOL-HPTLC plates, and PLC plates with a layer thickness of 500 μm, 1000 μm, and 2000 μm) from Merck KGaA were used in this chapter and a complete list of the TLC is provided in Table 11.9.

Test Mixture Preparation. The TLC-FAPA-MS test mixture was prepared by weighing caffeine, nicotine, acetaminophen, and cortisone, 10 mg each, into individual 10 mL volumetric flasks and filling up with HPLC-grade methanol to obtain stock solutions with final concentrations of 1 mg/mL. Afterwards, stock solutions were combined and merged with a 1 mg/mL caffeine-¹³C₃ reference standard to obtain a standard test mixture with a final concentration of 0.1 mg/mL for each compound.

TLC Separation and Conditioning. To perform a TLC separation the following general procedure was applied. Each sample solution (2 μL) was deposited with a syringe on a marked starting line on the TLC plate. The samples were applied in ~5 mm wide and ~2 mm broad lines. Solvent was evaporated at room temperature for two minutes. Separation of the analyte mixture was then performed by placing the TLC plate in a MINIPLAK developing chamber (Fungilab Inc.) and using a mobile phase solvent mixture of isopropyl alcohol, n-heptane, and water (ratio of 7:3:1 (v/v/v)). Separation was typically completed within in 25 minutes. Subsequently, the

TLC plate was immediately dried for 15 minutes on a hot plate at 50 °C (if not stated differently below) and then placed in front of the ADI source ready to be probed.

Preparation of Energy Drink Samples for TLC-FAPA-MS. For quantitative analysis of the caffeine content in energy drinks via stable isotope dilution analysis an aliquot of 80 μL energy drink (nominal caffeine content stated by the manufacturer was 32 mg/100 mL, purchased in a local store) was spiked with 20 μL of a 1 mg/mL caffeine- $^{13}\text{C}_3$ reference standard. The mixture was vortexed for 20 seconds to ensure homogenization. Afterwards the mixture was directly spotted on a TLC silica plate, to be separated before mass spectral analysis. TLC development and drying were performed as stated above.

Desorption Electrospray Ionization. In this chapter, two different home-built ADI sources namely DESI⁶ and FAPA^{9,10} were used. A DESI probe with a central quartz capillary of 0.05 mm i.d. and 0.19 mm o.d. was used in combination with a concentric outer quartz capillary of 0.25 mm i.d. and 0.36 mm o.d. A solvent mixture of acetonitrile and bidistilled water (50:50 (v/v)) with 0.1% formic acid (FA) was injected to the DESI source via a syringe pump at a flow rate of 10 $\mu\text{L}/\text{min}$. The electrospray was maintained by applying a direct current (DC) voltage of 5.0 kV to the spray solvent while N_2 gas (1.2 L/min, 99.999%, Messer Industriegase GmbH) was used as nebulizing gas. The DC voltage was generated by the ESI power supply of the mass spectrometer.

Flowing Atmospheric-Pressure Afterglow. For direct surface analysis of the TLC plates by FAPA-MS, a p2c-geometry of the FAPA source, described by Shelley *et al.*,¹¹ was used. A stainless-steel pin-electrode (1.6 mm o.d.) was positioned inside a ceramic discharge chamber (Macor[®], Schröder Spezialglas GmbH). The tip of the pin-electrode inside the discharge chamber was sharpened to a point. The distance between this pin-electrode towards the back end of a capillary electrode on the other side of the ceramic chamber was 8 mm. The plasma was operated by applying a negative potential (25 mA, 663 V, constant current mode) to the pin-electrode through a 5 k Ω ballast resistor while the capillary anode was grounded. For power generation a Kepco BHK 1000-0.2MG DC power supply (Kepco Inc.) was used. Helium (99.999%, Messer Industriegase GmbH) with a flow rate of 0.5 L/min was used as the plasma gas. The FAPA was mounted in a 60° angle towards the horizontal sample surface plate. The TLC plate was positioned approximately 0.5 mm

below the inlet capillary of the mass spectrometer and 3 mm below the FAPA source, while the distance between the FAPA and inlet capillary was kept at 2 mm.

High-Resolution Mass Spectrometry. For mass spectral analysis, a high-resolution mass spectrometer (Exactive, Thermo Fisher Scientific GmbH), equipped with an Orbitrap mass analyzer was used. To install the ADI source in front of the inlet capillary of the mass spectrometer, the electrospray ionization housing was removed and the conventional inlet capillary was replaced by a 4-cm extended inlet capillary (0.6 mm i.d.). The mass spectrometer was calibrated daily before the ADI-MS experiments were performed to ensure precise m/z measurement. For mass calibration, a solution of caffeine (Sigma-Aldrich Inc.), MRFA (Met-Arg-Phe-Ala acetate salt, Sigma-Aldrich Inc.), and Ultramark 1621 (Sigma-Aldrich Inc.) was used. The Exactive instrument parameters used for mass spectral analysis with DESI-MS and FAPA-MS are listed in Table 11.4.

Mass Spectral Imaging and Data Processing. Line scans across the TLC plates were performed with a motorized translational x-y-stage (Newport Corporation) with a translational speed of 0.3 mm/second and a line-to-line distance of 0.5 mm. The stage was controlled by a self-written LabVIEW (National Instruments) routine with a triggered line scan signal to start the data acquisition of the mass spectrometer. Mass spectral data was acquired via the Exactive Tune 1.0 software (Thermo Fisher Scientific GmbH). For further data processing the extracted-ion chromatograms (EICs) of the analytes (*e.g.*, caffeine at m/z 195.0879 ± 8 ppm) were extracted from the mass spectrometer software to Origin 2017 (OriginLab Corporation). In a subsequent step the line scans were combined to a contour plot and the detected analyte spots (bands) were integrated to compare the analyte signal abundance in respect to the analyzed stationary phases. An example for this data processing procedure is presented in Figure 6.2 and more a detailed explanation of the data processing steps can be found in chapter 11.4.

6.3 Results and Discussion

Comparison of Selected Spray-Based and Plasma-Based ADI-MS Sources for Direct Screening of TLC Plates. Until today, ESI- and APCI-MS are the state-of-the-art techniques for mass spectral analysis of intact molecules on TLC plates. The transfer of the analytes from the TLC plate to the ionization source can be done either by manual extraction (instrumental detection limits (IDL) for caffeine reported to be 2 $\mu\text{g}/\text{band}$ (5 $\mu\text{L}/\text{band}$ applied))¹⁶⁵ or by commercially available plunger-based extraction devices (reported IDL of 0.75 ng/band (10 $\mu\text{L}/\text{band}$ applied)).¹⁶⁶ Kertesz *et al.*¹⁶⁷ as well as Harry *et al.*¹⁶⁸ analyzed RP-TLC plates with a commercially available DESI-MS setup and reported IDLs of 39.4 ng/band (0.25 $\mu\text{L}/\text{band}$ applied) and 16 $\mu\text{g}/\text{cm}^2$ (6 $\mu\text{L}/\text{band}$ applied) for caffeine, respectively. Additionally, a systematic study was performed with the DESI source to compare ultra-thin-layer chromatography plates and porous silica to other frequently used DESI substrates such as polymethylmethacrylate (PMMA) and polytetrafluoroethylene (PTFE).¹⁶⁹ Except from the aforementioned work, no further systematic studies are known to the authors, which directly compare different TLC stationary phases for ADI-MS analysis. Consequently, a comprehensive and systematic comparison of different stationary phases via TLC-FAPA-MS is presented in the first part of this chapter.

For the following measurements, caffeine, acetaminophen, and nicotine were selected as model standards because they are known to be well accessible by DESI and FAPA desorption/ionization. First, the performance of FAPA-MS is compared to DESI-MS for direct qualitative screening of a mixture of spotted compounds after RP-HPTLC separation. In Figure 6.1, the corresponding mass spectra for a spot of standard and $^{13}\text{C}_3$ -labeled caffeine are exemplarily presented.

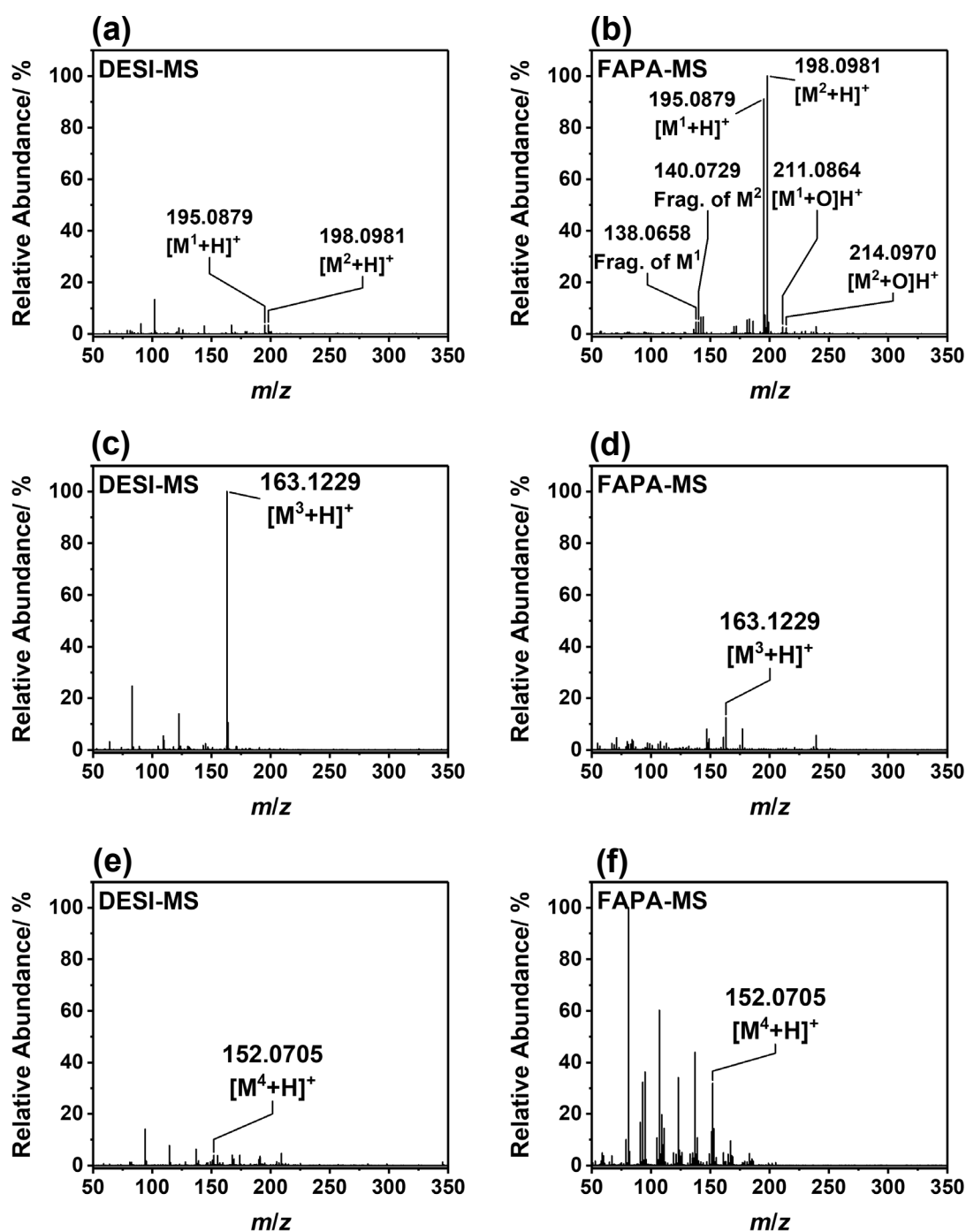


Figure 6.1 Mass spectra of caffeine ($[M^1+H]^+$, m/z 195.0879), caffeine- $^{13}C_3$ ($[M^2+H]^+$, m/z 198.0981) nicotine ($[M^3+H]^+$, m/z 163.1229), and acetaminophen ($[M^4+H]^+$, m/z 152.0705) standards directly desorbed from an RP-HPTLC plate by DESI-MS (a, c, e) and FAPA-MS (b, d, f) in positive-ion detection mode. Peak identification was facilitated via accurate mass detection with an RMA better than ± 2 ppm. Mass spectral analysis was performed after TLC separation, in which the caffeine standards were spatially separated from nicotine and acetaminophen. The peak heights of the analytes M^1 , M^2 , M^4 are normalized to the most abundant ion produced by the FAPA source and for analyte M^3 the peak height is normalized to the most abundant ion produced by the DESI source.

The experimental parameters for the performed HPTLC-DESI-MS analysis were adapted from the literature¹⁶⁰ and were carefully optimized for best performance with the home-built experimental setup. In the mass spectrum detected by DESI-MS (*cf.* Figure 6.1a) $[M+H]^+$ signals were detected for caffeine (M^1 , m/z 195.0879) and isotope-labeled caffeine- $^{13}C_3$ (M^2 , m/z 198.0981). In addition to these signals, no further adduct ions, such as $[M+Na]^+$, $[M+NH_4]^+$, or $[M+K]^+$, were detected and no analyte fragmentation was observed. The mass spectra of nicotine and acetaminophen detected by DESI-MS are presented in Figure 6.1c and e. Similarly to caffeine, nicotine was observed as protonated molecule ($[M+H]^+$, m/z 163.1229) and neither adducts nor fragment ions were observed. In the case of acetaminophen, a sodium adduct at m/z 174.05317 was detected in addition to the $[M+H]^+$ -peak (m/z 152.0705). The mass accuracies of the aforementioned ion signals in this paragraph were better than ± 3.6 ppm.

The same sample mixture was separated on a second RP-HPTLC plate and analyzed via FAPA-MS. For all three analytes, the $[M+H]^+$ -ion could be detected (*cf.* Figure 6.1b, d, and f), while no adduct ions were observed. Analyte fragmentation was only observed for caffeine and caffeine- $^{13}C_3$, for which fragment ions at m/z 138.0658 ($[M-(O=C=NCH_3)]^+$) and m/z 140.0729 ($[M-(O=C=N^{13}CH_3)]^+$) were observed, respectively. These fragment ions are also typically formed by (desorption) electrospray ionization and are reported in literature.^{167,170} Further, analyte oxidation by oxygen radicals produced in the FAPA plasma source^{11,13} was observed to a relatively small extent to give rise to $[(M^1+O)+H]^+$ (m/z 211.0864) and $[(M^2+O)+H]^+$ (m/z 214.0970) ions, which were observed at relatively low abundances (<2%).

Direct comparison of the DESI- and FAPA-MS mass spectra reveal approximately 20- and 8-fold higher signal abundances for caffeine and acetaminophen, respectively, when analyzing the sample mixture with FAPA-MS (*cf.* Figure 6.1b and f). For nicotine an opposite trend was found with 8-fold higher signal abundance for the $[M+H]^+$ -ion with DESI-MS (*cf.* Figure 6.1c). A possible explanation for the observed higher nicotine signal abundances for DESI-MS might be found in the solubility of the three chemicals. Caffeine and acetaminophen have a rather low solubility in water of 21 mg/mL and 14 mg/L (both at 25 °C), respectively.^{171,172} Hence, the two analytes are moderately extracted from the RP-HPTLC plate by the acetonitrile/water solvent mixture used for the DESI spray. In contrast, nicotine has an approximately 50-fold higher solubility in water (1000 mg/mL at 25 °C)¹⁷³ in comparison to caffeine and acetaminophen. It is

assumed here that the extraction of nicotine via the DESI spray solvent is more efficient compared to caffeine and acetaminophen, and, thus, results in the opposing trend of the analytes' signal abundances discussed above. Furthermore, the higher signal abundance of caffeine in the FAPA-MS mass spectrum in comparison to the DESI-MS measurement can be explained by the compounds' sublimation temperature of 178 °C.¹⁷¹ This temperature is similar to the temperature range typically reported for the FAPA plasma afterglow¹¹ and consequently the desorption of caffeine via the FAPA source is considered to be very efficient.

For (semi-) quantitative comparison of analyte signals detected by ADI-MS, mass spectral imaging was performed with consecutive line scans across the TLC plate in the direction and in the order of the blue arrows shown in Figure 6.2. The EIC of each analyte of interest (*e.g.*, caffeine, acetaminophen, nicotine, and cortisone) was extracted for each line scan and exported to the data processing software. The m/z windows of the analyte EICs were defined for all presented results to be 8 ppm above and below the detected exact mass of the analyte (*e.g.*, caffeine: m/z 195.0879 \pm 8 ppm corresponds to the m/z window from m/z 195.0864 to m/z 195.0895). Subsequently, the EICs were combined for each individual TLC plate to a contour plot, which was then used to integrate each analyte spot and to obtain semiquantitative information for the analyte spot. To do so, a ROI was defined that would completely cover the analyte spot (*cf.* blue box in Figure 6.2b). In a next step, all voxels, which are illustrated as small yellow boxes within the ROI, were summed up to a sum of voxel volumes. Similarly, to a peak integration approach in conventional liquid chromatography, the determined signal abundance was found to be proportional to the amount of analyte on the probed surface.

To determine the linearity and the IDL of the HPTLC-FAPA-MS method, an external calibration plot for a caffeine standard on RP-HPTLC plates was established. After analyte separation on RP-HPTLC plates, and solvent residue evaporation, mass spectral imaging was performed via FAPA-MS. The calibration plot was created after data export and data processing of the eight analyte levels ($n=4/\text{level}$, 5 $\mu\text{L}/\text{band}$ deposited), described in the paragraph above. By using a log-log plot for the resulting calibration plot a linear regression ranging from 1 to 500 $\mu\text{g}/\text{mL}$ with a determination coefficient of $R^2=0.996$ was found (*cf.* Figure 11.10). For the calculation of the IDL the recommended data processing routine for HR-MS data by the U.S. Environmental Protection Agency (EPA; Title 40, Part 136, Appendix B) was used (as explained in chapter 11.5).¹⁷⁴ With this data processing method an IDL of 0.6 ng/band (5 $\mu\text{L}/\text{band}$ applied) was found for caffeine when deposited on a RP-HPTLC plate. In comparison to the aforementioned detection limits of the plunger-

based extraction device and the direct analysis via DESI-MS, the detection limits determined via FAPA-MS are as well in the single digit ng/band range.

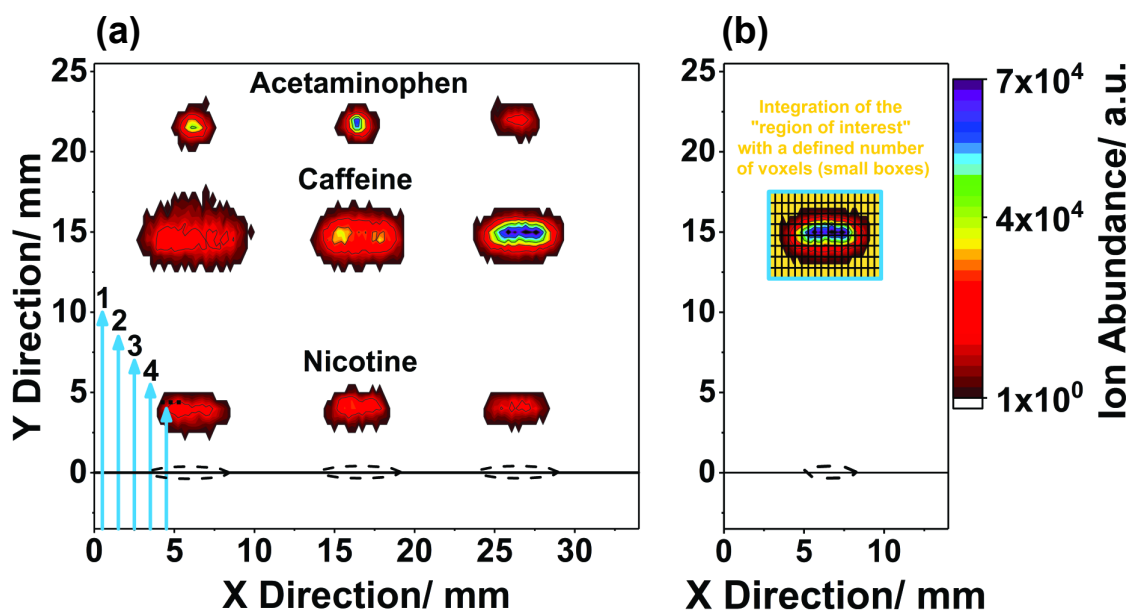


Figure 6.2 (a) Combined mass spectral image of nicotine (m/z 163.1229 \pm 8 ppm), caffeine (m/z 195.0879 \pm 8 ppm), and acetaminophen (m/z 152.0705 \pm 8 ppm) detected via HPTLC-FAPA-MS after separation of the analyte mixture on a NP-HPTLC plate (three spots deposited in dashed ellipses). The blue arrows indicate the scan direction and order of the FAPA-MS line scans (step size 0.5 mm) performed for mass spectral imaging. (b) EIC of the protonated molecular ion of caffeine. For better visualization purposes only the EIC of m/z 195.0879 \pm 8 ppm for the third analyte spot in (a) is shown. The ROI for data evaluation is illustrated by a large blue square. The small yellow rectangles represent the individual voxels, which are summed up and contribute to the overall abundance of the analyte.

Comparison of Different Post-Separation Drying Conditions for HPTLC-FAPA-MS. The mobile phase in TLC is typically a combination of organic solvents, deionized/distilled water, and small amounts of additives (*e.g.*, acids or bases) and is carefully selected based on the polarity of the solid phase/analytes. After carrying out the separation, the TLC plate is typically conditioned (*e.g.*, solvent evaporation, staining, derivatization) before further diagnostic tools are used for analyte spot detection and identification. These conditioning steps can also have an influence on the subsequent ADI-MS analysis. Because TLC staining and derivatization methods are more likely to be useful for the optical detection of analyte spots the two methods are not addressed in this chapter. However, residues of the

mobile phase on the TLC plate might have an influence on the desorption and ionization properties of the ADI-MS technique.

In the past, Song *et al.* proposed the theory of transient microenvironments (TMEs) for DART-MS,¹²² in which it was reported that the sample matrix (*e.g.*, solvents) may surround the analyte molecules during the sample desorption process and therefore shield the analyte molecules from direct exposure to the plasma. The TMEs are formed by the desorption of the analyte containing matrix. Subsequently, the matrix molecules are ionized by the plasma in an intermediate step followed by gas-phase ion/molecule reactions in which the analyte is ionized by the matrix. Similarly, in this chapter the influence of post-separation conditioning and the degree of remaining solvent on the TLC plate on the mass spectral response was investigated to address the question, whether or not a beneficial effect in TLC-FAPA-MS could be observed. Here, a caffeine test-mixture was separated on NP-HPTLC and CN-HPTLC plates (*cf.* Figure 6.3).

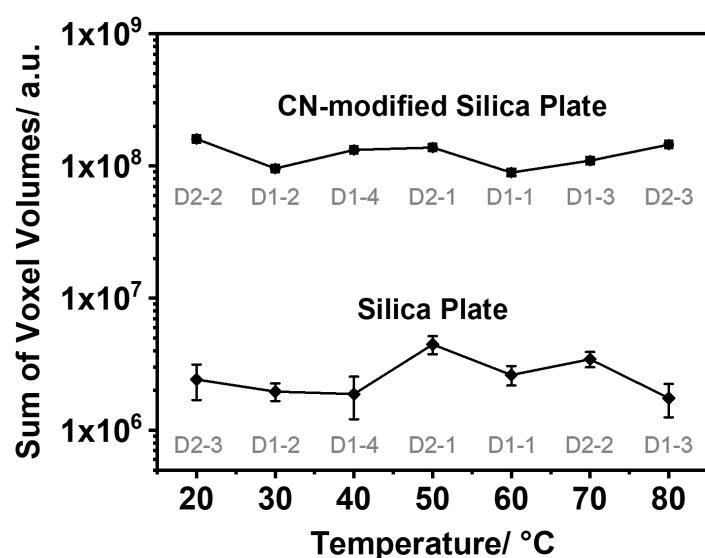


Figure 6.3 Sum of voxel volumes for the protonated molecular ion of caffeine (m/z 195.0879 \pm 8 ppm, $n=3$) relative to the post-separation drying temperature of the HPTLC plate. The error bars originate from the standard deviation of three replicate measurements performed for each data point. The experiments per plate were performed on different days in a random order to avoid, *e.g.*, drift effects. The measurement order can be identified as follows: the label “D2-3” corresponds to the second measurement day and the third measurement on said day.

Afterwards, the HPTLC plate was dried for 15 minutes at various temperatures (20–80 °C, in 10 °C steps) before it was probed by the FAPA source.

The signal abundance of the caffeine spots was determined semi-quantitatively by mass spectral imaging of the complete HPTLC plate. The experiment was also performed with RP-HPTLC, NH₂-HPTLC, and DIOL-HPTLC plates (*cf.* Figure 11.18c-e). To avoid a drift in the measurement results the experiments with different stationary phases and different drying temperatures were performed on different days in a random order.

Figure 6.3 illustrates the influence of the HPTLC drying temperature on the signal abundance of the protonated molecular ion of caffeine. Even though the caffeine signal abundances vary between $1.7 \cdot 10^6$ a.u. and $4.4 \cdot 10^6$ a.u. (NP-HPTLC silica plate, coefficient of variation: $\sim 37\%$) for the different HPTLC drying temperatures, no significant signal trend can be observed. Similar observations can be made for the experiments with other stationary phases presented in Figure 11.18a-e. The coefficients of variation for each data point in the scatter diagrams (*cf.* Figure 11.18a-e) are summarized in Table 6.1 in respect to the stationary phase type.

Table 6.1 Coefficient of variation for the HPTLC-FAPA-MS analysis of caffeine deposited on different stationary phases (conditioned at different drying temperatures).

Type of stationary phase	Coefficient of variation range
Silica plate (NP)	13-35%
Reversed-phase-modified silica plate (RP)	13-20%
Cyano-modified silica plate (CN)	5-15%
Amino-modified silica plate (NH ₂)	2-13%
Diol-modified silica plate (DIOL)	3-26%

For the theory of TME to be applicable for this type of experiment one would expect drastically increased signals towards lower drying temperatures – more solvent residues on the HPTLC plate – compared to measurements with higher drying temperatures. Based on these findings, it is suggested that the HPTLC-FAPA-MS response is not significantly influenced by a post-separation drying step (up to 80 °C). Clearly, the sampling geometry compared to the original publication on TME is different as well (stainless steel mesh of an OpenSpot card versus TLC plate) and further studies should be performed to investigate TME in plasma-based ADI-MS.

For the experiments discussed below, a drying temperature of 50 °C was selected because this temperature was found to result in slightly elevated ion abundances (*cf.* Figure 6.3).

Influence of Stationary Phase Chemistry on Analyte Ion Abundance in HPTLC-FAPA-MS. Similar to HPLC, different types of stationary phases (*e.g.*, RP-modified silica plates, CN-modified silica plates, NH₂-modified silica plates, and DIOL-modified silica plates) of silica-based HPTLC plates are commercially available to match the stationary phase to the analyzed sample and to enhance the separation. By changing said material, the polarity and possible chemical interactions between the analyte molecule and the stationary phase are changed, which might also have an impact on the desorption parameters for ADI-MS techniques. Therefore, the sensitivity of HPTLC-FAPA-MS is tested with selected analytes and different HPTLC stationary phases (*cf.* Figure 6.4).

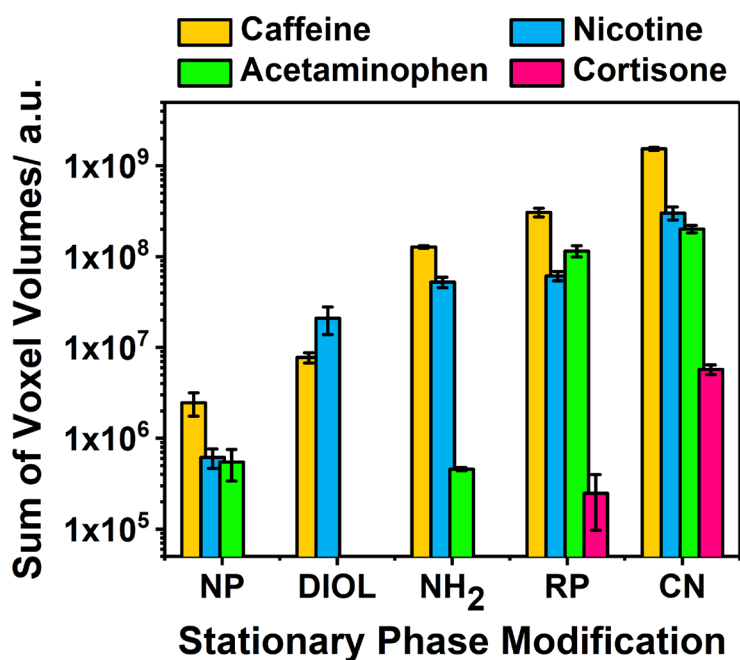


Figure 6.4 Sum of voxel volumes for selected analytes relative to different commercially available stationary phases. The error bars in the column diagram correspond to the standard deviation of $n=3$ measurements for each data point. Before FAPA-MS analysis the TLC plates were dried on a hot plate at 50 °C for 15 minutes. The analyte spots were visualized by extraction of a selected EIC for caffeine (orange, m/z 195.0879 \pm 8 ppm, [M+H]⁺), nicotine (blue, m/z 163.1229 \pm 8 ppm, [M+H]⁺), acetaminophen (green, m/z 152.0705 \pm 8 ppm, [M+H]⁺), and cortisone (pink, m/z 301.2020 \pm 8 ppm, [M-C₂H₄O₂+H]⁺). For analyte spot integration all voxel volumes of the analyte spot were summarized.

Figure 6.4 depicts the influence of the TLC stationary phase material on the signal response of caffeine (m/z 195.0879 \pm 8 ppm, $[M+H]^+$), nicotine (m/z 163.1229 \pm 8 ppm, $[M+H]^+$), and acetaminophen (m/z 152.0705 \pm 8 ppm, $[M+H]^+$), in addition to a fragment ion of cortisone (m/z 301.2020 \pm 8 ppm, $[M-C_2H_4O_2+H]^+$). The column diagram shows a trend of steadily increasing signal abundances for all analytes for the stationary phase in the order of NP, DIOL, NH₂, RP, and CN. In this context, it is observed – especially for caffeine – that the standard deviations of the replicate measurements for the individual stationary phases are comparatively low (<25%) and the detected signal abundances are significantly different from each other (confirmed by a 99% confidence interval). To avoid a bias by the measurement order of the stationary phases, the experiments were repeated in a random order during the course of two days. A solvent mixture of isopropyl alcohol, n-heptane, and water (7:3:1 (v/v/v)) was used as the mobile phase for all different stationary phases to ensure that the remaining solvent residues on the analyzed TLC plates were same for each measurement. This, however, degraded the separation power in some cases and somewhat broad analyte spots were observed on the TLC plates. For example, very blurred analyte spots of acetaminophen with poor separation were observed on the DIOL stationary phase. This observation was caused by low interactions of the analyte with the stationary phase in combination with the used mobile phase and therefore distinct analyte diffusion might have caused the blurred acetaminophen spots on the DIOL plate. Consequently, the sum of voxel volumes could not be determined in this case and no signal for acetaminophen related to the DIOL stationary phase is presented in Figure 6.4. The presented results do not provide more detailed knowledge of the desorption process initiated by the FAPA source itself, but are highlighting the influence of the HPTLC stationary phase on the analyte desorption process for this plasma-based ADI source. In this regard, polar interactions of the analyte, *e.g.*, hydrogen bonding or dipole interactions, with the polar silica stationary phase cause a stronger retardation, which leads to lower retardation factors (R_f) during the sample separation. These strong interactions are assumed to result in a less efficient analyte desorption from the NP-HPTLC surface, and in a reduced signal abundance when compared to *e.g.* results with RP- or CN-HPTLC. The slightly less polar DIOL- and NH₂-stationary phases can be used in a normal-phase separation system and in a reversed-phase system, depending on the used solvent (less polar solvent (mixture) for NP system and more polar solvent (mixture) for RP system). This flexible separation mechanism is established by the polar modification of the stationary phase and the non-polar propyl group, which is

used to bind the DIOL- and NH₂-group to the silica. It is assumed that the lower polarity of the functional group and also the influence of the non-polar propyl group are the reason why better signal abundances for caffeine (3- and 50-fold compared to NP plates, respectively) and nicotine (30- and 80-fold compared to NP plates, respectively) are obtained. In contrast to the aforementioned analytes a neglectable change in the signal abundance of acetaminophen is observed when changing the stationary phase from NP to NH₂ silica plates (sum of voxel volumes for both $\sim 5 \cdot 10^5$ a.u.). This observation goes along with increasing R_f values (*cf.* Table 11.10) for caffeine and nicotine while the R_f value for acetaminophen slightly decreases. Increasing or decreasing R_f values indicate stronger or weaker interactions between the analyte and the stationary phase, respectively, when a mobile phase with an identical polarity is used. Consequently, acetaminophen forms stronger interactions with the NH₂ silica plate compared to the other two analytes (*e.g.*, by hydrogen bonds) and, therefore, analyte desorption via FAPA-MS is not as efficient. For CN- and RP-modified silica plates, the two least polar stationary phases, a further increased signal abundance was observed for caffeine, nicotine, and acetaminophen (*e.g.*, ~ 2 orders of magnitude signal increase for caffeine and nicotine compared to NP plates). Additionally, a fragment-ion of cortisone (m/z 301.2020, $[M-C_2H_4O_2+H]^+$) could be detected from these stationary phases. Due to the missing polar groups on the RP stationary phase only weaker interactions (*e.g.*, Van-der-Waals interactions) compared to polar interactions with NP or DIOL plates can be established with the analytes. Hence, polar analytes are more easily desorbed from RP silica plates. However, the highest detected signal abundances for all analytes were obtained with the moderately polar CN-HPTLC stationary phase. Because the mobile phase polarity was kept the same for all stationary phases the increased R_f values of, *e.g.*, caffeine (*cf.* Table 11.10) can be seen as an indication for relatively less solute and stationary phase interaction. Additionally, CN functional groups are good hydrogen-bond acceptors due to their electron lone pair at the terminal nitrogen atom. Because the analytes caffeine, nicotine,¹⁷⁵ acetaminophen, and cortisone are good hydrogen-bond acceptors as well, weaker chemical interactions are expected between the solutes and the CN stationary phase in comparison to analyte interactions with, *e.g.*, NP silica plates or DIOL silica plates. Hence, it is assumed that higher analyte signal abundances are obtained for CN plates due to easier analyte desorption. Another observation made during the comparison of the stationary phase modifications was a trend of the relative standard deviation from high to low RSDs. Specifically, for each of the four analytes comparatively high RSDs of 25-40% were observed for the stationary phases with

low ion abundances (*e.g.*, NP plates), while RSDs below 15% were detected especially for the RP- and CN-modified stationary phases with high ion abundances.

The aforementioned results suggest a direct correlation between the used stationary phase and the signal abundance of the analyzed compounds. In the future, these findings have to be considered for the development of quantitative TLC-ADI-MS methods. This holds especially true in case the analyte concentration is close to the limit of quantification. Furthermore, the poor separation of acetaminophen on the DIOL stationary phase demonstrates that not only the stationary phase modification has an impact on the quantification limit but also the shape of the analyte spot. In this regard, very blurred spots cannot be integrated for quantification due to overlapping analyte bands and broad spots distribute the analyte over a larger surface area. This ultimately decreases the maximum detectable ion abundance for the respective analyte spot and consequently impairs the limit of detection and quantification. Therefore, it is recommended for the future applications of TLC-FAPA-MS to carefully optimize the separation conditions for narrow and sharp analyte spots and to evaluate the benefit of an enhanced analyte desorption for different stationary phase modifications.

Influence of the TLC Grade on TLC-FAPA-MS Response. During the last decades, the physical properties of the TLC stationary materials have been optimized to enhance the separation performance of this chromatography technique. For this purpose, the size and shape of the silica particles (HPTLC and LiChrospher), as well as the purity of the used material (MS Grade and Premium Purity) have been optimized. Because the different properties of these stationary materials might have an influence on the analyte desorption process for FAPA-MS, the stationary phases are directly compared for the first time in this chapter (*cf.* Figure 6.5).

In Figure 6.5, the comparison of regular silica-based plates, the highest signal abundances for caffeine and nicotine can be observed with the coarse-grained TLC plates. In comparison to the TLC plates, a signal loss for caffeine between 50-85% is observed for the other types of stationary phases. For nicotine a signal loss of 80% for HPTLC and LiChrospher as well as a loss of 96% for Premium Purity was observed. Interestingly, no signal is detected for nicotine when analyzing the sample mixture on a MS Grade plate. Acetaminophen was detected with TLC, HPTLC, and LiChrospher stationary phases at similar signal abundances (~30% relative variation), while for the MS Grade and Premium Purity plates the analyte signal decreased by 70-90%. By reviewing the characteristics of TLC, HPTLC, LiChrospher, MS Grade, and Premium Purity silica materials a critical factor for the above presented results

was identified. The silica particle size and size distribution of TLC plates (size: 10-12 μm , distribution: 5-20 μm) differs significantly from HPTLC (size: 5-6 μm , distribution: 4-8 μm) and LiChrospher (size: 7 μm , distribution: 6-8 μm) plates.¹⁵⁰ Hence, an explanation for the higher signal abundances in case of the TLC plates could be that the analytes are more easily released into the gas phase from the more porous TLC material. Additionally, the total surface area of smaller particles (*e.g.*, HPTLC) packed into a fixed volume is much larger in comparison to larger particles (TLC) packed into the same volume. Consequently, less analyte interaction points are available on TLC plates, which might also enhance the analyte desorption in comparison to HPTLC, LiChrospher, MS Grade, and Premium Purity silica plates.

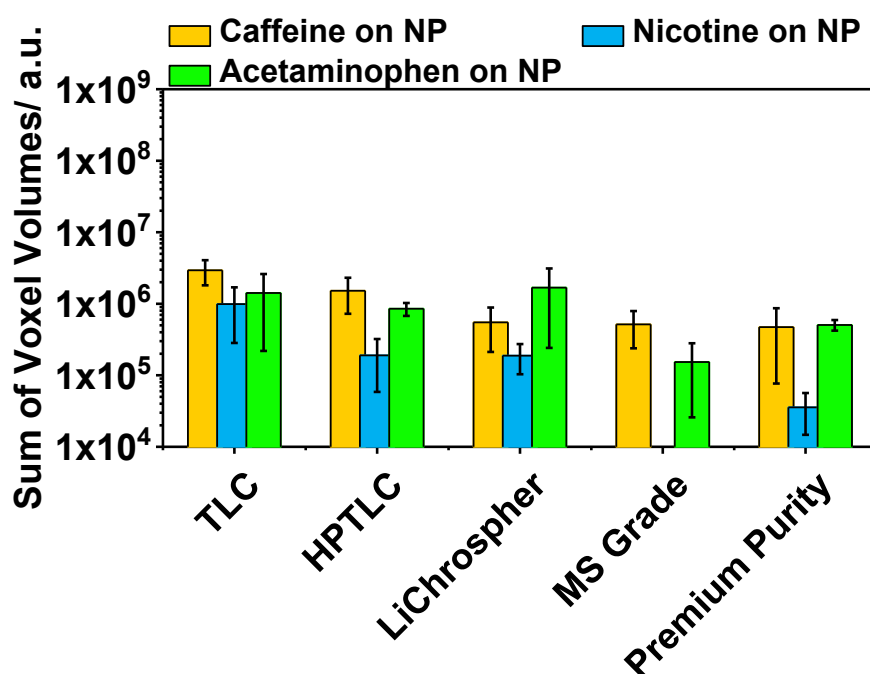


Figure 6.5 Signal abundance of caffeine (orange, m/z 195.0879 \pm 8 ppm, $[\text{M}+\text{H}]^+$), nicotine (blue, m/z 163.1229 \pm 8 ppm, $[\text{M}+\text{H}]^+$), and acetaminophen (green, m/z 152.0705 \pm 8 ppm, $[\text{M}+\text{H}]^+$) for the direct desorption/ionization by FAPA-MS from different silica plates. The error bars originate from the standard deviation of $n=3$ measurements for the respective analyte and type of stationary phase.

Influence of Stationary Phase Thickness and Particle Size on TLC-FAPA-MS Response. Despite the regular analytical TLC plates with typical stationary phase layer thicknesses of 100 μm (HPTLC), 200 μm (HPTLC) and 250 μm (TLC), also silica plates for preparative purposes with a layer thicknesses of 500 μm to 2000 μm are commercially available. These PLC plates can be loaded with a larger

sample amount for subsequent analyte isolation. In 2014 Griesinger *et al.* found that HPTLC plates with a decreased stationary phase thickness of 100 μm can enhance the analyte ion abundance of phosphatidylcholines and phosphatidylethanolamines when analyzed via MALDI-MS.¹⁷⁶ Consequently, the question arises whether or not the stationary phase thickness has an influence on the analyte desorption process of plasma-based ADI-sources. Therefore, TLC plates with different stationary phase thicknesses were probed with FAPA-MS and the results for caffeine are presented in Figure 6.6.

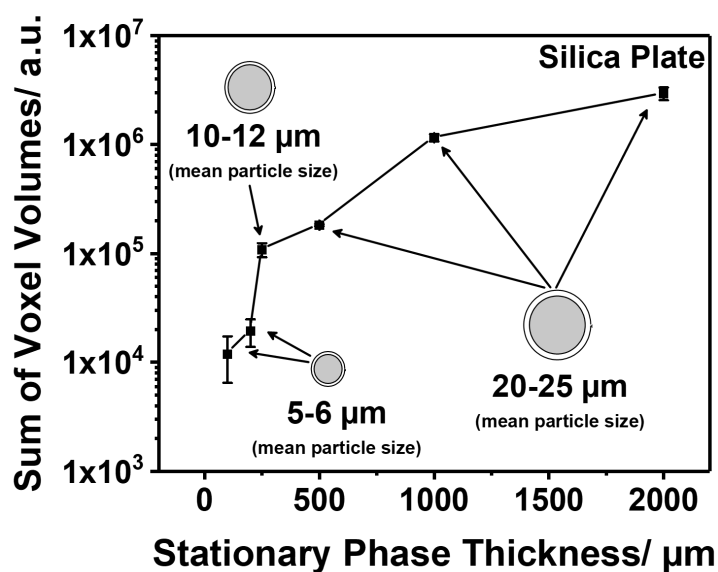


Figure 6.6 Sum of voxel volumes for caffeine (m/z 195.0879 \pm 8 ppm, $[\text{M}+\text{H}]^+$, $n=3$, error bars represent the standard deviation of replicate measurements) determined via TLC-FAPA-MS with TLC plates inhabiting different thicknesses of the stationary phase (100–2000 μm).

A steady signal increase for caffeine is observed with increasing thickness of the stationary phase (despite the fact that the same amount of sample volume and concentration was applied to all TLC plates). The same observations can be made for nicotine and acetaminophen. With increasing stationary phase thickness from 100 μm to 200 μm (both HPTLC silica plates) the detected signal abundance doubled from $1 \cdot 10^4$ a.u. to $2 \cdot 10^4$ a.u. Unfortunately, rather high RSDs of 45% and 30% were observed for these ion abundances of the 100 μm and 200 μm thick silica plates, respectively, and both standard deviation ranges overlap. For the 250 μm plate ($1 \cdot 10^5$ a.u., RSD: 14%, TLC silica plate) a significant signal increase by approximately one order of magnitude was observed in comparison to the 100 μm plate ($1 \cdot 10^4$ a.u.,

RSD: 45%). These findings can be partially explained with observations made in the previous section. Due to the larger and more coarse particle size of the TLC grade material, which was used for the 250 μm thick plates, the packing of the stationary phase particles is not as dense as for the HPTLC material (100 μm and 200 μm), which might ease the sample desorption. A further increase of the stationary phase thickness from 250 μm to 500 μm , 1000 μm , and 2000 μm causes a steady enhancement of the caffeine ion abundance from $2 \cdot 10^5$ a.u. to $3 \cdot 10^6$ a.u. (*cf.* Figure 6.6) and also steadily decreasing RSDs of $<14\%$ were observed for these thicker stationary phases. These findings can be explained with the same explanation given above, in which the increasing particle size and size distribution of the stationary phase was suggested to be the cause of the enhanced analyte signal. Compared to HPTLC and TLC, larger mean particle sizes (20-25 μm) as well as larger particle size distributions (5-40 μm) are used for PLC plates.^{150,151} Due to the larger particles the capillary channels between the particles become larger and consequently desorbed/evaporated analytes can leave the labyrinth of silica channels more easily.

Caffeine Quantification in Energy Drinks via TLC-FAPA-MS. In addition to the comparison of different TLC stationary phases TLC-FAPA-MS was also applied to quantify the content of caffeine in energy drinks. Because energy drinks contain many other ingredients such as sucrose, sodium citrate, taurine, vitamins, and food colors, in addition to caffeine, the quantification via FAPA-MS can be complicated due to matrix interferences. TLC can serve as a fast and cheap method to separate the beverage matrix from the caffeine analyte to avoid these interferences.

For the quantification of caffeine ($M=194.2$ g/mol) in energy drinks of three different brands (A, B, and C) via HPTLC-FAPA-MS the degassed energy drink samples were spiked with a caffeine- $^{13}\text{C}_3$ reference standard ($M=197.2$ g/mol). After homogenization of the mixtures the samples were deposited on the NP-HPTLC silica plate, analytes were separated, and solvent residues were evaporated prior FAPA-MS analysis. Subsequent mass spectral imaging was performed via line scans. Data extraction of the $[\text{M}+\text{H}]^+$ signals for caffeine (m/z 195.0879 \pm 8 ppm) and caffeine- $^{13}\text{C}_3$ (m/z 198.0981 \pm 8 ppm) result in the mass spectral images shown in Figure 6.7.

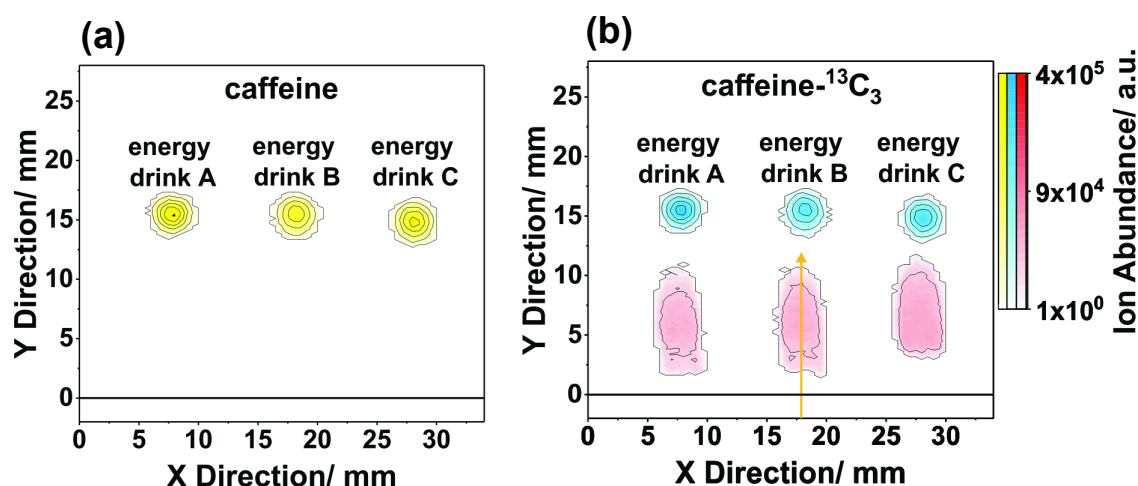


Figure 6.7 Mass spectral image using FAPA-MS of (a) m/z 195.0879 \pm 8 ppm (caffeine) and (b) m/z 198.0981 \pm 8 ppm (caffeine-¹³C₃) of the energy drink from brand A, B, and C on a NP-HPTLC silica plate after separation of the spiked energy drink liquids (after separation the solvent was evaporated at 50 °C for 15 min prior to mass spectral imaging). The orange arrow indicates the scan direction of a line scan performed in an additional experiment to investigate the cause of the two analyte spots originating from the m/z 198.0981 (*cf.* Figure 11.19). The black lines represent the starting line of the separation (lower line) and the solvent front at the end of the separation (upper line).

In Figure 6.7a, the mass spectral image of the caffeine analyte in the energy drinks of manufacturer A, B, and C is shown. In Figure 6.7b, the mass trace of the caffeine-¹³C₃ standard is presented. In the latter, for each of the spiked energy drink mixtures two spots are visible suggesting that the caffeine-¹³C₃ standard is split into two separate spots. However, further investigations of the high-resolution mass spectra revealed that the more retained spot is caused by a matrix substance, which causes an isobaric interference (caffeine-¹³C₃ standard: m/z 198.0981, matrix substance: m/z 198.0987). To elucidate the origin of the two bands at m/z 198, the mass spectra acquired along the orange arrow in Figure 6.7b were searched for interfering peaks. As a result, m/z 180.0881 was identified as the interfering species with a sum formula of C₇H₁₀ON₅ (mass accuracy 0.6 ppm). With the addition of a water molecule (18.0106 u) an ion at m/z 198.0987 (C₇H₁₂O₂N₅, mass accuracy 0.8 ppm) is formed which has a mass shift of 3 ppm (0.6 milli mass units) compared to the [M+H]⁺-ion of the caffeine-¹³C₃ standard. To visualize the correlation between the EICs of m/z 180.0881 and m/z 198.0981 the extracted ion-chronograms are depicted in Figure 11.19. In this figure, the EIC of the m/z 180.0881 and the caffeine-¹³C₃ standard rise and decrease at the same locations of the line scan (between 5 and 15 mm) on the TLC plate. Consequently, the detected interference spot can be

neglected for the quantification of caffeine in energy drinks. Due to careful optimization of the HPTLC separation conditions the interference and the caffeine- $^{13}\text{C}_3$ standard can be adequately separated from each other. Hence, this matrix effect can be neglected for further calculations. A complete separation of the caffeine- $^{13}\text{C}_3$ standard and the interfering substance was not possible with the CN-HPTLC silica plate and the tested solvent mixtures (data not shown).

By integrating the sum of voxel volumes in Figure 6.7 ($n=3$) the caffeine concentration for each brand was determined to be 0.32 mg/mL, 0.31 mg/mL, and 0.31 mg/mL for the energy drink A, B, and C, respectively. All determined concentrations have a standard deviation of ± 0.01 mg/mL. Detailed calculations can be found in the appendix (chapter 11.9). In comparison to the manufacturer values these findings are in very good agreement with the values stated by the manufacturers (0.32 mg/mL stated by all three manufacturers on the product label). Additionally, the IDL for caffeine on NP-HPTLC silica plates was determined to be 8 ng/band (5 μL /band applied) with a linear range for the analyte starting at the IDL up to a concentration of 250 ng/band (5 μL /band applied). In respect to the manufacturers' information (0.32 mg/mL), the found caffeine analyte concentration measured by HPTLC-FAPA-MS is $\sim 2\%$ lower, which is within the margin of error for this method (standard deviation of measurements: 0.01 mg/mL). For this experiment the IDL of NP-HPTLC-FAPA-MS is approximately one order of magnitude better in comparison to NP-HPTLC/UV detection (45 ng/band with 10 μL /band applied)¹⁷⁷ and in a similar ng/band range as NP-HPTLC-DESI-MS (39.4 ng/band with 0.25 μL /band applied).¹⁶⁷

To validate the results obtained by TLC-FAPA-MS the caffeine content in the energy drink was also quantified by HPLC/UV analysis. The detailed sample preparation method and the results of the HPLC/UV analysis can be found in the appendix (chapter 11.9). Here, a caffeine concentration of 0.31 mg/mL ± 0.01 mg/mL was found for all three brands, which confirms a caffeine concentration of 0.32 mg/mL, stated by the manufacturers on the sample container, and validates the HPTLC-FAPA-MS method. Further, the recovery of the extraction method used for the HPLC/UV method was tested with a caffeine standard (~ 0.30 mg/mL). It was found that the used sample preparation method has a recovery of 107%. The 7% higher concentration of caffeine might have been caused a contamination during the manual analyte extraction procedure.

6.4 Conclusion

In this chapter, a method for quantitative analysis of small molecules on TLC plates based on FAPA-MS was carefully evaluated and optimized for best performance. Different TLC stationary phases were evaluated for best mass spectrometric signal response. The results are interesting because a TLC separation before direct MS analysis can help to remove unwanted matrix compounds and reduce potential measurements artifacts due to competitive ionization and matrix effects in ambient desorption/ionization. As a proof-of-principle, quantitation of caffeine in energy drinks is demonstrated using HPTLC-FAPA-MS and isotope dilution. For caffeine an instrumental detection limit (IDL) in the low nanogram-per-band range was obtained via RP-HPTLC-FAPA-MS (0.6 ng/band (5 μ L/band applied)).

A large variety of different commercially available stationary phase polarities (NP-, RP-, CN-, NH₂-, DIOL-plates) as well as stationary phase layer thicknesses and particle sizes (TLC, HPTLC, MS Grade, LiChrospher, Premium Purity) were probed with FAPA-MS. The comparison of the stationary phase modification with polar and non-polar functional groups revealed that semi-polar stationary phases (CN-, RP-plates) caused significantly higher signal abundances (approximately two orders of magnitude) for the analyzed compounds in comparison to the polar NP stationary phase. Additionally, larger silica particles (*e.g.*, TLC plates) resulted in 50-85% higher signal abundances for caffeine and nicotine in comparison to high-performance stationary phases (*e.g.*, HPTLC, MS Grade) with smaller particles and particle size distributions. The influence of the TLC layer thickness (100 μ m to 2000 μ m) was tested via TLC-FAPA-MS and better signal abundances were observed for thicker stationary phases (200 μ m: $2 \cdot 10^4$ a.u., 2000 μ m: $3 \cdot 10^6$ a.u.). Lastly, NP-HPTLC-FAPA-MS was successfully applied for the first time to quantify caffeine at a concentration level of 0.32 mg/mL in energy drinks via stable isotope dilution analysis. The new method was validated by measurements with HPLC separation and UV light absorption detection (HPLC/UV).

In the future, the precise measurement of the interaction strength between the analyte and the different stationary phases should be addressed and compared to the results obtained by HPTLC-FAPA-MS. This will give a better understanding of the desorption process. Additionally, it is recommended to optimize the experimental conditions for the comparison of different TLC layer-thicknesses. Identical mean

particle sizes and particle size distributions will give a more realistic view on the impact of the layer thickness towards the ADI desorption process. In this work, the (HP)TLC plates have not been pre-washed with pure solvents. This could also be performed in future studies to decrease overall background signals. Moreover, reducing the presence of background substances may also decrease the problem of competitive molecule ionization observed for other plasma-based ADI sources,¹²³ eventually leading to further improvements in IDL.

Chapter 7

High-Performance Thin-Layer Chromatography Flowing Atmospheric-Pressure Afterglow Mass Spectrometry for Fast Antimalarial Agent Screening in Drug Tablets

7.1 Introduction

The malaria disease is the most dominant infectious disease in the world and in 2017 approximately 219 Mio. people were infected.¹⁷⁸ The most affected region worldwide is the Sub-Sahara region in Africa with 92% of the malaria cases (~200 Mio.), while in South-East Asia 5% and in the eastern mediterranean region 2% of the malaria cases are reported by the world health organization (WHO).¹⁷⁸ The infection is caused by Plasmodium parasites and is transferred by mosquitos into the human blood steam where the parasite multiplies and infects red blood cells. In 2017 this infection caused approximately 435,000 deaths, mostly children under 5 years of age. Despite the introduction of the new vaccination program of the WHO with the vaccination agent RTS,S/AS01 in the beginning of 2019,¹⁷⁹ the most effective treatment of the malaria disease is currently the artemisinin-based combination therapy (ACT). These preparations consist of the artemisinin active agent (and its derivates, *e.g.*, artesunate, artemether) combined with a second antimalaria drug (*e.g.*, lumefantrine, amodiaquine, atovaquone, proguanil).¹⁸⁰ Consequently, ACTs are nowadays the “first-line treatment policy” and due to its effectiveness, the WHO pursues “universal access” to ACTs in all regions of the world by 2030 to eradicate the malaria disease.¹⁸¹ Depending on the disease severeness the medications are applied in different ways. An uncomplicated malaria caused by the Plasmodium falciparum parasite is usually treated by oral application of ACT tablets for three days, while more severe malaria is treated with injectable artesunate (an artemisinin derivate) followed by a 3-day ACT application.¹⁸¹

Due to the importance of these ACT medications for the malaria treatment, especially oral applied tablets are suspect of falsification which may cause severe consequences.¹⁸² Falsified (counterfeit) antimalarial drugs may be without any active agent, or may comprise a lower amount of the drug per dose. In case of no active agent in the medication tablet obviously no treatment and cure of the sickness is observed, which has severe consequences for the individual patient. However, lower amounts of the active agents might have even worse consequences due to the fact that lower active agent concentrations are not sufficient to fight the parasite and therefore the parasite can develop resistances for artemisinin-based medications over time.¹⁸³ In this regard, rapid screening tools for falsified (the term ‘counterfeit’ medication implies intellectual property issues and therefore the term ‘falsified’ is

used) medications are very important to further decrease the number of malaria infections and deaths to meet the WHO goals to eradicate the malaria disease by 2030.

Analytical tools for the analysis of antimalaria active agents which can be used in the field comprise colorimetric testing,¹⁸³⁻¹⁸⁵ IR spectroscopy,¹⁸⁶ Raman spectroscopy,¹⁸⁷ and TLC.¹⁸⁸⁻¹⁹⁰ With these non-destructive spectroscopy techniques the sample can be scanned very quickly, while the instruments are easy operate and have rather low operating/instrumentation costs (in comparison to more advanced analytical techniques *e.g.*, chromatography or mass spectrometry). However, the main disadvantage of spectroscopy techniques are the rather complex absorption spectra due to broad absorption bands (NIR) or fluorescent interfering compounds (Raman).¹⁸³ Colorimetric testing and TLC have the advantage of very low consumables costs and operating costs as well as the quickly obtained information about the active agents in the drug preparation. For this reason, both analysis techniques are used in field-kits (*e.g.*, GPHF-Minilab[®] of the Global Pharma Health Fund (GPHF)) and can be applied in not developed areas of the world for active agent screening. Unfortunately, these relatively low-cost techniques have limitations. In this regard, TLC requires expensive, synthesized standards to compare R_f values of the sample spot and the pure standard spot to identify the analyte. Further, colorimetric testing is sometimes limited by interfering active agent colors and drug indicator colors. Also, an experienced TLC operator is required to obtain comparable R_f values for the sample and standard, and co-eluting species cannot be considered/identified with this type of analysis. More advanced analysis techniques performed in the laboratory are GC,¹⁹¹ capillary electrophoresis (CE),¹⁹¹ HPLC/UV,¹⁹¹ fluorescence,¹⁹² or electrochemical detection^{193,194} as well as HPLC-MS¹⁹⁵⁻¹⁹⁷ and ADI-MS¹⁹⁸⁻²⁰⁰ and can be applied for antimalarial screening and identification of the drug ingredients. GC and HPLC instruments are widely available in laboratories around the world and are powerful tools for the identification and quantification of pharmaceuticals. In combination with mass spectrometry the performance and sensitivity of the methods is further enhanced and the mass spectrometer enables structural elucidation of the analyzed molecules.^{201,202} However, these techniques require appreciable amounts of solvents for the sample preparation/analysis and to avoid contamination of the chromatography system sample preparation can be time extensive. Mass spectrometry on its own became a versatile tool for direct sample and surface analysis when DESI-MS was introduced in 2004.⁶ This spray-based ADI source and the later on developed plasma-, and laser-based ADI sources were applied qualitatively and quantitatively in the past 15 years to a large variety of sample matrixes (*e.g.*, drugs, explosives, agricultural products, and

biological samples).^{1,36,38} For more complex sample types researchers developed finger printing techniques and automated data processing by principle component analysis, to identify *e.g.*, falsified (antimalarial) drugs.¹⁹⁹ In the regard of complex sample matrices, ADI sources have also been combined with chromatography to minimize matrix effects and competitive ionization, due to the sensitivity of the ADI sources towards these effects.^{160,163}

In this chapter, the FAPA source is combined with high-performance thin-layer chromatography (HPTLC) to couple chromatography with mass spectrometry. In doing so, the benefits of both analysis techniques can be used to ensure quick screening of antimalarials in the field. Also, in case of justified doubts of the medication purity further mass spectral analysis can be directly performed from the HPTLC plate. In previous studies the combination of plasma-based HPTLC-ADI-MS was already presented,^{143,198} but antimalarials could not be analyzed from these substrates without external heating.²⁰⁰ Certainly, the FAPA source plasma has a temperature of ~ 250 °C and is capable of desorbing such analytes. Because no external heating of the HPTLC plate is needed spatially resolved information is obtained for the analytes on the HPTLC and semiquantitative information of the analytes can be obtained by mass spectral imaging.

7.2 Experimental Section

Reagents. The solvents acetone (for analysis, 99%) and ammonium hydroxide (25%) were bought from Fisher Scientific GmbH. LC-MS grade water (HiPerSolv CHROMANORM) was purchased from VWR (Langenfeld, Deutschland). The antimalarial drug preparation Coartem[®] (Novartis, Basel, Switzerland) was bought in a local pharmacy store.

Standard and Sample Preparation. The Coartem[®] tablets were grinded in a mortar and approximately 30 mg of the powder were weighed in separate vials. The active agent was extracted with 2 mL of acetone and vortex homogenization for 30 seconds. After filtration with a 0.45 μm pore size syringe filter (Carl Roth GmbH & Co. KG, Karlsruhe, Germany), to remove the filling material of the tablets, the sample was diluted by the factor of 1:10 with acetone.

HPTLC Separation and Conditioning. For the analyte separation 2 μL of the drug sample solution was deposited on the HPTLC plate with a syringe. A solvent mixture of acetone, water, and ammonium hydroxide solution (25%) was prepared in a ratio of 80:20:1 (v/v/v) and used as the mobile phase for the HPTLC separation. After completion of the chromatography (approximately 5 minutes) the mobile phase remaining on the HPTLC plate was evaporated at 50 $^{\circ}\text{C}$ for 10 minutes on a temperature controlled hot plate.

Flowing Atmospheric-Pressure Afterglow. For HPTLC-MS coupling the identical FAPA source described in chapter 6 with a p2c-geometry, introduced by Shelley *et al.*,¹¹ was used. For the analysis of the antimalarial active agents the plasma inside home-built FAPA source was operated with a negative potential (730 V at 35 mA, fed through a 5 k Ω ballast resistor, operated in constant-current mode) applied to the stainless-steel pin-electrode (1.6 mm o.d.). The capillary anode (11 mm length, 1.3 mm i.d.) on the other side of the ceramic discharge chamber (Macor[®], Schröder Spezialglas GmbH) was grounded. Power generation was done by a Kepco BHK 1000-0.2MG DC power supply (Kepco Inc.). Helium (99.999%, Messer Industriegase GmbH) with a flow rate of 0.5 L/min served as plasma gas. The distance between the pin-electrode and the capillary electrode was 8 mm. The FAPA positioning for HPTLC analysis was identical to experiments performed in the previous chapter 6 in a 60 $^{\circ}$ angle towards the sample surface.

High-Resolution Mass Spectrometry. Mass spectral analysis was performed by a high-resolution mass spectrometer equipped with an Orbitrap mass analyzer (Exactive Thermo Fisher Scientific GmbH). On a daily basis, the mass spectrometer was calibrated with a mass calibration standard, containing caffeine (Sigma-Aldrich Inc.), MRFA (Met-Arg-Phe-Ala acetate salt, Sigma-Aldrich Inc.), and Ultramark 1621 (Sigma-Aldrich Inc.) before the experiments were started. To position the ADI source in front of the mass spectrometer the electrospray ionization housing was removed and the conventional inlet capillary was replaced by a 4-cm extended capillary on the front end. The inner diameter of the inlet capillary (0.6 mm) was the same as the original inlet capillary for ESI-MS. Information of the experimental parameters of the mass spectrometer are listed in the appendix (*cf.* chapter 11.1, Table 11.5).

Mass Spectral Imaging and Data Processing. The antimalarial standards and medication active agents were analyzed by mass spectral imaging of the molecular distribution on the (HP)TLC plates. Therefore, line scans across the TLC plates were performed with a motorized translational x-y-stage (Newport Corporation) with a translational speed of 0.3 mm/s and a line to line distance of 0.5 mm. The stage was controlled by a self-written LabVIEW (National Instruments) routine with a triggered line scan signal to start the data acquisition of the mass spectrometer. Also, the control of the Exactive mass spectrometer and data processing was performed in the same manner as described previously in chapter 6. The EICs of the analytes (*e.g.*, lumefantrine at m/z 528.1624 \pm 8 ppm) were extracted from the Exactive Tune 1.0 software (Thermo Fisher Scientific GmbH) and processed in Origin 2017 (OriginLab Corporation) to obtain contour plots of the analyte signals. Semiquantitative comparison of the analyte signal was done by analyte spot (bands) integration by integrating a region of interest around the analyte band. The general principle of this data processing method is explained in chapter 11.4.

7.3 Results and Discussion

For the screening of antimalarial active agents in tablet samples HPTLC-FAPA-MS is applied in this chapter to the analysis of Coartem[®] tablets. HPTLC is a useful tool for spatial separation of these organic components and is applied to avoid competitive ionization and matrix effects during the mass spectral analysis. The subsequent analysis of the different analyte bands on the HPTLC plate is done by mass spectral imaging with FAPA-MS. To separate artemether (Art) and lumefantrine (Lum) in the present chapter, a CN-modified HPTLC silica plate was selected in combination with a mobile phase of acetone, water, and ammonium hydroxide solution (25%) (80:20:1 (v/v/v)). The successful separation of the analytes is visualized by a mass spectral image of m/z 249.1490 \pm 8 ppm and of m/z 528.1624 \pm 8 ppm, presented in Figure 7.1. These extracted mass windows correspond to the mass peak of an artemether fragment-ion and the protonated molecular-ion of lumefantrine, respectively.

Before chromatography the analyte containing extract of the Coartem[®] tablet was deposited on the HPTLC starting line, illustrated by the horizontal orange line at Y=0 mm in Figure 7.1. The solvent front at the end of the separation was at Y=35 mm. Due to the non-polar character of the lumefantrine molecule this analyte has a low retardation factor of $R_f=0.05$ (blue spot with a center at Y \approx 2 mm).

Artemether, due to the five oxygen atoms included into the molecular structure and its more polar structure, reaches a drastically higher retardation factor of $R_f=0.79$ (green spot with a center at $Y \approx 27.5$ mm). Furthermore, a stretched spot with m/z 528.1624 is observed at approximately $R_f=0.4$. The identity of this spot is discussed later in this chapter when the analyte fragmentation is discussed and decomposition/synthesis byproducts of the active agents are presented.

Due to the complete separation of the two Coartem[®] main components, desorption/ionization interferences between the analytes are minimized and mass spectra of the individual compounds can be interpreted without elaborative mass spectrum deconvolution (*cf.* Figure 7.2). An attempt of automated mass spectral deconvolution was presented by Bernier *et al.* for the analysis of ACT tablet preparations by DART-MS with the aid of principle component analysis (PCA).¹⁹⁸

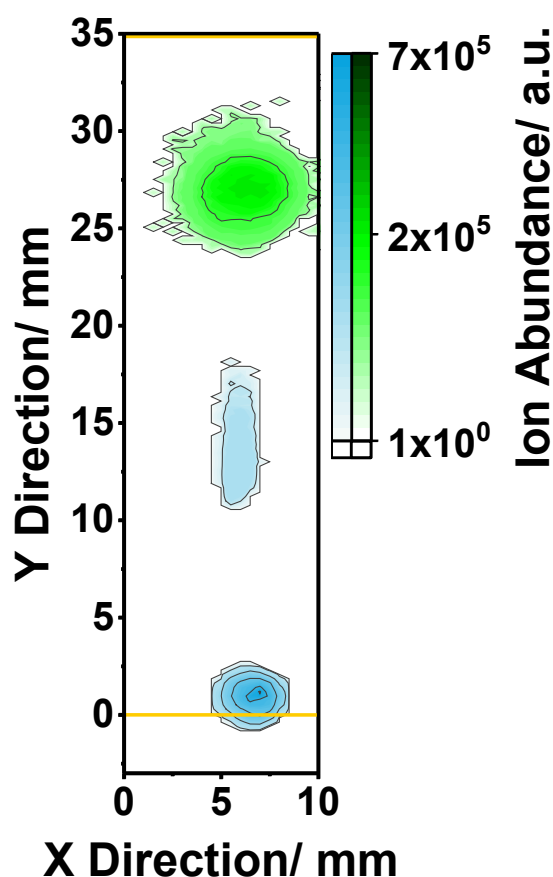


Figure 7.1 Mass spectral image of m/z 528.1624 ± 8 ppm (blue, Lumefantrine) and m/z 249.1490 ± 8 ppm (green, Artemether) extracted from a Coartem[®] tablet and separated on a CN-modified HPTLC silica plate prior FAPA-MS analysis (positive-ion detection mode).

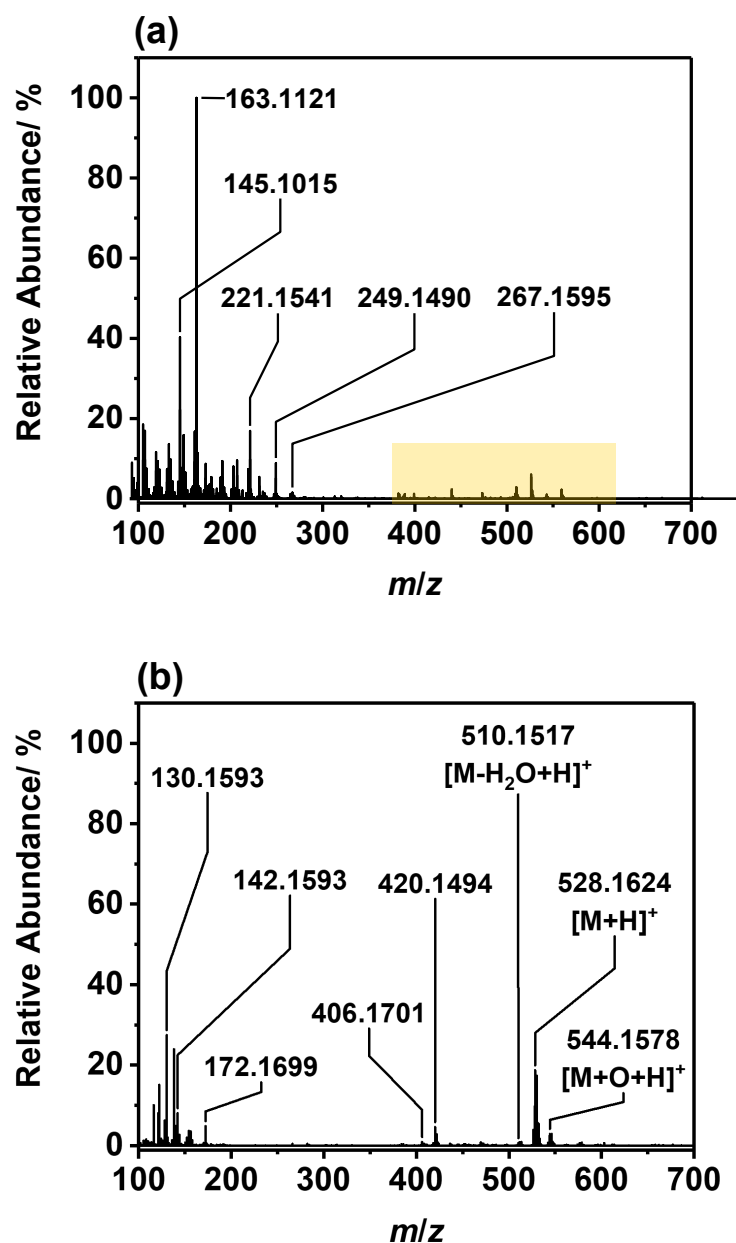


Figure 7.2 Mass spectra of artemether (a) and lumefantrine (b) detected by FAPA-MS in positive-ion detection mode. The analytes were separated on a CN-modified HPTLC plate and desorbed/ionized by the FAPA source prior HR-MS. The analyte peaks were identified with an RMA better than ± 3 ppm. For visualization purposes, the peak heights in both mass spectra are normalized to the most abundant ion in (a). The orange highlighted peaks do not originate from lumefantrine but from background signals.

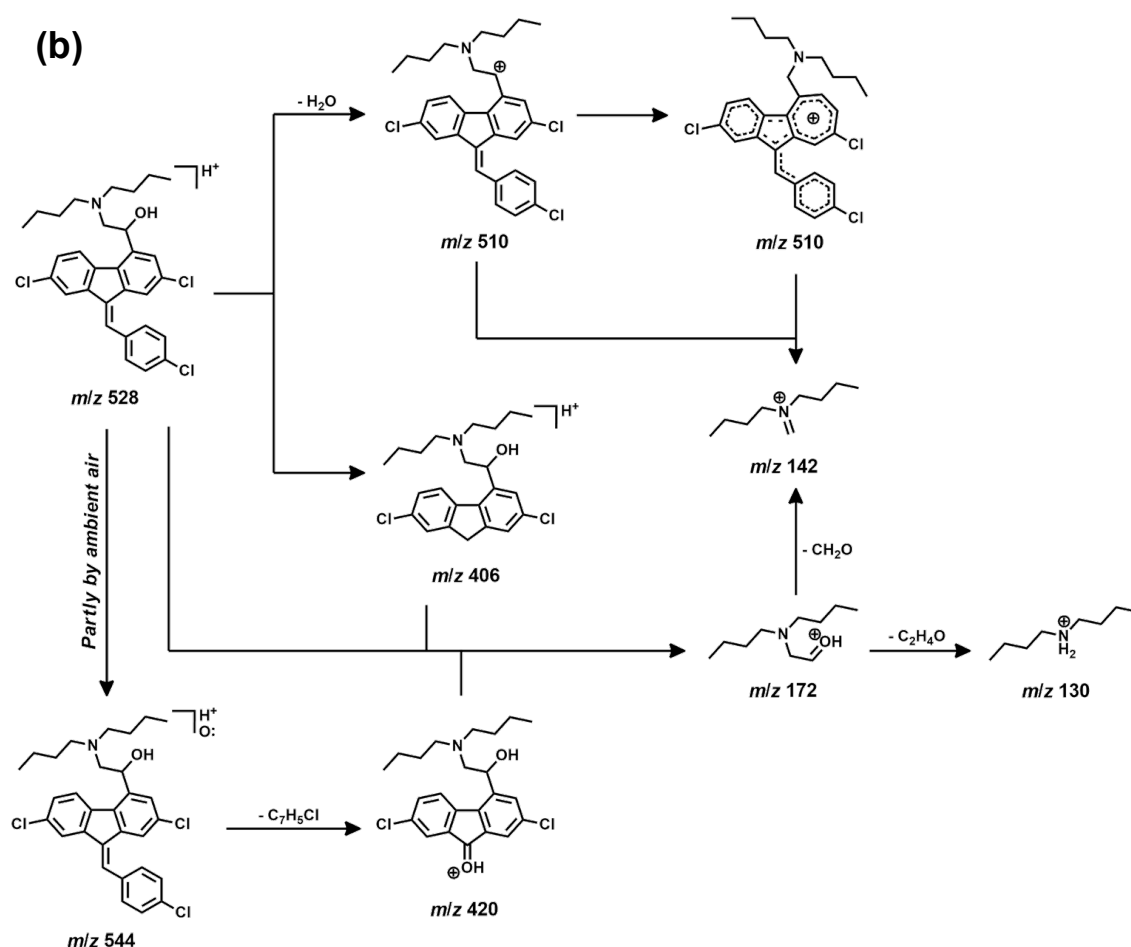


Figure 7.3 Continued.

The detection of the intact (protonated) artemether molecule at m/z 299 could not be achieved via FAPA-MS. However, eleven fragments of the artemether molecule could be identified by accurate mass detection (*cf.* Table 11.11 in the appendix) with an RMA better than 2.5 ppm. It is worth mentioning that in the literature artemether is described as a molecule very sensitive to fragmentation during the ionization process.^{202,204} Especially, when acidic protons are available in the solution or in the gas phase Art fragments even with soft ionization sources such as ESI.²⁰¹ Because one of the main ionization mechanisms of the FAPA source is based on protonation transfer to the analyte molecule by protonated water-clusters, fragmentation of artemether in the gas phase is difficult to be avoided with this plasma-based ADI source. In the literature different ESI fragmentation mechanisms were found for artemether. Santos *et al.* suggested a cleavage of the labile peroxide-ring in the artemether molecule aided by protons in combination by a ring-opening of the peroxide ring system.²⁰¹ The resulting molecule is an isobaric/isomeric

structure towards the original artemether molecule and initiates the further ion fragmentation (*cf.* Figure 7.3a).

The fragmentation of artemether divides in two main pathways which both contribute to the same fragmentation product at m/z 163, which is the base peak of the mass spectrum. Both fragmentation pathways start with the isomerization of the original artemether molecule and comprise a cleavage of the peroxide ring structure. In the first mechanism, the seven membered heterocycle is opened without breaking the peroxide bond. From this intermediate state the methoxy group on the six membered heterocycle is removed and an ion with m/z 267 is formed. In the other fragmentation pathway, the peroxide group as well as the seven membered heterocycle is cleaved; also followed by the abstraction of the methoxy group. In this case a lactone is formed on the six membered heterocycle and no ring opening is postulated in case the methoxy group is removed. In the following fragmentation steps the removal of a CO group (m/z 239) followed by subtraction a water molecule (m/z 249) – or vice versa – is suggested and the fragment at m/z 221 with the sum formula $C_{14}H_{21}O_2^+$ is obtained. In either of the two different fragmentation pathways the resulting molecule comprises a keto group on a *n*-butyl group attached to the molecule. In either fragmentation mechanism this keto group is removed and an ion at m/z 163 is obtained which is observed to be the base peak in the mass spectrum. Atecha *et al.* analyzed the lumefantrine analyte via LTP-MS and expanded this so far known fragmentation mechanism. The authors identified an additional ion at m/z 145 correlated to the sample, which was formed by the fragmentation of the aforementioned m/z 163 ion.²⁰⁰ However, further fragment ions could be identified for the analysis of artemether via FAPA-MS (*cf.* Table 11.11 in the appendix). First, an ion at m/z 219 with a mass difference of 2.0157 u (RMA 4.9 ppm) compared to the peak at m/z 221 is observed, which can be attributed to two hydrogen atoms removed from the analyte molecule. Second, it is suggested that the ions m/z 231 and m/z 203 are fragments of the above presented m/z 249 ion. For the former ion a water molecule is removed from the fragment ion at m/z 249 followed by the abstraction of a CO molecule which results in the ion at m/z 203. Third, the removal of a CH₂ group from the m/z 221 fragment-ion followed by the abstraction of a CO fragment corresponds to the ions observed at m/z 207 and m/z 179, respectively.

The instrumental detection limit of artemether was determined with a methanolic standard-solution of the analyte. Before mass spectral imaging by FAPA-MS the sample solution was deposited on a CN-modified HPTLC silica plate and separated with the chromatography conditions described in the experimental section.

A detailed description of the IDL determination and calculation procedure can be found in chapter 11.5. Due to the fact that no $[M+H]^+$ -ion for artemether could be detected via FAPA-MS the ion m/z 249 was used for the EIC data extraction and evaluation. Consequently, an IDL of 6 ng (absolute, 2 μ L deposited) for artemether was determined. It is important to note that the determined IDL can be only seen as an approximate value because analyte fragmentation is hugely depending on the operating conditions of the ADI source.

For the second analyte, lumefantrine, a less complex mass spectrum with minor fragmentation of the analyte molecule was observed (*cf.* Figure 7.2). The identified protonated analyte molecule and corresponding fragments are listed in Table 11.11 (*cf.* chapter 11.10) and are also reported in the literature for commercial API-MS measurements such as ESI-MS.²⁰¹ The RMA for all by exact mass measurement identified sum formulas was better than 2 ppm. Due to the stable molecular structure of lumefantrine a dominant monoisotopic $[M+H]^+$ peak at m/z 528 is observed. Because of three chlorine atoms in the molecular structure of the analyte, a characteristic isotope pattern with two peaks at m/z 528 (three ^{35}Cl isotopes) and m/z 530 (two ^{35}Cl isotopes and one ^{37}Cl isotope) and approximately identical height is observed. Further an isotope peak at m/z 532 (one ^{35}Cl isotope and two ^{37}Cl isotopes) is observed with a relative abundance of $\sim 30\%$ compared to the two peaks mentioned before. In addition to these peaks of the intact lumefantrine molecule fragmentation is observed. The abstraction of the hydroxy group is initiated by proton transfer of protonated water-clusters formed by the plasma and an ion at m/z 510 is formed. Further, an ion at m/z 406 is observed with an abundance of $\sim 1\%$ in respect to the $[M+H]^+$ analyte peak. It is assumed that this ion is formed by the removal of the p-chlorobenzyl group from the fluorene molecular skeleton. Evidence for this hypothesis is the accurate mass detection of the sum formula as well as the isotopic pattern of m/z 406, m/z 407, and m/z 408, which correlates well with the pattern of two chlorine atoms in a molecule with 23 carbon atoms. An ion with identical isotopic pattern and a mass shift of 14 u is observed at m/z 420. Exact mass measurement revealed that this ion is a desbenzylketo derivative of lumefantrine with the sum formula of $\text{C}_{23}\text{H}_{28}^{35}\text{Cl}_2\text{NO}_2^+$ (RMA 1 ppm). Despite the identical isotopic pattern, it is not clear whether or not this species originates from oxidation of m/z 406 by the plasma. However, to the best knowledge of the author of this thesis, oxidized analyte species which have been formed by the plasma have never been reported with a higher signal abundance compared to the respective non-oxidized species. Consequently, the m/z 420 ion most probably originates from

a different analyte oxidation reaction prior the interaction of plasma and analyte. Verbeken *et al.* investigated degradation products of lumefantrine which were produced by heat, light, acidic, alkaline, and oxidative stress during storage of the active agent. In their studies they also found the desbenzylketo derivative as a degradation product of oxidative and acidic stress.²⁰⁵ Because the Coartem® tablets and powder were stored in the laboratory at ambient air for several weeks and not under inert gas, it is assumed that the m/z 420 peak is also partially originating from lumefantrine oxidation by ambient oxygen and by protonation (acidic environment) of the oxidized analyte the m/z 420 fragment is formed. To clarify these hypothesis further investigations on the oxidation effects of ambient oxygen are advisable. Lastly, different amine-ion species with m/z 130 (dibutyl ammonium), m/z 142 (dibutyl methylene aminium), and m/z 172 ((2-(dibutylamino) ethylidene) oxonium) can be assigned to lumefantrine. The ions originate from the abstraction of the dibutylamine group, and derivatives, from the aromatic system of the molecule by the plasma source. Because multiple of the above mentioned lumefantrine fragments comprise these amine species in their molecular structure the origin of the amines can be formed by diverse fragmentation pathways. Examples of these pathways are presented in Figure 7.3b.

The publication by Verbeken *et al.*²⁰⁵ also presents other degradation products and synthesis by-products of lumefantrine such as (RS,Z)-2-(Dibutylamino)-2-(2,7-dichloro-9-(4-chloro-benzylidene)-9H-fluoren-4-yl)ethanol (impurity A). This isomeric compound of lumefantrine is a byproduct during the synthesis of the active agent, with a differently coordinated amine and alcohol group (*cf.* Figure 7.4b). Consequently, the compounds cannot be separated by HR-MS. However, due to the more exposed alcohol group in impurity A the compound can be separated by chromatography techniques such as HPTLC (shown in Figure 7.1). In the mass spectral image of artemether and lumefantrine on the CN-HPTLC plate a second spot with m/z 528 at $R_f=0.4$ was present, while the original spot for lumefantrine was found to be at $R_f=0.05$. By comparing the mass spectrum of lumefantrine and the impurity A in Figure 7.4a and b for lumefantrine ($[M+H]^+$ relative abundance $\sim 70\%$) higher signal abundances are observed compared to most of the other analyte fragments, while fragmentation for the impurity A seems to be more dominant. Relative to the $[M+H]^+$ -ion of impurity A (relative abundance $\sim 5\%$) the signal abundance of the dibutylaminium fragment is the dominant ion (relative abundance $\sim 70\%$) in the mass spectrum and 14-fold higher than the corresponding $[M+H]^+$ -ion.

For lumefantrine the dibutylammonium fragment abundance is only 1.5-fold higher than the $[M+H]^+$ -ion.

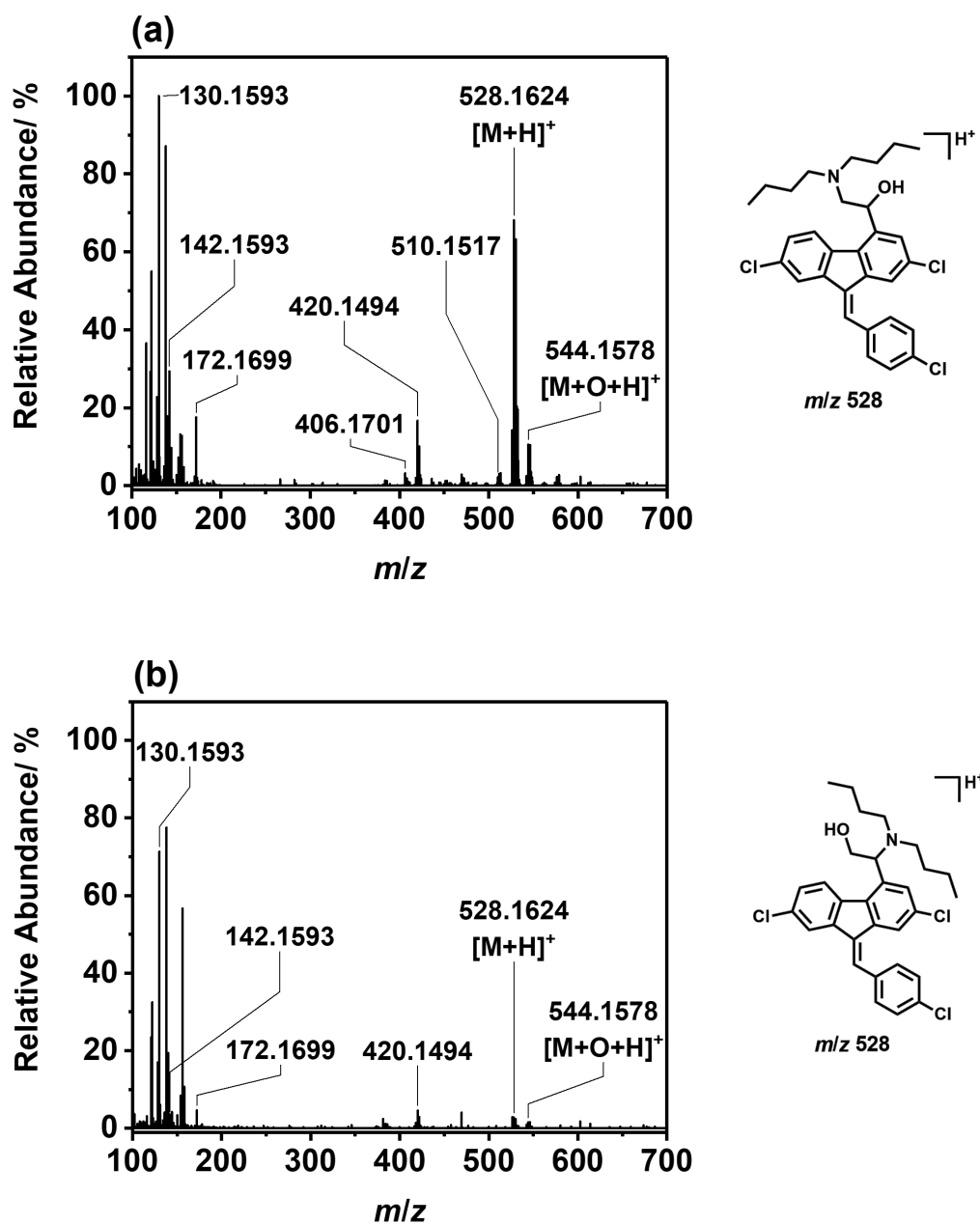


Figure 7.4 Molecular structure of lumefantrine (a) and the isomeric compound (impurity A, b) paired with the FAPA-MS mass spectra of respective compounds, respectively. Detection in positive-ion detection mode and mass accuracy better than 2 ppm. The analytes were desorbed from a CN-modified HPTLC silica plate.

7.4 Conclusion

Aim of this study was to develop a method for direct screening of antimalarial active agents, the identification of unwanted components and falsified antimalarial drug preparations. Therefore, the established and easy to use screening tool HPTLC was used to separate the ingredients of the antimalarial medication after a quick analyte extraction with organic solvents. The separation was performed in less than 10 minutes, while multiple samples were deposited on the HPTLC plate next to each other. In the above presented results a CN-modified HPTLC silica plate showed the best results for the separation of the Coartem[®] active agents (artemether and lumefantrine) and other byproducts such as the impurity A. After analyte separation and mobile phase evaporation the HPTLC plate directly probed by FAPA-MS, a mass spectral technique for direct surface screening. With the FAPA plasma source the analytes were desorbed and ionized for mass spectral analysis. The interpretation of the mass spectrum of artemether revealed a similar analyte fragmentation pattern in comparison to the mild ESI ionization source. However, the fragmentation pathway postulated by Santos *et al.*²⁰¹ and Vandercruyssen *et al.*²⁰³ was expanded with six fragments found in the FAPA-MS mass spectrum. The lumefantrine analyte was not as sensitive to fragmentation as artemether and the protonated molecular peak was found to be a dominant ion in the mass spectrum. Due to the easily cleavable bond of the amine group the fragmentation of a secondary dibutylamine was found to be the base peak in the FAPA-MS mass spectrum of lumefantrine. With the aid of the mass spectrometer the third analyte spot found on the CN-HPTLC plate could be identified to be impurity A (impurity described by Verbeken *et al.*²⁰⁵). Due to the isobaric m/z of lumefantrine with impurity A this contamination would not have been detected without the separation.

The benefit of the combined techniques is the easy preliminary screening with the HPTLC plate, which can be performed in the field and with low costs. In case of a suspicious antimalarial medication the already separated, and in the plate stored, sample can be shipped to a close by or far away laboratory for further mass spectral analysis. In this case direct mass spectral screening via FAPA-MS enables spatial resolved information of the components in the sample.

Chapter 8

Decomposition of P₄O₁₀ in DMSO

Based on: S. Johansson, C. Kuhlmann, J. Weber, T. Paululat,
C. Engelhard, J. Schmedt auf der Günne.
Chemical Communications, **2018**, *54*, 7605-7608.
DOI: 10.1039/C8CC03000F.

Contribution statement

My contribution to this publication was the mass spectral analysis of the freshly prepared reaction solution via FAPA-MS as well as the interpretation of the mass spectral data. The text in the manuscript and the electronic supporting information about the interpretation of the mass spectral data and the description of the experimental procedures for the FAPA-MS measurements was exclusively written by myself. Sebastian Johansson performed the reaction between phosphorus pentoxide (P₄O₁₀) and DMSO performed the nuclear magnetic resonance (NMR) measurements and NMR simulations. Furthermore, Sebastian Johansson evaluated the data for all NMR measurements and curated the data. The density functional theory (DFT) calculations were conducted by Dr. Johannes Weber and the ³¹P-COSY-NMR measurements were performed by Dr. Thomas Paululat. The original draft of this publication was written by Sebastian Johansson. For the draft, Dr. Johannes Weber and I provided the draft texts of the DFT data interpretation and mass spectral data interpretation, respectively. The manuscript was refined in collaboration with all coauthors and finally was finally edited by Prof. Dr. Carsten Engelhard and Prof. Dr. Jörn Schmedt auf der Günne.

Decomposition of P₄O₁₀ in DMSO†Cite this: *Chem. Commun.*, 2018, 54, 7605Sebastian Johansson,^a Christopher Kuhlmann,^b Johannes Weber,^a Thomas Paululat,^c Carsten Engelhard^b and Jörn Schmedt auf der Günne^{id}*^aReceived 15th April 2018,
Accepted 1st June 2018

DOI: 10.1039/c8cc03000f

rsc.li/chemcomm

Intermediate states of degradation of phosphorus pentoxide in dimethyl sulfoxide (DMSO), also known as Onodera reagent, are studied. We found that DMSO is not dissolving P₄O₁₀, but rather reacting with it. A rather complex mixture of phosphate species is formed, many with ester functions. Several not yet described phosphate species could be identified by NMR and MS. Finally, we present a possible decomposition scheme of P₄O₁₀ in DMSO.

Dimethyl sulfoxide (DMSO) is used in a variety of fields, e.g. in pharmacology,² biology³ and the medical sector.² DMSO is a strong polar, nucleophilic and aprotic solvent, which is less toxic than other members of this solvent family, while being able to dissolve many compounds.⁴

While the aforementioned applications use DMSO as solvent, in organic synthesis it is used as a mild oxidant, which is exemplified by the Pfitzner–Moffatt and the Swern oxidation.⁵ During these oxidations, DMSO acts as reactant. Usually, electrophiles are involved and alcohols are oxidized under very mild conditions.^{6–8} Despite the amount of literature about DMSO used in oxidations,^{5–11} no intermediates of these reactions have been found, but only suggested. One example is the system dimethyl sulfoxide and phosphorus pentoxide, also known as Onodera reagent.¹ Onodera *et al.* found in 1965 that it is possible to oxidize carbohydrates with dimethyl sulfoxide containing phosphorus pentoxide.

Recently, a low-temperature synthesis of organic and inorganic phosphates was published.¹² The idea of this synthesis is that a nitrate salt M(NO₃)_x (M²⁺ in this case being a monovalent or divalent inorganic or organic cation) reacts with P₄O₁₀ in DMSO. In this manuscript, we present an investigation of the system P₄O₁₀–DMSO without nitrates present, based on results from

³¹P NMR studies in the system followed by a detailed proposal of the reaction mechanism supported by mass spectrometry measurements and DFT calculations. According to our hypothesis, DMSO is not only a solvent but a reactant – actively participating in the named system. Several questions arise. Can we detect stable intermediate molecules? Can we identify novel phosphate species? How does a possible decomposition happen?

In order to answer these questions, ³¹P NMR was utilized to identify the P–O–P backbone of possible intermediates. Fig. 2 shows a ³¹P{¹H} NMR spectrum (bottom) and the corresponding ³¹P spectrum (top). One would expect a broad peak at δ = –45.9 ppm for P₄O₁₀, which is built of Q³ [PO₄] tetrahedra.

Assigning the decomposition products, which occur during the reaction of P₄O₁₀ in DMSO, was done by analyzing the occurring multiplets, their isotropic chemical shifts and *J*-couplings. Several molecules were identified and spin systems were assigned (Table 1). Having all the occurring phosphate species tabulated, one can derive a scheme for the decomposition reaction (Fig. 1).

Table 1 Assigned spin systems to the molecules found by NMR. R is an unknown residue

Peak	Molecule (substance identifier)	Spin system	Coupling isotopes
1	H ₃ PO ₄ (I)	A	A = ³¹ P
2	Unknown Q ⁰ -species	Unknown	
3	(OP)(O–CH ₂ R) ₃ (II)	A ₆ X	A = ¹ H, X = ³¹ P
4	(O ₂ P)(O–CH ₂ R) ₂ -anion (III)	A ₄ X	A = ¹ H, X = ³¹ P
5	(O ₃ P)(O–CH ₂ R) ²⁻ -anion (IV)	A ₂ X	A = ¹ H, X = ³¹ P
6	(RCH ₂ O) ₂ –OP–O–PO ₃ -anion (V)	A ₂ X	A = ¹ H, X = ³¹ P
7	P ₂ O ₇ ⁴⁻ -anion (VI)	A ₂	A = ³¹ P
8	(RCH ₂ O)–(PO ₂)–O–PO ₃ -anion (VII)	A ₂ X	A = ¹ H, X = ³¹ P
9	Tetraphosphate-anion (VIII)	AXX'A'	A = ³¹ P, X = ³¹ P
10	PO ₃ –O–PO ₂ –O–PO ₃ -anion (IX)	A ₂ X ^a	A = ³¹ P, X = ³¹ P
11	(RCH ₂ O)–PO ₂ –O–PO ₂ –(OCH ₂ R) (X)	A ₂ XX'A ₂ '	A = ¹ H, X = ³¹ P
12	P ₄ O ₁₂ ⁴⁻ -anion (XI)	A ₄	A = ³¹ P
13	Tetraphosphate-anion (VIII)	AXX'A'	A = ³¹ P, X = ³¹ P
14	Unknown Q ² -species	Unknown	
15	PO ₃ –O–PO ₂ –O–PO ₃ -anion (IX)	A ₂ X ^a	A = ³¹ P, X = ³¹ P
16	Unknown Q ³ -species	Unknown	

^a ²*J*(³¹P, ³¹P)-coupling of 25.2 Hz.

^a Inorganic Materials Chemistry, Department of Chemistry and Biology, University of Siegen, Adolf-Reichwein-Str. 2, Siegen 57076, Germany. E-mail: gunnej@chemie.uni-siegen.de

^b Department of Chemistry and Biology, University of Siegen, Adolf-Reichwein-Str. 2, Siegen 57076, Germany

^c Department of Chemistry and Biology, University of Siegen, Adolf-Reichwein-Str. 2, Siegen 57076, Germany

† Electronic supplementary information (ESI) available. See DOI: 10.1039/c8cc03000f

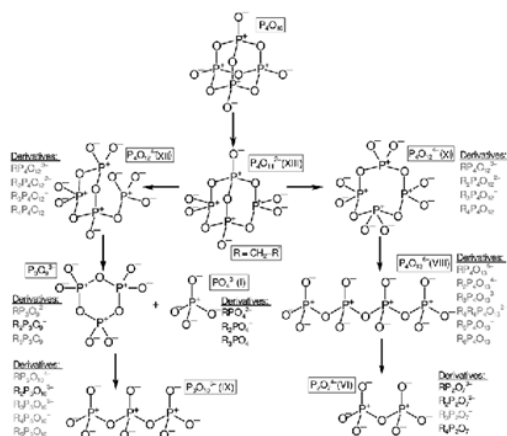


Fig. 1 Scheme of the decomposition of P_4O_{10} with DMSO. Possible derivatives are shown next to the phosphate species with sum formulas. It is to be read as follows: RPO_4^{2-} stands for $R'-CH_2-PO_4^{2-}$, meaning that one CH_2 function is present. R' is an unknown residue. Species which are found in the NMR spectra are written in black, possible decomposition products are written in light grey. Roman numbers act as substance identifiers.

The molecule $(RCH_2O)-PO_2-O-PO_2-(OCH_2R)$ (X) could be identified by performing simulations with the program Simpson.¹³ We found a spin system of higher order, $A_2XX'A_2'$, with a $^2J(^{31}P, ^{31}P)$ J -coupling of 22.8 Hz and a $^3J(^1H, ^{31}P)$ J -coupling of 16.1 Hz. The experimental data have been compared with the simulation (Fig. 3).

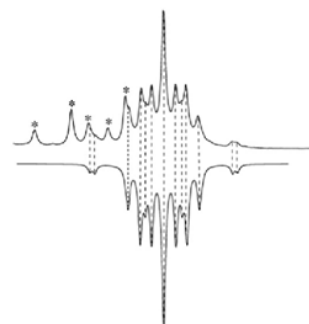


Fig. 3 Top: Measured ^{31}P liquid-state NMR spectrum. The multiplet can be seen in Fig. 1 in the insert box at $\delta = -16.4$ ppm. Bottom: Simulated ^{31}P liquid-state NMR spectrum of the $A_2XX'A_2'$ -spin system. $(RCH_2O)_2OP-O-PO(OCH_2R)_2$ (X) is responsible for that splitting, R being an unknown residue. Asterisks mark other phosphate species.

To investigate the, to this point, unknown Q^3 -species, a 0.5 mmol l^{-1} solution of P_4O_{10} in d_6 -DMSO was analyzed by ^{31}P COSY NMR (Fig. 4). The resulting COSY spectrum was treated as follows: first the sum projections were extracted, J -couplings, isotropic chemical shifts and multiplets were taken from a single pulse ^{31}P NMR experiment, if extraction was possible. Then 2D COSY spectra were simulated with the program Simpson,¹³ and from these sum projections were extracted (input files for the simulations see ESI†). Simulations for the molecule $[P_4O_{11}]^{2-}$, which is the first decomposition product (Fig. 4), show a J -coupling $^2J(^{31}P_A, ^{31}P_X)$ of 29.15 Hz.

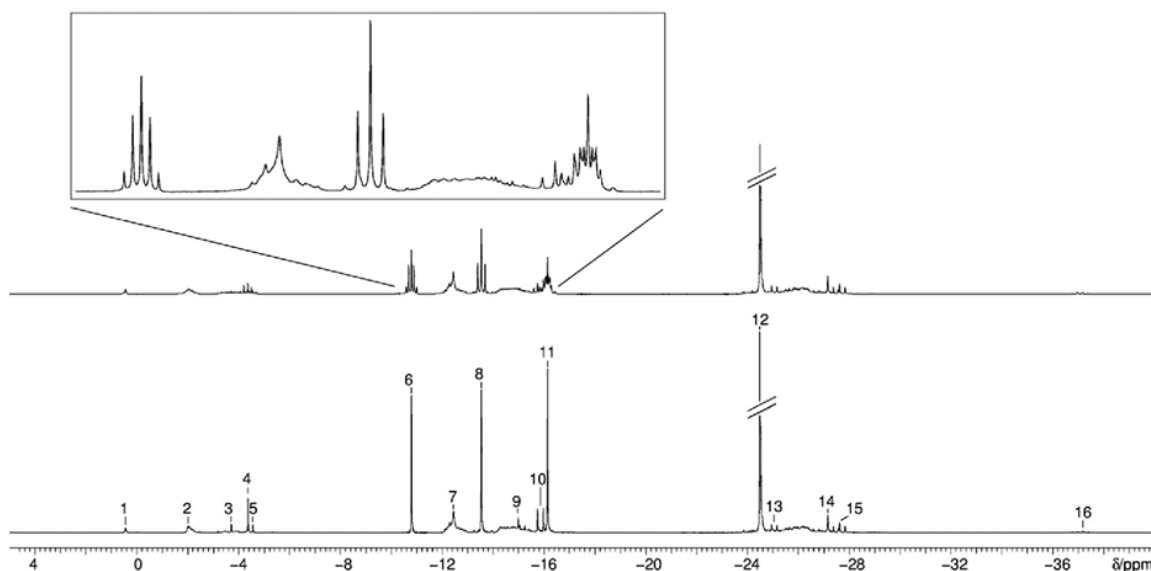


Fig. 2 Bottom spectrum: $^{31}P(^1H)$ NMR spectrum of P_4O_{10} in DMSO; peak 1: H_3PO_4 (I), peak 2: unknown Q^0 -species, peak 3: $(OP)(O-CH_2R)_3$ (II), peak 4: $(O_2P)(O-CH_2R)_2$ -anion (III), peak 5: $(O_3P)(O-CH_2R)_2^{2-}$ (IV), peak 6: $(RCH_2O)_2-(PO)-O-PO_3$ -anion (V) (P-O-P-bridge is not stable on the NMR timescale), peak 7: $P_2O_7^{4-}$ -anion (VI), peak 8: $(RCH_2O)-(PO)_2-O-PO_3$ -anion (P-O-P-bridge is not stable on the NMR timescale), peak 9 + 13: tetraphosphate-anion (VII), peak 10 + 15: $PO_3-O-PO_2-O-PO_3$ -anion (VIII), peak 11: $(RCH_2O)_2OP-O-PO(OCH_2R)_2$ (IX), peak 12: $P_4O_{12}^{4-}$ -anion (X), peak 14: unknown Q^2 -species, peak 16: unknown Q^3 -species; R is an unknown residue. Top spectrum: ^{31}P NMR spectrum of P_4O_{10} in DMSO; areas with occurring multiplets are shown magnified. Roman numbers in brackets function as substance identifiers. Details about isotropic chemical shifts and J -couplings are given in the ESI.†

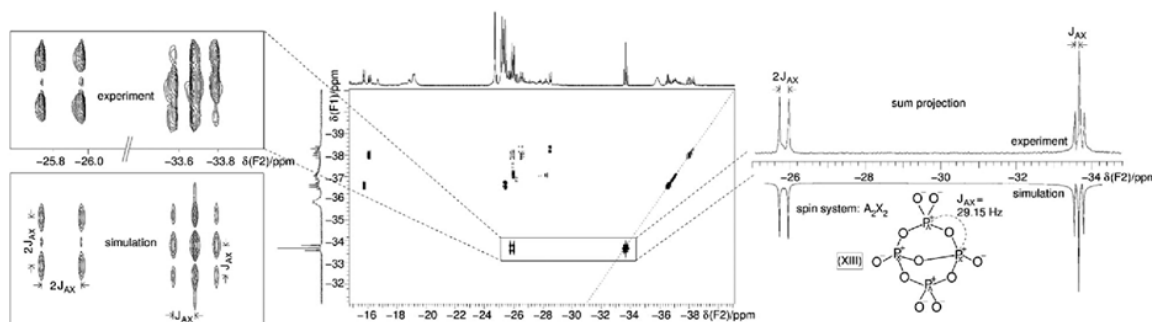


Fig. 4 Zoom in of a ^{31}P COSY spectrum (middle). On the x and y axis ^{31}P single excitation spectra are shown. On the right top the sum projection of the section from the COSY spectrum surrounded by the box is shown versus a simulated sum projected of a μ -oxido-cyclotetraphosphate-anion (XIII) with an A_2X_2 spin system. On the left top a zoom in the section is shown versus the simulation of the COSY spectrum of the A_2X_2 spin system. Details about isotropic chemical shifts and J -couplings are given in the ESI.†

The sum projection of the experiment is in good agreement with the sum projection extracted from simulation. This is also supported by experimental 2D COSY spectrum and the 2D simulation itself, meaning that the hypothesis of μ -oxido-cyclotetraphosphate-anion $[\text{P}_4\text{O}_{11}]^{2-}$ (A_2X_2 spin system) could be confirmed as the first step of the decomposition reaction. A $[\text{N}(\text{PPh}_3)_2]^+$ salt of this species was recently synthesized.¹⁴

The aforementioned conclusions resulting from ^{31}P NMR interpretation are supported by mass spectrometric analysis of the P_4O_{10} -DMSO mixture. The reaction mixture is deposited on a stainless-steel mesh and subsequently probed by the flowing atmospheric-pressure afterglow (FAPA)¹⁵ ambient desorption/ionization source. Resulting gas-phase ions are detected by a high-resolution mass spectrometer (HR-MS) in positive-ion mode (Fig. 5).

In the mass spectrum of the mixture (Fig. 5B) protonated DMSO dimer cations $([\text{M}_2 + \text{H}]^+)$, mass-to-charge ratio (m/z) 157.03457, mass accuracy (MA) -3.7 ppm) and protonated DMSO molecules $([\text{M} + \text{H}]^+)$, m/z 79.02109, MA -0.8 ppm) are the two dominant species detected directly after the sample is deposited between the FAPA desorption/ionization source and MS. Furthermore, $\text{C}_2\text{H}_5\text{S}^+$ ions $([\text{M}-\text{O}-\text{H}]^+)$, m/z 61.01073, MA 1.4 ppm) can be observed in the Onodera reagent. In comparison to these results, $\text{C}_2\text{H}_5\text{S}^+$ ions cannot be observed in the mass spectrum of pure DMSO (Fig. 5A and Fig. S1, ESI†), which supports the hypothesis that $\text{C}_2\text{H}_5\text{S}^+$ is formed by the reaction of DMSO and P_4O_{10} .

Mass spectra detected in negative-ion mode give further information on possible reaction products. In Fig. 6, the species $\text{P}_4\text{O}_{12}^{4-}$ is detected at m/z 78.95811 (MA -11.3 ppm), and the sum formula $\text{C}_2\text{H}_7\text{O}_7\text{P}_2\text{S}^-$ can be related to m/z 236.93585 (MA -14.6 ppm). These findings correlate well with the results of the ^{31}P NMR measurements. Additionally, various oxidized sulphate- and phosphate-species (Fig. 6 and Fig. S2, ESI†) can be observed in negative-ion mode. These species might result from oxidation processes in the reaction mixture or gas-phase reactions after the liquid is desorbed from the sample target.

From the six calculated isomers of $[\text{C}_2\text{H}_5\text{S}]^+$ the cyclic singlet structure is the most stable one according to our DFT calculations,

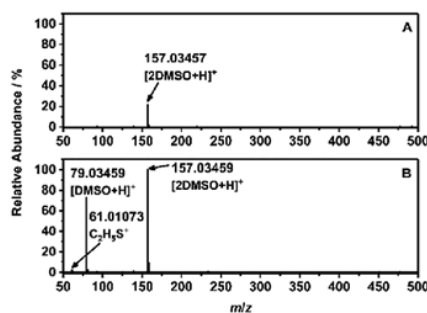


Fig. 5 Positive-ion mode mass spectra of (A) DMSO and (B) the P_4O_{10} -DMSO mixture detected via FAPA-MS. (A) Mass spectrum of pure DMSO shows dimer formation from solvent molecules. (B) Mass spectrum of the DMSO- P_4O_{10} mixture. Peak identification was carried out by high-resolution mass spectrometry with a relative mass accuracy of ≤ -4 ppm. Peak heights in (A) and (B) were normalized to the largest peak (m/z 157) in (B) for visualization purposes.

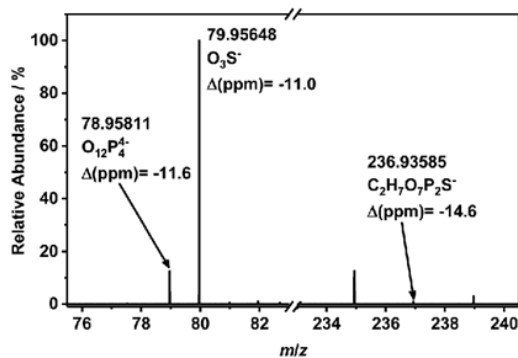
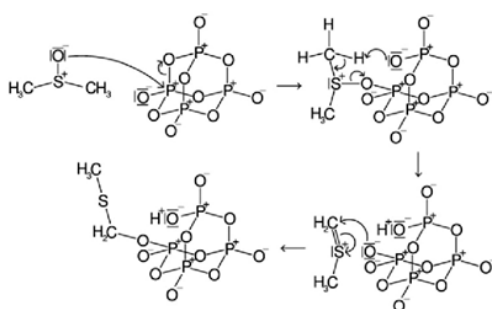


Fig. 6 Excerpt of the negative-ion mode mass spectrum of the Onodera reagent. Peak identification was carried out by accurate mass measurements (MA ≤ -14.6 ppm).

irrespective of the temperature and the method to compute the energies. It may be noted though, that the next stable structure (singlet $[\text{H}_2\text{C}-\text{S}-\text{CH}_3]^+$) has an energy difference below 20 kJ mol^{-1}

Table 2 Results of the DFT calculations at PBE1PBE/aug-cc-pVTZ level, energy values are given at 430 K, which is approximately the temperature of the MS experiments. Thermal correction, hindered rotor correction and ΔE are given in kJ mol^{-1} . ΔE_{total} is the total energy difference between the present and the lowest energetic isomer

Isomer	Structure	Thermal correction	Hindered rotor correction	ΔE_{total}
$\text{C}_2\text{H}_5\text{S}^+$		27.23	-0.063	317.29
Cyclo- $\text{C}_2\text{H}_5\text{S}^+$		21.2	0	0
$\text{H}_2\text{C-S-CH}_3^+$		24.11	-3.473	18.36



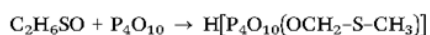
Scheme 1 Schematic drawing of the suggested reaction mechanism between DMSO and P_4O_{10} . The first step of a possible cracking of the adamantane cage of P_4O_{10} is shown. The suggested pathway follows a Pummerer-like rearrangement.^{21–24}

and therefore is assumed to be easily accessible at elevated temperatures (Table 2).^{16–20}

One way to explain the formation of the intermediate states, might be a Pummerer-like rearrangement^{21–24} reaction (Scheme 1).

The nucleophilic oxygen atom of DMSO attacks one phosphorus atom of the adamantane-like cage of phosphorus pentoxide, while the P–O binding breaks, forming an intermediate adduct. Afterwards, one hydrogen is shifted towards the newly formed negatively charged oxygen and the spare electron pair forms a double bond between carbon and sulfur, meaning that a $\text{C}_2\text{H}_5\text{S}^+$ molecule is formed as intermediate. Finally, oxygen attacks the carbon of the $\text{C}_2\text{H}_5\text{S}^+$ molecule and a phosphate ester is formed.

For the first decomposition step the following hypothetical reaction equation applies.



The decomposition mechanism of P_4O_{10} in DMSO suggests the formation of stoichiometric amounts of protons which, as Lewis acids, further accelerate the decomposition reaction of the nucleophilic compound DMSO. This is in agreement with the observation that multidimensional NMR only serves to identify the initial products. The lifetime of the produced oligophosphates becomes shorter the longer the reaction is

ongoing, so that multidimensional NMR becomes prohibitively long, *i.e.* the decomposition reaction has an autocatalytic character.

To conclude, our study reveals that a complex mixture of phosphate esters is formed from the reaction of DMSO and P_4O_{10} , including uncommon phosphate species like the μ -oxido-cyclotetraphosphate-anion, $(\text{P}_4\text{O}_{11})^{2-}$, and species like the *O*-phosphono-cyclotriphosphate-anion, $(\text{P}_3\text{O}_9\text{PO}_3)^{4-}$ ²⁵ which remains to be isolated. The suggested mechanism may help to direct the understanding of more complex name reactions, which build on P_4O_{10} /DMSO mixtures.

The authors want to thank Peter Mayer, LMU Munich, for recording the ^{31}P and $^{31}\text{P}\{^1\text{H}\}$ spectra. The machine shop in the Department of Chemistry and Biology is gratefully acknowledged.

Conflicts of interest

There are no conflicts to declare.

References

- 1 K. Onodera, S. Hirano and N. Kashimura, *J. Am. Chem. Soc.*, 1965, **87**, 4651–4652.
- 2 J. A. M. Bleeker, J. Geiss and M. Huber, *The Century of Space Science*, Kluwer Academic, 2001.
- 3 R. Chakrabarti and C. E. Schutt, *Gene*, 2001, **274**, 293–298.
- 4 K. Balakin, N. Savchuk and I. Tetko, *Curr. Med. Chem.*, 2006, **13**, 223–241.
- 5 T. T. Tidwell, *Synthesis*, 1990, 857–870.
- 6 K. Omura and D. Swern, *Tetrahedron*, 1978, **34**, 1651–1660.
- 7 W. W. Epstein and F. W. Sweat, *Chem. Rev.*, 1967, **67**, 247–260.
- 8 A. J. Mancuso and D. Swern, *Synthesis*, 1981, 165–185.
- 9 D. H. Ball, E. D. M. Eades and L. Long, *J. Am. Chem. Soc.*, 1964, **86**, 3579–3580.
- 10 H. Metzger, H. König and K. Seelert, *Tetrahedron Lett.*, 1964, **5**, 867–868.
- 11 A. H. Fenselau and J. G. Moffatt, *J. Am. Chem. Soc.*, 1966, **88**, 1762–1765.
- 12 M. Mangstl, V. R. Celinski, S. Johansson, J. Weber, F. An and J. Schmedt auf der Günne, *Dalton Trans.*, 2014, **43**, 10033–10039.
- 13 M. Bak, J. T. Rasmussen and N. C. Nielsen, *J. Magn. Reson.*, 2000, **147**, 296–330.
- 14 Y. Jiang, K. Chakarawet, A. L. Kohout, M. Nava, N. Marino and C. C. Cummins, *J. Am. Chem. Soc.*, 2014, **136**, 11894–11897.
- 15 J. T. Shelley, J. S. Wiley and G. M. Hieftje, *Anal. Chem.*, 2011, **83**, 5741–5748.
- 16 S.-W. Chiu, Y.-S. Cheung, N. L. Ma, W.-K. Li and C. Y. Ng, *J. Mol. Struct.: THEOCHEM*, 1997, **397**, 87–101.
- 17 S.-W. Chiu, Y.-S. Cheung, N. Ling Ma, W.-K. Li and C. Y. Ng, *J. Mol. Struct.: THEOCHEM*, 1998, **452**, 97–115.
- 18 S.-W. Chiu, Y.-S. Cheung, N. L. Ma, W.-K. Li and C. Y. Ng, *J. Mol. Struct.: THEOCHEM*, 1999, **468**, 21–37.
- 19 S.-W. Chiu, K.-C. Lau, W.-K. Li, N. L. Ma, Y.-S. Cheung and C. Y. Ng, *J. Mol. Struct.: THEOCHEM*, 1999, **490**, 109–124.
- 20 R. Pummerer, *Ber. Dtsch. Chem. Ges.*, 1909, **42**, 2282–2291.
- 21 J. Henn, D. Leusser and D. Stalke, *J. Comput. Chem.*, 2007, **28**, 2317–2324.
- 22 A. Padwa, D. E. Gunn, Jr. and M. H. Osterhout, *Synthesis*, 1997, 1353–1377.
- 23 R. Pummerer, *Ber. Dtsch. Chem. Ges.*, 1910, **43**, 1401–1412.
- 24 O. de Lucchi, U. Miotti and G. Modena, *Org. React.*, John Wiley & Sons, Inc., Hoboken, NJ, USA, 1991, pp. 157–405.
- 25 T. C. Myers, T. Glonek, P. Z. Han and J. R. Van Wazer, *J. Am. Chem. Soc.*, 1970, **92**, 7214–7216.

Supporting Information

Decomposition of P₄O₁₀ in DMSO

Sebastian Johansson^[a], Christopher Kuhlmann^[b], Johannes Weber^[a], Thomas Paululat^[c], Carsten Engelhard^[b] and Jörn Schmedt auf der Günne^{*[a]}

Abstract: The oxidation power of activated dimethyl sulfoxide (DMSO) with phosphorus pentoxide, better known as Onodera reagent^[1], is not yet understood. Possible intermediates were studied in this manuscript. We found that DMSO is not dissolving P₄O₁₀, but rather reacting with it. The system was studied with ³¹P, ³¹P{¹H} single excitation NMR, ³¹P{¹H} correlation (COSY) NMR and high-resolution mass spectrometry. The findings are supported by ³¹P{¹H} and ³¹P NMR simulations, performed using the program SIMPSON^[2]. We found that a rather complex mixture of phosphate species is formed, many with ester function. We explain the findings by a pummerer like transposition when the nucleophilic oxygen of the DMSO attacks the electrophilic phosphorus atom of the phosphorus pentoxide. The suggestion of a molecule occurring as intermediate, C₂H₅S⁺, could be supported by high-resolution mass spectrometry. Its most stable conformation has been found by DFT calculations. Finally, we present a possible reaction mechanism for the decomposition of P₄O₁₀ in DMSO. Finally, we present a possible decomposition scheme of P₄O₁₀ in DMSO.

DOI: 10.1039/C8CC03000F

-
- [a] S. Johansson, Dr. J. Weber, Prof. Dr. J. Schmedt auf der Günne
Inorganic Materials Chemistry, Department of Chemistry and Biology
University of Siegen, Adolf-Reichwein-Str. 2, 57076 Siegen, Germany, E-mail: gunnej@chemie.uni-siegen.de
- [b] C. Kuhlmann, Prof. Dr. C. Engelhard
Department of Chemistry and Biology
University of Siegen, Adolf-Reichwein-Str. 2, 57076 Siegen, Germany
- [c] Dr. T. Paululat
Department of Chemistry and Biology
University of Siegen, Adolf-Reichwein-Str. 2, 57076 Siegen, Germany

Table of Contents

1. Experimental Procedures

2. Results and discussion

2.1. Mass spectrometry

2.2. ³¹P COSY Simulations

2.3. Quantum-chemical calculations

2.4. Input files for SIMPSON and gnuplot

2.5. Chemical information of phosphates identified by NMR

1. Experimental Procedures

Handling the samples

In order to try to prevent water entering the reaction, a series of measures were taken. A high-purity batch of DMSO was bought. This was additionally dried with freshly preheated molecular sieve and all samples and the DMSO were handled in Schlenk flasks which we additionally dried under vacuum with a heat gun. Sample handling where necessary included a glove box. The Ar used was purified using several reagents including P₄O₁₀ and Ti-sponge. Used syringes and flasks were flushed with Ar and evacuated several times before usage. The reagent P₄O₁₀ was coming from a fresh high-grade batch. Its container was partially opened in a desiccator, immediately transferred into a glove box and remained there. Because of ¹H NMR experiments, which were done earlier and which allow to trace even small quantities of water, we were confident that the anhydrous grades could be trusted. Even small amounts of water are visible from ¹H NMR experiments.

NMR: ³¹P and ³¹P{¹H} spectroscopy

Single pulse and decoupled spectra were measured on a JEOL Eclipse EX-270 spectrometer with standard pulse sequences. 1% TMS in CDCl₃ was used as external reference. 0.5 mmol (141.9 mg) phosphorus pentoxide (Riedel de Haën, 99%) was dissolved in 1 mL DMSO.

NMR: ³¹P correlation spectroscopy

The COSY spectrum was measured on a Varian VNMR-S 600 MHz spectrometer equipped with a 5 mm dual broadband probe. Pulse sequences were taken from Varian pulse sequence library. These spectra are recorded in 150 µl of solvent at T = 25°C (T = 35°C for DMSO-d₆, Pyridine-d₅). Spectra are referenced with respect to external H₃PO₄. 1.5 mmol (425.8 mg) phosphorus pentoxide (Sigma-Aldrich, 99.98%) was dissolved in 3 mL d₆-DMSO.

Mass spectrometry

High-resolution mass spectrometric analysis was performed with an Exactive mass spectrometer (Thermo Fisher Scientific Inc., Bremen, Germany). The conventional inlet capillary was replaced by a 4 cm extended stainless-steel capillary (i.d. 0.8 mm, o.d. 1.58 mm). For direct sample desorption/ionization a home-built FAPA source (pin-to-capillary geometry, described by Shelley *et al.*^[1]) powered by a model BHK 1000-0.2MG DC power supply (Kepco Inc., Flushing, NY, USA) was used. A negative potential (25 mA, 705 V) was applied to the stainless-steel pin electrode with a 5 kW ballast resistor as part of the circuitry. The stainless-steel capillary anode was connected to ground potential of the power supply. Helium (99.999%, Messer Industriegase GmbH, Siegen, Germany) was used as discharge gas. It was fed through an additional port with 500 mL min⁻¹ into the ceramic discharge chamber made out of Macor (Schröder Spezialglas GmbH, Ellerau, Germany). The FAPA was positioned on-axis in front of the MS inlet capillary with a distance of 7 mm. For sample analysis, 0.5 µL of the reaction mixture was deposited on a stainless-steel metal mesh at ambient conditions. The prepared sample was positioned between the FAPA source and the MS inlet capillary at a distance of 1 mm towards the MS inlet capillary. A schematic diagram of this experimental setup can be found in Figure S3.

Background signals (ambient air etc.) were subtracted from the mass spectra by using the "subtract background" function of the vendor data processing software Xcalibur (Thermo Fisher Scientific Inc., Bremen, Germany).

Quantum-chemical calculations

All calculations were performed using Gaussian 09 at either HF/6-31G(d,p) level^[3,4] or hybrid DFT level (PBE1PBE^[5-7]) with aug-cc-pVTZ^[8] basis set. Tight convergence criteria were set for the SCF cycles (scf=tight, corresponding to $\Delta E < 10^{-8}$ hartree and a change in the density matrix elements $< 10^{-8}$ in subsequent steps), as well as the structure optimization (opt=tight, corresponding to a combined criterion of the scf=tight condition, and maximum residual forces and displacements on individual atoms of 0.000015 hartree/bohr and 0.000060 bohr, respectively). On RMS average over all nuclei these quantities were not allowed to be larger than 0.000010 hartree/bohr and 0.000040 bohr). In the DFT calculation the "ultrafine" integration grid was used, corresponding to pruned grid of 99 radial shells and 590 angular points per shell on each atom. This combination should lead to reliable structures as well as relative energies^[9]. At the converged structures, harmonic frequencies using analytic second derivatives^[10] were calculated to prove that the optimized structure belongs to a local minimum on the potential energy surface and to obtain the total energy of the molecule. The zero point energy was added to the electronic energy, and thermal corrections were included by thermal populations of the harmonic levels according to^[11] with a special treatment of soft vibrations that might belong to internal rotations according to Truhlar *et al.* (keyword: freq=HindRot)^[12-14]. For HF/6-31G** frequencies a scaling of 0.89 was used, while no factor was used for the DFT frequencies.

NMR simulations

The program SIMPSON^[2] was used to perform simulations. An offset of -5580 Hz was applied to every simulation by manually moving the chemical shifts. This was done in order to be able to maintain the sw parameter from the experiment

2. Results and Discussion

2.1. Mass spectrometry

In Figure S1, the mass spectrum of pure DMSO detected by FAPA-MS is depicted. The mass spectrum does not contain a peak at m/z 61.01073, which would correspond to the $C_2H_5S^+$ cation (MA 1.4 ppm) found in the Onodera reagent (see Figure 1B). This finding confirms that $C_2H_5S^+$ is not formed during the desorption/ionization process by the FAPA source.

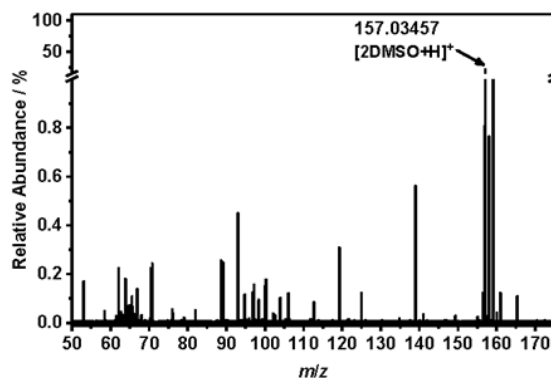


Figure S1. Mass spectrum of pure DMSO in the mass range between m/z 50 and 150 detected by FAPA-MS in positive-ion mode. For visualization purposes the peak height was normalized to the largest peak (m/z 157) in Figure 5B.

In negative-ion mode FAPA-MS analysis of the Onodera reagent, multiple phosphate- and sulphate-species can be observed due to possible oxidation processes inside the reaction mixture, at ambient conditions, or the exposure of the analyte to the plasma source. A list of all peaks at different m/z is provided in Table S1 and a corresponding mass spectrum is depicted in Figure S2.

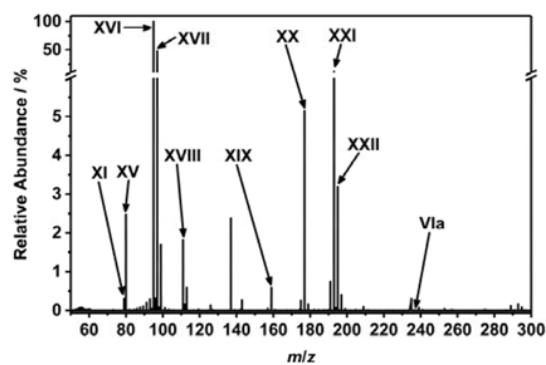


Figure S2. Mass spectrum of the P₄O₁₀-DMSO mixture detected by FAPA-MS in negative-ion mode (mass accuracy limit for peak identification $\leq \pm 15$ ppm).

Table S1. List of identified peaks in the mass spectrum of the P₄O₁₀-DMSO mixture detected by FAPA-MS (negative-ion mode).

No.	Observed m/z	Sum formula	Theoretical mass	Relative mass accuracy
XI	78.95811	O ₁₂ P ₄ ⁺	78.95905	-11.3 ppm
XV	79.95648	O ₃ S ⁻	79.95736	-11.0 ppm
XVI	94.97986	CH ₃ SO ₃ ⁻	94.98084	-10.3 ppm
XVII	96.95914	SO ₄ H ⁻	96.96010	-9.9 ppm
XVIII	110.97471	CH ₃ O ₄ S ⁻	110.97575	-9.4 ppm
XIX	158.91459	O ₆ PS ⁻	158.91587	-8.1 ppm
XX	176.92536	H ₂ O ₇ PS ⁻	176.92643	-6.1 ppm
XXI	192.95663	CH ₆ O ₇ PS ⁻	192.95773	-5.7 ppm
XXII	194.93596	H ₄ O ₆ PS ⁻	194.93700	-5.3 ppm
VIa	236.93585	C ₂ H ₇ O ₇ P ₂ S ⁻	236.93932	-14.7 ppm

In Figure S3 the experimental setup of transmission-mode FAPA-MS is depicted. The FAPA source was positioned on-axis in front of the inlet capillary of the mass spectrometer with a distance of 7 mm. The distance between stainless-steel mesh and MS inlet capillary was 1 mm.

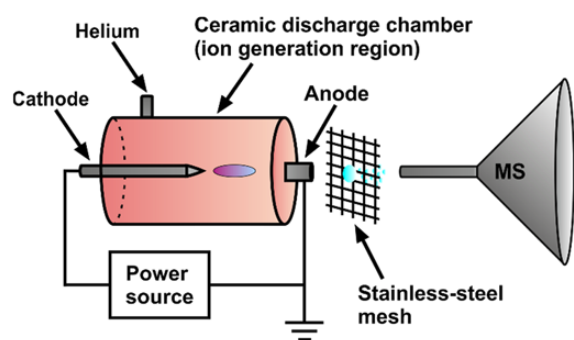


Figure S3. Instrumental setup of transmission-mode FAPA-MS.

2.2. ^{31}P -COSY simulations

Besides the μ -oxido-cyclotetraphosphate anion – substance XIII, spin system A_2X_2 - two more phosphates could be identified, both being ortho-phosphono-tricyclophosphate anions. In the case of substance XII, the two Q^2 phosphorus atoms are anisochronous, while in substance XIV these atoms are isochronous. The sum projections of the COSY spectrum can be seen in **Figure S4** and **Figure S5**.

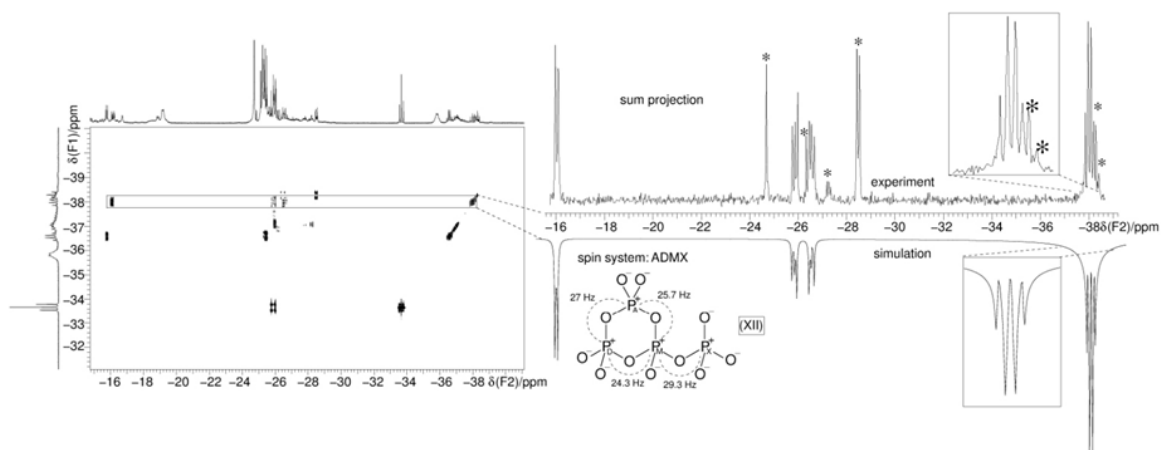


Figure S4: Zoom in of a ^{31}P COSY spectrum (middle). On the x and y axis ^{31}P single excitation spectra are shown. On the right top the sum projection of the section from the COSY spectrum surrounded by the box is shown versus a simulated sum projection. On the left top a zoom in the section is shown versus the simulation of the COSY spectrum of the ortho-phosphono-tricyclophosphate anion with ADMX spin system. The found J-couplings are depicted in the figure. Asterisks in the experimental sum projection mark peaks from other phosphate species, coming from overlapping signals in the 2D spectrum.

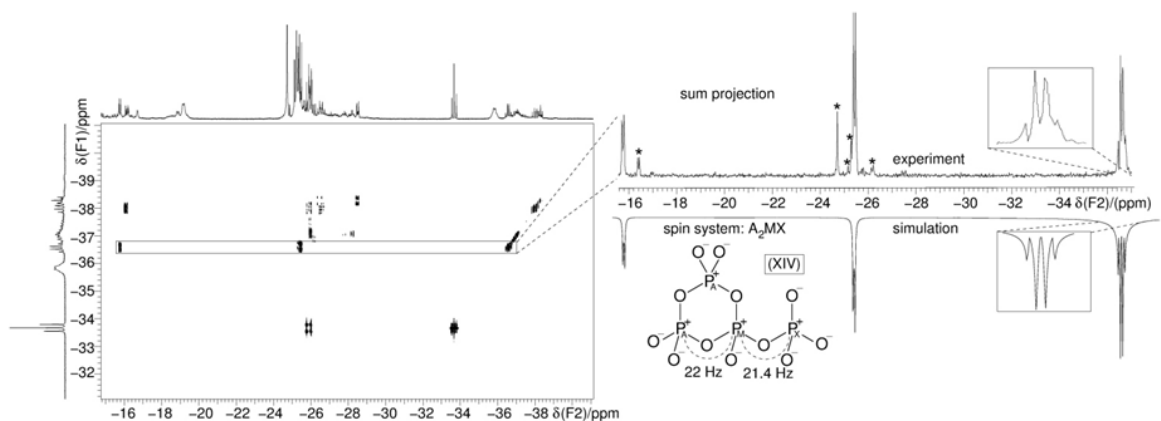


Figure S5: Zoom in of a ^{31}P COSY spectrum (middle). On the x and y axis ^{31}P single excitation spectra are shown. On the right top the sum projection of the section from the COSY spectrum surrounded by the box is shown versus a simulated sum projection. On the left top a zoom in the section is shown versus the simulation of the COSY spectrum of another ortho-phosphono-tricyclophosphate anion with A_2MX spin system. The found J-couplings are depicted in the figure. Asterisks in the experimental sum projection mark peaks from other phosphate species, coming from overlapping signals in the 2D spectrum.

2.3. Quantumchemical calculations

Table S2. Results of the calculations at HF/6-31G(d,p) level. ΔE_{total} is the total energy difference between the present and the lowest energetic isomer.

Molecule	E(HF/6-31G(d,p))	ZPE(HF)	Thermal correction ^a to H _i at T=			Hindered rotor correction, T=			ΔE_{total}	ΔE_{total}	ΔE_{total}	Symmetry
			298.15K=25° C	430K=157° C	500K=227° C	@298.15K	@430K	@500K	@298.15K	@430K	@500K	
			in a.u.	kJ/mol	kJ/mol	kJ/mol	kJ/mol	kJ/mol	kJ/mol	kJ/mol	kJ/mol	
C ₂ H ₅ S ⁺	-475.71054	169.37	15.14	26.44	33.39	0	0	-0.004	415.88	419.13	415.88	C ₂
cyclo-C ₂ H ₅ S ⁺	-475.87315	183.3	12.25	20.3	25.96	0	0	0	0	0	0	C _s
H ₂ C-S-CH ₃ ⁺	-475.871	180.81	14.6	26.18	32.72	-3.694	-4.523	-4.895	1.799233	4.5002	1.80	C _s
t-C ₂ H ₅ S ⁺	-475.79086	158.1	17.17	30.53	38.02	-2.276	-3.791	-4.548	193.4875	197.28	193.48	C ₂
t-cyclo-C ₂ H ₅ S ⁺	-475.63501	163.04	15.37	28.04	35.19	0	0	0	608.075	612.695	608.07	C ₁
t-H ₂ C-S-CH ₃ ⁺	-475.82411	169.95	15.41	27.64	34.58	-0.854	-1.527	-1.883	117.698	121.205	117.69	C _s

^a a scaling factor of 0.89286 was included

Table S3. Results of the DFT calculations at PBE1PBE/aug-cc-pVTZ level. ΔE_{total} is the total energy difference between the present and the lowest energetic isomer.

Molecule	E(PBE1PBE/aug-cc-pVTZ)	ZPE(DFT)	Thermal correction to H _i at T=			Hindered rotor correction, T=			ΔE_{total}	ΔE_{total}	ΔE_{total}	Symmetry
			298.15K=25° C	430=157° C	500K=227° C	298.15K	430K	500K	@298K	@430K	@500K	
			in a.u.	kJ/mol	kJ/mol	kJ/mol	kJ/mol	kJ/mol	kJ/mol	kJ/mol	kJ/mol	
C ₂ H ₅ S ⁺	-476.78829	155.53	15.78	27.23	34.23	-0.013	-0.063	-0.1	315.16	317.29	318.22	C ₂
cyclo-C ₂ H ₅ S ⁺	-476.91272	170.89	11.93	21.2	27.23	0	0	0	0.00	0.00	0.00	C _s
H ₂ C-S-CH ₃ ⁺	-476.90468	168.71	14.18	24.11	30.36	-2.556	-3.473	-3.887	18.62	18.36	18.17	C _s
t-C ₂ H ₅ S ⁺	-476.79251	149.09	16.77	28.85	36.15	-1.477	-2.565	-3.138	297.18	298.91	299.60	C ₁ (l)
t-cyclo-C ₂ H ₅ S ⁺	-476.79251	149.09	16.77	28.85	36.15	-1.477	-2.565	-3.138	297.18	298.91	299.60	C ₁ (ring opening)
t-H ₂ C-S-CH ₃ ⁺	-476.83018	158.53	15.46	26.65	33.49	-0.866	-1.548	-1.9	207.02	208.26	208.72	C _s

The optimized structures are shown in Fig. S6.

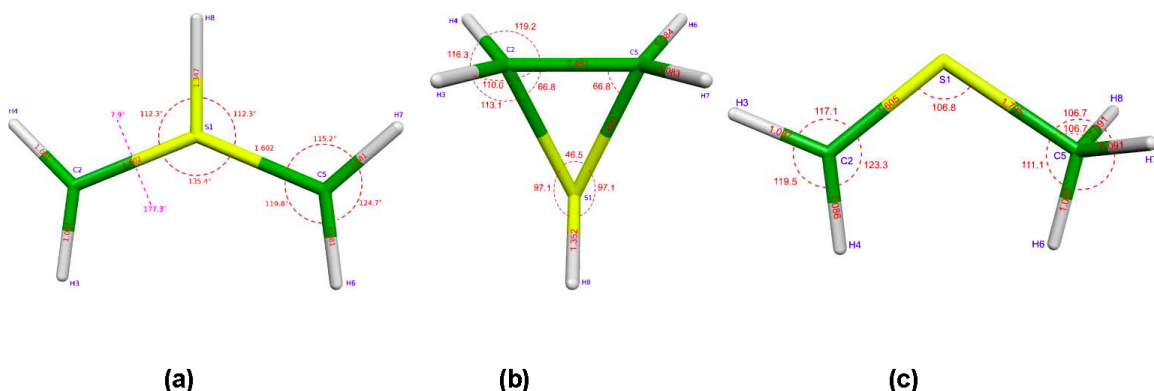


Figure S6. Optimized Structures on DFT (PBE1PBE/aug-cc-pVTZ) level. (a) C₂H₅S⁺, (b) cyclo-C₂H₅S⁺, (c) H₂C-S-CH₃⁺

2.4. SIMPSON input files**2.4.1 2D COSY simulation for Substance XII**

```

spinsys {
  channels 31P
  nuclei 31P 31P 31P 31P
  jcoupling 1 2 25.7 0 0 0 0
  jcoupling 2 3 27 0 0 0 0
  jcoupling 1 3 24.3 0 0 0 0
  jcoupling 1 4 29.3 0 0 0 0
  shift 1 -3651 0 0 0 0
  shift 2 -857 0 0 0 0
  shift 3 -687 0 0 0 0
  shift 4 1693 0 0 0 0
}

par {
  proton_frequency 600e6
  method direct
  spin_rate 0
  gamma_angles 1
  crystal_file alpha0beta0
  np 4096
  ni 512
  variable si 4096
  start_operator lnz
  detect_operator lnp
  verbose 11111111111111
  sw 13665
  sw1 11160
  variable lb 6
  variable resolution 0.0
}

proc pulseq {} {
  global par spinsys

  #DQ-Filter
  matrix set 1 totalcoherence {+1}
  matrix set 2 totalcoherence {0}

  #---evolution in t2 ----
  reset
  delay [expr 1.0e6/$par(sw)]
  store 2

  #---evolution in t1 ----
  reset
  delay [expr 1.0e6/$par(sw1)]
  store 1

  #---core program ----

  for {set i 0} {$i < $par(ni)} {incr i 2} {

    foreach ph {0.0 90.0} {
      reset

      pulseid 1 250000 $ph
      prop 1 [expr {$i/2}]
      filter 1
      pulseid 1 250000 90
      acq $par(np) 2
    }
  }
}

```

```

    }
  }
}
proc main {} {
  global par spinsys

# ----- start powder loop -----
  set f [fsimpson]

  fzerofill $f $par(si) $par(si)
  faddlb $f $par(lb) 0 $par(lb) 0 -phsens
  fft $f 0 0 0 0 -phsens

  for {set i 1} {$i <= $par(si)} {incr i} {
    for {set j 1} {$j <= $par(si)} {incr j} {
      set old [lindex $f $i $j]
      set re [lindex $old 0]
      set im [lindex $old 1]
      fsetindex $f $i $j [expr {sqrt($re*$re+$im*$im)}] 0.0
    }
  }
  fsave $f $par(name).spe -gnu2d
  funload $f
}

```

2.4.2 2D COSY simulation SIMPSON input file Substance XIII – Spin system part only

```

spinsys {
  channels 31P
  nuclei 31P 31P 31P 31P
  jcoupling 1 2 29.15 0 0 0 0 0
  jcoupling 1 3 29.15 0 0 0 0 0
  jcoupling 2 4 29.15 0 0 0 0 0
  jcoupling 3 4 29.15 0 0 0 0 0
  shift 1 -639 0 0 0 0 0
  shift 2 -2582 0 0 0 0 0
  shift 4 -639 0 0 0 0 0
  shift 3 -2582 0 0 0 0 0
}

```

2.4.3 2D COSY simulation SIMPSON input file Substance XIV – Spin system part only

```

spinsys {
  channels 31P
  nuclei 31P 31P 31P 31P

  jcoupling 1 2 22 0 0 0 0 0
  jcoupling 1 3 22 0 0 0 0 0
  jcoupling 1 4 21.4 0 0 0 0 0

  shift 1 -3311 0 0 0 0 0
  shift 2 -566 0 0 0 0 0
  shift 3 -566 0 0 0 0 0
  shift 4 1766 0 0 0 0 0
}

```

2.4.4. Gnuplot script for plotting 2D COSY spectrum of Substance XIII

```

set title "2D contourplot"
unset surface

```

```

set timestamp "%Y-%m-%d"
set contour
set cntrparam levels discrete 7 10000,540000,360000,240000,160000,130000
set view 0,90,1
set xlabel "SQ(F1)/ppm"
set ylabel "DQ(F2)/ppm"
set yrange [-12:-2]
set xrange [-11:-10]
set size square
splot "cosy-magnitude.spe" u ($1/242.828):($2/242.828):3 w l
set term postscript eps enhanced solid color
set output "cosy.eps"
replot

```

2.5. Chemical information of phosphates identified by NMR

I: H_3PO_4 : ^{31}P -NMR (270 MHz, DMSO, 25°C, TMS): $\delta_{\text{iso}}=0.44$ ppm
 II: $(\text{OP})(\text{O}-\text{CH}_2\text{R})_3$: ^{31}P -NMR (270 MHz, DMSO, 25°C, TMS): $\delta_{\text{iso}}=-3.7$ ppm
 III: $(\text{O}_2\text{P})(\text{O}-\text{CH}_2\text{R})_2$ -anion: ^{31}P -NMR (270 MHz, DMSO, 25°C, TMS): $\delta_{\text{iso}}=-4.36$ ppm
 IV: $(\text{O}_3\text{P})(\text{O}-\text{CH}_2\text{R})$ -anion: ^{31}P -NMR (270 MHz, DMSO, 25°C, TMS): $\delta_{\text{iso}}=-4.56$ ppm
 V: $(\text{RCH}_2\text{O})_2$ -OP-O- PO_3 -anion: ^{31}P -NMR (270 MHz, DMSO, 25°C, TMS): $\delta_{\text{iso}}=-10.79$ ppm,
 VI: $\text{P}_2\text{O}_7^{4-}$ -anion: ^{31}P -NMR (270 MHz, DMSO, 25°C, TMS): $\delta_{\text{iso}}=-12.4$ ppm
 VII: $(\text{RCH}_2\text{O})(\text{PO}_2)\text{O}-\text{PO}_3$ -anion: ^{31}P -NMR (270 MHz, DMSO, 25°C, TMS): $\delta_{\text{iso}}=-13.54$ ppm
 VIII: Tetraphosphate-anion: ^{31}P -NMR (270 MHz, DMSO, 25°C, TMS): $\delta_{\text{iso}}=-15$ ppm, $\delta_{\text{iso}}=-25.06$ ppm
 IX: $\text{PO}_3\text{O}-\text{PO}_2\text{O}-\text{PO}_3$ -anion: ^{31}P -NMR (270 MHz, DMSO, 25°C, TMS): $\delta_{\text{iso}}=-15.87$ ppm, $\delta_{\text{iso}}=-27.61$ ppm
 X: $(\text{RCH}_2\text{O})_2\text{OP}-\text{O}-\text{PO}(\text{OCH}_2\text{R})_2$: ^{31}P -NMR (270 MHz, DMSO, 25°C, TMS): $\delta_{\text{iso}}=-16.14$ ppm ($^2J(^{31}\text{P}_\text{A}-^{31}\text{P})=22.8$ Hz, $^3J(^1\text{H}-^1\text{H}) = 16.1$ Hz)
 XI: $\text{P}_4\text{O}_{12}^{4-}$ -anion: ^{31}P -NMR (270 MHz, DMSO, 25°C, TMS): $\delta_{\text{iso}}=-24.5$ ppm
 XII: $(\text{P}_3\text{O}_9\text{PO}_3)^4-$ -anion: ^{31}P -NMR (600 MHz, d_6 -DMSO, 25°C, TMS): $\delta_{\text{iso}}=-38$ ppm (q, $^2J(^{31}\text{P}_\text{A}-^{31}\text{P}_\text{M})=25.7$ Hz, $^2J(^{31}\text{P}_\text{M}-^{31}\text{P}_\text{X})=29.3$ Hz), $^2J(^{31}\text{P}_\text{D}-^{31}\text{P}_\text{M})=24.3$ Hz), -26.5 ppm (t, $^2J(^{31}\text{P}_\text{A}-^{31}\text{P}_\text{D})=27$ Hz, $^2J(^{31}\text{P}_\text{A}-^{31}\text{P}_\text{M})=25.7$ Hz), -25.8 ppm (t, $^2J(^{31}\text{P}_\text{A}-^{31}\text{P}_\text{D})=27$ Hz, $^2J(^{31}\text{P}_\text{D}-^{31}\text{P}_\text{M})=24.3$ Hz), -16 ppm (d, $^2J(^{31}\text{P}_\text{M}-^{31}\text{P}_\text{X})=29.3$ Hz)
 XIII: $\text{P}_4\text{O}_{11}^{2-}$ -anion: ^{31}P -NMR (600 MHz, d_6 -DMSO, 25°C, TMS): $\delta_{\text{iso}}=-33.6$ ppm (t, $^2J(^{31}\text{P}_\text{A}-^{31}\text{P}_\text{X})=29.15$ Hz), -25.6 ppm (d, $^2J(^{31}\text{P}_\text{A}-^{31}\text{P}_\text{X})=29.15$ Hz)
 XIV: $(\text{P}_3\text{O}_9\text{PO}_3)^4-$ -anion: ^{31}P -NMR (600 MHz, d_6 -DMSO, 25°C, TMS): $\delta_{\text{iso}}=-36.6$ ppm (q, $^2J(^{31}\text{P}_\text{A}-^{31}\text{P}_\text{M})=22$ Hz, $^2J(^{31}\text{P}_\text{M}-^{31}\text{P}_\text{X})=21.4$ Hz), -25.3 ppm (d, $^2J(^{31}\text{P}_\text{A}-^{31}\text{P}_\text{M})=22$ Hz), -15.7 ppm (d, $^2J(^{31}\text{P}_\text{M}-^{31}\text{P}_\text{X})=21.4$ Hz)

References

- [1] K. Onodera, S. Hirano, N. Kashimura, *J. Am. Chem. Soc.* **1965**, *87*, 4651–4652.
- [2] M. Bak, J. T. Rasmussen, N. C. Nielsen, *J. Magn. Reson.* **2000**, *147*, 296–330.
- [3] P. C. Hariharan, J. A. Pople, *Theor. Chim. Acta* **1973**, *28*, 213–222.
- [4] W. J. Hehre, R. Ditchfield, J. A. Pople, *J. Chem. Phys.* **1972**, *56*, 2257–2261.
- [5] J. P. Perdew, K. Burke, M. Ernzerhof, *Phys. Rev. Lett.* **1996**, *77*, 3865–3868.
- [6] J. P. Perdew, K. Burke, M. Ernzerhof, *Phys. Rev. Lett.* **1997**, *78*, 1396–1396.
- [7] "G03 Manual: DFT," can be found under http://www.ict.jussieu.fr/manuels/Gaussian03/g_ur/k_dft.htm, n.d.
- [8] T. H. Dunning, *J. Chem. Phys.* **1989**, *90*, 1007–1023.
- [9] G. I. Csonka, A. Ruzsinszky, J. P. Perdew, *J. Phys. Chem. B* **2005**, *109*, 21471–21475.
- [10] P. Pulay, *Adv. Chem. Phys.* **1987**, *69*, 241–286.
- [11] D. A. McQuarrie, *Molecular Thermodynamics*, University Science Books, **1999**.
- [12] Y.-Y. Chuang, D. G. Truhlar, *J. Chem. Phys.* **2000**, *112*, 1221–1228.
- [13] Y.-Y. Chuang, D. G. Truhlar, *J. Chem. Phys.* **2004**, *121*, 7036–7036.
- [14] Y.-Y. Chuang, D. G. Truhlar, *J. Chem. Phys.* **2006**, *124*, 179903.
- [15] T. Glonek, J. R. Van Wazer, R. A. Kleps, T. C. Myers, *Inorg. Chem.* **1974**, *13*, 2337–2345.

Author Contributions

- Sebastian Johansson: writing of original draft, data curation, analysis of NMR measurements, NMR simulations (lead)
- Christopher Kuhlmann: mass spectrometry measurements and data analysis (supporting)
- Dr. Johannes Weber: DFT calculations (supporting)
- Dr. Thomas Paululat: measuring of ³¹P-COSY-NMR (supporting)
- Prof. Dr. Jörn Schmedt auf der Günne: project administration, funding acquisition, analysis of NMR measurements, NMR simulations (lead)

Chapter 9

Concluding Remarks and Future Perspectives

9.1 Summary and Conclusion

In this doctoral dissertation, fundamental properties of plasma-based ambient desorption/ionization mass spectrometry (ADI-MS) techniques were investigated. Furthermore, new applications for fast screening, mass spectral imaging, and quantitative analysis of small molecules by plasma-based ADI-MS were developed.

In chapter 2, important parameters for the optimization of plasma-based ADI sources were introduced. Specifically, different instrumental modifications of direct analysis in real time (DART) and the flowing atmospheric-pressure afterglow (FAPA) source were explained and the benefits for these instrumental modifications were discussed. Furthermore, the desorption and ionization process for plasma-based ADI sources were briefly explained and examples from the literature were used to demonstrate how the analyte desorption and ionization can be modified with altered settings of the respective ADI source. In the following part, sample introduction devices for reproducible specimen introduction in front of the ADI source were presented. This overview comprised methods for analyte preconcentration by solid-phase microextraction (SPME) as well as the reproducible sample introduction via transmission-mode (TM) ADI-MS. Lastly, possible modifications to the mass spectrometers' atmospheric pressure interface were highlighted and the benefits for enhanced ion transfer from the sample surface into the mass spectrometer were presented.

In chapter 3, fundamental parameters of the FAPA source were optimized and the influence of these parameters towards the detected ion abundance were studied. First, the FAPA source angle towards the horizontal sample surface as well as the distance of the ADI source to the mass spectrometer inlet capillary were optimized. It was found that the maximum ion abundance of the caffeine model analyte was detected at a distance of 2 mm in combination with an FAPA angle of 60° and 70° and an identical ion abundance was detected at a distance of 3 mm with an angle of 50°. Furthermore, infrared (IR) thermography was performed on the analyte sampling surface when a FAPA source with differently long anode capillaries was operated right above the surface in a 60° angle. It was found that with the 11-mm long anode capillary enhanced surface temperatures of 213 °C (40 mA) on the glass plate were achieved in comparison of 111 °C (40 mA) for the 25-mm long capillary. The interelectrode distance of the pin cathode and the capillary anode was also tested and optimized for best ion abundance of the caffeine model analyte. Here it was found

that the ion abundance as well as the power consumption of the FAPA source linearly increased with the interelectrode distance. Lastly, a temperature-controlled sample platform with a water-cooled Peltier element was developed and successfully applied for the analysis of extremely volatile lithium-ion battery electrolytes via low-temperature plasma (LTP) mass spectrometry. The cooled analyte platform was needed for the analysis to avoid too fast analyte evaporation and the exact surface temperature was measured via IR-thermography.

In chapter 4, DART-, FAPA-, and LTP-MS were compared for the analysis of liquid crystals. For this task, liquid crystals standards, standard mixtures as well as liquid crystals extracted from a liquid crystal display (LCD) were analyzed by the ADI sources in transmission-mode. The analyte desorption was mainly caused by external heating of the metal wire screen so the analyte ion abundance was not limited by the molecule desorption. Therefore, a comparison of the ADI source ionization capabilities for such analytes could be made. It was found that with FAPA- and LTP-MS all probed analytes could be detected, due to the versatile ionization pathways via proton transfer or charge transfer ionization for both ADI sources. The observation that some analytes could not be detected by DART-MS is most probably attributed to less diverse cocktail of ionic species which ionized the analyte molecules. Because future application for liquid-crystal analysis may comprise the spatial resolved analysis of these compounds out of an LCD it is concluded that the DART (with a built-in plasma gas heater) and FAPA sources are the most promising techniques because both ADI sources were capable to thermally desorb the liquid-crystal analytes without externally heating the sample target.

In subsequent investigations, presented in chapter 5, mass spectral imaging was performed on LCD test cells via FAPA-MS. The spatially resolved distribution of the liquid crystals and adhesive materials in the test cell were compared to mass spectral imaging by laser ablation (LA) h-FAPA-MS. With both techniques it was possible to localize and differentiate small droplets of liquid crystals in the size range of 0.5-2 mm while the mass spectral images detected via LA-h-FAPA-MS appeared to include more details of even smaller sized droplets. Due to the small laser spot size of $\sim 20 \mu\text{m}$ a spatial resolution of at least 0.6 mm (full width at half maximum) was calculated for the method. Furthermore, it was demonstrated that with both methods even small irregularities such as liquid-crystal droplets intercalated into the adhesive material were spatially resolved.

In chapter 6, thin-layer chromatography (TLC) plates were coupled to mass spectrometry via the FAPA source and the influence of the stationary phase modification, particle size, and layer thickness on the detected analyte signal was

investigated. For these experiments the model analytes caffeine, nicotine, acetaminophen, and cortisone were chosen. The experimental results demonstrate that especially larger particle sizes and larger particle size distributions caused higher analyte signal abundances for TLC-FAPA-MS. These findings were presumably caused by the larger capillary channels in between the silica particles and the lower number of interaction spots for the analyte molecules on the particle surfaces. Accordingly, the thermal desorption of the analytes was enhanced. Furthermore, a steadily increasing ion abundance for the model analytes was observed with increasing thickness of the stationary phase (100-2000 μm). However, the assumption that thicker stationary phases cause an enhanced analyte signal was not completely clarified yet, because for the available TLC plates, the particle size and size distribution simultaneously increased with the thickness of the stationary phase. In consecutive experiments, silica plates with different surface modifications by bonded polar, medium polar, and non-polar functional groups were compared. For all model analytes, a significant increase of the detected ion abundance was observed when desorbed from non-polar and medium polar stationary phases in comparison to polar silica plates. Lastly, the TLC-FAPA-MS method was applied for quantitative analysis of caffeine in energy drinks. In this experiment, the chromatography enabled the separation of the beverage matrix from the analyte molecules to avoid *e.g.*, ion suppression by competitive ionization. Quantification was performed by stable isotope dilution analysis with a caffeine- $^{13}\text{C}_3$ standard and the obtained caffeine concentration confirmed the amount of caffeine stated by the energy drink container. The method was validated by quantifying the caffeine content in the same energy drinks via high-performance liquid chromatography and UV absorption detection (HPLC/UV).

The TLC-FAPA-MS method was further applied to the analysis of antimalarial active agents in chapter 7. In this chapter the literature known fragmentation mechanism of the two fragile artemether and lumefantrine molecules could be extended with five ions specific for the FAPA source. Furthermore, the development of a TLC separation method enabled the separation of the lumefantrine active agent from an isomeric synthesis by product prior FAPA-MS analysis, which is very useful for the quantification of lumefantrine in future applications.

Lastly, in chapter 8, FAPA-MS was applied for the direct analysis of a phosphorus pentoxide (P_4O_{10}) and dimethyl sulfoxide (DMSO) reaction mixture. Mass spectra were detected in positive- and negative-ion detection mode and several decomposition products of P_4O_{10} could be identified as well as the intermediate

product $C_2H_5S^+$. In combination with nuclear magnetic resonance (NMR) measurements and density functional theory (DFT) calculations the mass spectral data helped to elucidate the reaction mechanism between the two compounds.

9.2 Future Perspectives

In this thesis, important settings of the FAPA-MS technique were optimized and promising results for the analysis of real-world samples were reported. To further improve the performance of FAPA-MS the following suggestions are made for future research in this field.

For the analysis of liquid crystals some critical points were identified which significantly influence the quality of the spatially resolved information gained by FAPA-MS and LA-h-FAPA-MS. Most importantly, the formation of small droplets on the opened LCD test cell raised the issue that possible display failure spots might migrate on the glass surface in the moment the LCD was opened. To avoid this problem, a new sample preparation method has to be developed, which enables the opening of the LCD without the formation of the above-mentioned droplets. A possible way to achieve this goal might be the transfer of the liquid crystals into the crystalline state before opening the LCD. Also, the precise determination of the spatial resolution of the FAPA source and for the LA-h-FAPA-MS setup needs to be performed. Especially for the FAPA source this information was rarely found in the literature and therefore this information would be of great value for future spatial resolved analysis by FAPA-MS.

For TLC-MS coupling promising results with low detection limits were obtained for the analysis of model analytes via FAPA-MS. However, the influence of the silica particle size needs to be further investigated to validate the hypothesis made in chapter 6 that the particle size significantly influences the analyte desorption process. Furthermore, to correctly prove the trend of an enhanced analyte signal abundance with increasing stationary phase thickness further studies have to be made with TLC plates of various layer thicknesses but with identical particle sizes. Only under these circumstances it can be ensured that the trend of the analyte signal abundance originates from the altered layer thickness and not from a simultaneously changed particle size. Another critical aspect for future studies is to measure the interactions between the analyte molecules and the stationary phase. Because it is assumed that the analyte and stationary phase interactions influence the analyte desorption process the investigations on such interactions most probably improve the

understanding of the respective ADI-MS desorption process. A possible method to study such interactions might be the modification of an atomic force microscopy (AFM) cantilever with a model analyte so the binding strength between analyte and stationary phase can be measured.

Lastly, analyte quantification is still a challenging task for ADI-MS techniques due to competitive ionization between analytes or matrix effects. Consequently, expensive isotope-labeled standards are often used to circumvent these issues. However, TLC was found to be a promising tool for the separation of *e.g.* matrix and analyte and therefore TLC-FAPA-MS shall be more closely evaluated for analyte quantification without expensive standards.

References

- (1) Weston, D. J. *Analyst* **2010**, *135*, 661-668.
- (2) Alberici, R. M.; Simas, R. C.; Sanvido, G. B.; Romao, W.; Lalli, P. M.; Benassi, M.; Cunha, I. B.; Eberlin, M. N. *Anal. Bioanal. Chem.* **2010**, *398*, 265-294.
- (3) Chen, H.; Gamez, G.; Zenobi, R. *J. Am. Soc. Mass. Spectrom.* **2009**, *20*, 1947-1963.
- (4) Shelley, J. T.; Hieftje, G. M. *J. Anal. At. Spectrom.* **2011**, *26*, 2153-2159.
- (5) Albert, A.; Shelley, J. T.; Engelhard, C. *Anal. Bioanal. Chem.* **2014**, *406*, 6111-6127.
- (6) Takats, Z.; Wiseman, J. M.; Gologan, B.; Cooks, R. G. *Science* **2004**, *306*, 471-473.
- (7) Cody, R. B.; Laramée, J. A.; Durst, H. D. *Anal. Chem.* **2005**, *77*, 2297-2302.
- (8) Harper, J. D.; Charipar, N. A.; Mulligan, C. C.; Zhang, X. R.; Cooks, R. G.; Ouyang, Z. *Anal. Chem.* **2008**, *80*, 9097-9104.
- (9) Andrade, F. J.; Shelley, J. T.; Wetzel, W. C.; Webb, M. R.; Gamez, G.; Ray, S. J.; Hieftje, G. M. *Anal. Chem.* **2008**, *80*, 2646-2653.
- (10) Andrade, F. J.; Shelley, J. T.; Wetzel, W. C.; Webb, M. R.; Gamez, G.; Ray, S. J.; Hieftje, G. M. *Anal. Chem.* **2008**, *80*, 2654-2663.
- (11) Shelley, J. T.; Wiley, J. S.; Hieftje, G. M. *Anal. Chem.* **2011**, *83*, 5741-5748.
- (12) Schilling, G. D.; Shelley, J. T.; Broekaert, J. A. C.; Sperline, R. P.; Denton, M. B.; Barinaga, C. J.; Koppenaal, D. W.; Hieftje, G. M. *J. Anal. At. Spectrom.* **2009**, *24*, 34-40.
- (13) Shelley, J. T.; Wiley, J. S.; Chan, G. C. Y.; Schilling, G. D.; Ray, S. J.; Hieftje, G. M. *J. Am. Soc. Mass. Spectrom.* **2009**, *20*, 837-844.
- (14) Badal, S. P.; Michalak, S. D.; Chan, G. C.; You, Y.; Shelley, J. T. *Anal. Chem.* **2016**, *88*, 3494-3503.
- (15) Zeiri, O. M.; Storey, A. P.; Ray, S. J.; Hieftje, G. M. *Anal. Chim. Acta* **2017**, *952*, 1-8.
- (16) Badal, S. P.; Ratcliff, T. D.; You, Y.; Breneman, C. M.; Shelley, J. T. *J. Am. Soc. Mass. Spectrom.* **2017**, *28*, 1013-1020.
- (17) Johansson, S.; Kuhlmann, C.; Weber, J.; Paululat, T.; Engelhard, C.; Schmedt Auf der Gunne, J. *Chem. Commun.* **2018**, *54*, 7605-7608.
- (18) Kuhlmann, C.; Heide, M.; Engelhard, C. *Anal. Bioanal. Chem.* **2019**, *411*, 6213-6225.
- (19) Kuhlmann, C.; Shelley, J. T.; Engelhard, C. *J. Am. Soc. Mass. Spectrom.* **2019**, *30*, 2101-2113.
- (20) Yamashita, M.; Fenn, J. B. *J. Phys. Chem.* **1984**, *88*, 4451-4459.

- (21) Horning, E. C.; Horning, M. G.; Carroll, D. I.; Dzidic, I.; Stillwell, R. N. *Anal. Chem.* **1973**, *45*, 936-943.
- (22) Robb, D. B.; Covey, T. R.; Bruins, A. P. *Anal. Chem.* **2000**, *72*, 3653-3659.
- (23) Bruins, A. P. *Mass Spectrom. Rev.* **1991**, *10*, 53-77.
- (24) Karas, M.; Bachmann, D.; Hillenkamp, F. *Anal. Chem.* **1985**, *57*, 2935-2939.
- (25) Honig, R. E. *J. Appl. Phys.* **1958**, *29*, 549-555.
- (26) Barber, M.; Bordoli, R. S.; Sedgwick, R. D.; Tyler, A. N. *Nature* **1981**, *293*, 270-275.
- (27) Monge, M. E.; Harris, G. A.; Dwivedi, P.; Fernandez, F. M. *Chem. Rev.* **2013**, *113*, 2269-2308.
- (28) Nemes, P.; Vertes, A. *Anal. Chem.* **2007**, *79*, 8098-8106.
- (29) Schwartz, A. J.; Shelley, J. T.; Walton, C. L.; Williams, K. L.; Hieftje, G. M. *Chem. Sci.* **2016**, *7*, 6440-6449.
- (30) Na, N.; Zhang, C.; Zhao, M.; Zhang, S.; Yang, C.; Fang, X.; Zhang, X. *J. Mass Spectrom.* **2007**, *42*, 1079-1085.
- (31) Na, N.; Zhao, M.; Zhang, S.; Yang, C.; Zhang, X. *J. Am. Soc. Mass. Spectrom.* **2007**, *18*, 1859-1862.
- (32) McEwen, C. N.; McKay, R. G.; Larsen, B. S. *Anal. Chem.* **2005**, *77*, 7826-7831.
- (33) Ratcliffe, L. V.; Rutten, F. J.; Barrett, D. A.; Whitmore, T.; Seymour, D.; Greenwood, C.; Aranda-Gonzalvo, Y.; Robinson, S.; McCoustra, M. *Anal. Chem.* **2007**, *79*, 6094-6101.
- (34) Takats, Z.; Cotte-Rodriguez, I.; Talaty, N.; Chen, H. W.; Cooks, R. G. *Chem. Commun.* **2005**, *0*, 1950-1952.
- (35) Cotte-Rodríguez, I.; Mulligan, C. C.; Cooks, R. G. *Anal. Chem.* **2007**, *79*, 7069-7077.
- (36) Ding, X.; Duan, Y. *Mass Spectrom. Rev.* **2015**, *34*, 449-473.
- (37) Chen, J.; Tang, F.; Guo, C. a.; Zhang, S.; Zhang, X. *Anal. Methods* **2017**, *9*, 4908-4923.
- (38) Shelley, J. T.; Badal, S. P.; Engelhard, C.; Hayen, H. *Anal. Bioanal. Chem.* **2018**, *410*, 4061-4076.
- (39) Gross, J. H. *Anal. Bioanal. Chem.* **2014**, *406*, 63-80.
- (40) Kratzer, J.; Mester, Z.; Sturgeon, R. E. *Spectrochim. Acta, Part B* **2011**, *66*, 594-603.
- (41) Harris, G. A.; Fernández, F. M. *Anal. Chem.* **2009**, *81*, 322-329.
- (42) Chernetsova, E. S.; Revelsky, A. I.; Morlock, G. E. *Rapid Commun. Mass Spectrom.* **2011**, *25*, 2275-2282.

- (43) Perez, J. J.; Harris, G. A.; Chipuk, J. E.; Brodbelt, J. S.; Green, M. D.; Hampton, C. Y.; Fernandez, F. M. *Analyst* **2010**, *135*, 712-719.
- (44) Häbe, T. T.; Morlock, G. E. *Rapid Commun. Mass Spectrom.* **2016**, *30*, 321-332.
- (45) Cody, R. B. *Anal. Chem.* **2009**, *81*, 1101-1107.
- (46) Häbe, T. T.; Morlock, G. E. *Rapid Commun. Mass Spectrom.* **2015**, *29*, 474-484.
- (47) Jecklin, M. C.; Gamez, G.; Touboul, D.; Zenobi, R. *Rapid Commun. Mass Spectrom.* **2008**, *22*, 2791-2798.
- (48) Wiley, J. S.; Garcia-Reyes, J. F.; Harper, J. D.; Charipar, N. A.; Ouyang, Z.; Cooks, R. G. *Analyst* **2010**, *135*, 971-979.
- (49) Nilles, J. M.; Connell, T. R.; Durst, H. D. *Analyst* **2010**, *135*, 883-886.
- (50) Pfeuffer, K. P.; Schaper, J. N.; Shelley, J. T.; Ray, S. J.; Chan, G. C. Y.; Bings, N. H.; Hieftje, G. M. *Anal. Chem.* **2013**, *85*, 7512-7518.
- (51) Schaper, J. N.; Pfeuffer, K. P.; Shelley, J. T.; Bings, N. H.; Hieftje, G. M. *Anal. Chem.* **2012**, *84*, 9246-9252.
- (52) Orejas, J.; Pfeuffer, K. P.; Ray, S. J.; Pisonero, J.; Sanz-Medel, A.; Hieftje, G. M. *Anal. Bioanal. Chem.* **2014**, *406*, 7511-7521.
- (53) Venter, A.; Nefliu, M.; Graham Cooks, R. *Trends Anal. Chem.* **2008**, *27*, 284-290.
- (54) Manova, R. K.; Claassen, F. W.; Nielen, M. W.; Zuilhof, H.; van Beek, T. A. *Chem. Commun.* **2013**, *49*, 922-924.
- (55) Shelley, J. T.; Chan, G. C. Y.; Hieftje, G. M. *J. Am. Soc. Mass. Spectrom.* **2012**, *23*, 407-417.
- (56) Maleknia, S. D.; Vail, T. M.; Cody, R. B.; Sparkman, D. O.; Bell, T. L.; Adams, M. A. *Rapid Commun. Mass Spectrom.* **2009**, *23*, 2241-2246.
- (57) Chan, G. C. Y.; Shelley, J. T.; Wiley, J. S.; Engelhard, C.; Jackson, A. U.; Cooks, R. G.; Hieftje, G. M. *Anal. Chem.* **2011**, *83*, 3675-3686.
- (58) Penning, F. M. *Naturwissenschaften* **1927**, *15*, 818.
- (59) Dzidic, I.; Carroll, D. I.; Stillwell, R. N.; Horning, E. C. *Anal. Chem.* **1976**, *48*, 1763-1768.
- (60) Carroll, D. I.; Dzidic, I.; Stillwell, R. N.; Haegele, K. D.; Horning, E. C. *Anal. Chem.* **1975**, *47*, 2369-2373.
- (61) Cunningham, A. J.; Payzant, J. D.; Kebarle, P. J. *Am. Chem. Soc.* **1972**, *94*, 7627-7632.
- (62) Kebarle, P.; Hogg, A. M. *J. Chem. Phys.* **1965**, *42*, 798-799.
- (63) Vaclavik, L.; Cajka, T.; Hrbek, V.; Hajslova, J. *Anal. Chim. Acta* **2009**, *645*, 56-63.
- (64) Haunschmidt, M.; Klampfl, C. W.; Buchberger, W.; Hertsens, R. *Analyst* **2010**, *135*, 80-85.

- (65) Wright, J. P.; Heywood, M. S.; Thurston, G. K.; Farnsworth, P. B. *J. Am. Soc. Mass. Spectrom.* **2013**, *24*, 335-340.
- (66) Ellis, W. C.; Lewis, C. R.; Openshaw, A. P.; Farnsworth, P. B. *J. Am. Soc. Mass. Spectrom.* **2016**, *27*, 1539-1549.
- (67) Na, N.; Xia, Y.; Zhu, Z. L.; Zhang, X. R.; Cooks, R. G. *Angew. Chem. Int. Ed.* **2009**, *48*, 2017-2019.
- (68) Vaclavik, L.; Zachariasova, M.; Hrbek, V.; Hajslova, J. *Talanta* **2010**, *82*, 1950-1957.
- (69) Steiner, R. R.; Larson, R. L. *J. Forensic Sci.* **2009**, *54*, 617-622.
- (70) Pfeuffer, K. P.; Shelley, J. T.; Ray, S. J.; Hieftje, G. M. *J. Anal. At. Spectrom.* **2013**, *28*, 379-387.
- (71) Jeckelmann, N.; Haefliger, O. P. *Rapid Commun. Mass Spectrom.* **2010**, *24*, 1165-1171.
- (72) Jones, C. M.; Fernandez, F. M. *Rapid Commun. Mass Spectrom.* **2013**, *27*, 1311-1318.
- (73) Jagerdeo, E.; Abdel-Rehim, M. J. *J. Am. Soc. Mass. Spectrom.* **2009**, *20*, 891-899.
- (74) Wang, X.; Li, X.; Li, Z.; Zhang, Y.; Bai, Y.; Liu, H. *Anal. Chem.* **2014**, *86*, 4739-4747.
- (75) Rodriguez-Lafuente, A.; Mirnaghi, F. S.; Pawliszyn, J. *Anal. Bioanal. Chem.* **2013**, *405*, 9723-9727.
- (76) Haunschmidt, M.; Klampfl, C. W.; Buchberger, W.; Hertsens, R. *Anal. Bioanal. Chem.* **2010**, *397*, 269-275.
- (77) Dumlao, M. C.; Jeffress, L. E.; Gooding, J. J.; Donald, W. A. *Analyst* **2016**, *141*, 3714-3721.
- (78) Mirabelli, M. F.; Wolf, J.-C.; Zenobi, R. *Anal. Chem.* **2016**, *88*, 7252-7258.
- (79) Mirnaghi, F. S.; Pawliszyn, J. *Anal. Chem.* **2012**, *84*, 8301-8309.
- (80) Gómez-Ríos, G. A.; Pawliszyn, J. *Chem. Commun.* **2014**, *50*, 12937-12940.
- (81) Takats, Z.; Wiseman, J. M.; Cooks, R. G. *J. Mass Spectrom.* **2005**, *40*, 1261-1275.
- (82) Wu, S.; Zhang, K.; Kaiser, N. K.; Bruce, J. E.; Prior, D. C.; Anderson, G. A. *J. Am. Soc. Mass. Spectrom.* **2006**, *17*, 772-779.
- (83) Yu, S.; Crawford, E.; Tice, J.; Musselman, B.; Wu, J.-T. *Anal. Chem.* **2009**, *81*, 193-202.
- (84) Garimella, S.; Xu, W.; Huang, G.; Harper, J. D.; Cooks, R. G.; Ouyang, Z. *J. Mass Spectrom.* **2012**, *47*, 201-207.
- (85) Harris, G. A.; Galhena, A. S.; Fernandez, F. M. *Anal. Chem.* **2011**, *83*, 4508-4538.

- (86) Huang, G. M.; Xu, W.; Visbal-Onufrak, M. A.; Ouyang, Z.; Cooks, R. G. *Analyst* **2010**, *135*, 705-711.
- (87) Soparawalla, S.; Tadjimukhamedov, F. K.; Wiley, J. S.; Ouyang, Z.; Cooks, R. G. *Analyst* **2011**, *136*, 4392.
- (88) Albert, A.; Engelhard, C. *Spectrochim. Acta, Part B* **2015**, *105*, 109-115.
- (89) Lu, X.; Laroussi, M. *J. Appl. Phys.* **2005**, *98*, 023301.
- (90) Pfeuffer, K. P.; Ray, S. J.; Hieftje, G. M. *J. Am. Soc. Mass. Spectrom.* **2014**, *25*, 800-808.
- (91) Campbell, D. I.; Dalgleish, J. K.; Cotte-Rodriguez, I.; Maeno, S.; Cooks, R. G. *Rapid Commun. Mass Spectrom.* **2013**, *27*, 1828-1836.
- (92) Albert, A.; Engelhard, C. *Anal. Chem.* **2012**, *84*, 10657-10664.
- (93) Schuster, N.; Kolobrodov, V. G. In *Infrarotthermographie*; Wiley-VCH: Berlin, 2004, pp 50-77.
- (94) Testo SE & Co. KGaA. Emissivities of the most important materials (in German), https://www.testo.com/de-DE/Emissionsgrade+der+wichtigsten+Materialien/services_knowledgeable_thermography_emissivity_table, (accessed on 11.02.2019).
- (95) Bogaard, R. H. In *Thermal Conductivity 18*, Ashworth, T.; Smith, D. R., Eds.; Springer: Boston (MA), 1985, pp 175-185.
- (96) Assael, M. J.; Gialou, K. *Int. J. Thermophys.* **2003**, *24*, 1145-1153.
- (97) Vogt, P. F.; Gerulis, J. J. In *Ullmann's Encyclopedia of Industrial Chemistry*; Wiley-VCH: Weinheim, 2012, pp 699-718.
- (98) Pokorný, V.; Štejfa, V.; Fulem, M.; Červinka, C.; Růžička, K. *J. Chem. Eng. Data* **2017**, *62*, 3206-3215.
- (99) Pokorný, V.; Štejfa, V.; Fulem, M.; Červinka, C.; Růžička, K. *J. Chem. Eng. Data* **2017**, *62*, 4174-4186.
- (100) Jung, H.-G.; Hassoun, J.; Park, J.-B.; Sun, Y.-K.; Scrosati, B. *Nat. Chem.* **2012**, *4*, 579-585.
- (101) Li, F.-S.; Wu, Y.-S.; Chou, J.; Winter, M.; Wu, N.-L. *Adv. Mater.* **2015**, *27*, 130-137.
- (102) Henschel, J.; Schwarz, J. L.; Glorius, F.; Winter, M.; Nowak, S. *Anal. Chem.* **2019**, *91*, 3980-3988.
- (103) Vortmann, B.; Nowak, S.; Engelhard, C. *Anal. Chem.* **2013**, *85*, 3433-3438.
- (104) Terborg, L.; Nowak, S.; Passerini, S.; Winter, M.; Karst, U.; Haddad, P. R.; Nesterenko, P. N. *Anal. Chim. Acta* **2012**, *714*, 121-126.

- (105) Terborg, L.; Weber, S.; Blaske, F.; Passerini, S.; Winter, M.; Karst, U.; Nowak, S. *J. Power Sources* **2013**, *242*, 832-837.
- (106) Smith, C. A. *Circuit World* **2008**, *34*, 35-41.
- (107) Kelly, S. M.; O'Neill, M. In *Liquid Crystals, Display and Laser Materials*, Nalwa, H. S., Ed.; Academic Press, 2001, pp 1-66.
- (108) Dishoungh, T. J.; Dube, M.; Pecht, M.; Wyler, J. J. *Electron. Packaging* **1999**, *121*, 126-127.
- (109) Miyaki, S.; Yoshida, A.; Yamamoto, Y.; Takeuchi, K. *Appl. Surf. Sci.* **2003**, *203*, 836-841.
- (110) Müller, J.-C.; Berg, T.; Enders, C.; Leonhard, P.; Karst, U. *Anal. Chim. Acta* **2019**, *1055*, 56-64.
- (111) Takatsuiji, H. *Mater. Sci. Semicond. Process.* **2001**, *4*, 309-312.
- (112) Haddad, R.; Sparrapan, R.; Eberlin, M. N. *Rapid Commun. Mass Spectrom.* **2006**, *20*, 2901-2905.
- (113) Chen, H. W.; Venter, A.; Cooks, R. G. *Chem. Commun.* **2006**, 2042-2044.
- (114) Haddad, R.; Sparrapan, R.; Kotiaho, T.; Eberlin, M. N. *Anal. Chem.* **2008**, *80*, 898-903.
- (115) Ratcliffe, L. V.; Rutten, F. J. M.; Barrett, D. A.; Whitmore, T.; Seymour, D.; Greenwood, C.; Aranda-Gonzalvo, Y.; Robinson, S.; McCoustra, M. *Anal. Chem.* **2007**, *79*, 6094-6101.
- (116) Hajslova, J.; Cajka, T.; Vaclavik, L. *Trends Anal. Chem.* **2011**, *30*, 204-218.
- (117) Chernetsova, E. S.; Morlock, G. E.; Revelsky, I. A. *Russ. Chem. Rev.* **2011**, *80*, 235-255.
- (118) Krechmer, J.; Tice, J.; Crawford, E.; Musselman, B. *Rapid Commun. Mass Spectrom.* **2011**, *25*, 2384-2388.
- (119) Albert, A.; Kramer, A.; Scheeren, S.; Engelhard, C. *Anal. Methods* **2014**, *6*, 5463-5471.
- (120) Jecklin, M. C.; Gamez, G.; Zenobi, R. *Analyst* **2009**, *134*, 1629-1636.
- (121) Jackson, A. U.; Garcia-Reyes, J. F.; Harper, J. D.; Wiley, J. S.; Molina-Diaz, A.; Ouyang, Z.; Cooks, R. G. *Analyst* **2010**, *135*, 927-933.
- (122) Song, L. G.; Gibson, S. C.; Bhandari, D.; Cook, K. D.; Bartmess, J. E. *Anal. Chem.* **2009**, *81*, 10080-10088.
- (123) Shelley, J. T.; Hieftje, G. M. *J. Anal. At. Spectrom.* **2010**, *25*, 345-350.
- (124) Bramson, M. A. In *Infrared Radiation: A Handbook for Applications*, Wolfe, W. L., Ed.; Plenum Press: New York, 1968, p 132.
- (125) Einolf, N.; Munson, B. *Int. J. Mass Spectrom. Ion Physics* **1972**, *9*, 141-160.

- (126) Kuklya, A.; Engelhard, C.; Kerpen, K.; Telgheder, U. *J. Anal. At. Spectrom.* **2016**, *31*, 1574-1581.
- (127) National Center for Biotechnology Information. PubChem Database. N-(4-Methoxybenzylidene)-4-butylaniline, CID=33363, <https://pubchem.ncbi.nlm.nih.gov/compound/33363>, (accessed on 22.05.2019).
- (128) Ascenzi, D.; Franceschi, P.; Guella, G.; Tosi, P. *J. Phys. Chem. A* **2006**, *110*, 7841-7847.
- (129) Callahan, J. L.; Grasselli, R. K.; Milberger, E. C.; Strecker, H. A. *Ind. Eng. Chem. Prod. Res. Dev.* **1970**, *9*, 134-142.
- (130) Chan, G. C. Y.; Shelley, J. T.; Jackson, A. U.; Wiley, J. S.; Engelhard, C.; Cooks, R. G.; Hieftje, G. M. *J. Anal. At. Spectrom.* **2011**, *26*, 1434-1444.
- (131) Kertesz, V.; Van Berkel, G. J. *Rapid Commun. Mass Spectrom.* **2008**, *22*, 2639-2644.
- (132) Ifa, D. R.; Gumaelius, L. M.; Eberlin, L. S.; Manicke, N. E.; Cooks, R. G. *Analyst* **2007**, *132*, 461-467.
- (133) Wiseman, J. M.; Ifa, D. R.; Zhu, Y.; Kissinger, C. B.; Manicke, N. E.; Kissinger, P. T.; Cooks, R. G. *Proc. Natl. Acad. Sci. U.S.A.* **2008**, *105*, 18120-18125.
- (134) Perez, C. J.; Bagga, A. K.; Prova, S. S.; Yousefi Taemeh, M.; Ifa, D. R. *Rapid Commun. Mass Spectrom.* **2018**, *33*, 27-53.
- (135) Morlock, G.; Ueda, Y. *J. Chromatogr. A* **2007**, *1143*, 243-251.
- (136) Liu, Y.; Ma, X.; Lin, Z.; He, M.; Han, G.; Yang, C.; Xing, Z.; Zhang, S.; Zhang, X. *Angew. Chem. Int. Ed.* **2010**, *49*, 4435-4437.
- (137) Galhena, A. S.; Harris, G. A.; Nyadong, L.; Murray, K. K.; Fernández, F. M. *Anal. Chem.* **2010**, *82*, 2178-2181.
- (138) Fowble, K. L.; Teramoto, K.; Cody, R. B.; Edwards, D.; Guarrera, D.; Musah, R. A. *Anal. Chem.* **2017**, *89*, 3421-3429.
- (139) Shelley, J. T.; Ray, S. J.; Hieftje, G. M. *Anal. Chem.* **2008**, *80*, 8308-8313.
- (140) Badu-Tawiah, A. K.; Eberlin, L. S.; Ouyang, Z.; Cooks, R. G. *Annu. Rev. Phys. Chem.* **2013**, *64*, 481-505.
- (141) Smith, N. J.; Domin, M. A.; Scott, L. T. *Org. Lett.* **2008**, *10*, 3493-3496.
- (142) Kim, H. J.; Jang, Y. P. *Phytochem. Anal* **2009**, *20*, 372-377.
- (143) Morlock, G.; Chernetsova, E. S. *Cent. Eur. J. Chem.* **2012**, *10*, 703-710.
- (144) Block, R. J.; Durrum, E. L.; Zweig, G. In *A Manual of Paper Chromatography and Paper Electrophoresis*; Academic Press Inc.: New York, 1955, pp 6-17.
- (145) Sherma, J. *Anal. Chem.* **1996**, *68*, 1-20.

- (146) Liu, J. J.; Wang, H.; Manicke, N. E.; Lin, J. M.; Cooks, R. G.; Ouyang, Z. *Anal. Chem.* **2010**, *82*, 2463-2471.
- (147) Wang, H.; Liu, J.; Cooks, R. G.; Ouyang, Z. *Angew. Chem. Int. Ed.* **2010**, *49*, 877-880.
- (148) Sherma, J. In *Handbook of Thin-Layer Chromatography*, Sherma, J.; Fried, B., Eds.; Marcel Dekker: New York, 2003, pp 1-61.
- (149) Spangenberg, B.; Poole, C. F.; Weins, C. In *Quantitative Thin-Layer Chromatography*, Spangenberg, B.; Poole, C. F.; Weins, C., Eds.; Springer: Heidelberg, 2011, pp 53-80.
- (150) Rabel, F. M. In *Handbook of Thin-Layer Chromatography*, Sherma, J.; Fried, B., Eds.; Marcel Dekker: New York, 2003, pp 129-176.
- (151) Nyiredy, S. In *Handbook of Thin-Layer Chromatography*, Sherma, J.; Fried, B., Eds.; Marcel Dekker: New York, 2003, pp 399-441.
- (152) Sherma, J. *J. Chromatogr. A* **2000**, *880*, 129-147.
- (153) Kushi, Y.; Handa, S. *J. Biochem.* **1985**, *98*, 265-268.
- (154) Nakagawa, Y.; Iwatani, K. *J. Chromatogr. B* **1991**, *562*, 99-110.
- (155) Guittard, J.; Hronowski, X. L.; Costello, C. E. *Rapid Commun. Mass Spectrom.* **1999**, *13*, 1838-1849.
- (156) Gusev, A. I.; Proctor, A.; Rabinovich, Y. I.; Hercules, D. M. *Anal. Chem.* **1995**, *67*, 1805-1814.
- (157) Luftmann, H. *Anal. Bioanal. Chem.* **2004**, *378*, 964-968.
- (158) Van Berkel, G. J.; Sanchez, A. D.; Quirke, J. M. E. *Anal. Chem.* **2002**, *74*, 6216-6223.
- (159) Van Berkel, G. J.; Tomkins, B. A.; Kertesz, V. *Anal. Chem.* **2007**, *79*, 2778-2789.
- (160) Van Berkel, G. J.; Ford, M. J.; Deibel, M. A. *Anal. Chem.* **2005**, *77*, 1207-1215.
- (161) Pasilis, S. P.; Kertesz, V.; Van Berkel, G. J.; Schulz, M.; Schorcht, S. *Anal. Bioanal. Chem.* **2008**, *391*, 317-324.
- (162) Haddad, R.; Milagre, H. M. S.; Catharino, R. R.; Eberlin, M. N. *Anal. Chem.* **2008**, *80*, 2744-2750.
- (163) Morlock, G.; Schwack, W. *Anal. Bioanal. Chem.* **2006**, *385*, 586-595.
- (164) Ceglowski, M.; Smoluch, M.; Reszke, E.; Silberring, J.; Schroeder, G. *Anal. Bioanal. Chem.* **2016**, *408*, 815-823.
- (165) Prosek, M.; Golc-Wondra, A.; Vovk, I.; Andrensek, S. *J. Planar Chromat.* **2000**, *13*, 452-456.
- (166) Aranda, M.; Morlock, G. *Rapid Commun. Mass Spectrom.* **2007**, *21*, 1297-1303.

- (167) Kertesz, V.; Van Berkel, G. J. *Rapid Commun. Mass Spectrom.* **2008**, *22*, 3846-3850.
- (168) Harry, E. L.; Reynolds, J. C.; Bristow, A. W. T.; Wilson, I. D.; Creaser, C. S. *Rapid Commun. Mass Spectrom.* **2009**, *23*, 2597-2604.
- (169) Kauppila, T. J.; Talaty, N.; Salo, P. K.; Kotiah, T.; Kostianen, R.; Cooks, R. G. *Rapid Commun. Mass Spectrom.* **2006**, *20*, 2143-2150.
- (170) Pellegrini, M.; Marchei, E.; Rossi, S.; Vagnarelli, F.; Durgbanshi, A.; Garcia-Algar, O.; Vall, O.; Pichini, S. *Rapid Commun. Mass Spectrom.* **2007**, *21*, 2693-2703.
- (171) National Center for Biotechnology Information. PubChem Database. Caffeine, CID=2519, <https://pubchem.ncbi.nlm.nih.gov/compound/Caffeine>, (accessed on 19.06.2019).
- (172) National Center for Biotechnology Information. PubChem Database. Acetaminophen, CID=1983, <https://pubchem.ncbi.nlm.nih.gov/compound/Acetaminophen>, (accessed on 19.06.2019).
- (173) National Center for Biotechnology Information. PubChem Database. Nicotine, CID=89594, <https://pubchem.ncbi.nlm.nih.gov/compound/Nicotine>, (accessed on 19.06.2019).
- (174) *Definition and Procedure for the Determination of the Method Detection Limit*; 40 CFR 136; U.S. Environmental Protection Agency: Washington, DC, 2011; pp 343-346.
- (175) Graton, J.; Berthelot, M.; Gal, J.-F.; Laurence, C.; Lebreton, J.; Le Questel, J.-Y.; Maria, P.-C.; Robins, R. *J. Org. Chem.* **2003**, *68*, 8208-8221.
- (176) Griesinger, H.; Fuchs, B.; Süß, R.; Matheis, K.; Schulz, M.; Schiller, J. *Anal. Biochem.* **2014**, *451*, 45-47.
- (177) Aranda, M.; Morlock, G. *J. Chromatogr. A* **2006**, *1131*, 253-260.
- (178) WHO. *World Malaria Report 2018*; World Health Organization: Geneva, 2018.
- (179) World Health Organization. Geneva. Malaria Vaccine Implementation Programme (MVIP), https://www.who.int/immunization/diseases/malaria/malaria_vaccine_implementation_programme/about/en/, (accessed on 23.04.2019).
- (180) Nosten, F.; White, N. J. In *Defining and Defeating the Intolerable Burden of Malaria III: Progress and Perspectives*, Breman, J. G.; Alilio, M. S.; White, N. J., Eds.; American Society of Tropical Medicine and Hygiene: Northbrook (IL), 2007, pp 181-192.

- (181) WHO. *Guidelines for the treatment of malaria*, 3rd ed.; World Health Organization: Geneva, 2015.
- (182) Newton, P. N.; Green, M. D.; Mildenhall, D. C.; Plançon, A.; Nettey, H.; Nyadong, L.; Hostetler, D. M.; Swamidoss, I.; Harris, G. A.; Powell, K.; Timmermans, A. E.; Amin, A. A.; Oponi, S. K.; Barbereau, S.; Faurant, C.; Soong, R. C. W.; Faure, K.; Thevanayagam, J.; Fernandes, P.; Kaur, H.; Angus, B.; Stepniewska, K.; Guerin, P. J.; Fernández, F. M. *Malar. J.* **2011**, *10*, 352-374.
- (183) Green, M. D.; Hostetler, D. M.; Nettey, H.; Swamidoss, I.; Ranieri, N.; Newton, P. N. *Am. J. Trop. Med. Hyg.* **2015**, *92*, 8-16.
- (184) Green, M. D.; Nettey, H.; Rojas, O. V.; Pamanivong, C.; Khounsaknalath, L.; Ortiz, M. G.; Newton, P. N.; Fernández, F. M.; Vongsack, L.; Manolin, O. J. *Pharm. Biomed. Anal.* **2007**, *43*, 105-110.
- (185) Hall, K. A.; Pizzanelli, D.; Green, M. D.; Dondorp, A.; De Veij, M.; Mayxay, M.; Fernandez, F. M.; Vandenabeele, P.; Newton, P. N. *Am. J. Trop. Med. Hyg.* **2006**, *75*, 804-811.
- (186) Camps, C.; Toussirot, M.; Quennoz, M.; Simonnet, X. J. *Near Infrared Spectrosc.* **2011**, *19*, 191-198.
- (187) de Veij, M.; Vandenabeele, P.; Hall, K. A.; Fernandez, F. M.; Green, M. D.; White, N. J.; Dondorp, A. M.; Newton, P. N.; Moens, L. J. *Raman Spectrosc.* **2007**, *38*, 181-187.
- (188) Quennoz, M.; Bastian, C.; Simonnet, X.; Grogg, A. F. *CHIMIA* **2010**, *64*, 755-757.
- (189) Khuluza, F.; Kigera, S.; Jähnke, R. W. O.; Heide, L. *Malar. J.* **2016**, *15*, 215-221.
- (190) Bate, R.; Tren, R.; Hess, K.; Mooney, L.; Porter, K. *Afr. J. Pharm. Pharmacol.* **2009**, *3*, 165-170.
- (191) McCalley, D. V. J. *Chromatogr. A* **2002**, *967*, 1-19.
- (192) Samanidou, V. F.; Evaggelopoulou, E. N.; Papadoyannis, I. N. *J. Pharm. Biomed. Anal.* **2005**, *38*, 21-28.
- (193) Navaratnam, V.; Mansor, S. M.; Chin, L. K.; Mordi, M. N.; Asokan, M.; Nair, N. K. J. *Chromatogr. B* **1995**, *669*, 289-294.
- (194) Karbwang, J.; Na-Bangchang, K.; Molunto, P.; Banmairuroi, V.; Congpuong, K. J. *Chromatogr. B* **1997**, *690*, 259-265.
- (195) Hoffmann, C. V.; Lämmerhofer, M.; Lindner, W. *Anal. Bioanal. Chem.* **2008**, *393*, 1257-1265.
- (196) Gatti, R.; Gioia, M. G.; Cavrini, V. *Anal. Chim. Acta* **2004**, *512*, 85-91.

- (197) Habyalimana, V.; Mbinze, J. K.; Tshilombo, N. K.; Dispas, A.; Loconon, A. Y.; Sacré, P.-Y.; Widart, J.; De Tullio, P.; Counerotte, S.; Ntokamunda, J.-L. K.; Ziemons, E.; Hubert, P.; Djang'eing'a, R. M. *Am. J. Analyt. Chem.* **2015**, *06*, 977-994.
- (198) Bernier, M. C.; Li, F.; Musselman, B.; Newton, P. N.; Fernández, F. M. *Anal. Methods* **2016**, *8*, 6616-6624.
- (199) Fernández, F. M.; Cody, R. B.; Green, M. D.; Hampton, C. Y.; McGready, R.; Sengaloundeth, S.; White, N. J.; Newton, P. N. *ChemMedChem* **2006**, *1*, 702-705.
- (200) Ateacha, D. N.; Kuhlmann, C.; Engelhard, C. *Anal. Methods* **2019**, *11*, 566-574.
- (201) Santos, V. G. d.; Alves, R. J.; Eberlin, M. N.; Pianetti, G. A.; César, I. C. *J. Braz. Chem. Soc.* **2012**.
- (202) Xing, J.; Yan, H.; Zhang, S.; Ren, G.; Gao, Y. *Rapid Commun. Mass Spectrom.* **2006**, *20*, 1463-1468.
- (203) Vandercruyssen, K.; D'Hondt, M.; Vergote, V.; Jansen, H.; Burvenich, C.; De Spiegeleer, B. *J. Pharm. Anal.* **2014**, *4*, 37-52.
- (204) Shi, B.; Yu, Y.; Li, Z.; Zhang, L.; Zhong, Y.; Su, S.; Liang, S. *Chromatographia* **2006**, *64*, 523-530.
- (205) Verbeken, M.; Suleman, S.; Baert, B.; Vangheluwe, E.; Van Dorpe, S.; Burvenich, C.; Duchateau, L.; Jansen, F. H.; De Spiegeleer, B. *Malar. J.* **2011**, *10*, 51-59.

Appendix

11.1 Mass Spectrometer Operating Conditions for ADI-MS

Table 11.1 Mass spectrometer operating conditions used for the FAPA-MS and LTP-MS experiments in chapter 3.

	FAPA-MS (Exactive)	LTP-MS (Exactive)
Scan range	m/z 50-1000	m/z 50-1000
Fragmentation	HCD Gas: on fragmentation energy: off	HCD Gas: on fragmentation energy: off
Resolution	High (50,000)	High (50,000)
Polarity	Positive	Positive
Micro scan count	1	1
Lock mass	off	off
AGC target	1,000,000	1,000,000
Maximum injection time	10 ms	10 ms
Transfer capillary temperature	275 °C	275 °C
Transfer capillary voltage	27.5 V	27.5 V
Tube lens voltage	90.0 V	90.0 V
Skimmer voltage	30.0 V	30.0 V

Table 11.2 Operating conditions of the Exactive mass spectrometer used for analysis of liquid crystals via plasma-based ADI-MS in chapter 4.

	LTP-MS (Exactive)	DART-MS (Exactive Plus)	FAPA-MS (Exactive Plus)
Scan range	m/z 50-1000	m/z 140-1000	m/z 140-1000
Fragmentation	HCD Gas: on fragmentation energy: off	HCD gas: on Fragmentation energy: off	HCD gas: on Fragmentation energy: off
Resolution	High (50,000)	Ultra High (140,000)	Ultra High (140,000)
Polarity	Positive	Positive	Positive
Micro scan count	1	1	1
Lock mass	off	off	off
AGC target	1,000,000	1,000,000	1,000,000
Maximum injection time	10 ms	250 ms	250 ms
Transfer capillary temperature	275 °C	300 °C	300 °C
Transfer capillary voltage	27.5 V	10 V	10 V
S lens voltage	NA ^a	25 V	25 V
Tube lens voltage	90.0 V	NA ^a	NA ^a
Skimmer voltage	30.0 V	15 V	15 V

^a NA: not applicable

Table 11.3 Exactive operating conditions for the analysis of the LCD test cell via mass spectral imaging by FAPA-MS and LA-h-FAPA-MS in chapter 5.

	FAPA-MS (Exactive)	LA-h-FAPA-MS (Exactive)
Scan range	m/z 50-600	m/z 50-600
Fragmentation	HCD Gas: on fragmentation energy: off	HCD Gas: on fragmentation energy: off
Resolution	Medium (25,000)	High (50,000)
Polarity	Positive	Positive
Micro scan count	1	1
Lock mass	off	off
AGC target	1,000,000	1,000,000
Maximum injection time	50 ms	50 ms
Transfer capillary temperature	280 °C	280 °C
Transfer capillary voltage	95.0 V	95.0 V
Tube lens voltage	110.0 V	110.0 V
Skimmer voltage	34.0 V	34.0 V

Table 11.4 Exactive operating conditions for the comparison between DESI- and FAPA-MS for direct sample analysis on HPTLC plates. These Exactive settings were also used for all FAPA-MS experiments presented in chapter 6.

	FAPA-MS (Exactive)	DESI-MS (Exactive)
Scan range	m/z 50-1000	m/z 50-1000
Fragmentation	HCD Gas: on fragmentation energy: off	HCD Gas: on fragmentation energy: off
Resolution	High (50,000)	High (50,000)
Polarity	Positive	Positive
Micro scan count	1	1
Lock mass	off	off
AGC target	1,000,000	1,000,000
Maximum injection time	10 ms	20 ms
Transfer capillary temperature	275 °C	300 °C
Transfer capillary voltage	27.5 V	48.0 V
Tube lens voltage	90 V	75 V
Skimmer voltage	30 V	36 V

Table 11.5 Mass spectrometer settings used for the analysis of antimalarial active agents via TLC-FAPA-MS in chapter 7.

FAPA-MS (Exactive)	
Scan range	m/z 50-1000
Fragmentation	HCD Gas: on fragmentation energy: off
Resolution	High (50,000)
Polarity	Positive
Micro scan count	1
Lock mass	off
AGC target	1,000,000
Maximum injection time	10 ms
Transfer capillary temperature	275 °C
Transfer capillary voltage	27.5 V
Tube lens voltage	90.0 V
Skimmer voltage	30.0 V

11.2 IR-Thermography

Determination of the Reflected Temperature. It is important to determine the reflected temperature with a fixed experimental setup (fixed alignment between FAPA, sample plate, and mass spectrometer) in order to measure the same reflected temperature in all measurements. In case IR radiation of the plasma itself is reflected to the thermal camera the measured reflected temperature is also dependent on the current applied to the FAPA source. Therefore, the reflected temperature is determined for all different currents used in this chapter.

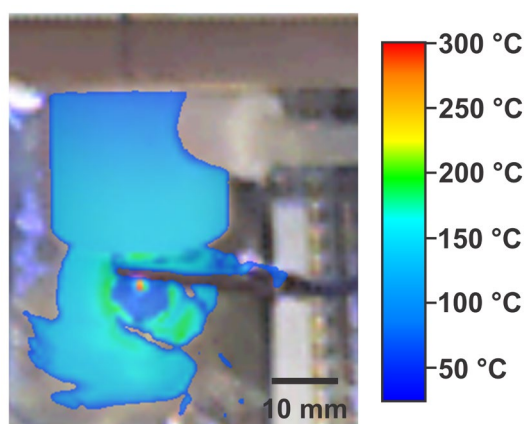


Figure 11.1 Overlay of a picture and an IR image of the FAPA source (short capillary, 40 mA) with an aluminum plate used as a sample surface. The reflected temperature presented in Figure 11.2 was detected at the point where the afterglow was impacting on the aluminum plate (red point in this image).

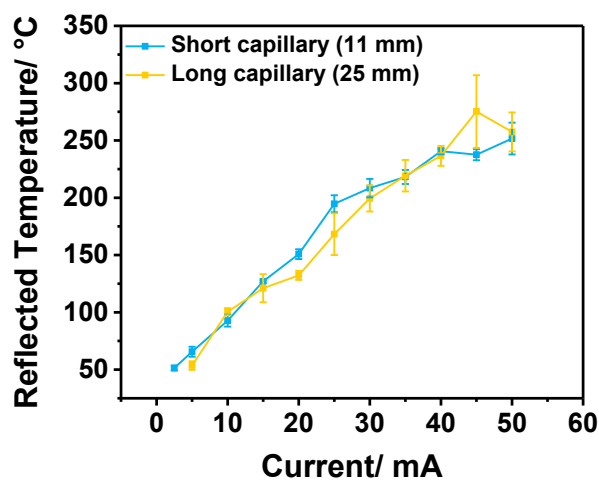
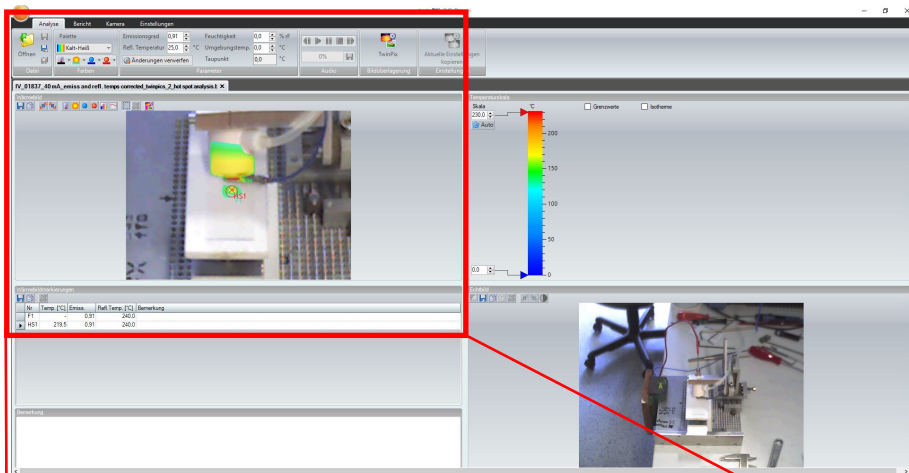


Figure 11.2 Reflected temperature measured by IR-thermography at different operation currents of the FAPA source.

In Figure 11.1 an example measurement of the FAPA source with short (11 mm) anode capillary and 40 mA applied is presented. The reflected temperature was determined for the position where the plasma afterglow was pointing on the aluminum surface. This position can be identified by the red dot in the image. An overview of the reflected temperature measured at different FAPA operating currents is presented in Figure 11.2.

Description of the Data Processing via IRSoft. After the IR images are recorded with the IR camera the measured data was evaluated in the IRSoft software. In Figure 11.3 a screenshot of the software is presented. The overall emissivity and the reflected temperature can be adjusted in the tool bar at the top. A more detailed adjustment of the emissivity and the reflected temperature can be done with the turquoise colored tool. The area affected by this, and all other tools, can be adjusted in size and shape to give different sample areas different emissivities and reflected temperatures. This has been done for the experiments evaluated in this chapter.

(a)



(b)

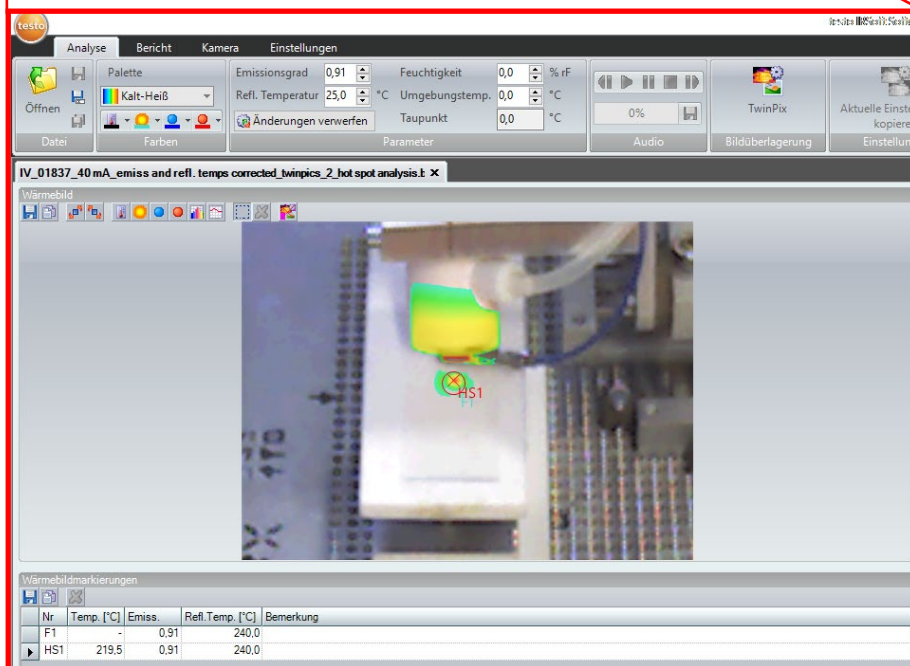


Figure 11.3 Screenshot of the IRSoft software used for data evaluation after IR imaging (a). In (b) a zoom-in of the top left corner of (a) (red square) is shown for visualization purposes.

To measure the glass plate surface temperature at the impact spot of the plasma afterglow the emissivity and reflected temperature of the spot was corrected with a circular correction tool (*cf.* turquoise circle with label “F1” in Figure 11.4). Subsequently, the highest surface temperature within this circle was detected with the “hot spot” tool (*cf.* red circle with label “HS1” in Figure 11.4). This temperature was chosen for the comparison of the two different FAPA anode capillaries at different operation currents.

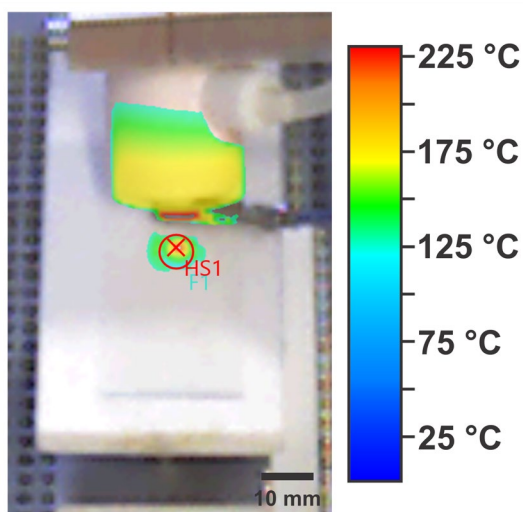


Figure 11.4 Overlay of the IR image and the picture taken of the FAPA source and glass microscope slide.

11.3 Data Evaluation Procedure for Transient Signals

For the semiquantitative comparison of analyte signals the transient analyte signals obtained by *e.g.*, TM-FAPA-MS were integrated with the software Origin 2017 (OriginLab Corporation). Prior peak integration the raw data of the ion of interest (*e.g.*, m/z 170.0965 \pm 8 ppm) was exported from the Xcalibur software to Origin 2017 and a graph similar to Figure 11.5 was created. The integration borders were selected to be 0.1 minutes to the left of the peak maximum (*cf.* blue arrow in Figure 11.5) and 0.6 minutes to the right of the peak maximum (*cf.* red arrow in Figure 11.5) and result in a integration region highlighted by the orange square.

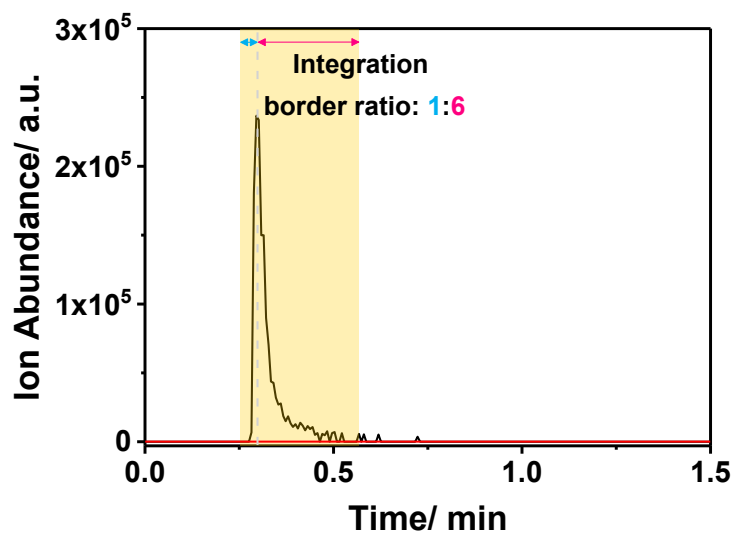


Figure 11.5 Transient signal of m/z 170.0965 \pm 8 ppm ($[M+H]^+$ peak of DPA) analyzed by TM-FAPA-MS.

11.4 Data Evaluation Procedure for Mass Spectral Imaging

Direct mass spectral imaging of analyte distributions on sample substrates was performed with a motorized translational x-y-stage by Newport Corporation in combination of a self-written LabVIEW (National Instruments) routine to control the translational stages. The samples were analyzed via consecutive line scans (line-to-line distance 0.5 mm) across the sample surface and the mass spectrometer data acquisition was started by a trigger signal sent by the LabVIEW software in the event of a line scan start.

Due to missing imaging software, which sufficiently exports and processes the Exactive Raw-files without loss of the high-mass-resolution, the data was manually exported to Origin 2017 (OriginLab Corporation) for further data processing. Therefore, a mass window, specific for the analyte of interest (*e.g.*, the mass window for caffeine at m/z 195.0879 \pm 8 ppm was m/z 195.0864 to m/z 195.0895) was selected. With Origin 2017 the analysis time was transferred into the line scan distance with the translational speed of 0.3 mm/s of the x-y-stage and the EIC of the analyte is transformed into a transient ion-signal in respect to the separation distance of the chromatography (cf. Figure 11.6).

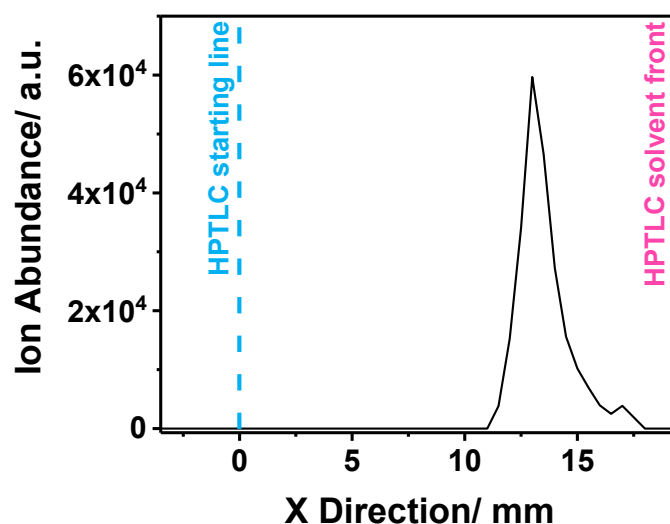


Figure 11.6 Ion abundance of caffeine (m/z 195.0879 \pm 8 ppm) detected via a line scan with FAPA-MS across a HPTLC silica plate. The x direction on the x axis corresponds to the chromatography direction and distance.

To visualize the analyte spot in a three-dimensional plot, multiple of these line scans are grouped together in a x-y-matrix. For the results presented in this manuscript the data points detected by the mass spectrometer along one line-scan – into the direction of the chromatography separation – are plotted along the x direction and the line scans (line-to-line distance 0.5 mm) are plotted next to each other along the y direction. The analyte signal abundance of the matching x and y coordinates is inserted into the matrix fields and corresponds to the voxel volume information of the respective field. Plotted in a waterfall diagram the analyte spot is visualized for further data interpretation (*cf.* Figure 11.7).

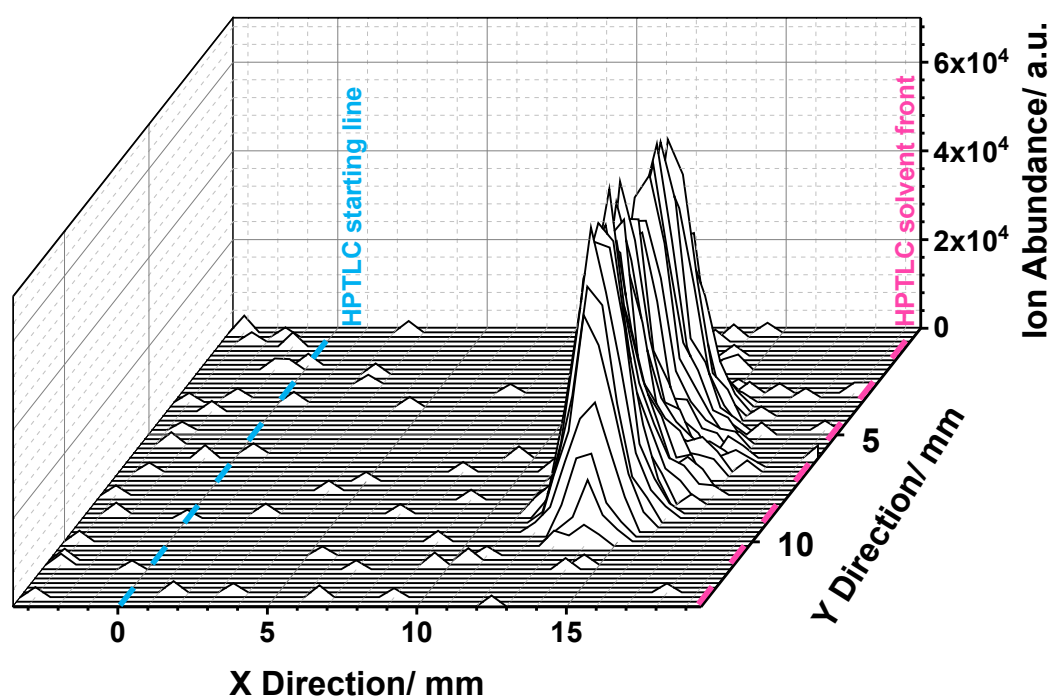


Figure 11.7 3D plot of the caffeine ion abundance (m/z 195.0879 \pm 8 ppm) in x and y direction on the HPTLC plate. The x direction on the x axis corresponds to the chromatography direction.

For mass spectral imaging an often-used diagram type is the contour plot in which the geometry information – x and y direction – is given by the x and y axis and the signal abundance is given by the color at the respective position. In Figure 11.8a a contour plot is presented for the separation of acetaminophen, caffeine, and nicotine on a NP-HPTLC silica plate. The blue arrows demonstrate the line scans performed by FAPA-MS across the HPTLC plate. The dashed circles on the black horizontal line symbolize the deposited sample bands and the starting line of the chromatography. For the semiquantitative comparison of the signal abundance the analyte spots are integrated by establishing a ROI (pink box in Figure 11.8b) around each analyte spot. Within the ROI the single voxel volumes (blue rectangles in Figure 11.8b) are summarized to obtain the integrated spot signal, namely the sum of voxel volumes, which can be used for semiquantitative comparison of the analyte.

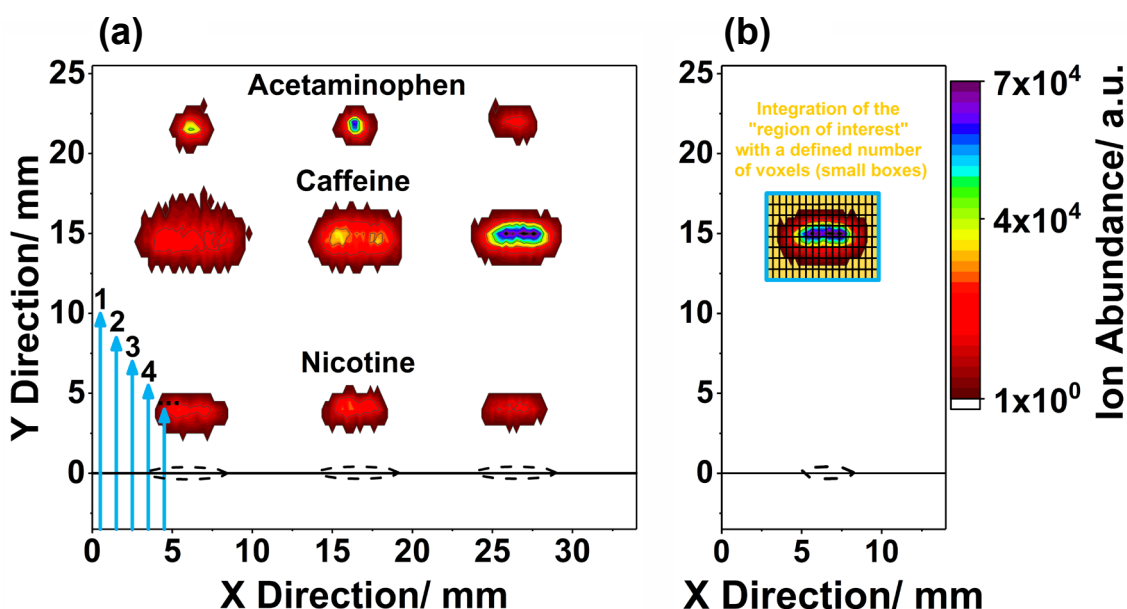


Figure 11.8 (a) Combined mass spectral image of nicotine (m/z 163.1229 \pm 8 ppm), caffeine (m/z 195.0879 \pm 8 ppm), and acetaminophen (m/z 152.0705 \pm 8 ppm) detected via HPTLC-FAPA-MS after separation of the analyte mixture on a NP-HPTLC plate (three spots deposited in dashed ellipses). The blue arrows indicate the scan direction and order of the FAPA-MS line scans (step size 0.5 mm) performed for mass spectral imaging. (b) EIC of the protonated molecular ion of caffeine. For better visualization purposes only the EIC of m/z 195.0879 \pm 8 ppm for the third analyte spot in (a) is shown. The ROI for data evaluation is illustrated by a large blue square. The small yellow rectangles represent the individual voxels, which are summed up and contribute to the overall abundance of the analyte.

11.5 Data Evaluation Procedure for the Determination of Instrumental Detection Limits Measured with High-Resolution Mass Spectrometry

For all experiments in this chapter a high-resolution mass spectrometer was used. This type of instruments is often capable to resolve the mass spectral background from the analyte signal. Consequently, the IDLs cannot be determined by methods which require an analyte background signal and therefore a guideline of the U. S. Environmental Protection Agency (U.S. EPA) was used to determine the IDL of caffeine in this chapter.¹⁷⁴

Before the IDL can be determined the IDL has to be estimated via an external calibration curve. For this purpose, six calibration standards of DPA were prepared in chapter 3 (concentration range: 2-100 mg/mL, 2 μ L deposited, n=7) and deposited on a stainless-steel mesh. In chapter 6 a caffeine standard with eight calibration levels in a concentration range of 0.001-0.5 mg/mL (5 μ L/band deposited, n=4) were prepared and deposited on RP-HPTLC silica plates. Lastly, in chapter 7 calibration curves for quinine and artemether (both deposited on NP- and CN-HPTLC silica plates) were determined with calibration standards in the range of 0.05-20 mg/mL (nine calibration levels, n=5) and 0.03-2 mg/mL (four calibration levels, n=5), respectively. A detailed description of the analyte measurements and data processing are described in the experimental section of the respective chapters.

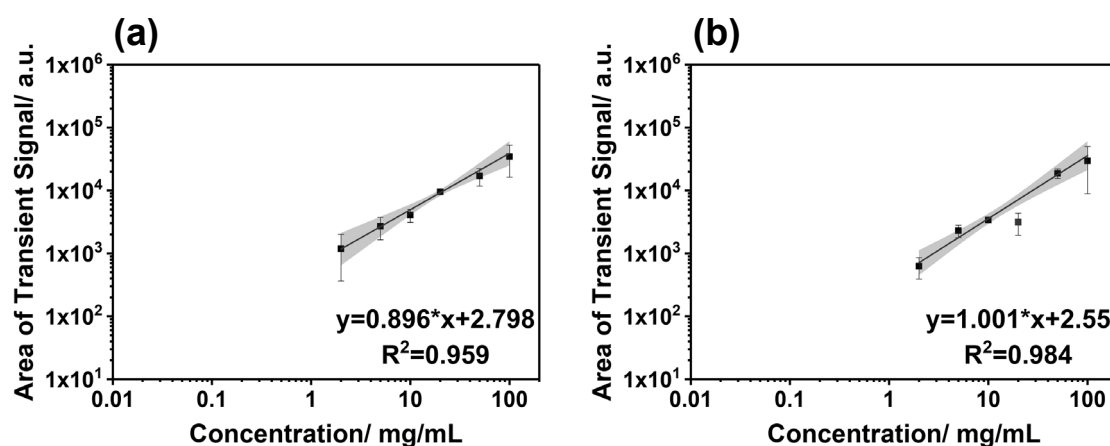


Figure 11.9 Calibration curves for DPA measured with TM-FAPA-MS with a 25 mm (a) and 11 mm (b) anode capillary.

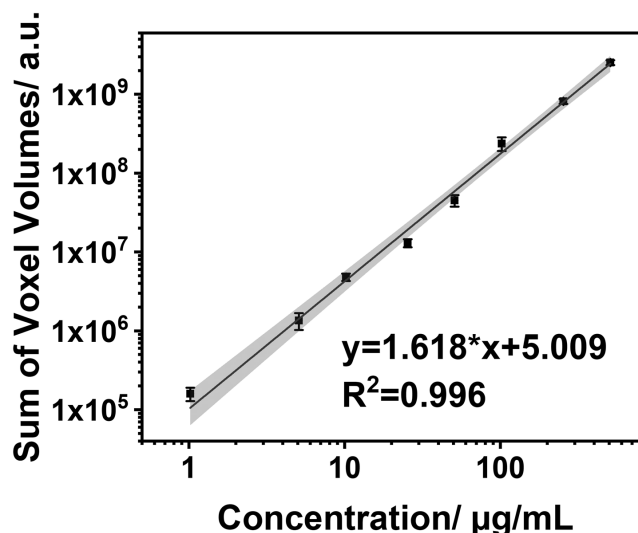


Figure 11.10 External calibration graph of caffeine separated on a RP-HPTLC plate and analyzed via FAPA-MS. The concentration range was selected between 1 µg/mL and 500 µg/mL (5 µL/band deposited).

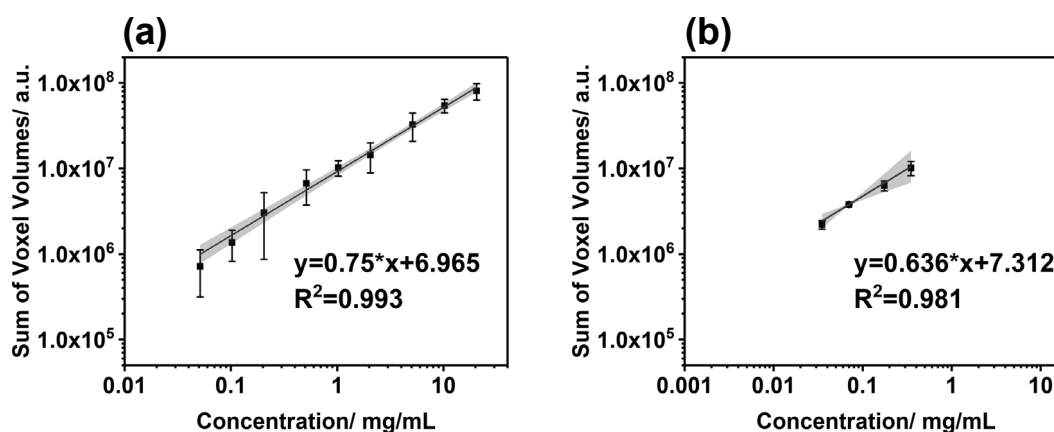


Figure 11.11 External calibration curves for quinine (a) and artemether (b) analyzed by CN-HPTLC-FAPA-MS.

From the established external calibration curves (*cf.* Figure 11.9, Figure 11.10, and Figure 11.11) approximate IDLs of 2 mg/mL (DPA), 1 µg/mL (caffeine), 0.5 mg/mL (quinine), and 0.6 mg/mL (artemether) were estimated. In a subsequent step seven replicate measurements of the estimated lowest detectable concentration level of the respective analyte was detected and the analyte signals were integrated. These analyte signals were used to determine the variance (S^2) and standard deviation (S) of the seven replicate measurements via Equation 11.1 and Equation 11.2. The IDL was computed via Equation 11.3.

$$S^2 = \frac{1}{n-1} \left[\frac{\sum_{i=1}^n x_i^2 - (\sum_{i=1}^n x_i)^2}{n} \right] \quad \text{Equation 11.1}$$

$$S = (S^2)^{\frac{1}{2}} \quad \text{Equation 11.2}$$

$$IDL = t_{(n-1, 1-\alpha=0.99)} \cdot S \quad \text{Equation 11.3}$$

S^2	variance of the replicate measurements
S	standard deviation of the replicate measurements
n	number of aliquots
x	sum of voxel volumes for aliquots $i=1$ to n
$t_{(n-1, 1-\alpha=0.99)}$	students' t value appropriate for 99% confidence level and a standard deviation estimate with $n-1$ degrees of freedom

11.6 Supporting Information for the Analysis of Lithium-Ion Batteries

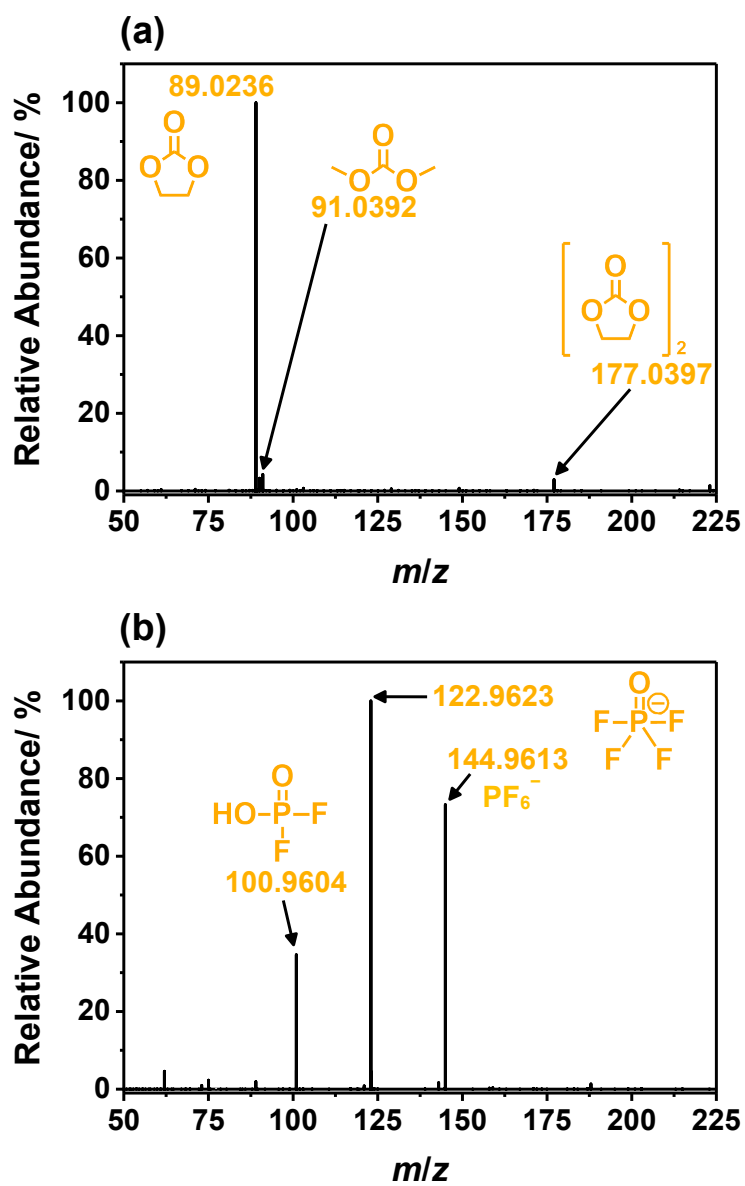


Figure 11.12 Mass spectra of LP30 before thermal aging detected in positive-ion (a) and negative-ion (b) detection mode via LTP-MS. The sampling surface temperature was set to 50 °C to aid analyte desorption.

11.7 Supporting Information for the Analysis of Liquid Crystals via Plasma-Based ADI-MS

Table 11.6 List and detailed information of all liquid crystals analyzed in chapter 4.

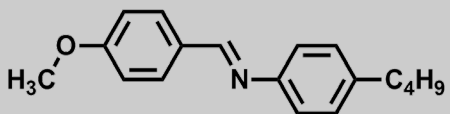
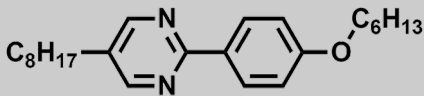
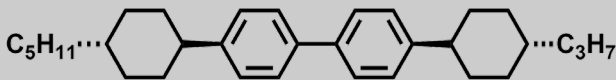
Information	Ion	Theoretical <i>m/z</i>	Observed <i>m/z</i>	Rel. mass accuracy
LC-I				
				
Prod. name: ST00484 ^a	[M] ⁺	267.1618	267.1617	-0.4 ppm
MW ^d : 267.37 g/mol	[M+H] ⁺	268.1696	268.1691	-1.8 ppm
Formula: C ₁₈ H ₂₁ NO	[(M+O)+H] ⁺	284.1645	284.1646	0.3 ppm
LC-II				
				
Prod. name: ST00552 ^a	[M] ⁺	368.2822	368.2826	1.0 ppm
MW: 368.56 g/mol	[M+H] ⁺	369.2900	369.2897	-0.8 ppm
Formula: C ₂₄ H ₃₆ N ₂ O				
LC-III				
				
Prod. name: ZLI-1544 ^b	[M] ⁺	430.3594	430.3594	-0.3 ppm
MW: 430.71 g/mol				
Formula: C ₃₂ H ₄₆				

Table 11.6 Continued.

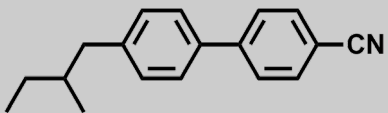
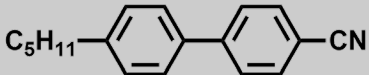
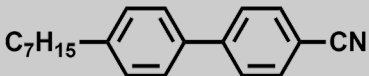
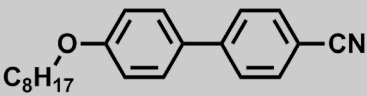
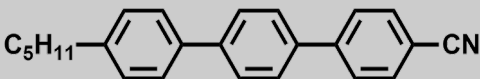
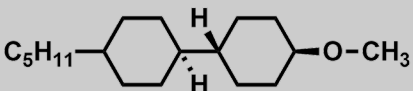
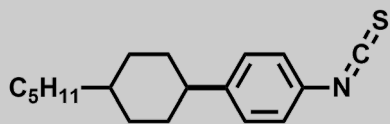
Information	Ion	Theoretical <i>m/z</i>	Observed <i>m/z</i>	Rel. mass accuracy
LC-IV				
				
	[M] ⁺	249.1512	249.1512	-0.1 ppm
Prod. name: CB15 ^c	[M+H] ⁺	250.1590	250.1588	-1.1 ppm
MW ^d : 249.35 g/mol	[M-H+O] ⁺	264.1383	264.1383	0.3 ppm
Formula: C ₁₈ H ₁₉ N	[M+NH ₄] ⁺	267.1856	267.1853	-1.1 ppm
	[M ₂ +H] ⁺	499.3108	499.3105	-0.6 ppm
LC-V				
				
	[M] ⁺	249.1512	249.1512	-0.1 ppm
Prod. name: 5CB ^c	[M+H] ⁺	250.1590	250.1588	-1.1 ppm
MW: 249.35 g/mol	[M-H+O] ⁺	264.1383	264.1383	0.3 ppm
Formula: C ₁₈ H ₁₉ N	[M+NH ₄] ⁺	267.1856	267.1853	-1.1 ppm
	[M ₂ +H] ⁺	499.3108	499.3105	-0.6 ppm
LC-VI				
				
Prod. name: 7CB ^c	[M] ⁺	277.1825	277.1823	-0.6 ppm
MW: 277.40 g/mol	[M+H] ⁺	278.1903	278.1900	-1.2 ppm
Formula: C ₂₀ H ₂₃ N	[M+NH ₄] ⁺	295.2169	295.2166	-0.9 ppm

Table 11.6 Continued.

Information	Ion	Theoretical <i>m/z</i>	Observed <i>m/z</i>	Rel. mass accuracy
LC-VII				
				
Prod. name: 8OCB ^c	[M+H] ⁺	308.2003	308.2010	-0.4 ppm
MW: 307.43 g/mol	[M+NH ₄] ⁺	325.2274	325.2274	-0.1 ppm
Formula: C ₂₁ H ₂₅ NO				
LC-VIII				
				
Prod. name: 5CT ^c	[M+H] ⁺	326.1903	326.1902	-0.2 ppm
MW: 325.45 g/mol	[M+NH ₄] ⁺	343.2169	343.2169	-0.1 ppm
Formula: C ₂₄ H ₂₃ N				
LC-IX				
				
Prod. name: ZLI-3005 ^c	[M+H] ⁺	267.2682	267.2681	-1.8 ppm
MW: 266.46 g/mol				
Formula: C ₁₈ H ₃₄ O				
LC-X				
				
No commercial product ^e	[M] ^{+•}	287.1702	287.1701	-0.3 ppm
MW: 287.46 g/mol				
Formula: C ₁₈ H ₂₅ NS				

^a Product name of Synthion Chemicals, Wolfen, Germany. ^b Product name of AstaTECH Inc., Bristol (PA), USA. ^c Product name of Merck KGaA, Darmstadt, Germany. ^d MW: molecular weight. ^e Synthesized by Prabin Rai, research group of Prof. Dr. Robert Twieg, Kent State University, Kent (OH), USA.

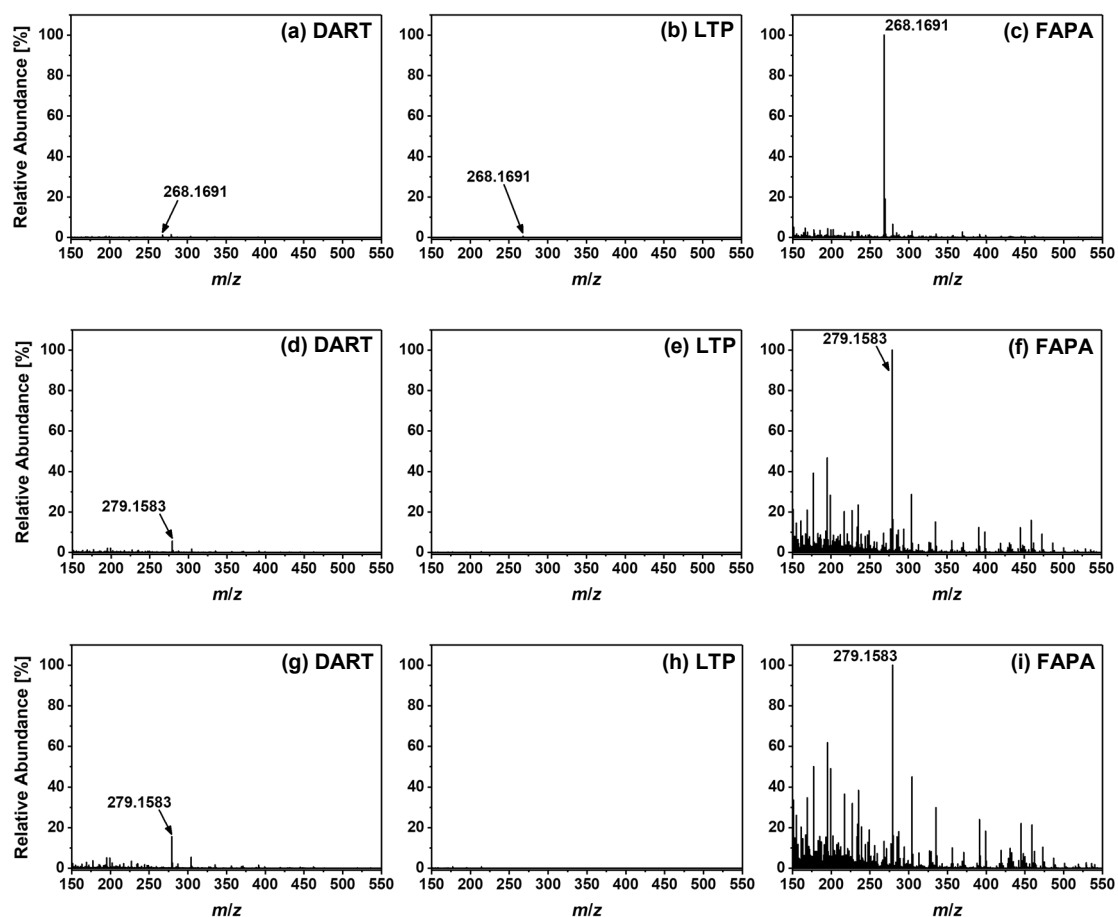


Figure 11.13 Mass spectra (positive-ion detection mode) of ST00484 (a-c), ST00552 (d-f), and ZLI-1544 (g-i) detected by DART-, LTP-, and FAPA-MS without external heating of the sample holder. Analyte signals were identified via accurate mass with an RMA within ± 2 ppm. For visualization purposes, the peak heights are normalized to the most abundant ion produced by any of the three ADI sources.

For the determination of the instrumental detection limit, the EIC of each compound was integrated after background signal subtraction. Therefore, the mass traces of the $[M]^{++}$ and the corresponding ^{13}C -isotope signal (± 8 ppm) of m/z 318.17 were combined to a combined EIC (*cf.* Figure 11.14a-c). Further, the integrated peak areas were averaged over three measured replicates ($n=3$) and plotted in calibration diagrams (*cf.* Figure 11.14d-f). The limit of detection was derived by dividing three times the standard deviation of the background signal divided by the slope of the calibration curve. Five measurement points were used for the calibration curve.

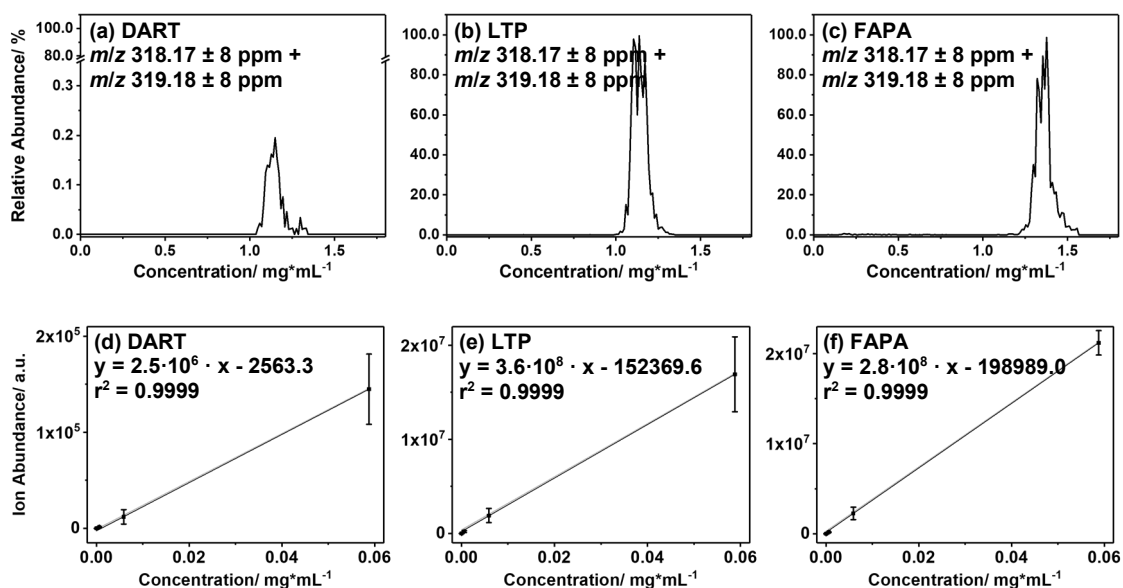


Figure 11.14 Combined extracted-ion chromatograms of m/z 318.17 and m/z 319.18 detected with DART- (a), LTP- (b), and FAPA-MS (c). In (d-f) the corresponding dilution series with five measurement points is shown in a concentration range from 100 ng to 12 pg absolute deposited amount of sample (95% confidence interval shown in grey)

11.8 Supporting Information for Spatially-Resolved Liquid Crystal Analysis via FAPA-MS and LA-h-FAPA-MS

Table 11.7 Liquid crystals employed in the LCD test cell.

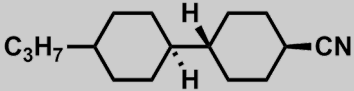
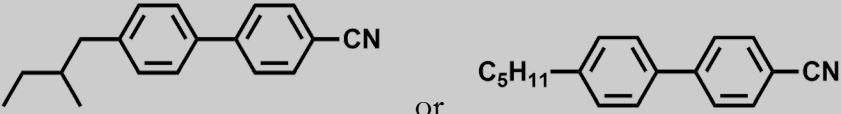
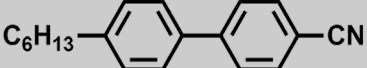
Information	Ion	Theoretical <i>m/z</i>	Observed <i>m/z</i>	Rel. mass accuracy
LC-XI				
				
Prod. name: ZLI-1184				
MW: 233.39 g/mol	[M+H] ⁺	234.2216	234.2215	-0.1 ppm
Formula: C ₁₆ H ₂₇ N				
LC-IV and LC-V				
				
Prod. name: CB15 or 5CB ^a				
MW: 249.35 g/mol	[M+H] ⁺	250.1590	250.1588	-1.1 ppm
Formula: C ₁₈ H ₁₉ N				
LC-XII				
				
Prod. name: K18				
MW: 263.38 g/mol	[M+H] ⁺	264.1747	264.1746	-0.1 ppm
Formula: C ₁₉ H ₂₁ N				

Table 11.7 Continued.

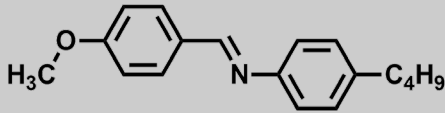
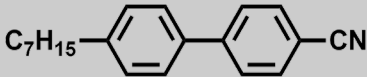
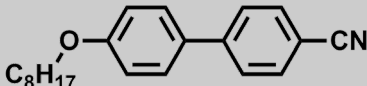
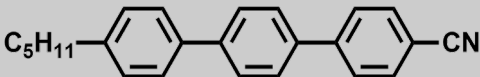
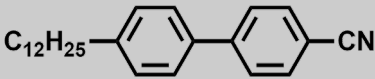
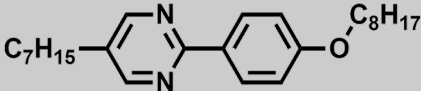
Information	Ion	Theoretical <i>m/z</i>	Observed <i>m/z</i>	Rel. mass accuracy
LC-I				
				
Prod. name: ST00484				
MW: 267.37 g/mol	[M+H] ⁺	268.1696	268.1694	-0.9 ppm
Formula: C ₁₈ H ₂₁ NO				
LC-VI				
				
Prod. name: 7CB ^a				
MW: 277.40 g/mol	[M+H] ⁺	278.1903	278.1901	-0.4 ppm
Formula: C ₂₀ H ₂₃ N				
LC-VII				
				
Prod. name: 8OCB ^a				
MW: 307.43 g/mol	[M+H] ⁺	308.2003	308.2010	0.4 ppm
Formula: C ₂₁ H ₂₅ NO				
LC-VIII				
				
Prod. name: 5CT ^a				
MW: 325.45 g/mol	[M+H] ⁺	326.1903	326.1902	-0.2 ppm
Formula: C ₂₄ H ₂₃ N				

Table 11.7 Continued.

Information	Ion	Theoretical <i>m/z</i>	Observed <i>m/z</i>	Rel. mass accuracy
LC-XIII				
				
Prod. name: K36				
MW: 347.54 g/mol	[M+H] ⁺	348.2286	348.2688	-0.2 ppm
Formula: C ₂₅ H ₃₃ N				
LC-XIV				
				
Prod. name: ST00551				
MW: 382.58 g/mol	[M+H] ⁺	383.3057	383.3052	-0.5 ppm
Formula: C ₂₅ H ₃₈ N ₂ O				

^a Component part of the E7 liquid crystals mixture.

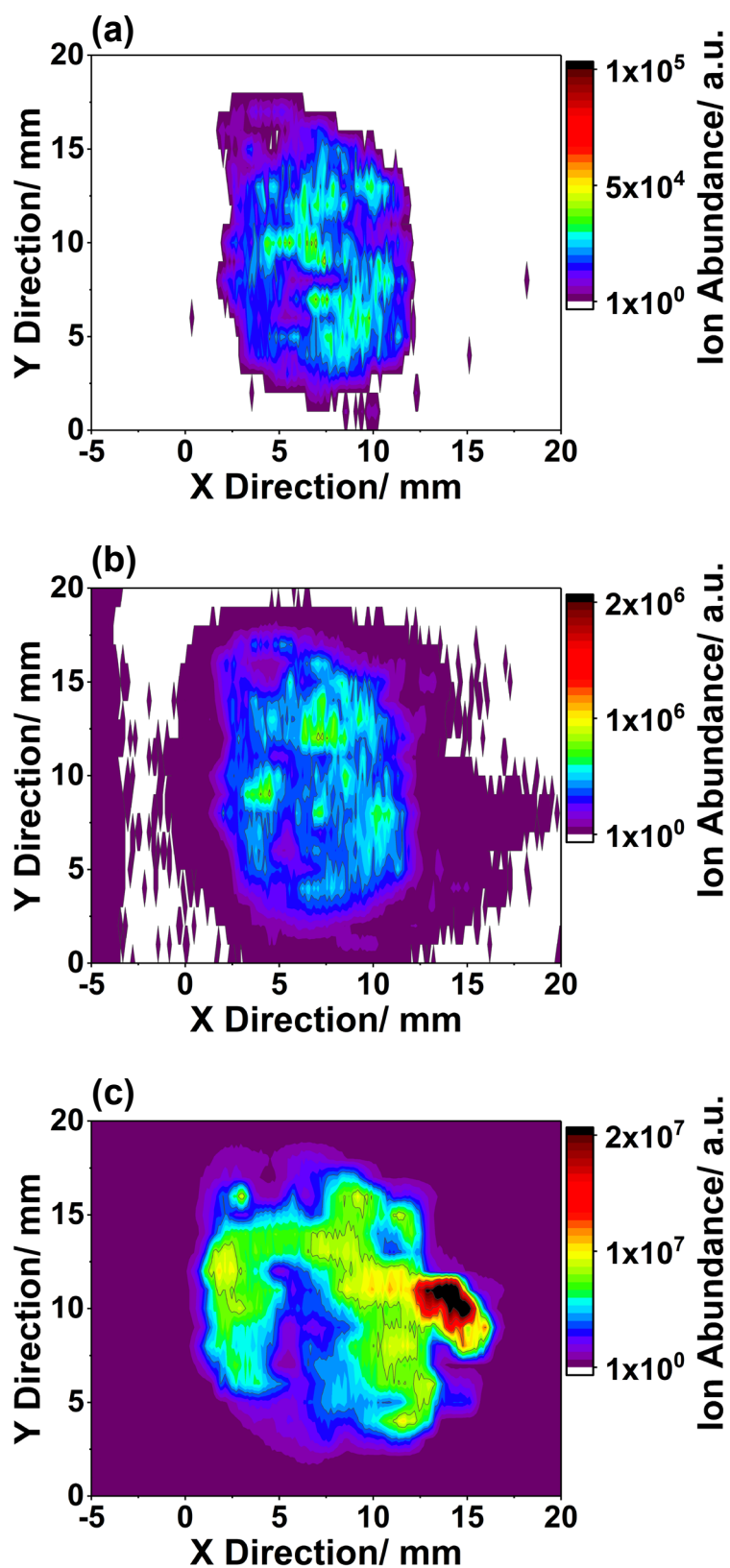


Figure 11.15 Mass spectral image of the protonated molecular ions for the liquid crystals LC-XIII (a, m/z 348.2688), LC-IV/V (b, m/z 250.1588), and LC-I (c, m/z 268.1699). The EIC of the three ions were each exported with a mass window of ± 8 ppm around the m/z of the peak's maximum.

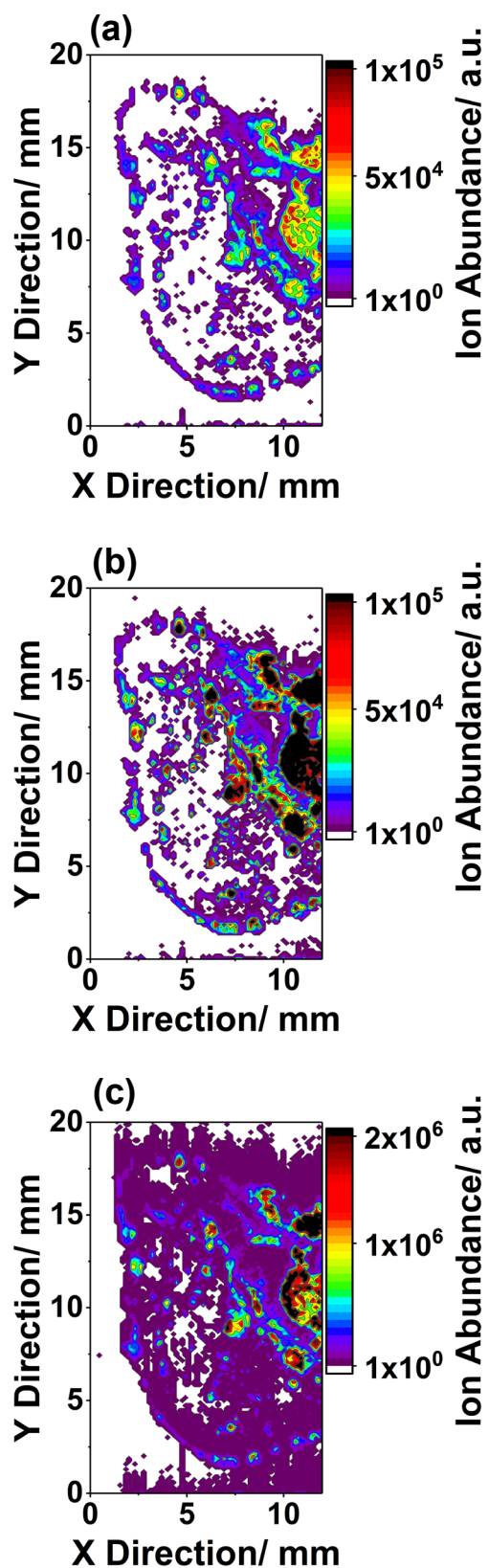
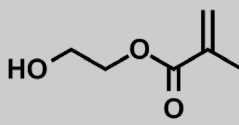
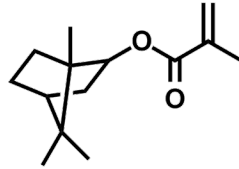
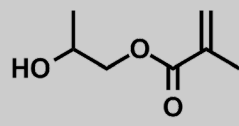
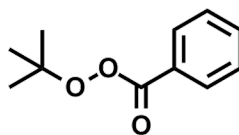
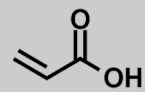
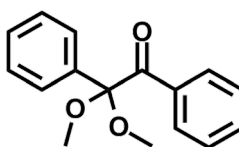
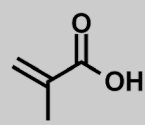


Figure 11.16 Mass spectral image of the protonated molecular ions for the liquid crystals LC-XIII (a, m/z 348.2688), LC-IV/V (b, m/z 250.1588), and LC-I (c, m/z 268.1699). The EIC of the three ions were each exported with a mass window of ± 8 ppm around the m/z of the peak's maximum.

Table 11.8 List of chemicals in the Loctite 352 adhesive by Henkel.^a

Information	Molecular structure
2-Hydroxyethyl methacrylate MW: 130.14 g/mol Formula: C ₆ H ₁₀ O ₃	
Isobornyl methacrylate MW: 222.32 g/mol Formula: C ₁₄ H ₂₂ O ₂	
Hydroxypropyl methacrylate MW: 144.17 g/mol Formula: C ₇ H ₁₂ O ₃	
<i>tert</i> -Butyl peroxybenzoate MW: 194.23 g/mol Formula: C ₁₁ H ₁₄ O ₃	
Acryl acid MW: 72.06 g/mol Formula: C ₃ H ₄ O ₂	
2,2-Dimethoxy-1,2-diphenyl ethanone MW: 256.30 g/mol Formula: C ₁₆ H ₁₆ O ₃	
Methacrylic acid MW: 86.09 g/mol Formula: C ₄ H ₆ O ₂	

^a Information obtained from the material safety data sheets (MSDS) of Loctite 352.

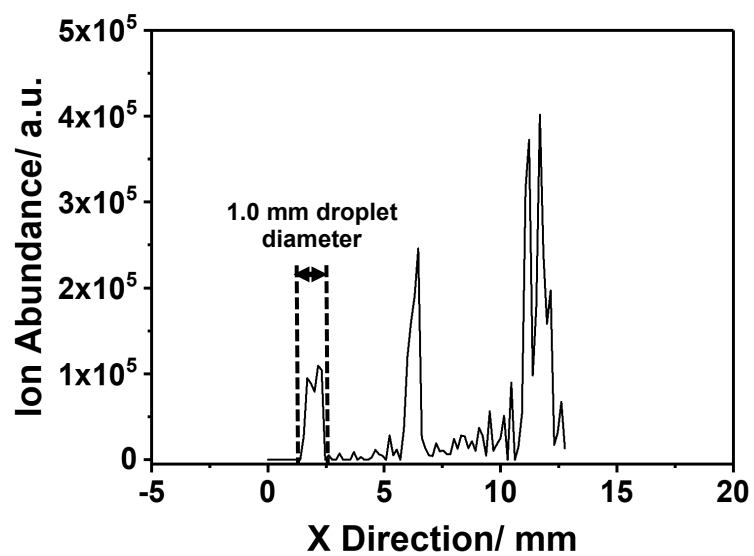


Figure 11.17 EIC of LC-XIV (m/z 383.3062 \pm 8 ppm) detected in positive-ion detection mode with a line scan by LA-h-FAPA-MS across the LCD test cell at $y=14.15$ mm.

11.9 Supporting Information for the Analysis of TLC plates via FAPA-MS

Table 11.9 List of TLC stationary phases used in this chapter.

Type of stationary phase	Grade of stationary phase	Order no.
Silica plate (NP)	TLC	1.05729.0001
	HPTLC	1.05642.0001
	MS Grade	1.00934.0001
	LiChrospher	1.15445.0001
	Premium Purity	1.05648.0001
Extra-thin silica plate (tNP)	HPTLC	1.11764.0001
Preparative silica plate (PLC)	PLC 500 μm	1.05744.0001
	PLC 1000 μm	1.13895.0001
	PLC 2000 μm	1.05717.0001
Reversed-phase-modified silica plate (RP)	HPTLC	1.16225.0001
	MS Grade	1.51161.0001
	LiChrospher	1.05646.0001
Cyano-modified silica plate (CN)	HPTLC	1.16464.0001
Amino-modified silica plate (NH₂)	HPTLC	1.15647.0001
Diol-modified silica plate (DIOL)	HPTLC	1.12668.0001

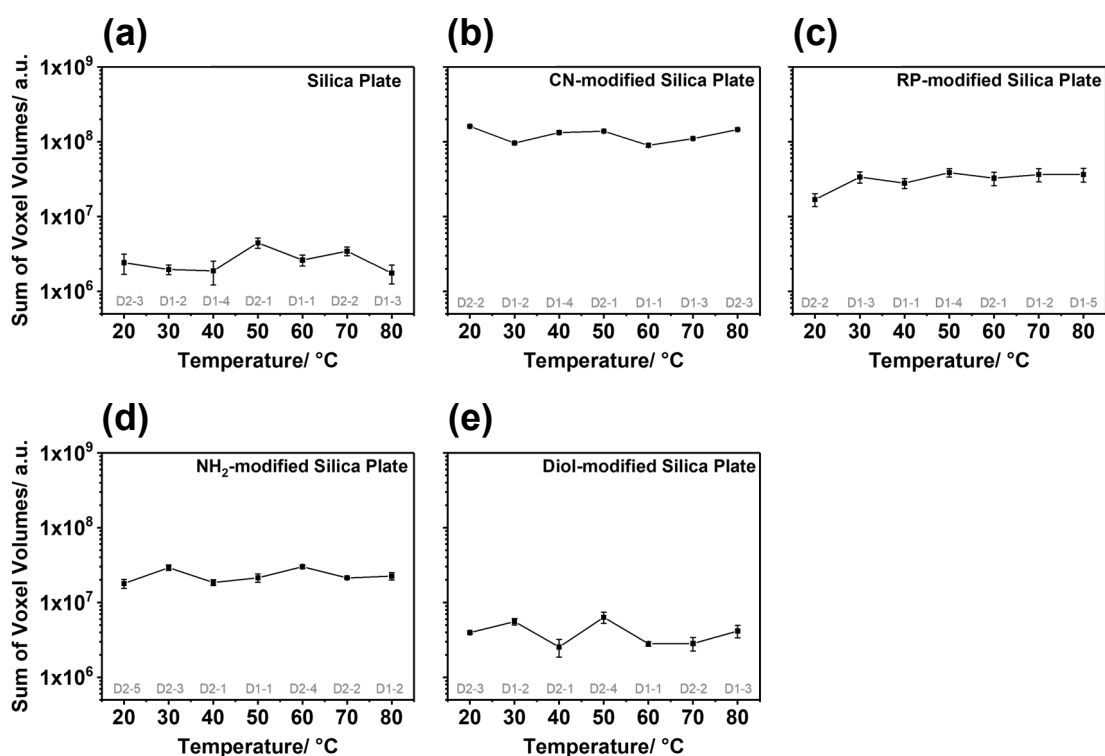


Figure 11.18 Sum of voxel volumes for the $[M+H]^+$ -ion of caffeine ($m/z \approx 195.0879 \pm 8$ ppm, $n=3$) relative to the drying temperature of the HPTLC plate. The experiments per plate were performed on different days in random order. The measurement order can be identified as follows: the label “D2-3” corresponds to the second measurement day and the third measurement on said day.

Table 11.10 R_f values for the analytes in the test mixture separated on different HPTLC stationary phases.

	R_f for caffeine	R_f for nicotine	R_f for acetaminophen	R_f for cortisone
NP	0.72	0.13	0.83	-
DIOL	0.54	<0.01	-	-
NH ₂	0.85	0.96	0.72	-
RP	0.73	0.05	0.83	0.83
CN	0.85	0.02	0.85	0.85

Preliminary experiments of the caffeine quantification in energy drinks (FAPA-MS with isotope dilution analysis) resulted in caffeine concentrations that did not match the caffeine concentration provided by the manufacturer (detected concentration $\sim 50\%$ lower than to be expected). After a careful review of the sample preparation and the TLC-FAPA-MS method, a strong discrepancy between the spot shape of caffeine and caffeine- $^{13}\text{C}_3$ standard on the TLC plate was identified as a potential source of error. In a separate experiment, mass spectra of the separated energy drink were detected via a line scan across the TLC plate. These were searched for mass spectral interferences and revealed an isobaric interference with a matrix component at m/z 180.0881. In Figure 11.19 the EICs of caffeine (m/z 195.0879 ± 8 ppm), caffeine- $^{13}\text{C}_3$ (m/z 198.0981 ± 8 ppm), and m/z 180.0881 ± 8 ppm are shown to demonstrate these observations. The addition of a water molecule with mass 18.0106 u to the matrix component at m/z 180.0881 forms an ion at m/z 198.0987, which has a mass shift of 3 ppm (0.6 milli mass units) compared to the $[\text{M}+\text{H}]^+$ -ion of the caffeine- $^{13}\text{C}_3$ standard. Fortunately, with a slightly longer separation time of 25 minutes instead of 20 minutes, the interference can be separated from the caffeine analyte by TLC (*cf.* Figure 11.19), so an accurate quantification of caffeine in energy drinks is possible.

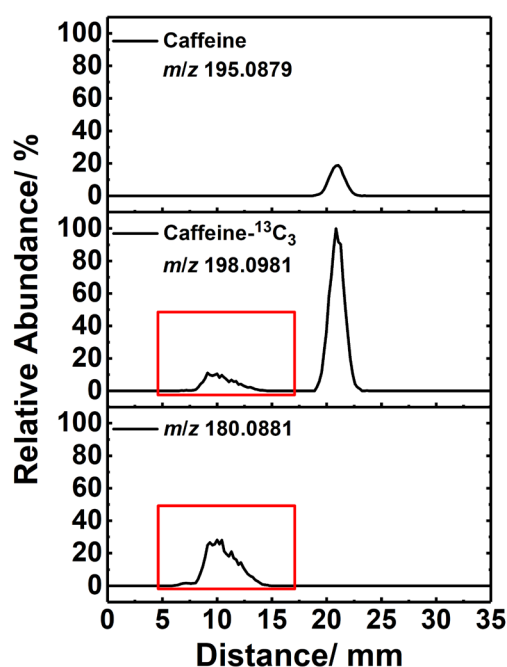


Figure 11.19 Extracted ion-chromatogram (EIC) of the protonated molecular-ion of caffeine (m/z 195.0879) and caffeine- $^{13}\text{C}_3$ (m/z 198.0981) in comparison to a matrix compound (m/z 180.0881). The addition of water to the matrix compound leads to an isobaric interference with the isotope-labeled standard, which is highlighted with two red boxes.

Isotope Dilution Analysis Calculations. For Quantification of caffeine in energy drinks was performed with stable-isotope dilution analysis. Equation 11.4 was used to calculate the caffeine concentration

$$c[\text{sample}] = \frac{c[\text{std}] \cdot m[\text{std}] \cdot M[\text{sample}]}{m[\text{sample}] \cdot M[\text{std}]} \cdot \frac{A[\text{std}] - R \left[\frac{^{12}\text{C}}{^{13}\text{C}} \right] \cdot B[\text{std}]}{R \left[\frac{^{12}\text{C}}{^{13}\text{C}} \right] \cdot B[\text{sample}] - A[\text{sample}]} \quad \text{Equation 11.4}$$

c[std]:	concentration of the caffeine- ¹³ C ₃ reference standard dissolved in methanol
m[std]:	weighted amount of caffeine- ¹³ C ₃ reference standard
M[sample]:	molar mass of caffeine
m[sample]:	weighted amount of energy drink sample
M[std]:	molar mass of caffeine- ¹³ C ₃
A[std]:	abundance of ¹² C-isotope in standard
B[std]:	abundance of ¹³ C-labeled isotope in standard
A[sample]:	abundance of ¹² C-isotope in sample
B[sample]:	abundance of ¹³ C-labeled isotope in sample
R[¹² C/ ¹³ C]:	measured isotope ratio

Because of the different solvent densities for the sample (water with large amounts of dissolved sugar) and the caffeine-¹³C₃ reference standard (methanol) the densities of the two liquids have to be considered in the calculation. Therefore, the Equation 11.4 is modified to Equation 11.5 for the final calculations

$$c[\text{sample}] = \frac{c[\text{std}] \cdot m[\text{std}] \cdot \rho[\text{sample solvent}] \cdot M[\text{sample}]}{m[\text{sample}] \cdot \rho[\text{std solvent}] \cdot M[\text{std}]} \cdot \frac{A[\text{std}] - R \left[\frac{^{12}\text{C}}{^{13}\text{C}} \right] \cdot B[\text{std}]}{R \left[\frac{^{12}\text{C}}{^{13}\text{C}} \right] \cdot B[\text{sample}] - A[\text{sample}]} \quad \text{Equation 11.5}$$

ρ [sample solvent]	density of the sample solvent
ρ [std solvent]	density of the standard solvent

The density of the liquids was determined experimentally by weighting a defined volume of the liquids ($n=3$), so ρ [sample solvent] is found to be 1.04 g/mL and ρ [std solvent] was 0.73 g/mL.

Sample Preparation of External Standards and Energy Drink Samples.

For caffeine analyte calibration, a 1.0 mg/mL stock solution was prepared with methanol used as solvent. With this stock solution, an external calibration was established in the range of 0.04 mg/mL to 1.0 mg/mL.

Caffeine in energy drinks was extracted by liquid-liquid extraction. Specifically, 5 mL of the energy drink were combined with 5 mL of bidistilled water and 1 mL of sodium carbonate (20%). The aqueous phase was extracted with chloroform (3x20 mL) and the organic phases were combined afterwards. Chloroform was evaporated to dryness of the extract via a TurboVap II (Biotage, Uppsala, Sweden). The walls of the sample container were rinsed three times (10 mL, 5 mL, and 3 mL, respectively) during the solvent evaporation process to avoid sample loss. The dry sample was dissolved in methanol and transferred to a 5 mL volumetric flask. For sample analysis the solution was transferred into the analysis vials after filtration with a 0.45 μ m syringe filter.

To determine the recovery of the extraction method a caffeine standard with a concentration of \sim 0.30 mg/mL ($n=3$) was prepared and treated the same way the energy drink sample was prepared in the prior analysis.

HPLC/UV Measurements for Caffeine Quantification in Energy Drinks. HPLC/UV measurements were performed with an Agilent 1200 HPLC system (Agilent, Santa Clara, CA, USA). Data processing was performed with OpenLab CDS Workstation 2.2 (Agilent). Separation was performed on a RP-18 column (XBridge, 4.6x75 mm, 2.5 μ m particle size, Waters, Eschborn, Germany) with a mobile phase consisting of 55% methanol, 45% bidistilled water, and 0.1% FA at a flow rate of 0.6 mL/min (injection volume 5 μ L). Detection was performed at a wavelength of 210 nm. The separation was completed in approximately 6 minutes.

Calculations for the Determination of the Caffeine Concentration in Energy Drinks and the Recovery Rate of the Caffeine Analyte. The caffeine concentration of the brand A energy drink was determined by external calibration. Therefore, the peak area of the integrated chromatography peak was inserted into the following calibration Equation 11.6. The formula was determined by the external calibration graph shown in Figure 11.20. The recovery rate for the extraction method was determined with a spiked caffeine sample with known concentration (~ 0.30 mg/mL ($n=3$)), which was also manually extracted and quantified with the method described above. A recovery rate of 106% was determined using Equation 11.6.

$$c[\text{sample}] = 14094.0 \cdot x + 100.8 \quad (R^2 = 0.9999) \quad \text{Equation 11.6}$$

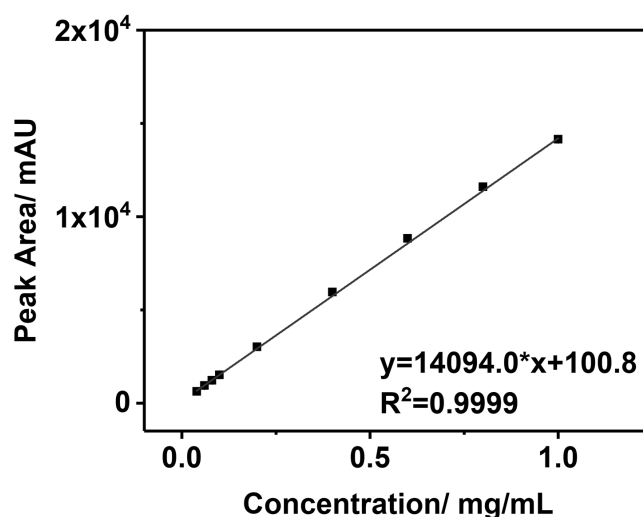


Figure 11.20 External calibration graph of caffeine in methanol in a concentration range between 0.04 mg/mL and 1.0 mg/mL determined via HPLC/UV.

11.10 Supporting Information for the Analysis of Antimalarial Agent Screening via HPTLC-FAPA-MS

Table 11.11 List of detected and identified ions for artemether and lumefantrine when analyzed by FAPA-MS.

Nominal mass (<i>m/z</i>)	Exact mass (<i>m/z</i>)	Rel. mass accuracy/ ppm	Ion
Artemether			
145	145.1015	2.4	C ₁₁ H ₁₃ ⁺
163	163.1121	2.0	C ₁₁ H ₁₅ O ⁺
179	179.1072	2.3	C ₁₁ H ₁₅ O ₂ ⁺
203	203.1435	2.4	C ₁₄ H ₁₉ O ⁺
207	207.1386	2.3	C ₁₃ H ₁₉ O ₂ ⁺
219	219.1384	2.0	C ₁₄ H ₁₉ O ₂ ⁺
221	221.1541	2.4	C ₁₄ H ₂₁ O ₂ ⁺
231	231.1385	2.0	C ₁₅ H ₁₉ O ₂ ⁺
239	239.1646	1.7	C ₁₄ H ₂₃ O ₃ ⁺
249	249.1490	1.9	C ₁₅ H ₂₁ O ₃ ⁺
267	267.1595	1.4	C ₁₅ H ₂₃ O ₄ ⁺
299	N.D. ^a	N.D. ^a	C ₁₆ H ₂₇ O ₅ ⁺
Lumefantrine			
130	130.1593	1.9	C ₈ H ₂₀ N ⁺
142	142.1593	1.9	C ₉ H ₂₀ N ⁺
172	172.1699	1.9	C ₁₀ H ₂₂ NO ⁺
406	406.1701	0.4	C ₂₃ H ₃₀ ³⁵ Cl ₂ NO ⁺
420	420.1494	0.9	C ₂₃ H ₂₈ ³⁵ Cl ₂ NO ₂ ⁺
510	510.1517	0.1	C ₃₀ H ₃₁ ³⁵ Cl ₃ N ⁺
528	528.1624	0.2	C ₃₀ H ₃₃ ³⁵ Cl ₃ NO ⁺
530	530.1594	0.3	C ₃₀ H ₃₃ ³⁵ Cl ₂ ³⁷ ClNO ⁺
544	544.1578	0.9	C ₃₀ H ₃₃ ³⁵ Cl ₃ NO ₂ ⁺
546	546.1542	0.1	C ₃₀ H ₃₃ ³⁵ Cl ₂ ³⁷ ClNO ₂ ⁺

^a N.D.: not detected

Abbreviations

AC	Alternating-current
ADI	Ambient desorption/ionization
AFM	Atomic force microscopy
APCI	Atmospheric-pressure chemical ionization
APGD	Atmospheric-pressure glow discharge
API	Atmospheric-pressure interface
APPI	Atmospheric-pressure photoionization
ASAP	Atmospheric-pressure solids analysis probe
C-G discharge	Corona-to-glow discharge
C18-PAN	C18-modified polyacrylonitrile
CI	Chemical ionization
CN	Cyano
CNT	Carbon nanotubes
Ø	Diameter
DAPCI	Desorption atmospheric-pressure chemical ionization
DART	Direct analysis in real time
DBDI	Dielectric-barrier discharge ionization
DC	Direct-current
DESI	Desorption electrospray ionization
DeSSI	Desorption sonic spray ionization
DFT	Density functional theory
DIOL	Diol
DMOA	<i>N,N</i> -Dimethyloctan-1-amine
DMSO	Dimethyl sulfoxide
DOD	Drop-on-demand
DoE	Design-of-experiments
DPA	Diphenylamine
ϵ	Emissivity
EASI	Easy ambient sonic-spray ionization
EESI	Extractive electrospray ionization
EIC	Extracted ion-chronogram

ESI	Electrospray ionization
FA	Formic acid
FAB	Fast atom bombardment
FAPA	Flowing atmospheric-pressure afterglow
FWHM	Full width at half maximum
G-A discharge	Glow-to-arc discharge
GC	Gas chromatography
GPU	Graphics processing unit
He*	Helium metastable atom
HNP	5-Nitro-1 <i>H</i> -pyridin-2-one
HPLC	High-performance liquid chromatography
HPTLC	High-performance thin-layer chromatography
HR	High-resolution
i.d.	Inner diameter
IDL	Instrumental detection limits
IR	Infrared
IT-SPME	In-tube solid-phase microextraction
ITO	Indium tin oxide
LA	Laser ablation
LAESI	Laser ablation electrospray ionization
LTP	Low-temperature plasma
m/z	Mass-to-charge ratio
MALDI	Matrix-assisted laser desorption ionization
MRFA	Met-Arg-Phe-Ala acetate salt
MS	Mass spectrometry
MSDS	Material safety data sheets
NH ₂	Amino
NMR	Nuclear magnetic resonance
NP	Silica plate (normal phase)
o.d.	Outer diameter
p2c	Pin-to-capillary
p2p	Pin-to-plate
P ₄ O ₁₀	Phosphorus pentoxide
PADI	Plasma-assisted desorption/ionization
PALDI	Plasma-assisted laser desorption ionization

PLC	Preparative-layer chromatography
PM	Probe-mode
PMMA	Polymethylmethacrylate
PS	Paper spray
PTFE	Polytetrafluoroethylene
PVDF	Polyvinylidene difluoride
ρ	Reflected temperature
RMA	Relative mass accuracy
ROI	Region-of-interest
RP	Reversed-phase
RSD	Relative standard deviation
SIMS	Secondary-ion mass spectrometry
SPME	Solid-phase microextraction
TLC	Thin-layer chromatography
TM	Transmission-mode
ToF	Time-of-flight
wt%	Percentage by weight

List of Figures

Figure 2.1 Schematic of the DART source instrumental setup published by Cody <i>et al.</i> ⁷ (a) and schematic of the DART ID-Cube (b).	8
Figure 2.2 Schematic of the h-FAPA source in front of the mass spectrometer inlet.	12
Figure 3.1 Schematic of the instrumental setup for FAPA-MS measurements operated in surface-sampling mode (a) and transmission-mode (b).....	33
Figure 3.2 Schematic of the instrument setup for direct surface-sampling by LTP-MS.	34
Figure 3.3 Absolute ion-abundance of caffeine (EIC of m/z 195.0879 \pm 8 ppm) detected via FAPA-MS with altered distance between FAPA anode tip and MS inlet capillary tip.....	40
Figure 3.4 Photograph of the 11 mm (upper) and 25 mm (lower) anode capillary used for the FAPA source.....	42
Figure 3.5 IR-thermography of the glass slide surface temperatures at the afterglow impact position of the FAPA source relative to the applied discharge current (a). Thermographic images of the FAPA with long (b) and short (c) anode capillary operated at 40 mA DC.	42
Figure 3.6 Mass spectra of DPA analyzed via TM-FAPA-MS with the 25 mm (a) and 11 mm (b) anode capillary of the FAPA source (positive-ion detection mode).	44
Figure 3.7 Integrated transient signal abundance of the $[M+H]^+$ -ion (black), the $[M-H+O]^+$ -ion (orange), and the $[(M+O)+H]^+$ -ion (blue) analyzed by the FAPA source with 25 mm (a) and 11 mm (b) anode capillary.....	46
Figure 3.8 Influence of the FAPA (11 mm version) interelectrode distance with respect to the signal abundance of the model substances caffeine (m/z 195.0879 \pm 8 ppm) and nicotine (m/z 163.1229 \pm 8 ppm) (a) and change of the power consumption of the FAPA source with altered electrode distance (b).	48

Figure 3.9 IR-thermography images of the cooled (a) and heated (b) sample well plate (quartz glass) and overview of the measured surface temperature in relation to the voltage applied to the Peltier element (c).	50
Figure 3.10 Mass spectra of LP30 after 7 days of thermal aging detected in positive-ion (a) and negative-ion (b) detection mode via LTP-MS.	52
Figure 3.11 Integrated ion abundance of electrolyte degradation products and raw electrolyte compounds after the electrolyte LP30 was thermally stressed for two weeks, and subsequently analyzed via LTP-MS in negative-ion detection mode.....	54
Figure 3.12 Extracted-ion chronogram of the electrolyte EC (a, m/z 89.0236 \pm 8 ppm), the m/z 126.9951 \pm 8 ppm (b) and m/z 125.0804 \pm 8 ppm (c) detected by an LTP-MS line scan across a cycled LIB electrode.....	55
Figure 4.1 Mass spectra of ST00484 (a-c), ST00552 (d-f), and ZLI-1544 (g-i) detected by DART-, LTP-, and FAPA-MS in positive-ion detection mode.....	67
Figure 4.2 Possible reaction pathway of the fragmentation and oxidation of ST00484 by FAPA-MS (a), followed by the oxidation of the fragmentation product (b).	70
Figure 4.3 Mass spectra of the CB15/E7 liquid crystal mixture analyzed by DART-, LTP-, and FAPA-MS (a-c) with an Exactive Plus mass spectrometer. External heating was used to enhance sample desorption. In (d-f) no external heating but the plasma source was exclusively used for sample desorption.....	75
Figure 4.4 Extracted-ion chronograms (EICs) of m/z 250, 278, 499, and 527 are shown (a-c).	77
Figure 4.5 Mass spectra of a liquid crystal mixture extracted from a commercially available LCD provided by Merck KGaA. The mixture was analyzed by DART- (a), LTP- (b), and FAPA-MS (c) (Exactive Plus) in positive-ion detection mode.	79
Figure 4.6 Mass spectra of the diluted liquid crystal model mixture analyzed by DART- (a), LTP- (b), and FAPA-MS (c) in positive-ion detection mode with an Exactive Plus mass spectrometer.	85

Figure 5.1 Schematic of the LA-h-FAPA-MS setup.....	95
Figure 5.2 Photograph (a) of the LCD test cell and mass spectral image (b) of the protonated molecular-ion of LC-XIV (m/z 383.3062 \pm 8 ppm) detected via FAPA-MS (positive-ion detection mode).	96
Figure 5.3 EIC of LC-XIV (m/z 383.3062 \pm 8 ppm) detected in positive-ion detection mode by a FAPA-MS line scan across the LCD test cell at $y=16$ mm.	98
Figure 5.4 Photograph (a) of the LCD test cell and mass spectral image (b) of the protonated molecular-ion of LC-XIV (m/z 383.3062 \pm 8 ppm) detected via LA-h-FAPA-MS (positive-ion detection mode).....	99
Figure 5.5 Excerpt of Figure 5.4b with the mass spectral image of LC-XIV (m/z 383.3062 \pm 8 ppm) detected via LA-h-FAPA-MS.	101
Figure 5.6 Mass spectrum of the Loctite 352 adhesive detected via FAPA-MS in positive-ion detection mode.....	102
Figure 5.7 Spatial distribution of the Loctite 352 adhesive in the LCD test cell detected via mass spectral imaging by FAPA-MS (a) and LA-h-FAPA-MS (b).	103
Figure 6.1 Mass spectra of caffeine ($[M^1+H]^+$, m/z 195.0879), caffeine- $^{13}C_3$ ($[M^2+H]^+$, m/z 198.0981) nicotine ($[M^3+H]^+$, m/z 163.1229), and acetaminophen ($[M^4+H]^+$, m/z 152.0705) standards directly desorbed from an RP-HPTLC plate by DESI-MS (a, c, e) and FAPA-MS (b, d, f) in positive-ion detection mode.....	116
Figure 6.2 (a) Combined mass spectral image of nicotine (m/z 163.1229 \pm 8 ppm), caffeine (m/z 195.0879 \pm 8 ppm), and acetaminophen (m/z 152.0705 \pm 8 ppm) detected via HPTLC-FAPA-MS after separation of the analyte mixture on a NP-HPTLC plate (three spots deposited in dashed ellipses).....	119
Figure 6.3 Sum of voxel volumes for the protonated molecular ion of caffeine (m/z 195.0879 \pm 8 ppm, $n=3$) relative to the post-separation drying temperature of the HPTLC plate.	120
Figure 6.4 Sum of voxel volumes for selected analytes relative to different commercially available stationary phases.....	122

- Figure 6.5** Signal abundance of caffeine (orange, m/z 195.0879 \pm 8 ppm, [M+H]⁺), nicotine (blue, m/z 163.1229 \pm 8 ppm, [M+H]⁺), and acetaminophen (green, m/z 152.0705 \pm 8 ppm, [M+H]⁺) for the direct desorption/ionization by FAPA-MS from different silica plates. 126
- Figure 6.6** Sum of voxel volumes for caffeine (m/z 195.0879 \pm 8ppm, [M+H]⁺, n=3, error bars represent the standard deviation of replicate measurements) determined via TLC-FAPA-MS with TLC plates inhabiting different thicknesses of the stationary phase (100-2000 μ m)..... 127
- Figure 6.7** Mass spectral image using FAPA-MS of (a) m/z 195.0879 \pm 8 ppm (caffeine) and (b) m/z 198.0981 \pm 8 ppm (caffeine-¹³C₃) of the energy drink from brand A, B, and C on a NP-HPTLC silica plate after separation of the spiked energy drink liquids (after separation the solvent was evaporated at 50 °C for 15 min prior to mass spectral imaging). 129
- Figure 7.1** Mass spectral image of m/z 528.1624 \pm 8 ppm (blue, Lumefantrine) and m/z 249.1490 \pm 8 ppm (green, Artemether) extracted from a Coartem[®] tablet and separated on a CN-modified HPTLC silica plate prior FAPA-MS analysis (positive-ion detection mode). 139
- Figure 7.2** Mass spectra of artemether (a) and lumefantrine (b) detected by FAPA-MS in positive-ion detection mode..... 140
- Figure 7.3** Suggested fragmentation mechanism of positive-charged ions for artemether (a, modelled and expanded from reference ²⁰² and ²⁰³) and lumefantrine (b) occurring during the FAPA ionization process. 141
- Figure 7.4** Molecular structure of lumefantrine (a) and the isomeric compound (impurity A, b) paired with the FAPA-MS mass spectra of respective compounds, respectively..... 146
- Figure 8.1 (Fig. 1)** Scheme of the decomposition of P₄O₁₀ with DMSO..... 151
- Figure 8.2 (Fig. 2)** Bottom spectrum: ³¹P{¹H} NMR spectrum of P₄O₁₀ in DMSO; Top spectrum: ³¹P NMR spectrum of P₄O₁₀ in DMSO; areas with occurring multiplets are shown magnified. 151
- Figure 8.3 (Fig. 3)** Top: Measured ³¹P liquid-state NMR spectrum. Bottom: Simulated ³¹P liquid-state NMR spectrum of the A₂X'XA₂'-spin system.... 151

- Figure 8.4 (Fig. 4)** Zoom in of a ^{31}P COSY spectrum (middle). On the x and y axis ^{31}P single excitation spectra are shown. On the right top the sum projection of the section from the COSY spectrum surrounded by the box is shown versus a simulated sum projected of a μ -oxidocyclotetratephosphate-anion (XIII) with an A_2X_2 -spin system. On the left top a zoom in the section is shown versus the simulation of the COSY spectrum of the A_2X_2 -spin system.....152
- Figure 8.5 (Fig. 5)** Positive-ion mode mass spectra of (A) DMSO and (B) the P_4O_{10} -DMSO mixture detected via FAPA-MS.....152
- Figure 8.6 (Fig. 6)** Excerpt of the negative-ion mode mass spectrum of the Onodera reagent.152
- Figure 8.7 (Scheme 1)** Schematic drawing of the suggested reaction mechanism between DMSO and P_4O_{10}153
- Figure 8.8 (Figure S1)** Mass spectrum of pure DMSO in the mass range between m/z 50 and 150 detected by FAPA-MS in positive-ion mode.....156
- Figure 8.9 (Figure S2)** Mass spectrum of the P_4O_{10} -DMSO mixture detected by FAPA-MS in negative-ion mode.....157
- Figure 8.10 (Figure S3)** Instrumental setup of transmission-mode FAPA-MS.....158
- Figure 8.11 (Figure S4)** Zoom in of a ^{31}P COSY spectrum (middle). On the x and y axis ^{31}P single excitation spectra are shown. On the right top the sum projection of the section from the COSY spectrum surrounded by the box is shown versus a simulated sum projection. On the left top a zoom in the section is shown versus the simulation of the COSY spectrum of the *ortho*-phosphono-tricyclophosphate anion with ADMX spin system. The found J-couplings are depicted in the figure.....159
- Figure 8.12 (Figure S5)** Zoom in of a ^{31}P COSY spectrum (middle). On the x and y axis ^{31}P single excitation spectra are shown. On the right top the sum projection of the section from the COSY spectrum surrounded by the box is shown versus a simulated sum projection. On the left top a zoom in the section is shown versus the simulation of the COSY spectrum of another *ortho*-phosphono-tricyclophosphate anion with A_2MX spin system. The found J-couplings are depicted in the figure.....159
- Figure 8.13 (Figure S6)** Optimized structures on DFT (PBE1PBE/aug-cc-pVTZ) level. (a) $\text{C}_2\text{H}_5\text{S}^+$, (b) cyclo- $\text{C}_2\text{H}_5\text{S}^+$, (c) $\text{H}_2\text{C-S-CH}_3^+$160

- Figure 11.1** Overlay of a picture and an IR image of the FAPA source (short capillary, 40 mA) with an aluminum plate used as a sample surface. 187
- Figure 11.2** Reflected temperature measured by IR-thermography at different operation currents of the FAPA source. 187
- Figure 11.3** Screenshot of the IRSoft software used for data evaluation after IR imaging (a). In (b) a zoom-in of the top left corner of (a) (red square) is shown for visualization purposes. 189
- Figure 11.4** Overlay of the IR image and the picture taken of the FAPA source and glass microscope slide..... 190
- Figure 11.5** Transient signal of m/z 170.0965 \pm 8 ppm ($[M+H]^+$ peak of DPA) analyzed by TM-FAPA-MS..... 191
- Figure 11.6** Ion abundance of caffeine (m/z 195.0879 \pm 8 ppm) detected via a line scan with FAPA-MS across a HPTLC silica plate..... 192
- Figure 11.7** 3D plot of the caffeine ion abundance (m/z 195.0879 \pm 8 ppm) in x and y direction on the HPTLC plate. 193
- Figure 11.8** (a) Combined mass spectral image of nicotine (m/z 163.1229 \pm 8 ppm), caffeine (m/z 195.0879 \pm 8 ppm), and acetaminophen (m/z 152.0705 \pm 8 ppm) detected via HPTLC-FAPA-MS after separation of the analyte mixture on a NP-HPTLC plate (three spots deposited in dashed ellipses)..... 194
- Figure 11.9** Calibration curves for DPA measured with TM-FAPA-MS with a 25 mm (a) and 11 mm (b) anode capillary..... 195
- Figure 11.10** External calibration graph of caffeine separated on a RP-HPTLC plate and analyzed via FAPA-MS..... 196
- Figure 11.11** External calibration curves for quinine (a) and artemether (b) analyzed by CN-HPTLC-FAPA-MS. 196
- Figure 11.12** Mass spectra of LP30 before thermal aging detected in positive-ion (a) and negative-ion (b) detection mode via LTP-MS. 198
- Figure 11.13** Mass spectra (positive-ion detection mode) of ST00484 (a-c), ST00552 (d-f), and ZLI-1544 (g-i) detected by DART-, LTP-, and FAPA-MS without external heating of the sample holder. 202

- Figure 11.14** Combined extracted-ion chronograms of m/z 318.17 and m/z 319.18 detected with DART- (a), LTP- (b), and FAPA-MS (c). In (d-f) the corresponding dilution series with five measurement points is shown in a concentration range from 100 ng to 12 pg absolute deposited amount of sample (95% confidence interval shown in grey) 203
- Figure 11.15** Mass spectral image of the protonated molecular ions for the liquid crystals LC-XIII (a, m/z 348.2688), LC-IV/V (b, m/z 250.1588), and LC-I (c, m/z 268.1699). 207
- Figure 11.16** Mass spectral image of the protonated molecular ions for the liquid crystals LC-XIII (a, m/z 348.2688), LC-IV/V (b, m/z 250.1588), and LC-I (c, m/z 268.1699). 208
- Figure 11.17** EIC of LC-XIV (m/z 383.3062 \pm 8 ppm) detected in positive-ion detection mode with a line scan by LA-h-FAPA-MS across the LCD test cell at $y=14.15$ mm. 210
- Figure 11.18** Sum of voxel volumes for the $[M+H]^+$ -ion of caffeine (m/z 195.0879 \pm 8 ppm, $n=3$) relative to the drying temperature of the HPTLC plate. 212
- Figure 11.19** Extracted ion-chromatogram (EIC) of the protonated molecular-ion of caffeine (m/z 195.0879) and caffeine- $^{13}C_3$ (m/z 198.0981) in comparison to a matrix compound (m/z 180.0881). 213
- Figure 11.20** External calibration graph of caffeine in methanol in a concentration range between 0.04 mg/mL and 1.0 mg/mL determined via HPLC/UV. 216

List of Tables

Table 4.1 Comparison of specific DART-, LTP-, and FAPA parameter. ^{5,39}	61
Table 4.2 List of LCs analyzed by DART-, LTP-, and FAPA-MS.....	65
Table 4.3 Identified molecular cations for the CB15/E7 liquid crystal mixture detected by DART-, LTP-, and FAPA-MS.	72
Table 4.4 IDLs for the analysis of liquid crystals incorporated in an LCD by TM-ADI-MS. ^a	81
Table 4.5 Liquid crystal mixtures detected by DART- ^a , LTP- ^b , and FAPA-MS ^c	82
Table 6.1 Coefficient of variation for the HPTLC-FAPA-MS analysis of caffeine deposited on different stationary phases (conditioned at different drying temperatures).....	121
Table 8.1 (Table 1) Assigned spin systems to the molecules found by NMR. R is an unknown residue.....	150
Table 8.2 (Table 2) Results of the DFT calculations at PBE1PBE/aug-cc-pVTZ level, energy values are given at 430 K, which is approximately the temperature of the MS experiments. Thermal correction, hindered rotor correction and ΔE are given in kJ mol^{-1} . ΔE_{total} is the total energy difference between the present and the lowest energetic isomer.....	153
Table 8.3 (Table S1) List of identified peaks in the mass spectrum of the P_4O_{10} -DMSO mixture detected by FAPA-MS (negative-ion mode).	157
Table 8.4 (Table S2) Results of the calculations at HF/6-31G(d,p) level. ΔE_{total} is the total energy difference between the present and the lowest energetic isomer.	160
Table 8.5 (Table S3) Results of the DFT calculations at PBE1PBE/aug-cc-pVTZ level. ΔE_{total} is the total energy difference between the present and the lowest energetic isomer.	160
Table 11.1 Mass spectrometer operating conditions used for the FAPA-MS and LTP-MS experiments in chapter 3.	182
Table 11.2 Operating conditions of the Exactive mass spectrometer used for analysis of liquid crystals via plasma-based ADI-MS in chapter 4.....	183

Table 11.3 Exactive operating conditions for the analysis of the LCD test cell via mass spectral imaging by FAPA-MS and LA-h-FAPA-MS in chapter 5.....	184
Table 11.4 Exactive operating conditions for the comparison between DESI- and FAPA-MS for direct sample analysis on HPTLC plates.	185
Table 11.5 Mass spectrometer settings used for the analysis of antimalarial active agents via TLC-FAPA-MS in chapter 7.	186
Table 11.6 List and detailed information of all liquid crystals analyzed in chapter 4.	199
Table 11.7 Liquid crystals employed in the LCD test cell.	204
Table 11.8 List of chemicals in the Loctite 352 adhesive by Henkel. ^a	209
Table 11.9 List of TLC stationary phases used in this chapter.	211
Table 11.10 R _f values for the analytes in the test mixture separated on different HPTLC stationary phases.....	212
Table 11.11 List of detected and identified ions for artemether and lumefantrine when analyzed by FAPA-MS.	217

Acknowledgements

This doctoral thesis was compiled in the time between December 2013 and June 2019 at the Department of Chemistry and Biology of the University of Siegen. Without the help of several people this work would not have been possible and therefore I would like to acknowledge their companion during that period of time.

First and foremost, I would like to thank Prof. Dr. Carsten Engelhard, who gave me the opportunity to pursue the doctoral title in his research group with an interesting research topic. With his infrastructure of high-end mass spectrometers and scientific advice he significantly supported me in my work. Furthermore, I would like to thank the second dissertation reviewer, Prof. Dr. Ulrich Jonas, as well as the two members of the doctoral commission, Prof. Dr. Holger Schönherr and Prof. Dr. Heiko Ihmels, for their time to review of my scientific work.

I thank Prof. Dr. Jacob T. Shelley who was a mentor for me in the research field of ambient desorption/ionization mass spectrometry techniques. He gave me the opportunity to perform experiments for my dissertation in his laboratory for several months and I really appreciate his scientific advices during the past years. Additionally, he became a good friend who also supported me mentally during some stressful times of the doctoral thesis.

Furthermore, I thank the whole Engelhard research group, namely, Sigrid Hübner, Ulrike Koch, Narmina Heupel, Alessa Schneider, Derick Ateacha, Darya Mozhayeva, Bastian Spelz, Lothar Veith, Danica Heller, Anastasia Albert, Annika Schardt, Maximilian Heide, and especially Ingo Strenge. It was a pleasure to work with all of you and I will always remember the long working days in the lab with Ingo. For the most part, Ingo and I went through the ups and downs of our dissertations together and I'm so glad that we became very good friends during that time.

I would like to thank the researchers at the liquid crystal institute (LCI, Kent State University), Prof. Dr. Torsten Hegmann and Dr. Min Gao, and I also thank Prof. Dr. Robert Twieg and Dr. Prabin Rai (Department of Chemistry and Biochemistry, Kent State University) who shared their knowledge about liquid crystals with me and who gave me the opportunity to use their instrumental equipment at

KSU. Furthermore, Dr. Peter Leonard, Dr. Claudia Enders, Svetlana Fartowski, Hans Griesinger, Michael Schulz, and Michaela Oberle is gratefully acknowledged for their support with liquid crystal sample material, TLC plates, and analytical reference standards. I also thank this group of Merck KGaA employees for the fruitful scientific discussions.

I thank the German Academic Exchange Service (DAAD) for the financial support (Grant: 91597200) for my research stay in the laboratory of Prof. Dr. Jacob T. Shelley. Furthermore, I thank the Analytical Chemistry Division of the German Chemical Society for several conference travel grants.

I thank my colleagues and friend at the JCF Siegen. It was always fun to work with you guys and this voluntary work really helped to get a different perspective on my research. It was also a pleasure to strengthen the young chemists' community in Siegen together with all of you.

Lastly, I want to thank my parents Patricia and Heinz, my brother Philipp, my girlfriend Laura, and my friends who always supported me during the last few years. Even though most of you couldn't help me scientifically during the time I pursued the doctoral title, but you all supported me mentally so I made it through the stressful times in the lab and while I was writing my dissertation. Thank you so much!

Curriculum Vitae

List of Publications

Peer-reviewed Journals

C. Kuhlmann, M. Heide, C. Engelhard:

Fast Screening and Quantitative Mass Spectral Imaging of Thin-Layer Chromatography Plates with Flowing Atmospheric-Pressure Afterglow High-Resolution Mass Spectrometry,

Anal. Bioanal. Chem., **2019**, *411*, 6213-6225.

(DOI: 10.1007/s00216-019-02013-8)

C. Kuhlmann, J. T. Shelley, C. Engelhard:

Plasma-based Ambient Desorption/Ionization Mass Spectrometry for the Analysis of Liquid Crystals Employed in Display Devices,

J. Am. Soc. Mass Spectrom., **2019**, *30*, 2101–2113.

(DOI: 10.1007/s13361-019-02280-w)

D. N. Ateacha, C. Kuhlmann, C. Engelhard:

Rapid Screening of Antimalarial Drugs Using Low-Temperature Plasma Desorption/Ionization Orbitrap Mass Spectrometry,

Anal. Methods, **2019**, *11*, 566-574.

(DOI: 10.1039/C8AY02538J)

S. Johansson, C. Kuhlmann, J. Weber, T. Paululat, C. Engelhard,

J. Schmedt auf der Günne:

Decomposition of P4O10 in DMSO,

Chem. Commun., **2018**, *54*, 7605-7608.

(DOI: 10.1039/C8CC03000F)

P. Kodali, A. Jurkevica, J. Landero, C. Kuhlmann, J. Caruso, O. Adeoye:

Multiple liquid chromatography separations and nanoESI-ion trap detection of plasma proteins in search of stroke biomarkers – a pilot study,

J. Sep. Sci., **2012**, *35*, 2153-2161.

(DOI: 10.1002/jssc.201200216)

Invited Oral Presentations

C. Kuhlmann, J.T. Shelley, C. Engelhard:
Comparison of LTP-, FAPA-, and LA-hFAPA-MS for Direct Surface Analysis,
SciX 2017, Reno (NV), USA, October 2017.

Oral Presentations

C. Kuhlmann, M. Heide, C. Engelhard:
Comparison of TLC-LTP-MS and TLC-FAPA-MS: Fundamental Studies and
Selected Applications,
51. Annual Conference of the German Society of Mass Spectrometry (DGMS), Saarbrücken,
Germany, March 2018.

C. Kuhlmann, C. Engelhard:
Ambient Desorption/Ionization Mass Spectrometry: A Versatile Tool for Direct
Sample Analysis,
GDCh & JCF Colloquium of the Local Section Siegen, Siegen, Germany,
December 2017.

C. Kuhlmann, S.P. Badal, J.T. Shelley, C. Engelhard:
Liquid Crystal Display Surface Analysis for Fast Display Failure Investigation by
Ambient Desorption/Ionization Mass Spectrometry,
European Winter Conference on Plasma Spectrochemistry, St. Anton, Austria, February
2017.

C. Kuhlmann, V.A. Brückel, S.P. Badal, J.T. Shelley, C. Engelhard:
Liquid Crystal Display Surface Analysis for Fast Display Failure Investigation by
Ambient Desorption/Ionization Mass Spectrometry,
*Interdisciplinary PhD Candidate Seminar of the German Association for Analytical
Spectroscopy (DAAS)*, Ulm, Germany, March 2016.

C. Kuhlmann, V.A. Brückel, S.P. Badal, J.T. Shelley, C. Engelhard:
Direkte und ortsaufgelöste Charakterisierung von Flüssigkristalldisplays mittels
Laser Ablation, plasmabasierter Desorption/Ionisation und hochauflösender
Massenspektrometrie (LA-FAPA-HRMS),
49. Annual Conference of the German Society of Mass Spectrometry (DGMS), Hamburg,
Germany, February 2016.

Poster Presentations

C. Kuhlmann, M. Heide, C. Engelhard:
Fast Screening and Mass Spectral Imaging of Thin-Layer-Chromatography Plates with FAPA-MS: Fundamental Studies and Selected Applications,
Anakon, Münster, Germany, March 2019.

C. Kuhlmann, M. Heide, C. Engelhard:
TLC-MS Coupling: Fundamental Studies for Plasma-based ADI-MS Techniques,
20. Frühjahrsymposium, Konstanz, Germany, March 2018.

C. Kuhlmann, S.P. Badal, J.T. Shelley, C. Engelhard:
Fast Analysis of Liquid Crystal Displays by Plasma-based Ambient Desorption/Ionization Mass Spectrometry,
Anakon, Tübingen, Germany, March 2017.

C. Kuhlmann, C. Engelhard:
Plasma- and Spray-based Ambient Desorption/Ionization Mass Spectrometry for Quantitative Agent Screening on TLC Plates,
Anakon, Tübingen, Germany, March 2017.

C. Kuhlmann, C. Engelhard:
Plasma- and Spray-based Ambient Desorption/Ionization Mass Spectrometry for Quantitative Agent Screening on TLC Plates,
European Winter Conference on Plasma Spectrochemistry, St. Anton, Austria, February 2017.

C. Kuhlmann, C. Engelhard:
Direct Liquid Crystal Analysis by Plasma-based Ambient Desorption/Ionization Mass Spectrometry,
25. ICP-MS User Meeting and 12. Symposium of Mass Spectrometry Techniques for Elemental Trace Analysis, Siegen, Germany, September 2016.

C. Kuhlmann, S.P. Badal, J.T. Shelley, C. Engelhard:
Direct Liquid Crystal Analysis by Plasma-based Ambient Desorption/Ionization Mass Spectrometry,
Winter Conference on Plasma Spectrochemistry, Tucson (AZ), USA, January 2016.

C. Kuhlmann, C. Enders, P. Leonhard, C. Heiß, C. Engelhard:
Direct Analysis of Liquid Crystal Displays (LCDs) by Low-temperature Plasma
Ambient Desorption/Ionization High-Resolution Mass Spectrometry,
Anakon, Graz, Austria, March 2015.

C. Kuhlmann, I. Pastushkina, S. Nowak, C. Engelhard:
Direct Analysis of Degradation Products in Lithium-ion Batteries Using Low-
temperature Plasma Ambient Desorption/Ionization High-Resolution Mass
Spectrometry,
Anakon, Graz, Austria, March 2015.

C. Kuhlmann, I. Pastushkina, S. Nowak, C. Engelhard:
Direct Analysis of Degradation Products in Lithium-ion Batteries Using Low-
temperature Plasma Ambient Desorption/Ionization High-Resolution Mass
Spectrometry,
48. Jahreskonferenz der Deutschen Gesellschaft für Massenspektrometrie (DGMS),
Wuppertal, Germany, March 2015.

C. Kuhlmann, C. Enders, P. Leonhard, C. Heiß, C. Engelhard:
Direct Analysis of Liquid Crystal Displays (LCDs) by Low-temperature Plasma
Ambient Desorption/Ionization High-Resolution Mass Spectrometry,
European Winter Conference on Plasma Spectrochemistry, Münster, Germany, February
2015.

C. Kuhlmann, I. Pastushkina, S. Nowak, C. Engelhard:
Direct Analysis of Degradation Products in Lithium-ion Batteries Using Low-
temperature Plasma Ambient Desorption/Ionization High-Resolution Mass
Spectrometry,
European Winter Conference on Plasma Spectrochemistry, Münster, Germany, February
2015.

Erklärungen

Gemäß §7 der Promotionsordnung vom 8. Juni 2017

Ich erkläre,

1. dass mir die Promotionsordnung vom 8. Juni 2017 bekannt ist und von mir anerkannt wird.
2. dass ich weder früher noch gleichzeitig bei einer anderen Hochschule oder in einer anderen Fakultät ein Promotionsverfahren beantragt habe.
3. hiermit an Eides statt, dass ich die vorliegende Arbeit ohne unzulässige Hilfe Dritter und ohne Benutzung anderer, nicht angegebener Hilfsmittel angefertigt habe. Die aus anderen Quellen direkt oder indirekt übernommenen Daten und Konzepte sind unter Angabe der Quelle gekennzeichnet. Die Arbeit wurde bisher weder im In- noch im Ausland in gleicher oder ähnlicher Form einer anderen Prüfbehörde oder einer ähnlichen Organisation in Anspruch genommen.
4. dass keine Dienste eines Promotionsvermittlungsinstituts oder einer ähnlichen Organisation in Anspruch genommen wurden.
5. dass zu den vorgeschlagenen Mitgliedern der Promotionskommission keine verwandtschaftlichen Beziehungen, keine Verwandtschaft ersten Grades, Ehe, Lebenspartnerschaft oder eheähnliche Gemeinschaft besteht.
6. dass in meiner Dissertation Forschungsergebnisse verwendet worden sind, die in Zusammenarbeit mit den folgenden Wissenschaftlern gewonnen wurden (Namen, akademische Grade und Anschrift):

FAPA-MS	Prof. Dr. Jacob T. Shelley
Instrumentierung & Messungen	Department of Chemistry and Chemical Biology, Rensselaer Polytechnic Institute, Troy, NY 12180, USA

NMR Messungen, DFT Berechnungen	Prof. Dr. Jörn Schmedt auf der Günne, Dr. Johannes Weber, Sebastian Johansson Anorganische Materialchemie, Department Chemie/Biologie, Universität Siegen, Adolf-Reichwein-Str. 2, 57076 Siegen
------------------------------------	--

NMR Messungen

Dr. Thomas Paululat
Organische Chemie,
Department Chemie/Biologie,
Universität Siegen,
Adolf-Reichwein-Str. 2, 57076 Siegen

Siegen,
